UNIVERSITY OF CALIFORNIA SAN DIEGO

Ultrasonic Structural Monitoring via Passive Identification and Synthetic Aperture Imaging Techniques

A dissertation submitted in partial satisfaction of the requirements for the degree Doctor of Philosophy

in

Structural Engineering

by

Albert Yi-Ling Liang

Committee in charge:

Professor Francesco Lanza di Scalea, Chair
Professor William S. Hodgkiss
Professor Hyonny Kim
Professor Kenneth J. Loh
Professor Yu Qiao

2020

The Dissertation of Albert Yi-Ling Liang is approved, and it is acceptable in quality and form for publication on microfilm and electronically:

_____

_____

_____

_____

_____

Chair

University of California San Diego

2020

DEDICATION

To my wife, Demi, and to my parents, Yuann-wen and Dr. Fei-Lin. Your love has made me everything that I am today.

TABLE OF CONTENTS

LIST OF FIGURES

LIST OF TABLES

ACKNOWLEDGMENTS

This research was funded by Project Manager Dr. Robert Wilson with the US Federal Railroad Administration under grant FR-RRD-0027-11-01, DTFR5316C00024, and 693JJ619C000008. This work would not be possible without the financial support of the Federal Railroad Administration. Thank you to Brian Linderman, Anish Poudel, and the staff at Transportation Technology Center, Inc, along with Eric Sherrock and Jeff Meunier at Ensco, for their technical support during field test. This work would not be possible without their amazing support and guidance.

I am forever indebted to my advisor, Professor Francesco Lanza di Scalea for his guidance. Thank you for giving me this opportunity. Your enthusiasm, determination, and kindness have pushed me not only academically but also personally. I could not have wished for a better advisor and mentor.

I would like to thank my committee for the support of my research. A special thank you to Professor William S. Hodgkiss who was one of the best teachers I have had in my career. Thank you for always being available to discuss the technical challenges I've had. My interest and fascination with signal processing would not have happened without your lectures. Thank you to Professor Kenneth J. Loh for his cheerful attitude and introduction into the world of multifunctional materials, Professor Yu Qiao for his lectures on polymer manufacturing, and Professor Hyonny Kim for his coursework on composite analysis.

Much of the work would not have been possible without the collaboration with the members of the NDE/SHM Laboratory at UCSD – I'm grateful to have worked by you all: Xuan "Peter" Zhu, Simone Sternini, Margherita Capriotti, Diptojit Datta, and Ranting Cui. A profound thank you to Simone Sternini. His energy, patience, and technical ability are unparalleled and have served as a source of inspiration through my time here. Thank you

to Margherita Capriotti, whose numerous discussions have been instrumental in my personal and academic development. Lastly, thank you, to Diptojit Datta for his help with analysis on the final stages of this research.

Thank you to Andrew Ellison and Abdullah Hamid. I'm grateful for the friendship and support through the years. I've been extremely lucky to have known both of you.

Finally, I would like to thank my family: mom and dad for their love and patience, Alice and Amy for their never-ending support, and my wife for always being there.

Chapter 3, in part, has been published in Structural Health Monitoring, Sternini, S., Liang, A, Lanza di Scalea, F. (2018) with the title "Ultrasonic synthetic aperture imaging with interposed transducer–medium coupling path". The dissertation author was the primary author of this chapter.

Chapter 3, in part, has been published in The Journal of the Acoustical Society of *America*, Lanza di Scalea, F., Sternini, S., and Liang, A. (2018), with the title "Robust Passive Reconstruction of Dynamic Transfer Function in Dual-Output Systems". The dissertation author was the primary author of this chapter.

Chapter 5, in part, has been published in *Materials Evaluation*, Liang, A., Sternini, S., Lanza di Scalea, F. (2019) with the title "High-Speed Ultrasonic Rail Inspection by Passive Noncontact Technique". The dissertation author was the primary author of this chapter. The dissertation author was the primary author of this chapter.

Chapter 5, in part, has been published in *The Journal of the Acoustical Society of America*, Lanza di Scalea, F., Sternini, S., and Liang, A. (2018), with the title "Robust Passive Reconstruction of Dynamic Transfer Function in Dual-Output Systems". The dissertation author was the primary author of this chapter.

Chapter 5, in part, has been published in *The Journal of Nondestructive Evaluation, Diagnostics, and Prognostics of Engineering*, Lanza di Scalea, F., Zhu, X., Capriotti, M., Liang, A., Mariani, S., Sternini, S. (2018), with the title “Passive Extraction of Dynamic Transfer Function from Arbitrary Ambient Excitations: Application to High-Speed Rail Inspection from Wheel-Generated Waves”. The dissertation author was the primary author of this chapter.

Chapter 5, in part, is coauthored with Datta, Diptojit. The dissertation author was the primary author of this chapter.

Chapter 6, in part, has been published in *Materials Evaluation*, Sternini, S., Liang, A, Lanza di Scalea, F. (2019) with the title “Rail Flaw Imaging by Improved Ultrasonic Synthetic Aperture Focus Techniques”. The dissertation author was the primary author of this chapter.

VITA

2012 – 2016	Bachelor of Science in Structural Engineering
	University of California, San Diego
2016 – 2019	Master of Science in Structural Health Monitoring & Non-Destructive Evaluation
	University of California, San Diego
2016 – 2020	Doctor of Philosophy in Structural Engineering
	University of California, San Diego

PUBLICATIONS

Journal Articles:

- Liang, A. Y., Sternini, S., Capriotti, M., & Lanza di Scalea, F. (2019). High Speed Ultrasonic Rail Inspection by Passive Non-contact Technique. *Materials Evaluation*, *77*(7), 941-950.
- Sternini, S., Liang, A. Y., & Lanza di Scalea, F. (2019). Rail Flaw Imaging by Improved Ultrasonic Synthetic Aperture Focus Techniques. *Materials Evaluation*, *77*(7), 931-940.
- Sternini, S., Liang, A. Y., & Lanza di Scalea, F. (2018). Ultrasonic synthetic aperture imaging with interposed transducer–medium coupling path. *Structural Health Monitoring*, 1475921718805514.
- Lanza di Scalea, F., Sternini, S., & Liang, A. Y. (2018). Robust passive reconstruction of dynamic transfer function in dual-output systems. *The Journal of the Acoustical Society of America*, *143*(2), 1019-1028.
- Lanza di Scalea, F., Zhu, X., Capriotti, M., Liang, A. Y., Mariani, S., & Sternini, S. (2018). Passive extraction of dynamic transfer function from arbitrary ambient excitations: Application to high-speed rail inspection from wheel-generated waves. *Journal of Nondestructive Evaluation, Diagnostics and Prognostics of Engineering Systems*, *1*(1), 011005.

Conference Proceedings:

- Liang, A., Sternini, S., Capriotti, M., Zhu, P. X., Lanza di Scalea, F., & Wilson, R. (2019). Passive extraction of Green's function of solids and application to high-speed rail inspection. In *Sensors and Smart Structures Technologies for Civil, Mechanical, and Aerospace Systems 2019* (Vol. 10970, p. 109700R). International Society for Optics and Photonics.
- Liang, A. Y., Sternini, S., Lanza Di Scalea, F., Wilson, R., & Carr, G. (2018). Rail Flaw Identification Using Ultrasonic Imaging. *Transportation Research Board 97th Annual Meeting* (No. 18-01808).

- Lanza di Scalea, F., Zhu, X., Capriotti, M., Liang, A., Mariani, S., Sternini, S., & Wilson, R. (2018). High-speed non-contact ultrasound system for rail track integrity evaluation. In *Health Monitoring of Structural and Biological Systems XII*(Vol. 10600, p. 106000J). International Society for Optics and Photonics.
- Zhu, X., Sternini, S., Capriotti, M., Liang, A., Mariani, S., Lanza di Scalea, F., & Wilson, R. (2017). High-speed Non-contact Passive-only Ultrasonic Inspection of Rails from Deconvolutions of Wheel-generated Noise. *Structural Health Monitoring 2017*, (shm).
- Sternini, S., Liang, A., Lanza di Scalea, F., & Wilson, R. (2017). Pushing the Limits of Ultrasonic Imaging of Solids by Wave Mode Beamforming and GPU Processing. *Structural Health Monitoring 2017*, (shm).

ABSTRACT OF THE DISSERTATION

Ultrasonic Structural Monitoring
via
Passive Identification and Synthetic Aperture Imaging Techniques

by

Albert Yi-Ling Liang

Doctor of Philosophy in Structural Engineering

University of California San Diego, 2020

Professor Francesco Lanza di Scalea, Chair

Non-destructive Evaluation (NDE) is the process of using non-invasive procedures to inspect or characterize an object without altering its form, fit, or function. Ultrasonic testing is one of the most popular NDE techniques due to its wide range of applicable materials and non-hazardous operations to personnel or equipment. One of its disadvantages, traditionally, is the requirement for manual, in contact, inspection and extensive technical knowledge to interpret the results. This dissertation addresses these problems through experimental validation of a two-part inspection technique: passive transfer function defect detection followed by synthetic aperture imaging defect

quantification. First, results from full-scale experiments on rails up to 80 mph are used to validate the high-speed, non-contact, passive defect detection prototype. Next, results from a real-time ultrasonic imaging prototype for rail flaw sizing are used to demonstrate fast, straightforward, quantification of defect geometry.

Passive ultrasonic inspection and ultrasonic imaging are complementary technologies: the first is for high-speed detection of suspect regions but does not label the type or size of defects; whereas, the second is for defect verification of suspect regions and visually displays the precise defect size and orientation. The ability to quickly inspection regions of interest and subsequently accurately quantify the extent of damage is integral for a reliable and cost-effective resource management program.

CHAPTER 1

INTRODUCTION

1.1 Motivation

The aim of this dissertation is to advance the capabilities of ultrasonic testing in the field of NDE with more precise and cost-effective methods of inspection. Alternative methods of inspection are presented that not only maintain the object's future usefulness after inspection, but also reduces the associated cost and training with interpreting the inspection results. A method of passive ultrasonic inspection and structural ultrasonic tomography is proposed and applied to rail defect detection and quantification. The first method's goal is for inspections to take place on the structure by utilizing natural ambient excitations to develop a binary health state (defect or no defect). The latter generates easy-to-analyze visual data on regions flagged as suspect. Ultimately, the use of NDE as a diagnostic tool is dependent on the balance between economics and safety. By offering inspection tools that minimize maintenance disruptions and maximize the remaining useful-life data for asset stakeholders, both economics and safety can be improved.

1.2 Outline

The emphasis of this dissertation is on ultrasonic testing using bulk waves for ultrasonic imaging, and guided waves for passive ultrasonic defect detection. Although the primary application of this research was on rails, the signal processing algorithms proposed can be applied to data processing for inspection of other civil and aerospace structures.

Chapter 2 provides background information on bulk waves and guided waves. Bulk waves are used for ultrasonic imaging while guided waves are used for passive defect detection.

Chapter 3 focuses on the theoretical considerations of the signal processing algorithms for ultrasonic imaging using synthetic aperture focusing technique and for passive ultrasonic defect detection using a dual-output transfer function reconstruction model.

Chapter 4 presents background information on defect detection and ultrasonic testing in the railroad industry.

Chapter 5 is on the application of passive ultrasonic defect detection via non-contact air-coupled transducers. Results from 2016, 2018, and 2019 field tests are discussed along with the justification behind the signal processing parameters.

Chapter 6 presents results on the application of ultrasonic imaging on the defect characterization of rails. 2D and 3D imaging results are shown for natural and man-made defects.

Chapter 7 serves as the conclusion of this dissertation and summarizes key findings. A section on recommended further research is also included.

CHAPTER 2

ELASTIC WAVE PROPAGATION THEORY

2.1 Introduction

The goal of NDE is to analyze an object using available technology without detrimentally effecting the form, fit, or function of the object. NDE is a broad field and covers many techniques: liquid penetrant, magnetic particle, eddy current, radiology, thermography, microwave, optical, and lastly, ultrasonic testing (Shull, 2002). Ultrasonic testing is one of the most widely used NDE methods today due to the wide range of materials that can be inspected without requiring advanced safety training. The introduction of ultrasonic testing with industrial application started in the late 19th and 20th century (Lindsay, 1966).The earliest forms of ultrasonic testing consisted of the “tap test” where one taps on an object to sees if it “sounds healthy.” In order to detect flaws that were smaller and not sensitive to low, audible, frequencies, piezoelectric materials were used to generate high frequency waves required for modern ultrasonic testing.

This chapter provides a brief overview of the two main types of ultrasonic waves used for inspection (bulk and guided waves). Ultrasonic inspection is primarily used in either pitch-catch or pulse-echo mode. Pitch-catch, as the name suggests, uses two

transducers where one probe generates the ultrasonic wave and another listens. Pulse-echo is where one transducer is used that both sends and receives the ultrasonic wave. For ultrasonic imaging, a pulse-echo style of inspection is used whereas for passive defect detection, a style similar to pitch-catch ultrasonic inspection is used.

2.2 Bulk Waves

Bulk waves are the fundamental waves in ultrasound and are split into two types: transverse and longitudinal. Transverse waves, also known as S- or T-waves, move perpendicular to the particle direction; whereas, longitudinal waves, also known as P- or L-waves, move parallel to the direction of motion, as illustrated in Figure 2-1. The propagation of bulk waves forms the basis for ultrasonic imaging.

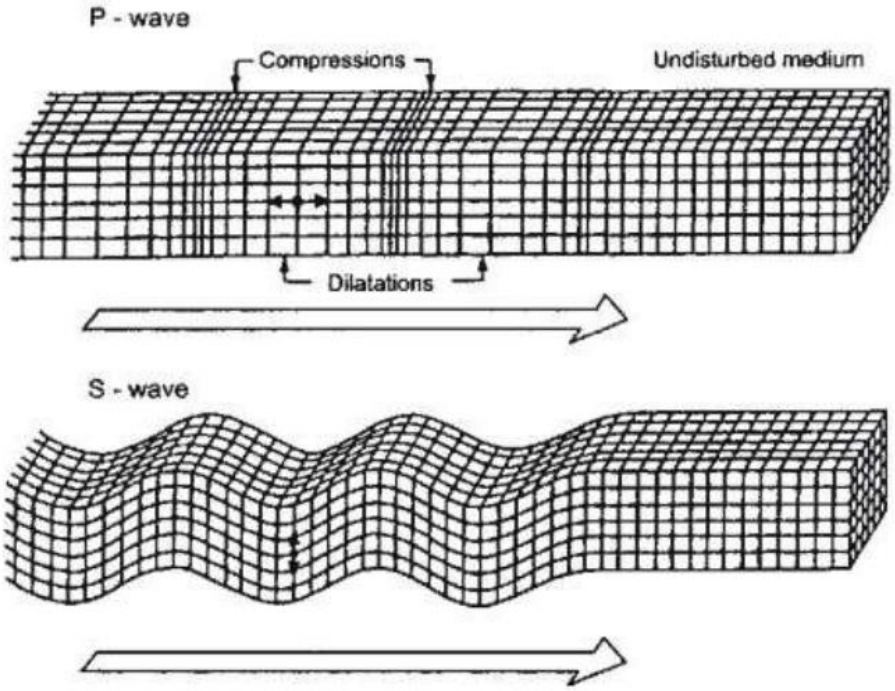

Figure 2-1: Longitudinal (P-Waves) and Transverse (S-Waves)

The derivation of the equation of motion that describes the two fundamental bulk waves (longitudinal and transverse modes) for an elastic isotropic solid is covered in many textbooks (Kolsky, 1963; Pollard, 1977; Rose, 2004). A summary of the derivation is provided below for completeness.

Consider a three-dimensional object with density, ρ. If the body forces are neglected, Newton's second law of motion gives:

$$\begin{aligned}
\frac{\partial \sigma_x}{\partial x} + \frac{\partial \tau_{xy}}{\partial y} + \frac{\partial \tau_{xz}}{\partial z} &= \rho \frac{\partial^2 u_x}{\partial t^2} \\
\frac{\partial \sigma_y}{\partial y} + \frac{\partial \tau_{xy}}{\partial x} + \frac{\partial \tau_{xz}}{\partial z} &= \rho \frac{\partial^2 u_y}{\partial t^2} \\
\frac{\partial \sigma_z}{\partial z} + \frac{\partial \tau_{xy}}{\partial y} + \frac{\partial \tau_{xz}}{\partial x} &= \rho \frac{\partial^2 u_z}{\partial t^2}
\end{aligned} \tag{2.2.1}$$

where u_x, u_y, and u_z are the displacements along the x, y, and z Cartesian coordinates. The stress and strain in the elastic material are related by the generalized form of Hooke's law:

$$\begin{Bmatrix} \sigma_{xx} \\ \sigma_{yy} \\ \sigma_{zz} \\ \sigma_{yz} \\ \sigma_{zx} \\ \sigma_{xy} \end{Bmatrix} = \begin{bmatrix} C_{11} & C_{21} & C_{31} & C_{41} & C_{51} & C_{61} \\ C_{12} & C_{22} & C_{32} & C_{42} & C_{52} & C_{62} \\ C_{13} & C_{23} & C_{33} & C_{43} & C_{53} & C_{63} \\ C_{14} & C_{24} & C_{34} & C_{44} & C_{54} & C_{64} \\ C_{15} & C_{25} & C_{35} & C_{45} & C_{55} & C_{65} \\ C_{16} & C_{26} & C_{36} & C_{46} & C_{56} & C_{66} \end{bmatrix} \begin{Bmatrix} \epsilon_{xx} \\ \epsilon_{yy} \\ \epsilon_{zz} \\ \epsilon_{yx} \\ \epsilon_{zx} \\ \epsilon_{xy} \end{Bmatrix} \tag{2.2.2}$$

where C_{ij} is the elastic constant of the material. For an anisotropic material, 21 independent elastic constants exist. For an isotropic solid, there are only two elastic constants and are commonly known as Lamé's constants: λ and μ. The stress-strain equation for an isotropic medium and then be expressed in tensor form as:

$$\sigma_{ij} = \lambda \delta_{ij} \epsilon_{kk} + 2\mu \epsilon_{ij} \tag{2.2.3}$$

where δ_{ij} is the Kronecker delta and $\epsilon_{kk} = \epsilon_{xx} + \epsilon_{yy} + \epsilon_{zz}$ is the dilation. Substituting (2.2.3) into (2.2.1) yields the Navier's equation of motion for an isotropic elastic medium:

$$(\lambda + \mu)\vec{\nabla}\left(\vec{\nabla} \cdot \vec{u}\right) + \mu\nabla^2\vec{u} = \rho\frac{\partial^2\vec{u}}{\partial t^2} \tag{2.2.4}$$

where $\vec{u}$ is the displacement vector, $\vec{\nabla}$ is the divergence vector, and $\nabla^2 = \frac{\partial^2}{\partial x^2} + \frac{\partial^2}{\partial y^2} + \frac{\partial^2}{\partial z^2}$ is the Laplacian differential operator. The displacement vector, $\vec{u}$, can be decomposed into dilation and rotation through vector potentials ϕ and $\vec{\psi}$ to yield:

$$\vec{u} = \vec{\nabla}\phi + \vec{\nabla} \times \vec{\psi} \;\; where \;\; \vec{\nabla} \cdot \vec{\psi} = 0 \tag{2.2.5}$$

Substituting (2.2.5) into (2.2.4):

$$\vec{\nabla}\left[(\lambda + 2\mu)\nabla^2\phi - \rho\frac{\partial^2\phi}{\partial t^2}\right] + \vec{\nabla} \times \left[\mu\nabla^2\vec{\psi} - \rho\frac{\partial^2\vec{\psi}}{\partial t^2}\right] = 0 \tag{2.2.6}$$

When both the scalar and vector potential vanish, the following decoupled wave equations result:

$$c_L^2\nabla^2\phi = \frac{\partial^2\phi}{\partial t^2} \tag{2.2.7}$$

$$c_T^2\nabla^2\vec{\psi} = \frac{\partial^2\vec{\psi}}{\partial t^2} \tag{2.2.8}$$

where c_L, the longitudinal wave velocity:

$$c_L = \sqrt{\frac{\lambda + 2\mu}{\rho}} \tag{2.2.9}$$

and c_T, the transverse wave velocity:

$$c_T = \sqrt{\frac{\mu}{\rho}} \tag{2.2.10}$$

2.3 Guided Waves

Guided waves are a phenomenon that develops in a bounded medium where one dimension can be modeled as a semi-infinite length while the cross-section has finite dimension. This type of geometry is commonly referred to as a waveguide and include structures such as, but not limited to plates, rods, pipes, cables, and rails. The waveguide results in stress waves traveling through the medium and experiencing multiple reflections and mode conversions, resulting in a complex domain of constructive and destructive interference. Further down the wave path, the combination of reflected, refracted, and mode-converted bulk waves forms a coherent wave packet known as an ultrasonic guided wave, as illustrated in Figure 2-2 (Rose, 2004).

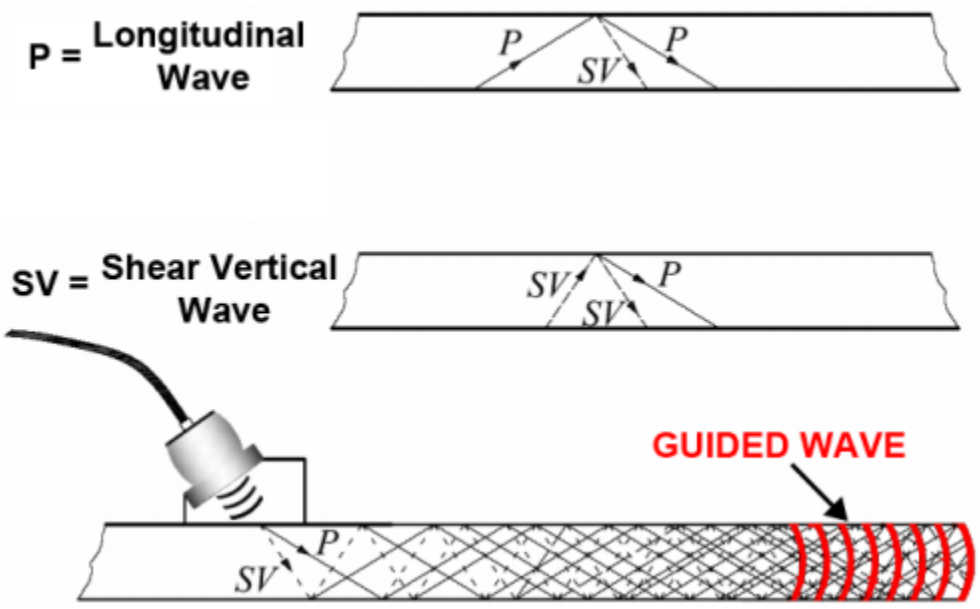

Figure 2-2: Generation of guided wave in a bounded semi-infinite medium (Rose, 2004).

The generated guided waves are multimodal dispersive, where an infinite number of modes coexists at any given frequency. Each mode is characterized by its own frequency-dependent velocity and attenuation. A type of surface acoustic guided wave, known as Rayleigh waves, are commonly used for defect detection due to their low attenuation. Named after Lord Rayleigh for his discovery in 1885, Rayleigh waves are the most common surface wave and decays exponentially with depth in the medium (a product of the traction-free surface properties). Rayleigh waves differ from other types of guided waves such as Lamb waves which propagate with the inside of plates. For rail inspection, Rayleigh waves are primarily used for defect detection.

Consider a homogenous, isotropic, linear elastic half-space with a traction-free surface. Assuming a plane strain formation, the displacement vector can be written as:

$$\vec{u} = \left(u_1, 0, u_3\right) \tag{2.3.1}$$

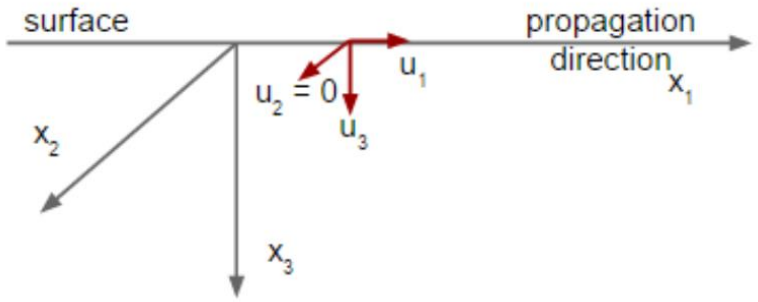

Figure 2-3: Particle displacement in an isotropic, traction-free surface, elastic plate.

Decomposing (2.2.5) with $u_2 = 0$ due to the traction-free surface condition for a Rayleigh wave:

$$\phi = \phi_2 = \phi\left(x_1, x_3, t\right) \tag{2.3.2}$$

$$\psi = \psi_2 = \psi\left(x_1, x_3, t\right) \tag{2.3.3}$$

The equation of displacement can then be expressed as:

$$\begin{aligned} u_1 &= \phi_1 - \psi_3 \\ u_2 &= 0 \\ u_3 &= \phi_3 - \psi_1 \end{aligned} \tag{2.3.4}$$

The solution for a harmonic wave traveling in the x_1 direction can be written as:

$$\begin{aligned} \phi &= A_1(x_3)e^{i(kx_1-\omega t)} \\ \psi &= A_2(x_3)e^{i(kx_1-\omega t)} \end{aligned} \tag{2.3.5}$$

Substituting (2.3.5) into (2.2.7) results in the solution for ϕ:

$$A_1(x_3)\xi^2 = A_1(x_3)_{33} \tag{2.3.6}$$

where

$$\xi^2 = k^2\left(1-\frac{c^2}{c_L^2}\right) \tag{2.3.7}$$

results in the solution:

$$A_1(x_3) = B_1e^{-\xi x_3} + B_2e^{\xi x_3} \tag{2.3.8}$$

Substituting (2.3.5) into (2.2.8) results in the solution for ψ:

$$C_1(x_3)\gamma^2 = C_1(x_3)_{33} \tag{2.3.9}$$

where

$$\gamma^2 = k^2\left(1-\frac{c^2}{c_T^2}\right) \tag{2.3.10}$$

results in the solution:

$$C_1\left(x_3\right) = D_1 e^{-\gamma x_3} + D_2 e^{\gamma x_3} \tag{2.3.11}$$

Since the physics of Rayleigh waves governs that the amplitude decays with increasing depth, the second term of both (2.3.8) and (2.3.11) is discarded since it does not attenuate as the depth, x_3, increases. The ϕ and ψ can then be written as:

$$\phi = B_1 e^{-kqx_3} e^{ik\left(x_1 - ct\right)} \tag{2.3.12}$$

$$\psi = D_1 e^{-ksx_3} e^{ik\left(x_1 - ct\right)} \tag{2.3.13}$$

where

$$q = \sqrt{1 - \left(\frac{c}{c_L}\right)^2} \tag{2.3.14}$$

$$s = \sqrt{1 - \left(\frac{c}{c_T}\right)^2} \tag{2.3.15}$$

$$c = \frac{\omega}{k} \tag{2.3.16}$$

The displacements, u_1 and u_3 can then be expressed by combining (2.3.4), (2.3.12), and (2.3.13) to yield:

$$\begin{aligned} u_1 &= \phi_1 - \psi_3 \\ &= k\left(iB_1 e^{-kqx_3} + sD_1 e^{-ksx_3}\right) e^{ik\left(x_1 - ct\right)} \end{aligned} \tag{2.3.17}$$

$$\begin{aligned} u_3 &= \phi_1 + \psi_3 \\ &= k\left(-qB_1 e^{-kqx_3} + iD_1 e^{-ksx_3}\right) e^{ik\left(x_1 - ct\right)} \end{aligned} \tag{2.3.18}$$

Using (2.2.3) for a homogenous isotropic material yields the following strain components expressed as displacements:

$$\begin{Bmatrix} \epsilon_{11} \\ \epsilon_{22} \\ \epsilon_{33} \\ \epsilon_{12} \\ \epsilon_{23} \\ \epsilon_{13} \end{Bmatrix} = \begin{Bmatrix} u_{11} \\ 0 \\ u_{33} \\ 0 \\ 0 \\ \frac{1}{2}\left(u_{13}+u_{31}\right) \end{Bmatrix} \tag{2.3.19}$$

With the boundary conditions for a traction-free surface:

$$\sigma_{33} = \sigma_{13} = 0 \quad for \quad x_3 = 0 \tag{2.3.20}$$

the following can be written:

$$\sigma_{33}\big|_{x_3=0} = rB_1 - 2isD_1 = 0 \tag{2.3.21}$$

$$\sigma_{13}\big|_{x_3=0} = 2iqB_1 - rD_1 = 0 \tag{2.3.22}$$

where

$$r = 2 - \frac{c^2}{c_T^2} \tag{2.3.23}$$

Solving (2.3.21) and (2.3.22) for B_1:

$$\begin{aligned} B_1 &= \frac{2is}{r} D_1 \\ B_1 &= \frac{r}{2iq} D_1 \end{aligned} \tag{2.3.24}$$

Then, combining equations (2.3.17), (2.3.18), and (2.3.24) to solve for u_1 and u_3:

$$u_1 = A\left(re^{-kqx_3} - 2sqe^{-ksx_3}\right)e^{ik(x_1-ct)} \tag{2.3.25}$$

$$u_3 = iA\left(re^{-kqx_3} - 2e^{-ksx_3}\right)e^{ik(x_1-ct)} \tag{2.3.26}$$

where

$$A = \frac{-kD_1}{2q} \tag{2.3.27}$$

Since the displacements, u_1 and u_3, must be real, the solution can be reduced:

$$\tilde{u}_1 = \frac{u_1}{A} = \left(re^{-kqx_3} - 2sqe^{-ksx_3} \right) \cos k\left(x - ct \right) \tag{2.3.28}$$

$$\tilde{u}_3 = \frac{u_3}{A} = q\left(-re^{-kqx_3} - 2e^{-ksx_3} \right) \sin k\left(x - ct \right) \tag{2.3.29}$$

From (2.3.21) and (2.3.22), the following can be shown:

$$r^2 - 4sq = 0 \tag{2.3.30}$$

Which is the characteristic equation for the surface wave problem. The following new variables are introduced to simplify the equation above:

$$\eta = \frac{k_T}{k} = \frac{c}{c_T} \tag{2.3.31}$$

$$\zeta = \frac{k_L}{k} = \frac{c_T}{c_L} \tag{2.3.32}$$

and from substitution and algebra to obtain the Rayleigh wave velocity equation:

$$\eta^6 - 8\eta^4 + 8\eta^2 \left(3 - 2\zeta^2 \right) + 16\left(\zeta^2 - 1 \right) = 0 \tag{2.3.33}$$

where

$$\zeta = \frac{c_T}{c_L} = \sqrt{\frac{1-2\nu}{2\left(1-\nu\right)}} \tag{2.3.34}$$

The three roots for η (real, imaginary, and complex) are a function of the Poisson's ratio ν. From each root where $n = c/c_T$, a Rayleigh surface wave velocity $c_R = c$, is found.

Since only one of the roots is real, only one Rayleigh surface wave velocity exists for each material and only depends on ν. Since c_R does not depend on frequency, Rayleigh surface waves are non-dispersive. Although non-dispersive, Rayleigh waves propagating around curved surface and corners may encounter velocity changes and reflection (Shull, 2002). As the Rayleigh wave propagates through the surface, a head wave is generated between the solid and the traction-free surface. The head wave radiates at a critical angle dependent on Snell's law and is used for non-contact air-coupled inspection.

CHAPTER 3

SIGNAL PROCESSING

3.1 Introduction

The following chapter discusses the signal processing steps used in ultrasonic defect identification and detection. For ultrasonic defect identification, where precise determination of the defect size, shape, and orientation is desired, ultrasonic imaging through time domain beamforming is proposed. In order to reduce image artifacts and improve operator usability, signal processing steps building on the traditional Delay-and-Sum algorithm were used. These include adaptive structural weights, raytracing for interposed coupling path, image compounding, maximum reflectivity normalization, and Graphics Processing Unit (GPU) processing. In terms of ultrasonic defect identification, a passive transfer function reconstruction using a dual output model coupled with a Mahalanobis distance outlier detection algorithm was used. The proposed signal processing procedure to enhance defect identification and detection expands the applicability of ultrasonic testing as a non-destructive evaluation method.

3.2 Time Domain Beamforming

Synthetic Aperture Focus (SAF) for ultrasonic imaging has been around since the late 1960s and has found numerous applications in the medical imaging and non-destructive testing fields (Flaherty et al., 1970; Karaman et al., 1993; Mahmoud et al., 2010; Schickert et al., 2003; Tanter and Fink, 2014). A typical SAF approach uses an array of piezoelectric transducers that can act as both transmitters and receivers of ultrasonic waves. The image is constructed by extracting features from the received ultrasonic waveforms that are appropriately backpropagated in time to account for delay due to the spatial position of the transmitter, receiver and focus point. This approach of temporal back propagation is also commonly known as Delay-and-Sum (DAS) algorithm. Another key aspect of SAF beamforming is the selection of weights attributed to each collected waveform.

Basic SAF algorithms use unity weights, or no weights applied, to the backpropagated and summed waveforms. Static apodization weights such as the Hanning or Kaiser-Bessel windows are also widely utilized to decrease artificial ringing effects in the image, but at the expense of smearing the image results and decreasing spatial resolution. The Hanning or Kaiser-Bessel windows are considered static since they are applied independently of the focus point.

An improved solution utilizes adaptive weights that “filter” the backpropagated waveforms to increase the gain of the array. For example, a simple adaptive weight accounts for geometrical spreading of propagating waves through amplitude decay in relation to the wave propagation distance. More sophisticated approaches are available and use scattering profiles from the defect or distortionless minimization techniques (Hall and Michaels, 2010). Adaptive weights utilizing scattering profiles are challenging to apply since they require precise knowledge of the scattering profile (Zhang et al., 2008).

Distortionless minimization techniques, popular in underwater acoustics, are derived under idealized assumptions of stationary noise and perform poorly in low signal-to-noise environments and have low tolerance for model inaccuracies (A.B. Baggeroer et al., 1993).

3.2.1 Delay-and-Sum

Consider an ultrasonic transducer array with *M* transmitters and *N* receivers. Let the spatial coordinates of each transmitter $i = 1, \dots, M$ be (x_i, y_i) and the spatial coordinates of each receiver $j = 1, \dots, N$ also be (x_j, y_j), as shown in Figure 3-1.

A standard DAS algorithm constructs an image $I\,(x, y)$ by summing, at each pixel $P\,(x, y)$, the amplitudes of the received signals, A, appropriately backpropagated, for each combination of transmitter i and receiver j. In the time domain, the backpropagated DAS algorithm is written as:

$$I^{DS}(x,y) = \sum_{i=1}^{M}\sum_{j=1}^{N} w_{ij,xy}\, A_{ij}\left(\tau_{ij,xy}\right) \tag{3.1.1}$$

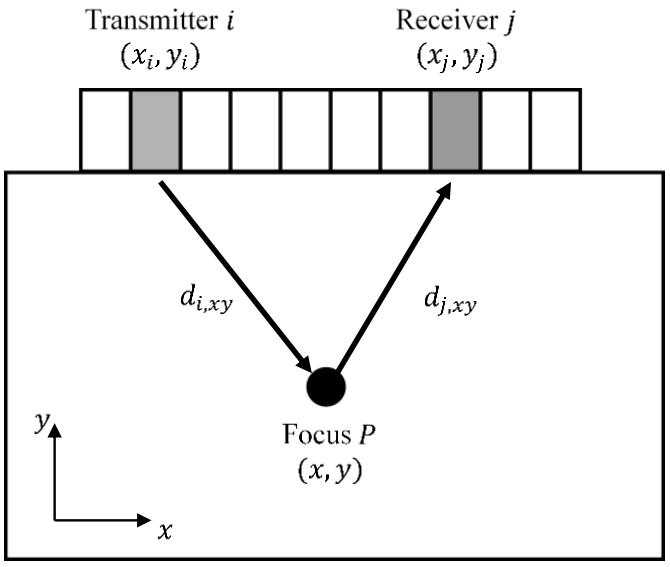

Figure 3-1: Synthetic Aperture Focus Array Setup

where $w_{ij,xy}$ represents the apodization weights previously discussed. The backpropagation time, $\tau_{ij,xy}$, corresponds to the travel time of the wave from the transmitter i, to the focus point $P\ (x, y)$, and back to the receiver j, and is calculated as:

$$\tau_{ij,xy} = \frac{\sqrt{\left(x_i - x\right)^2 + \left(y_i - y\right)^2}}{c_{L,S}} + \frac{\sqrt{\left(x_j - x\right)^2 + \left(y_j - y\right)^2}}{c_{L,S}} \tag{3.1.2}$$

where the denominators can be the longitudinal wave speed c_L or the shear wave speed c_s in the solid.

The received signal, A, in (3.1.1) can be computed directly from the raw waveforms, from an enveloped version of the raw waveforms, or from the analytical signal representation of the raw waveforms. In the latter case, each waveform is decomposed into its in-phase and phase-quadrature components through the Hilbert transform. (3.1.1) would then be applied to each of the Hilbert transformed components separately (Frazier and O'Brien, 1998). The final image would then be constructed by computing the modulus of the two contributions at each pixel (x, y). This method is utilized to generate the results shown in this report.

3.2.2 Adaptive Wave-Structure Weights

The possibility of using adaptive weights based on wave mode structure comes from the realization that, in general, a defect in a solid can reflect one or both of a longitudinal L-wave and a shear S-wave, through either same mode reflection or mode conversion. In the most general case, since the excitation from a transducer with a small footprint can produce both L-wave and S-wave, thus acting as a point source, there can exist up to four combinations of wave modes available for imaging in a bulk solid:

1. L-wave transmitted and reflected (LL)
2. L-wave transmitted and S-wave reflected (LS)
3. S-wave transmitted and reflected (SS)
4. S-wave transmitted and L-wave reflected (SL)

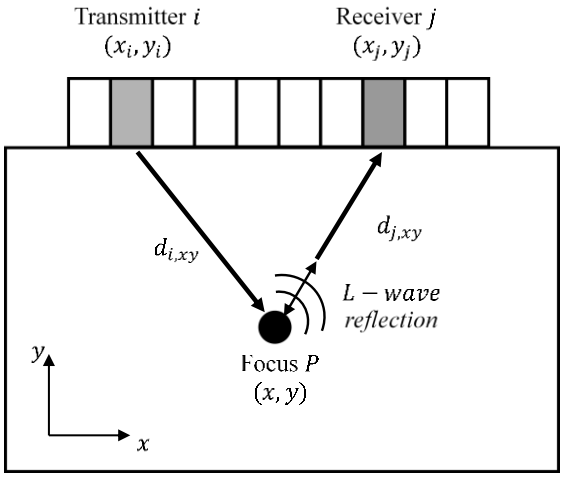

Figure 3-2: L-wave Reflection Structure

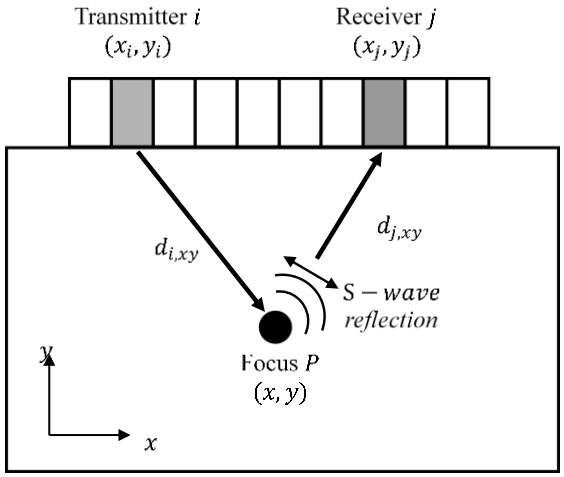

Figure 3-3: S-Wave Reflection Structure

Irrespective of the excitation, the signal strength received by the array will be modulated depending on the reflected mode structure (L- or S-wave reflected) and the reflector position $P\,(x,y)$. Therefore, array focusing will be performed only in reception (Lanza di Scalea et al., 2017).

Referring to Figure 3-2, for the case of an L-wave reflected by $P\,(x,y)$ and impinging on receiver j, the particle motion will be confined to the wave propagation direction. A typical ultrasonic transducer array that uses gel couplant is assumed to be sensitive to the out-of-plane motion of the surface (y-direction in Figure 3-2).

The distribution of out-of-plane displacements across the array due to an L-wave reflected by $P\,(x,y)$ and impinging on the array can be calculated by projecting the wave vector onto the out-of-plane direction *y*. The corresponding LL or SL adaptive weight with the addition of geometrical spreading is:

$$w_{ij,xy}^{LL\ or\ SL} = \frac{1}{\sqrt{d_{i,xy}\,d_{j,xy}}} \cdot \frac{\left|y_j - y\right|}{\sqrt{\left(x_j - x\right)^2 + \left(y_j - y\right)^2}} \tag{3.1.3}$$

The case of an S-wave reflected by the focus point onto the array can be derived analogously. For a shear wave, the particle motion is perpendicular to the direction of wave propagation as shown in Figure 3-3.

The amplitude distribution measured by a typical transducer array will be the out-of-plane component of the wave displacement at the array surface. In the case of an S-wave reflection with geometrical spreading, the adaptive weight will be:

$$w_{ij,xy}^{LS\ or\ SS} = \frac{1}{\sqrt{d_{i,xy}\,d_{j,xy}}} \cdot \frac{\left|x_j - x\right|}{\sqrt{\left(x_j - x\right)^2 + \left(y_j - y\right)^2}} \tag{3.1.4}$$

The weights proposed for LL, SL, LS, and SS wave modes can be applied to the DAS beamforming algorithm. Adapting (3.1.1) for the case of L-wave reflection (LL and SL wave modes) becomes:

$$I^{DS,\ LL\,or\,SL}(x,y)=\sum_{i=1}^{M}\sum_{j=1}^{N} w_{ij,xy}^{LL\ or\ SL}\, A_{ij}\left(\tau_{ij,xy}\right) \tag{3.1.5}$$

where the L-mode weights $w_{ij,xy}^{LL\ or\ SL}$ are given by (3.1.3) and the backpropagation time delays $\tau_{ij,xy}$ are given by (3.1.2), with the appropriate wave velocities at the denominators ($c_L\ or\ c_S$).

For the S-wave reflection case, the DAS beamforming with the new weights becomes:

$$I^{DS,\ LS\,or\,SS}(x,y)=\sum_{i=1}^{M}\sum_{j=1}^{N} w_{ij,xy}^{LS\ or\ SS}\, A_{ij}\left(\tau_{ij,xy}\right) \tag{3.1.6}$$

where the S-mode weights $w_{ij,xy}^{LS\ or\ SS}$ are given by (3.1.4) and the backpropagation time delays $\tau_{ij,xy}$ are given by (3.1.2), with the appropriate wave velocities at the denominators ($c_L\ or\ c_S$).

3.2.3 Imaging Algorithm with Interposed Coupling Path

Another technique commonly used in underwater acoustics and tomography is ray tracing (Brath and Simonetti, 2017; Iturbe et al., 2009; Munk et al., 1995; Peterson and Porter, 2013). Ray tracing computes the physically wave propagation path and tracks the changes along the path. This technique represents a simplification of the actual wavefield and propagation behavior which can be complex to model. Imaging of the test medium can be performed by computing the rays that propagate between transmitter-receiver pairs (so-called eigenrays) and then tracking the medium changes (e.g. wave speed changes or scatters) along the ray paths. An extension of raytracing to ultrasonic imaging with

transducer array wedges is presented. Specifically, the goal is to enhance the imaging of discontinuities whose orientation, geometry and/or location are such that an interposed coupling path (e.g. a wedge) is required between the transducer and the test medium for optimum detection via ultrasonic transmissions and reflections. A ray tracing method is utilized to account for the wave refractions at the interface between the interposed wedge and the test material.

As in classical DAS, the backpropagation time $\tau_{k,xy}$ depends on the location of the elements of the *k-th* transmitter-receiver pair and that of the focus point *P*(*x*,*y*). The wave propagation paths to focus point *P* for a transmitter-receiver pair *i*,*j* are shown in Figure 3-4 (a). Of importance here is the refraction of both transmitted wave and reflected wave at the wedge/medium interface.

Furthermore, consider a longitudinal (L-) wave propagation in the wedge material while allowing both a longitudinal (L-) wave and a shear (S-) wave propagation in the test medium. This assumption reflects the fact that typical ultrasonic transducer arrays with a conventional gel coupling layer generate and detect mostly L-waves due to the piezoelectric crystal geometry. The S-wave mode can then be generated through refractions at the wedge/medium interface and/or from mode-conversions at the reflector. In this general situation, the backpropagation time for the *i*,*j* pair can be expressed as:

$$\tau_{k,xy} = \tau_{ij,xy} = \frac{d_{i,xy}^{(1)}}{c_{LW}} + \frac{d_{i,xy}^{(2)}}{c_{L,S}} + \frac{d_{j,xy}^{(3)}}{c_{L,S}} + \frac{d_{j,xy}^{(4)}}{c_{LW}} \tag{3.1.7}$$

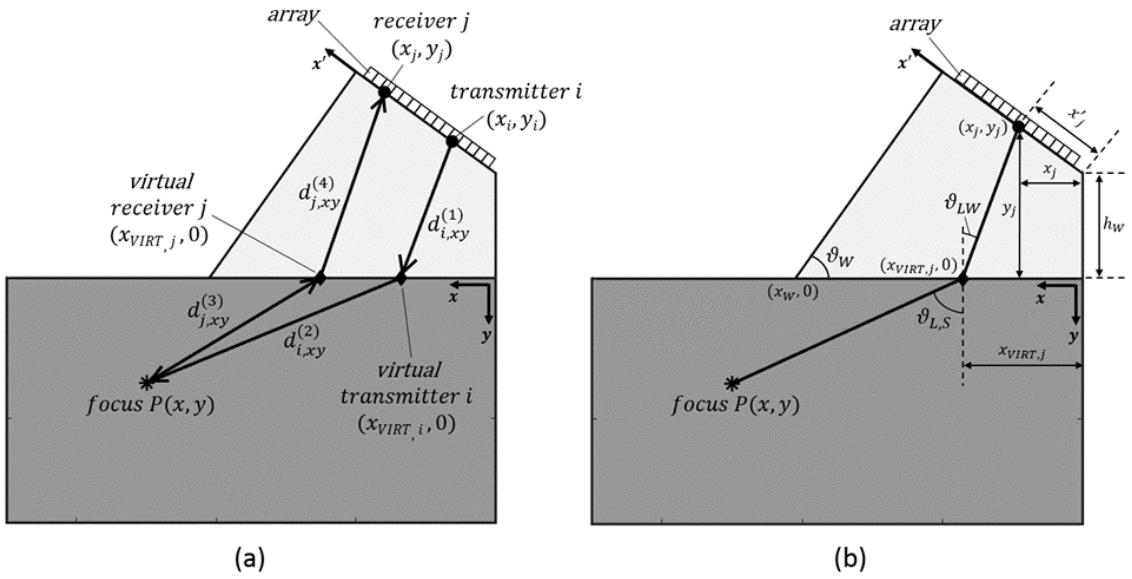

Figure 3-4: Transducer wedge imaging setup. (a) Wave propagation paths for focus point P(x,y) and a transmitter-receiver pair. (b) Ray tracing scheme for one focus point and one sensor.

In (3.1.7), c_{LW} is the L-wave velocity in the wedge material, and $c_{L,S}$ are the L-wave and S-wave velocities in the test medium, respectively. The terms at the numerators represent the paths traveled by the wave from the *i-th* transmitter, to focus point $P(x, y)$, and back to the *j-th* receiver. Since refraction at the wedge/medium interface refracts the wave paths through Snell's law, transmitters (or similarly receivers) will not be connected to the focus point by straight paths. Hence, the total wave path must be divided into four portions:

1. Transmitter to wedge/medium interface distance, $d_{i,xy}^{(1)}$
2. Wedge/medium interface to focus point distance, $d_{i,xy}^{(2)}$
3. Focus point to wedge/medium interface distance, $d_{j,xy}^{(3)}$
4. Wedge/medium interface to receiver distance, $d_{j,xy}^{(4)}$

In order to best express these distances, the array element locations are projected to "virtual" locations at the wedge/medium interface, as shown in Figure 3-4 (a). The "virtual" locations satisfy the physics of the refracted wave for a given focus point and wave mode. In this case, the four wave distances of (3.1.7) can be calculated by:

$$d_{i,xy}^{(1)} = \sqrt{(x_i - x_{VIRT,i})^2 + (y_i - y_{VIRT,i})^2} \tag{3.1.8}$$

$$d_{i,xy}^{(2)} = \sqrt{(x_{VIRT,i} - x)^2 + (y_{VIRT,i} - y)^2} \tag{3.1.9}$$

$$d_{j,xy}^{(3)} = \sqrt{(x_{VIRT,j} - x)^2 + (y_{VIRT,j} - y)^2} \tag{3.1.10}$$

$$d_{j,xy}^{(4)} = \sqrt{(x_j - x_{VIRT,j})^2 + (y_j - y_{VIRT,j})^2} \tag{3.1.11}$$

where (x_i, y_i) and (x_j, y_j) are the coordinates of the *i-th* transmitter and *j-th* receiver respectively, (x, y) are the coordinates of the focus point, and $(x_{VIRT,i}, y_{VIRT,i})$, $(x_{VIRT,j}, y_{VIRT,j})$ are the coordinates of the *i-th* "virtual" transmitter and the *j-th* "virtual" receiver, respectively. The "virtual" array coordinates are derived via raytracing.

The goal of the ray tracing approach is to find the rays that connect a given focus point to the various transducer elements in the array. Due to wave refraction, these rays do not have straight paths since they bend at the wedge/medium interface. The point at the interface where a ray connecting the focus point to a transducer element bends is the "virtual" position of that transducer. The "virtual" array can then be created by finding all the rays connecting a specific focus point to the physical array. Conceptually, the "virtual" array can be thought of as the positions that the transducer element must have on the medium surface, without a wedge, in order to create the same image obtained with the transducer wedge connected to the physical array.

The ray tracing algorithm is dependent on the position of the focus point $P(x, y)$, the position of the transducer on the wedge surface, and the specific wave mode considered. Following Snell's law, propagating modes with different wave speeds will have different refraction angles at the interface of two materials having acoustic impedance mismatch. Therefore, different wave modes will have different ray paths connecting the same focus point to the physical array. The mode-dependent nature of ray tracing allows the wave modes to be exploited independently as well as in combinations, to enhance the image gain.

Consider the usual focus point $P(x, y)$ and a transducer element of coordinates (x_j, y_j) on the $x - y$ reference system and coordinate x'_j along the x' axis - Figure 3-4 (b). Let x_b be the x-coordinate of the points at the wedge/medium interface, i.e. $0 \leq x_b < x_W$. The angle between the vertical direction and the path connecting the focus point to the points on the interface can be calculated as:

$$\vartheta_{L,S}(x, y, x_b) = \arctan\left(\frac{|x - x_b|}{y}\right) \tag{3.1.12}$$

where $\vartheta_{L,S}$ is the angle associated to the longitudinal wave mode or to the shear wave mode, respectively. For each point $(x_b, 0)$ on the interface, there is an angle $\vartheta_{L,S}$. However, only one position (therefore only one angle) will allow the ray to reach the transducer element considered. Therefore, each ray forming an angle $\vartheta_{L,S}$ at the interface will be refracted into an angle ϑ_{LW} in the wedge, that can be calculated from Snell's law:

$$\vartheta_{LW}(x, y, x_b) = \arcsin\left(\frac{c_{LW}}{c_{L,S}}\sin(\vartheta_{L,S}(x, y, x_b))\right) \tag{3.1.13}$$

where c_{LW} is the wave speed in the transducer wedge, $c_{L,S}$ is the longitudinal or shear wave velocity in the test medium, and $\vartheta_{L,S}$ is calculated from (3.1.12). (3.1.13) shows

that the propagation angle in the wedge ϑ_{LW} depends on the position along the wedge/medium interface. The coordinates of the *j-th* transducer can be rotated from the x' axis to the $x-y$ reference system with the following transformations:

$$x_j = x'_j \cdot \cos\left(\frac{\pi}{2} - \vartheta_W\right) \tag{3.1.14}$$

$$y_j = -\left(h_W + x'_j \cdot \sin\left(\frac{\pi}{2} - \vartheta_W\right)\right) \tag{3.1.15}$$

where ϑ_W and h_W are the wedge angle and height, respectively, also shown in Figure 3-4 (b). The minus sign outside the bracket in (3.1.15) is justified by the fact that the *y* axis points down in the figure.

Considering one focus point and one transducer element, for every point on the wedge-medium interface it is possible to calculate a height h_j that represents the projection of the ray propagating in the wedge onto the vertical direction passing through the *j-th* element. On the wedge interface, at the correct "virtual" position of the element considered, the height h_j will match with the vertical coordinate y_j of the element, whereas in other locations along the interface the resulting height will be either larger or smaller than the element vertical coordinate. The height h_j can be calculated as follows:

$$h_j(x, y, x_b) = (x_b - x_j) \cdot \tan\left(\frac{\pi}{2} - \vartheta_{LW}(x, y, x_b)\right) \tag{3.1.16}$$

where ϑ_{LW} and x_j are obtained from (3.1.13) and (3.1.14), respectively. As previously mentioned, the position x_b for which the height h_j is closest to the vertical coordinate of the *j-th* transducer element will represent the "virtual" position of that element along the wedge/medium interface. This concept can be formalized in the following expression:

$$x_{VIRT,j} = \arg\min_{x_b} \left| h_j(x, y, x_b) + y_j \right| \tag{3.1.17}$$

where the value of x_b that minimizes the absolute value on the right-hand side of (3.1.17) is taken as the "virtual" coordinate of the *j-th* transducer element. Notice that the summation sign inside the absolute value, instead of a minus sign, is used in (3.1.17) since the term y_j will always be negative in the $x - y$ reference system, which has the *y* axis pointing down according to Figure 3-4 (b).

By repeating the ray tracing procedure presented above for each focus point in the imaging medium and each transducer element in the array, it is possible to locate the "virtual" array on the wedge/medium interface for any possible wave path. Furthermore, by changing the wave speed $c_{L,S}$ in (3.1.13), different "virtual" arrays can be derived for different wave modes. In this way, each wave mode will have unique paths connecting the various focus points to the physical array. This fact creates an opportunity for combining or "compounding" independent information from different wave modes.

3.2.4 Image Compounding

Another strategy used in SAF imaging to increase array gain without increasing the physical array aperture is compounding images obtained with multiple independent information. Compounding exploits the consistency of the true reflectors and the randomness of the spatial noise through the different images. The multimodal nature of wave propagation can be successfully exploited to improve the array gain and image contrast without increasing its physical aperture. This idea is used, for example, in underwater acoustics and matched field processing (A. B. Baggeroer et al., 1988) (where images obtained from different frequencies are compounded) and in ultrafast biomedical imaging (where different transmission modes are compounded, e.g. plane-wave modes (Montaldo et al., 2009) or diverging-wave modes (Papadacci et al., 2014).

In general, the L-wave transmitted in the wedge can be refracted as both an L-wave and an S-wave in the test medium, as shown in Figure 3-5. Both wave modes can be reflected by the discontinuity within the test medium as same-mode reflections and as mode-converted reflections. Furthermore, both L-wave and S-waves can then refract back to the L-mode in the wedge that is then finally received by the array. There can therefore exist up to four combinations of wave modes available for imaging a bulk solid using a transducer wedge:

1. LLLL (L-wave transmitted in wedge, L-wave refracted in solid, L-wave reflected by reflector, L-wave refracted in wedge)
2. LSLL (L-wave transmitted in wedge, S-wave refracted in solid, L-wave reflected by reflector, L-wave refracted in wedge)
3. LLSL (L-wave transmitted in wedge, L-wave refracted in solid, S-wave reflected by reflector, L-wave refracted in wedge)
4. LSSL (L-wave transmitted in wedge, S-wave refracted in solid, S-wave reflected by reflector, L-wave refracted in wedge).

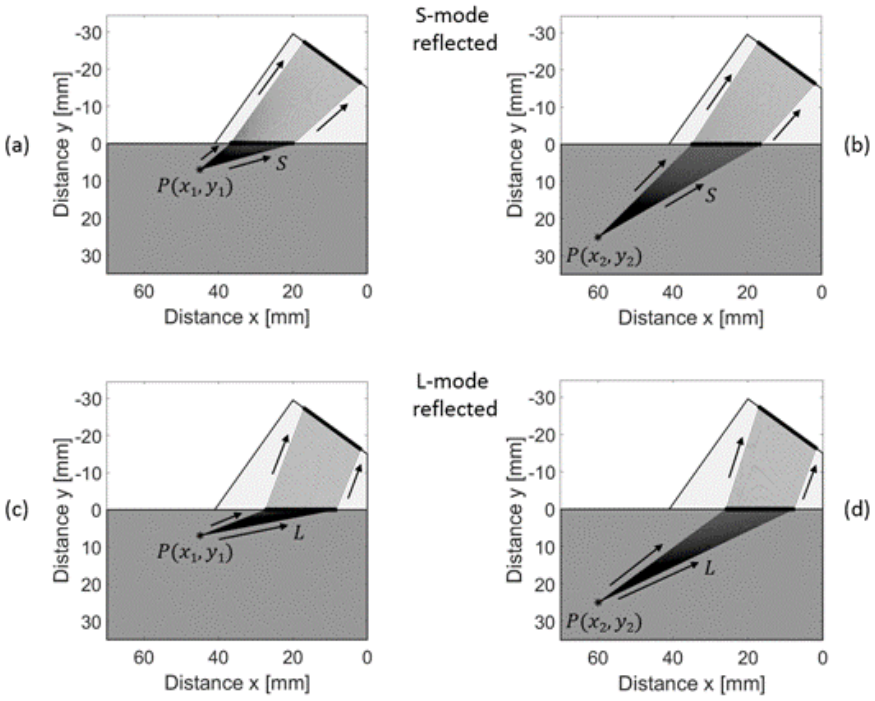

Figure 3-5: Ray paths for different propagating wave modes. (a) S-wave reflected in the near-field, (b) S-wave reflected in the far field, (c) L-wave reflected in the near-field, and (d) L-wave reflected in the far field.

Figure 3-5 illustrates how different wave modes propagate along different paths when refracted at the wedge interface. Figure 3-5 (a) and (b) show the propagation of the reflected S-wave and how the ray paths change for a reflection from a point $P(x_1, y_1)$ located in the near field and one from a point $P(x_2, y_2)$ located in the far field, respectively. Similarly, Figure 3-5 (c) and (d) refer to the L-wave reflected in the near field and in the far field, respectively. It is important to notice how the refraction angles inside the wedge change for the different wave modes. Consequently, the location of the “virtual” array at the wedge/medium interface changes when the wave mode combination changes, as well as when the focus point changes. The “virtual” array position is therefore adaptive to both the imaging volume and to the specific wave mode combination considered. This observation further highlights the importance of the ray tracing technique for an accurate computation of wave paths used in (3.1.7).

In general, there are two main ways to compound images: incoherent (Arthur B. Baggeroer et al., 1993, 1988; Makris, 1995; Michalopoulou and Porter, 1996) or coherent (Debever and Kuperman, 2007; Michalopoulou and Porter, 1996; Orris et al., 2000) compounding. Incoherent compounding is the simple summation of the image intensities and is analytically expressed as:

$$I_{TOT,\,incoherent}(x,y) = \sum_{MC=LL,LS,SL,SS} I^{MC}(x,y) \tag{3.1.18}$$

where the image $I^{MC}(x,y)$ (in decibels) for a given wave mode combination is calculated from (3.1.1) using the SAF-DAS algorithm. This approach takes advantage of the consistency of the true reflector throughout the images versus the random spatial noise.

Coherent compounding, instead, includes “cross-mode” terms because the summation is done before the squaring of the intensities. In this report, we focus on coherent compounding of wave modes. By coherently summing, this mode exploits the coherence across wave modes as received by the array and can be expressed as:

$$I_{TOT,\,coherent}(x,y) = \left(\sum_{MC=LL,LS,SL,SS} \left| \sqrt{I^{MC}(x,y)} \right| \right)^2 \tag{3.1.19}$$

where, as in the incoherent case, the images $I^{MC}(x,y)$ (in decibels) are given by (3.1.1). While the coherent approach should theoretically bring additional gain compared to its incoherent counterpart, the relative performance depends on the noise structure of the particular wavefield, as is known for frequency compounding in the matched-field processing imaging community (Debever and Kuperman, 2007; Michalopoulou and Porter, 1996).

3.2.5 Noise Filtering and Image Sharpening

The image obtained through coherent compounding presents the maximum achievable array gain. To further reduce artifacts without sacrificing the dynamic range, noise filtering through baseline subtraction and image sharpening through Point Spread Function (PSF) filtering is necessary (Dalitz et al., 2015). Baseline subtraction is obtained by subtracting waveforms recorded from a pristine portion of a specimen from the raw waveforms obtained in the presence of defect. PSF filtering is the deconvolution of the image with the impulse response of the array which can be either numerically modeled or obtained through experimental procedure. The impulse response of the array is the response of the system to a point reflector located at broadside with respect to the array. This deconvolution process is usually applied through an image deblurring process known as the Lucy-Richardson method.

3.2.6 Maximum Reflectivity Normalization

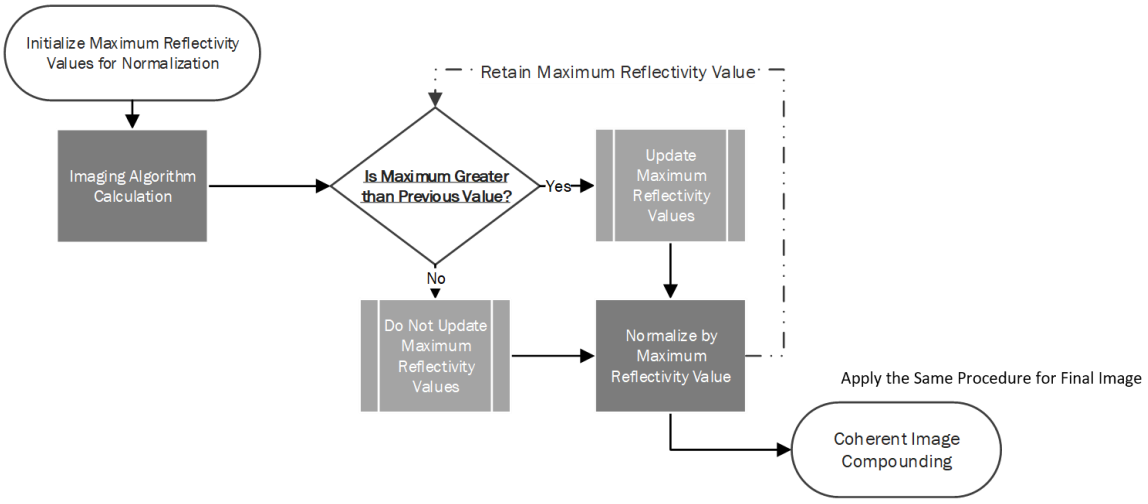

Figure 3-6: Maximum Reflectivity Normalization Procedure

A robust methodology to separate cases where a defect is present from those where only noise is present is required to reduce errors from operator judgement. The proposed maximum reflectivity normalization updates the normalization value adaptively, by retaining the maximum value from the previous image. This ensure that when a defect is found, the algorithm highlights the defect and suppresses any subsequent noise-only imaging results. A flow diagram of the normalization procedure is shown in Figure 3-6. The maximum value of the image obtained from either (3.1.18) or (3.1.19) is saved and compared to the previous image scan. If the previous maximum image intensity is greater, the normalization procedure does not change. Once a large reflector, such as a defect, is present, the pre-normalized image intensity will be significantly greater. Thus, a new maximum reflectivity value is used to normalize the image.

3.2.7 Graphics Processing Unit Acceleration

General-purpose computing on the GPU were first marketed by Nvidia to take advantage of a GPU's unique architecture. A traditional Central Processing Unit (CPU) in a standard PC has 4 to 6 cores whereas a GPU is composed of sets of multiprocessors, with each multiprocessor consisting of a set of scalar processors and can consist of thousands of mini cores. This architecture makes GPUs advantageous for performing large amounts of simple computations quickly, as in the case of a SAF beamforming algorithm (Martin-Arguedas et al., 2012).

3.2.8 Automatic 3D Image Compilation using an Encoder

The 3D imaging of structures can be performed by combining multiple 2D images obtained from the imaging algorithm. In the case of a rail track structure, two-dimensional images are obtained by scanning the rail head along its transverse dimension at regular intervals, as illustrated in Figure 3-7. In order to make the process automatic, an encoder is connected to the Data Acquisition System (DAQ) to trigger the signal transmission to

the linear array at each scanning location. The encoder consists of either a magnetic or a spring-loaded wheel attached to the ultrasonic probe assembly that can roll over the rail top surface following the scanning direction.

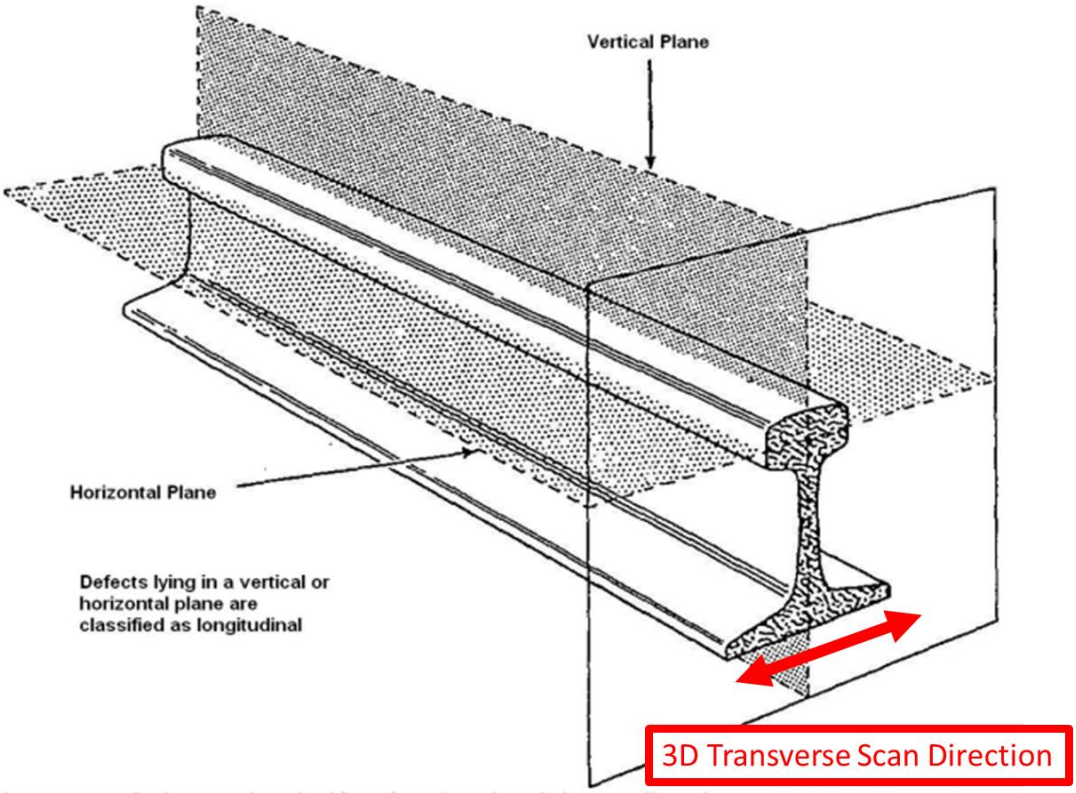

Figure 3-7: Example of 3D Image Scan Direction on a Rail Track Structure (Federal Railroad Administration, 2015)

The maximum resolution of the encoder (triggers/mm) is dependent on the encoder specification. At each trigger, a Transistor-Transistor Logic (TTL) pulse is sent to the data acquisition system through an I/O connector with programmable pins. The TTL pulse activates a counter on the DAQ and tags the current image acquisition data with the encoder count. The trigger type (quadrature, direction count, or forward backward) depends on the encoder hardware specification. Once determined, the trigger type is selected in the DAQ initialization settings file so that the TTL pulse is correctly converted

to an encoder count. Moreover, the encoder resolution and connection pins are specified in the settings file.

For example, by scanning the rail specimen along its transverse direction, it is possible to create multiple 2D slices, showing the internal flaws along the rail longitudinal plane, at different locations. Once all the 2D slices have been recorded, a stitching procedure can be implemented to create a final 3D representation of the internal flaws. This procedure can be implemented in MATLAB through 3D interpolation or point cloud visualization.

The method of interpolation is a multistep process requiring an evenly spaced grid of 2D images. First, the three-dimensional intensity matrix containing the 2D slices is passed through a smoothing filter in order to simplify the interpolation process. Subsequently, the filtered matrix is plotted through an isometric surface interpolator, which interpolates the intensity matrix and plots it at a specific value of intensity defined by the user. From the 3D image, it is then possible to calculate the dimensions of the rail flaw and obtain useful indications about its shape and orientation inside the rail head. The method of interpolation requires careful spacing and requires significantly slower scan speed and control to ensure the acquisition rate and scan step is synchronized. The preferred method is through point cloud visualization which allows the image algorithm to run at the maximum acquisition rate.

The method of point cloud visualization is a simpler process that does not require an evenly spaced grid of 2D images. The three-dimensional intensity matrix with the assigned 3D Cartesian coordinates is directly plotted on a 3D plot. Each point represents a value that is above the threshold chosen by the user. Point cloud visualization allows the user to quickly change the threshold while maintaining 3D visualization ability.

3.3 Transfer Function Reconstruction

The reconstruction of the dynamic transfer function, *H(f)*, in a system that is excited by a source input and monitored at one or more outputs is applicable to serval fields of study, including: signal channel characterization, dynamic characterization of various media, structural modal analysis, structural monitoring, and structural inspections. A realistic scenario is that of added noise at the output(s) that is uncorrelated with itself and with the source input. In the case of a linear Single-Input-Single-Output (SISO) system, Roth showed that a simple deconvolution of the excitation input from the output does not isolate the system's *H(f)* because it retains the noise power spectrum that is added to the output (Roth, 1971). He circumvented the colored transfer function by exploiting the fast that the cross-power spectrum of zero-mean uncorrelated signals tend to zero in an ensemble average sense. Accordingly, noise cancellation transfer function estimation in a SISO system can be achieved by an averaged cross-power spectrum between the source excitation and the output, normalized by an averaged auto-power spectrum of the source. Roth and other authors also showed than an analogous operation can be performed to minimize noise in the estimation of the magnitude-squared coherence function of dynamic SISO systems (Carter et al., 1973a, 1973b; Carter, 1987).

The averaging is most often performed in the time domain by segmenting the signal time histories Time domain averaging is equivalent to the ensemble averaging if the process is ergodic (Welch, 1967). A classical window (e.g. Hamming) is applied to the time segments prior to performing the Fourier Transforms for the computation of the cross-power and auto-power spectra. The time averaging process to eliminate uncorrelated noise has been formalized by well-known algorithms such as the Weighted Overlapped-Segment Averaging (WOSA) technique, also known as Welch's Method (Welch, 1967). Welch's Method utilized overlapped segments to retain the information in the segment

ends that are normally discarded when applying a window. A 50% segment overlap is generally considered effective (Welch, 1967). Regardless of the specific averaging process, SISO transfer function estimation methods require knowledge of the excitation source spectrum.

In many recent applications of dynamic testing and structural health monitoring, significant focus has been devoted to extract the transfer function in a completely passive matter by exploiting excitation that are uncontrolled, non-stationary, and unknown. Many structures are subject to ambient excitations that are natural to its operation: traffic excitation of a bridge (Farrar and James III, 1997; Salvermoser et al., 2015), seismic ground shaking of a building (Snieder and Şafak, 2006), aerodynamic fluctuations in aircraft and turbine blades (Sabra et al., 2007b; Tippmann J. D. et al., 2015), and acoustic excitation of rail track from train wheels. In addition, underwater acoustics (Roux and Kuperman, 2004; Sabra et al., 2005b, 2005c), seismology (Campillo and Paul, 2003; Roux et al., 2005; Sabra et al., 2005a; Shapiro et al., 2005; Snieder, 2004), and ultrasonic structural inspection (Duroux et al., 2010; Lobkis and Weaver, 2001; Michaels and Michaels, 2005; Sabra et al., 2007a; Tippmann and Lanza di Scalea, 2015; van Wijk, 2006), all rely on the passive extraction of the system's time-domain Green's function, $G_{AB}(t)$, in the presence of random "diffuse" acoustic or ultrasonic fields for analysis. In all these cases, the typical scenario is to utilize at least two receivers that can measure the output at two points of the structure, A and B, with the goal to reconstruct the transfer function, $H_{AB}(f)$, or, in the time domain, $G_{AB}(t)$, of a dual-output system.

The most popular method to achieve passive transfer function reconstruction in dual-output systems is the time-averaged cross-correlation of the outputs at the two receivers. The cross-correlation operation, however, retains the source excitation spectrum. The source excitation spectrum can cause problems if the source is

nonstationary or random. Snieder showed that a deconvolution operation between the two receivers can successfully eliminate the source spectrum and isolate the “pure” transfer function of the structure (Snieder, 2004; Snieder and Şafak, 2006). However, previous studies on the dual-output methods for passive transfer function reconstruction did not consider the presence of uncorrelated noise that may be added to the two outputs. The simple analogy to the SISO system does not lead to a robust estimation in a dual-output counterpart because it does not eliminate the noise power spectrum at one of the receivers. The problem is that the normalization factor used for SISO is an auto-power spectrum computed *on the same averaging segments* of the signal (herein referred to as *“intra-segment”* averaging). Besides increasing the total number of averages using n segments to $n!/(2(n-2)!)$ averages versus $2n-1$ averages for a 50% overlap “intra-segment” averaging, the inter-segment operation effectively eliminates the uncorrelated noise at the output. In addition, the inter-segment operation eliminates the excitation power spectrum from the final transfer function estimation.

The proposed inter-segment method assumes that the excitation and the transfer function are stationary during the observation time window, also known as being piecewise-stationary. In many practical applications, the observation time windows can be made sufficiently short such that this requirement is satisfied.

3.3.1 Single Input Single Output System

A Single Input Single Output (SISO) system is composed, in the frequency domain, of an excitation spectrum $E(f)$, transfer function $H(f)$, and output spectrum $O(f)$, as shown in Figure 3-8.

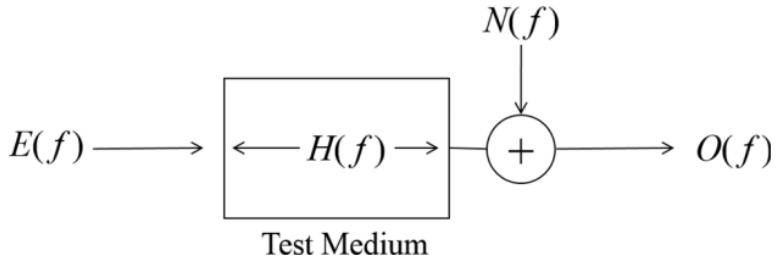

Figure 3-8: Schematic of SISO System for the Estimation of *H(f)*

Let us assume that the system is linear and piecewise-stationary, meaning that the statistics of the excitation *E(f)* do not change during the observation time window of *O(f)*. The excitation spectrum is also assumed to be known. Furthermore, a noise component with spectrum *N(f)* is added and assumed to be inherent in the observation. The noise is uncorrelated with the excitation and can come from a variety of sources. The goal is to estimate the system's transfer function, *H(f)*, with minimal effect from the noise, *N(f)*.

A simple deconvolution of the excitation from the output will retain the noise contribution in the estimation of *H(f)*:

$$Deconv = \frac{O(f)}{E(f)} = \frac{E(f)\cdot H(f) + N(f)}{E(f)} = H(f) + \frac{N(f)}{E(f)} \tag{3.3.1}$$

As shown in (3.3.1), the simple deconvolution operation is not ideal if the noise content is substantial. The solution in this case is to compute and "averaged" cross-power spectrum between the output and the excitation, normalized by an "averaged" auto-power spectrum of the excitation. This is based on the fact that the cross-power spectrum of two uncorrelated signals $S_1(f)$ and $S_2(f)$, each with zero DC component, tends to zero as an ensemble average. Hence:

$$\left\langle S_1^*(f)\cdot S_2(f)\right\rangle = 0 \quad \text{if } \left\langle S_1(t)\right\rangle = \left\langle S_2(t)\right\rangle = 0 \tag{3.3.2}$$

where * is the complex conjugate and $\langle\ \rangle$ is the ensemble average. The requirement for zero DC components is necessary for the ensemble to vanish as a result of destructive interference of the positive and negative uncorrelated realizations.

The ensemble averaged cross-power spectrum between the output and the excitations is:

$$\begin{aligned}\langle Cross\_Power\rangle &= \langle E^*(f)\cdot O(f)\rangle \\ &= \langle E^*(f)\cdot E(f)\cdot H(f)\rangle + \langle E^*(f)\cdot N(f)\rangle = |E(f)|^2\cdot H(f)\end{aligned} \tag{3.3.3}$$

since the term $\langle E^*(f)\cdot N(f)\rangle$ vanishes for uncorrelated noise. The noise term is therefore eliminated from the estimation of the transfer function, $H(f)$. The term, $|E(f)|^2$, is the auto-power spectrum of the excitation that "scales" or "colors" the transfer function estimation.

Therefore, normalizing the averaged cross-power spectrum of (3.3.3) by the auto-power spectrum of the excitation isolates the system's transfer function, $H(f)$ without the noise term:

$$\frac{\langle Cross\_Power\rangle}{\langle Auto\_Power\rangle} = \frac{\langle E^*(f)\cdot O(f)\rangle}{\langle E^*(f)\cdot E(f)\rangle} = \frac{|E(f)|^2\cdot H(f)}{|E(f)|^2} = H(f) \tag{3.3.4}$$

Experimentally, it is impractical to record ensemble averages. Instead, time averages are performed which has identical behavior if the random process is ergodic. A practical way to perform time averages is to divide the time signals into multiple segments, compute the spectra for each segment, and then average over the various segments. If the signals are divided into *n* time segments, the normalized cross-power spectrum operation becomes:

$$\frac{\langle Cross\_Power \rangle}{\langle Auto\_Power \rangle} = \frac{\frac{1}{n}\sum_{i=1}^{n} E_i^*(f)\cdot O_i(f)}{\frac{1}{n}\sum_{i=1}^{n} E_i^*(f)\cdot E_i(f)} = H(f) \tag{3.3.5}$$

where the spectra are computed separately for each segment *i*. Common practice is to apply a window, such as a Hamming window, to each time segment before computing the spectra via Fourier Transforms. In order to avoid the loss of information at the edges of the segment, a 50% overlap is commonly used. The 50% overlap with *n* segments increases the total number of averages to (2*n* – 1) terms.

In order to compute (3.3.4) and (3.3.5), knowledge of the excitation signal, $E(f)$, is required. Since each summation term in the numerator and denominator of (3.3.5) is computed for the same segment *i*, this method is defined as *inter-segment averaging*.

3.3.2 Dual-Output System

In contrast to a SISO system, a dual-output system is used when passive estimation of the transfer function of a system between point A and B is desired. A schematic diagram of a dual-output system is illustrated in Figure 3-9.

In structural health monitoring, knowledge of $H_{AB}(f)$ allows for the dynamic identification of the structure and defection of potential damage between two monitored locations. The excitation, $E(f)$, is not controlled or known, and it is assumed piecewise-stationary. A piecewise-stationary signal is a signal whose statistics do not change during the observation time windows of $O_A(f)$ and $O_B(f)$.

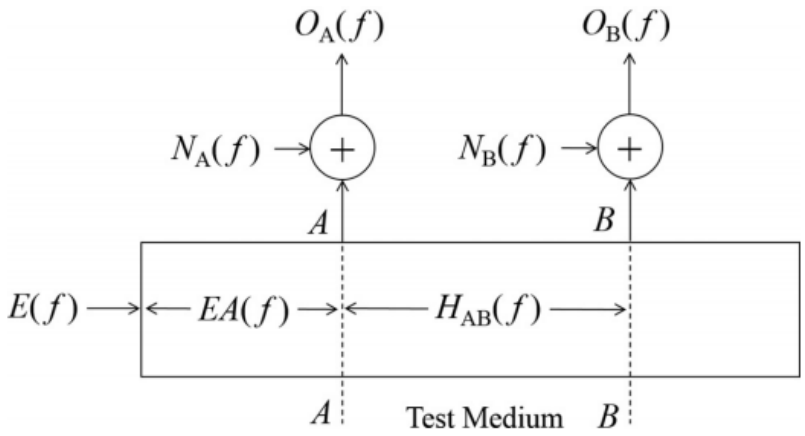

Figure 3-9: Schematic of Dual-Output System for the Estimation of $H_{AB}(f)$

Uncorrelated noise components, $N_A(f)$ and $N_B(f)$ are also assumed to be present at each of the two outputs. Thus, assuming linearity, the two outputs can be written as:

$$O_A(f) = E(f) \cdot EA(f) + N_A(f) \quad receiver\ A \tag{3.3.6}$$

$$O_B(f) = E(f) \cdot EA(f) \cdot H_{AB}(f) + N_B(f) \quad receiver\ B \tag{3.3.7}$$

where $EA(f)$ is the transfer function of the system from the excitation, $E(f)$, and the output, $A(f)$.

If one follows the same procedure outlined in the previous section consisting of the cross-power spectrum normalized by the auto-power spectrum in an ensemble average sense, the desired transfer function, $H_{AB}(f)$, is no longer isolated. Using equations (3.3.6) and (3.3.7), the ensembled averaged cross-power spectrum between the two outputs results in:

$$\langle Cross\_Power \rangle = \langle O_A^*(f) \cdot O_B(f) \rangle = \langle |E(f)|^2 \cdot |EA(f)|^2 \cdot H_{AB}(f) \rangle + \langle E^*(f) \cdot EA^*(f) \cdot N_B(f) \rangle + \langle E(f) \cdot EA(f) \cdot H_{AB}(f) \cdot N_A^*(f) \rangle + \langle N_A^*(f) \cdot N_B(f) \rangle = |E(f)|^2 \cdot |EA(f)|^2 \cdot H_{AB}(f) \quad (3.3.8)$$

In (3.3.8), averaged cross-power spectra of uncorrelated signals assumed with zero DC component, tend to zero. Consequently: $\langle E^*(f) \cdot EA^*(f) \cdot N_B(f) \rangle = 0$ because $N_A(f)$ is uncorrelated with either $E(f)$ or $EA(f)$; $\langle E(f) \cdot EA(f) \cdot H_{AB}(f) \cdot N_A^*(f) \rangle = 0$ because $N_A(f)$ is uncorrelated with either $E(f)$, $EA(f)$, or $H_{AB}(f)$; and $\langle N_A^*(f) \cdot N_B(f) \rangle = 0$ because $N_A(f)$ is uncorrelated with $N_B(f)$. In summary, the averaged cross-power spectrum of the two receiver outputs yields the desired function, $H_{AB}(f)$, but is "colored" by the power spectrum of the excitation, $|E(f)|^2$ and that of the transfer function between excitations and receiver A, $|EA(f)|^2$. Importantly, this operation also eliminates the noise components in both output at points *A* and *B*. Assuming an ergodic process, the ensemble average, $\langle O_A^*(f) \cdot O_B(f) \rangle$, can be replaced the time average. Using the classical "intra-segment averaging" of the previous section, time averaging for *n* segments yields:

$$\langle Cross\_Power \rangle = \frac{1}{n} \sum_{i=1}^{n} O_{A,i}^*(f) \cdot O_{B,i}(f) = |E(f)|^2 \cdot |EA(f)|^2 \cdot H_{AB}(f) \quad (3.3.9)$$

where the same segment *I* is used for each cross-power spectrum in the summation. If a 50% overlap between segments is utilized, the summation is carried out for (2*n* – 1) terms.

It is still quite necessary, however, to eliminate in (3.3.9) the effect of the excitation power spectrum, $|E(f)|^2$, since it is assumed uncontrolled and unknown. Using the auto-

power spectrum of output A as the normalization factor in analogy with the previous section, yields:

$$\begin{aligned}\langle Auto\_Power\rangle &= \left\langle O_A^*(f)\cdot O_A(f)\right\rangle = \left\langle \left|E(f)\right|^2\cdot\left|EA(f)\right|^2\right\rangle + \\ &\left\langle E^*(f)\cdot EA^*(f)\cdot N_A(f)\right\rangle + \left\langle E(f)\cdot EA(f)\cdot N_A^*(f)\right\rangle + \\ &\left\langle N_A^*(f)\cdot N_A(f)\right\rangle = \left|E(f)\right|^2\cdot\left|EA(f)\right|^2 + \left|N_A(f)\right|^2\end{aligned} \tag{3.3.10}$$

This result shows that the auto-power spectrum, if computed by the classical "intra-segment averaging," still contains the power spectrum of the noise, $\left|N_A(f)\right|^2$, because the auto-power spectrum of an uncorrelated signal does not vanish if it is taken in the same time segment. For example, for Gaussian white noise, $\left|N_A(f)\right|^2=\sigma^2$, the power spectrum is flat and is equal to the noise variance. Hence, the intra-segment averaged normalized cross-power spectrum for the dual output case yields:

$$\begin{aligned}\frac{\langle Cross\_Power\rangle}{\langle Auto\_Power\rangle} &= \frac{\frac{1}{n}\sum_{i=1}^{n} O_{A,i}^*(f)\cdot O_{B,i}(f)}{\frac{1}{n}\sum_{i=1}^{n} O_{A,i}^*(f)\cdot O_{A,i}(f)} \\ &= \frac{\left|E(f)\right|^2\cdot\left|EA(f)\right|^2\cdot H_{AB}(f)}{\left|E(f)\right|^2\cdot\left|EA(f)\right|^2+\left|N_A(f)\right|^2}\end{aligned} \tag{3.3.11}$$

and the transfer function, $H_{AB}(f)$, is not properly isolated because of the noise term, $\left|N_A(f)\right|^2$.

The solution to this problem is to realize the fact that the noise, $N_A(f)$, is assumed to be *uncorrelated* in time, and the cross-power spectrum of the same signal *between different time segments* tends to zero in the ensemble average sense. Therefore, an *inter-*

segment averaged auto-power spectrum can be formulated as the averaged cross-power spectrum of output A between two different time segments:

$$\begin{aligned}\left\langle Auto\_Power\right\rangle_{\mathrm{inter-segment}} &= \frac{1}{\bar{n}}\sum_{i=1}^{n-1}\sum_{j=i+1}^{n} O_{A,i}^{*}(f)\cdot O_{A,\mathrm{j}}(f) \\ &= \left|E(f)\right|^{2}\cdot\left|EA(f)\right|^{2} + \frac{1}{\bar{n}}\sum_{i,j} N_{A,i}^{*}(f)\cdot N_{A,j}(f) \\ &= \left|E(f)\right|^{2}\cdot\left|EA(f)\right|^{2}\end{aligned} \qquad (3.3.12)$$

where $\bar{n} = n!/2(n-2)!$ is the number of possible combinations of two different segments for a total of *n* segments. Segment overlapping may not be as beneficial in the inter-segment averaging since the same portions of the noise from different time realizations could be cross-correlated. The noise term, $N_A(f)$, is eliminated because the cross-power spectrum of the uncorrelated signal performed between different segments, $N_{A,i}^{*}(f)\cdot N_{A,j}(f)$, tends to zero on average. Strictly speaking, (3.3.12) is exact if the signals, $E(f)$ and $EA(f)$ are correlated in both amplitude and phase among the different segments. In general, this is not the case, since the segmentation cannot account for specific phase relations. Hence, a much more reasonable assumption is that $E(f)$ and $EA(f)$ between different segments are correlated in amplitude but not in phase. This is true, for example, if the total observation window is small compared to the expected variation time of the excitation. In order to properly deal with this case, (3.3.6) is reformulated to give:

$$O_A(f) = E(f)\cdot EA(f) + N_A(f) = S_A(f) + N_A(f) \qquad (3.3.13)$$

where $S_A(f)$ contains the correlated signals recorded at point A. Signal $S_A(f)$ is assumed to be time invariant during the observation window. Each inter-segment cross-power spectrum, $S^*_{A,i}(f)\cdot S_{A,\mathrm{j}}(f)$ will therefore have an amplitude that is consistent and a phase this random. Analytically:

$$\begin{aligned}\left\langle S^*_A(f)\cdot S_A(f)\right\rangle_{\mathrm{inter-segment}} &= \frac{1}{\bar{n}}\sum_{i=1}^{n-1}\sum_{j=i+1}^{n} S^*_{A,i}(f)\cdot S_{A,\mathrm{j}}(f)\\ &= \frac{1}{\bar{n}}\sum_{i,\,j}\left|S_{A,i}(f)\right|e^{-i\phi_{A,i}}\left|S_{A,\mathrm{j}}(f)\right|e^{i\phi_{A,\mathrm{j}}}\\ &= \frac{1}{\bar{n}}\sum_{i,\,j}\left|S_{A,i}(f)\right|\left|S_{A,\mathrm{j}}(f)\right|e^{i\Delta\phi_{A,ij}}\end{aligned} \qquad (3.3.14)$$

One option that could be considered to minimize the noise, $N_A(f)$, in light of the randomness of the inter-segment phase differences, $\Delta\phi_{A,ij}$, is taking the modulus of the cross-power spectra terms:

$$\left\langle\left|O^*_A(f)\cdot O_A(f)\right|\right\rangle_{\mathrm{inter-segment}} = \frac{1}{\bar{n}}\sum_{i=1}^{n-1}\sum_{j=i+1}^{n}\left|O^*_{A,i}(f)\cdot O_{A,\mathrm{j}}(f)\right| \qquad (3.3.15)$$

However, (3.3.15) will still contain the noise term since taking the modulus produces a non-zero DC bias that prevents the inter-segment auto-power spectrum of uncorrelated noise to tend to zero after averaging.

The best option to minimize the uncorrelated noise terms by inter-segment averaging and properly account for the phase decorrelation of the signal among the different segments is to appropriately shift the signals in each segment to force the segments in phase. The shifting procedure is analogous to the delay-and-sum procedure of synthetic aperture focusing in radar and ultrasonic imaging. If the signals in each segment are shifted in time such that their phases are aligned in all segments, phase

correlation is enforced, in addition to amplitude correlation. Furthermore, only the signal is correlated within the observation window while the noise is uncorrelated. The appropriate time lag for each segment pair can be determined by the peak of the cross-correlation function between the two segments:

$$\tau_{ij} = \arg\max\left(\int_{-\infty}^{+\infty} O_{A,i}^{*}(t)\, O_{A,j}(t+\tau)\, dt\right) \tag{3.3.16}$$

The shifted version of the inter-segment auto-power spectrum then becomes:

$$\begin{aligned}
\left\langle Auto-power \right\rangle_{\substack{inter-segment \\ shifted}} &= \frac{1}{\bar{n}} \sum_{i=1}^{n-1} \sum_{j=i+1}^{n} O_{A,i}^{*}(f) \cdot O_{A,j}(f) e^{-i2\pi f \tau_{ij}} \\
&= \left|S_A(f)\right|^2 + \frac{1}{\bar{n}} \sum_{i,j} N_{A,i}^{*}(f) \cdot N_{A,j}(f) \\
&= \left|S_A(f)\right|^2 = \left|E(f)\right|^2 \left|EA(f)\right|^2
\end{aligned} \tag{3.3.17}$$

The shifting procedure successfully eliminates the noise term for uncorrelated noise. Therefore, (3.3.17) is the final normalization term that needs to be applied to the averaged cross-power spectrum of (3.3.9) in the dual0output transfer function estimation problem:

$$\begin{aligned}
\frac{\left\langle Cross_Power \right\rangle_{intra-segment}}{\left\langle Auto_Power \right\rangle_{\substack{inter-segment \\ shifted}}} &= \frac{\frac{1}{n} \sum_{i=1}^{n} O_{A,i}^{*}(f) \cdot O_{B,i}(f)}{\frac{1}{\bar{n}} \sum_{i=1}^{n-1} \sum_{j=i+1}^{n} O_{A,i}^{*}(f) \cdot O_{A,j}(f) e^{-i2\pi f \tau_{ij}}} \\
&= \frac{\left|E(f)\right|^2 \cdot \left|EA(f)\right|^2 \cdot H_{AB}(f)}{\left|E(f)\right|^2 \cdot \left|EA(f)\right|^2} \\
&= H_{AB}(f)
\end{aligned} \tag{3.3.18}$$

In summary, the normalized cross-correlation spectrum computed according to (3.3.18) estimates passively, the transfer function between two receivers, A and B, without the influence of the excitation and without uncorrelated noise that may be present in either

one or both of the two receivers. The quantities averaged in (3.3.18) are calculated for the same segments in the numerator (intra-segment cross-power spectrum) and for different segments in the denominator (inter-segment auto-power spectrum).

3.4 Outlier Analysis

After extracting features from the reconstructed impulse response, an outlier analysis is used to compute a statically robust metric, commonly referred to as the Damage Index (Worden et al., 2002, 2000). Similar statistical analysis was implemented in active inspection methods of rail inspection systems (Coccia et al., 2011b, 2011a; Mariani et al., 2016; Mariani and Lanza di Scalea, 2018; Mariani Stefano et al., 2017). The Damage Index (D.I.) is related to the strength of the reconstructed transfer function. The D.I. is calculated using a Mahalanobis Squared Distance, defined in a multivariate sense:

$$D.I. = \left(x - \bar{x}\right)^T \cdot Cov^{-1} \cdot \left(x - \bar{x}\right) \tag{3.4.1}$$

where x is the feature vector extracted from passively-reconstructed transfer function, $\bar{x}$, is the mean vector of the baseline distribution, Cov is the covariance matrix of the baseline distribution, and $\left(\ \right)^T$ represents transposed. The statistical computation of the D.I. normalizes the data by the normal (baseline) data variability that occurs during a run. As such, compared to a simple deterministic metric, the D.I. in (3.4.1) dramatically increases the probability of detection and decreases the probability of false alarms, particularly in the context of dual-output passive inspection.

3.5 Acknowledgements

Chapter 3, in part, has been published in *Structural Health Monitoring*, Sternini, S., Liang, A, Lanza di Scalea, F. (2018) with the title “Ultrasonic synthetic aperture imaging

with interposed transducer–medium coupling path". The dissertation author was the primary author of this chapter.

Chapter 3, in part, has been published in *The Journal of the Acoustical Society of America*, Lanza di Scalea, F., Sternini, S., and Liang, A. (2018), with the title "Robust Passive Reconstruction of Dynamic Transfer Function in Dual-Output Systems". The dissertation author was the primary author of this chapter.

CHAPTER 4

APPLICATION TO RAIL INSPECTIONS

4.1 Introduction

Although the methods outlined in the previous chapter are applicable to a broad range of environments, the focus of this dissertation is on the application to rail track structures. In many ways, rails are a perfect application for nondestructive evaluation research and application. Rails are naturally subject to harsh, corrosive environments and endure complex, variable wheel-rail contact forces throughout its lifespan. Furthermore, due to their design, failure results in catastrophic damage if fatigue cracks and manufacturing inclusions are left undetected. In addition, since large quantities of rail steel are consumed annually (2.7 million tons in 2017, worldwide) and in-use currently (650 thousand miles in 2017, worldwide) inspection methods must be reliable and affordable (Basson, 2018; Internation Union of Railways, 2017). The combination of thermal and mechanical abuse during installation and operation, and lack of redundancy results in a need for a state-of-the-art asset management system. Nondestructive evaluation, such as ultrasonic inspection, has a vital role in the risk management system to ensure safe and cost-effective rail transportation infrastructure.

The primary purpose of this chapter is to provide background information on rail defects and inspection techniques before discussing research results in the following chapter. In the first section, the rail defects commonly found during manufacturing or operation are explained and illustrated. The next section gives a brief overview of current ultrasonic rail inspection methods.

4.2 Rail Defects

As a result of rail steel's low ductility, any presence of sharp cornered discontinuity will result in rapid and catastrophic crack growth and lead to fracture at most operating temperatures. Fatigue crack growth is primarily a result of bending and shear stresses imparted on the rail from static axle loads. In the U.S., these loads are approximately 30 to 32 tons. In addition to the primary static loads, contact stresses from wheel dynamics and uneven loading, thermal stresses from environmental effects, and residual stresses from manufacturing or installation play significant roles in critical fatigue flaw size (Cannon et al., 2003). A model of the static wheel-rail forces imparted is illustrated in Figure 4-1 (Orringer et al., 1988). The primary axle load is not centered on the neutral axis of the rail; thus, a bending moment is introduced into the rail specimen. The introduction of a crack or inclusion along with the rail-wheel forces results in the introduction of shear stress and subsequent crack growth, as shown in Figure 4-2 (Li et al., 2013; Zerbst and Beretta, 2011). Although a surface breaking crack is illustrated in Figure 4-2, the same forces apply to inclusions such as those found from hydrogen embrittlement. Furthermore, the introduction of dynamic forces from wheel flat spots due to wheel slide can significantly reduce the critical size of fatigue cracks before catastrophic growth. Although significant design and material improvements have been made since the first introduction of metal rails in the 18th century, rail defects are still a pressing problem.

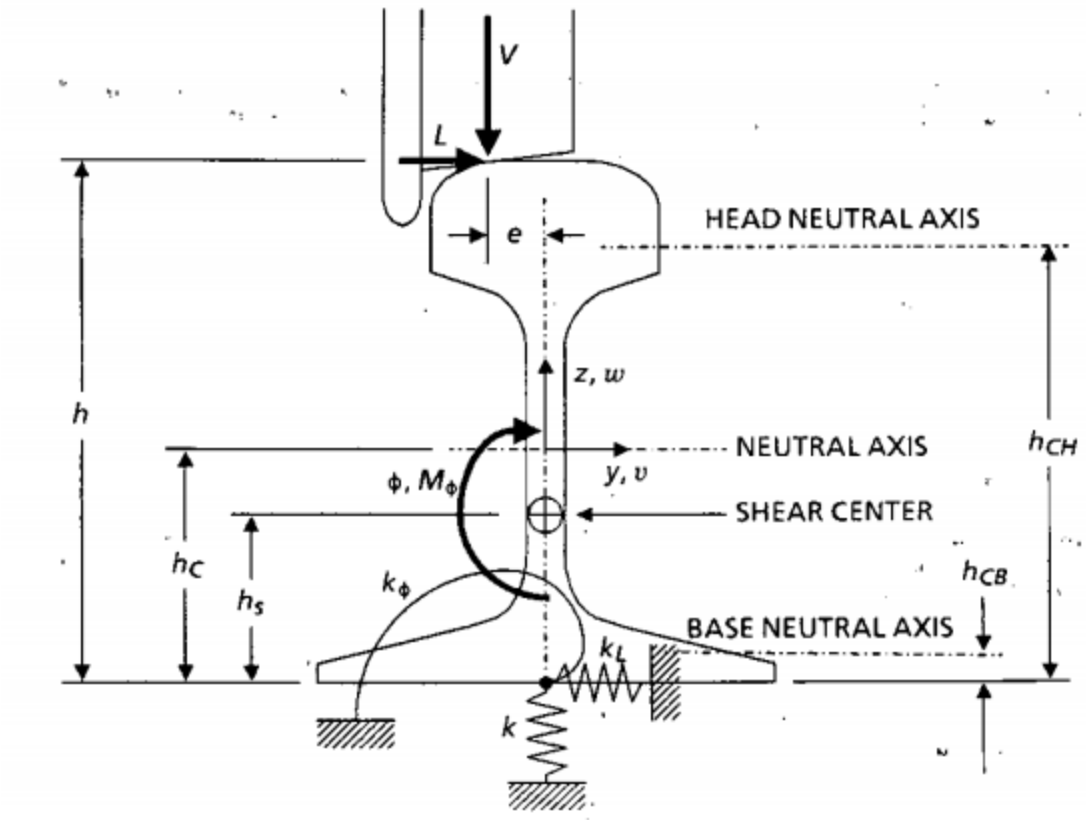

Figure 4-1: Model of wheel-rail forces of a rail as a beam on continuous elastic foundation (Orringer et al., 1988).

Rail defects are splits into three categories: rail head, web, and foot defects (Alahakoon et al., 2017). Rail head defects include local battering, flaking, and grove and line. Rail web defects include horizontal cracks at the web-head filet radius, horizontal cracks at the splitting of the web, and bolt hole fatigue. Rail foot defects include vertical cracks in the foot and fractures starting from the rail seat. The primary focus of this dissertation is on the detection of cracks arising from rail head defects. Rail head defects can result from the following groups: rail manufacturing defects, fatigue damage, and improper installation or use (Cannon et al., 2003).

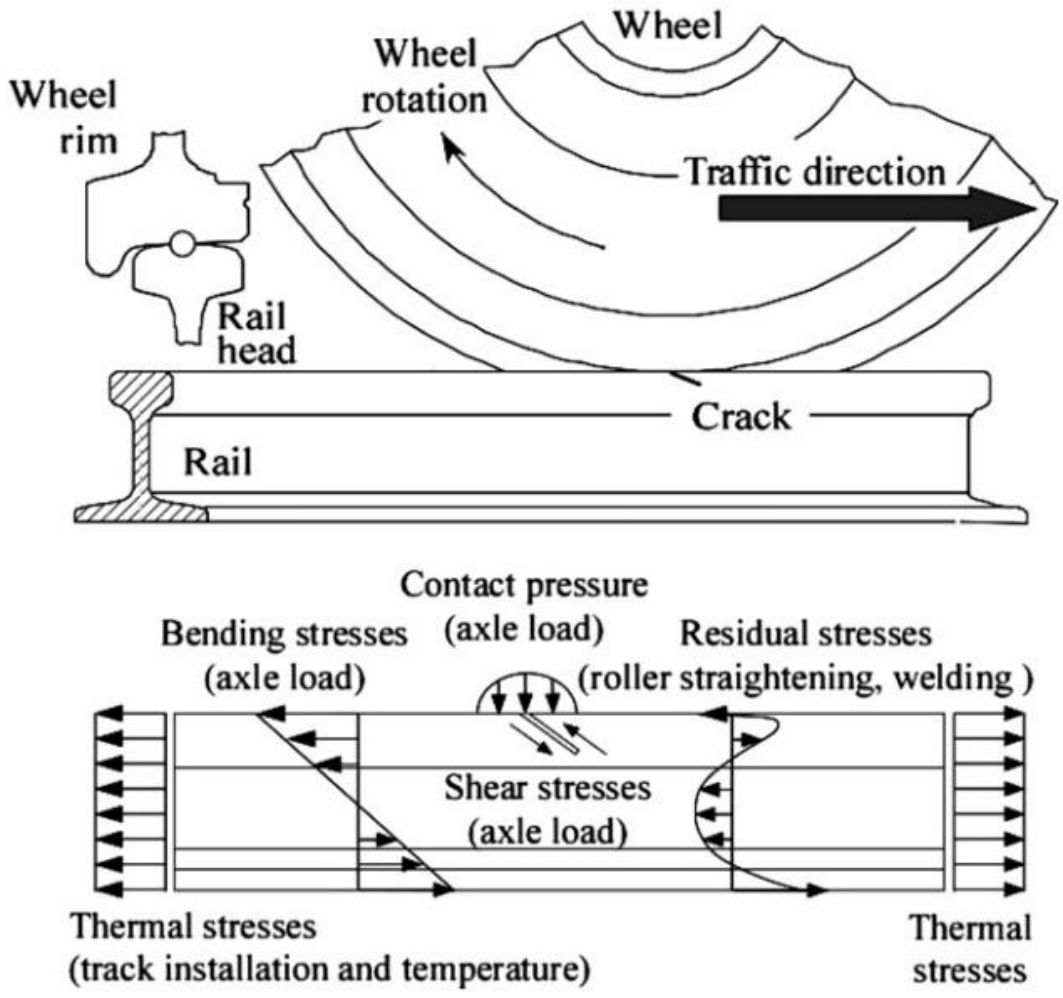

Figure 4-2: Stress distribution of a rail specimen with a crack when subject to wheel-rail static and dynamic forces (Zerbst and Beretta, 2011).

Rail manufacturing defects in the rail head include transverse fissures, compound fissures, horizontal split heads, and vertical split heads (Federal Railroad Administration, 2015). Transverse fissures, also known as Transverse Defects (TD), originate as manufacturing defects such as hydrogen flakes and brittle sub-surface inclusions (Jeong, 2003). These defects are characterized by the smooth surface development from the nucleus. An example of a TD is shown in Figure 4-3. The hydrogen embrittlement is due to presence of atomic hydrogen in the hot bloom. By controlling the cooling temperature to reduce the inclusion of hydrogen content, significant progress has been made in

reducing the number of TDs. Nevertheless, due to the large quantities of older rail steel in use and the statistical nature of manufacturing, TDs are still a source of rail failure that must be detected. A typical TD has a nucleus where the inclusion grows from. Once the growth encompasses 20 to 25 percent of the cross-sectional area of the rail head, also known as Head Area (HA), growth becomes accelerated.

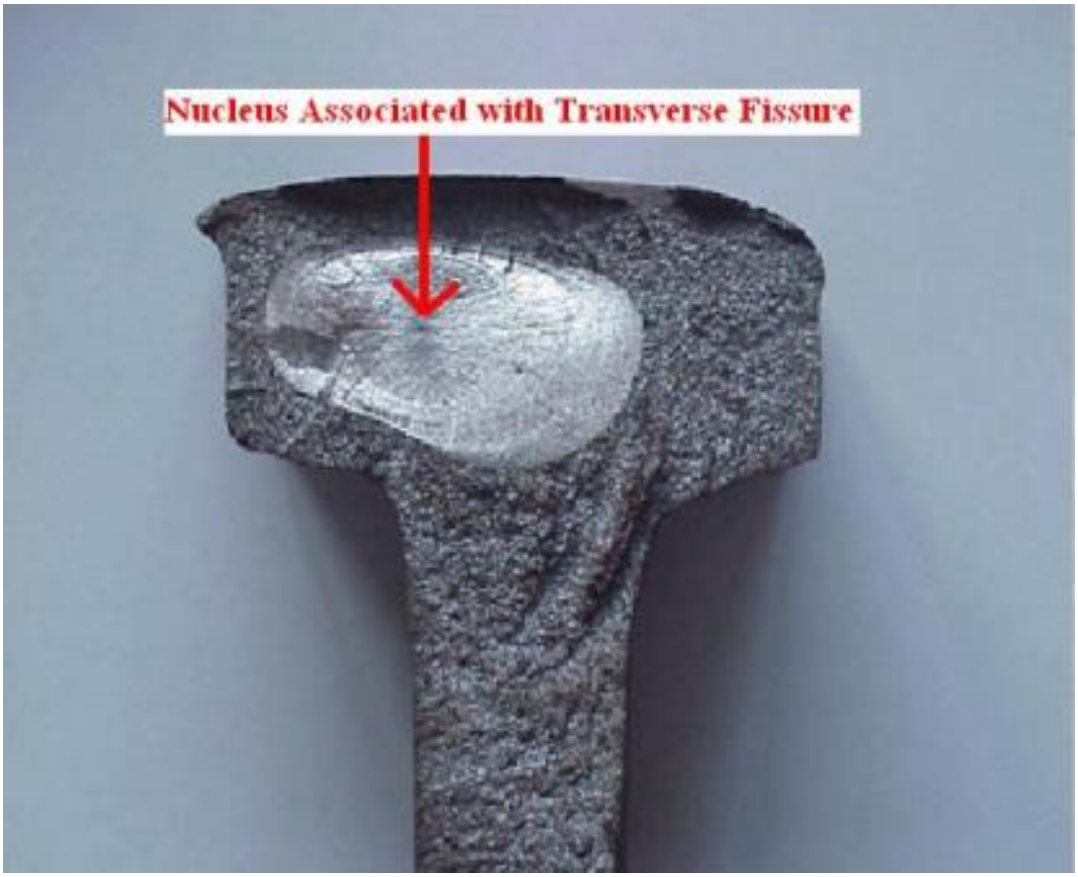

Figure 4-3: Transverse Fissure / Defect in the rail head (Federal Railroad Administration, 2015).

The next type of rail manufacturing defect, compound fissure, is characterized as a defect originating from horizontal separation that grows up, down, or in both directions in the head of the rail. An example of a compound fissure is illustrated in Figure 4-4. It differs from TDs in that the point of origin is due to a horizontal split head that changes its crack propagation direction, instead of one originating from the vertical plane.

Furthermore, the failure is typically in an oblique plane rather than vertical. Compound fissure growth is typically slow until 30 to 35 percent of HA.

Figure 4-4: Compound fissure defect in the rail head (Federal Railroad Administration, 2015).

Horizontal split heads are the last major type of manufacturing defect found in the rail head. These types of defect originate one-quarter inch or more below the surface of the rail head and are characterized by rapid development (Federal Railroad Administration, 2015). As previously mentioned, once horizontal split heads turn vertical, the defect is considered as a compound fissure. An example of a horizontal split head is shown in Figure 4-5.

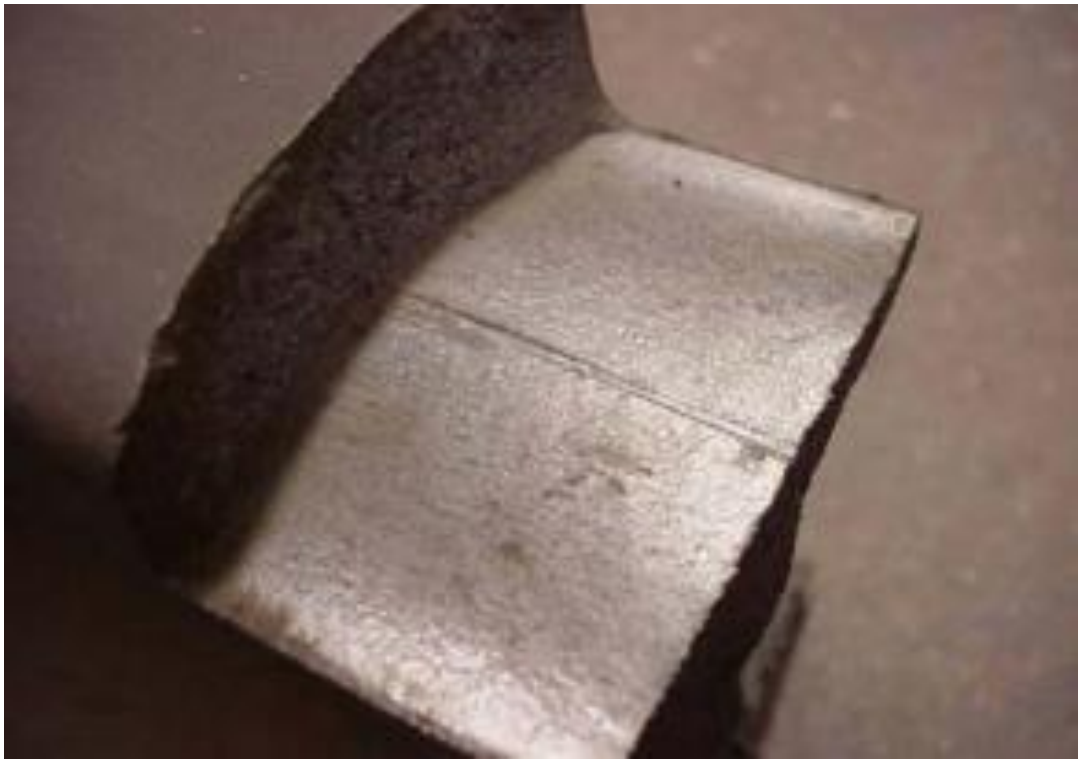

Figure 4-5: Horizontal split head in the rail head from an internal seam defect (Federal Railroad Administration, 2015).

Improved techniques over the years have reduced defects arising from manufacturing; however, detail fractures initiated from surface defects as a result of Rolling Contact Fatigue (RCF) are widespread and continue to grow (Cannon et al., 2003). RCF is a result of shear forces in the surface layer of rail from the combination of normal and tangential stresses during wheel-rail contact. Detail fractures can grow anytime there are shelly spots, head checks, or flaking. A few pictures of detail fractures are shown in Figure 4-6. Crack growth is normally slow until 10 to 15 percent of HA. Detail fractures can be prevented, but not eliminated, through maintenance techniques such as rail grinding. Nevertheless, with heavier and longer trains in use by the railroad industry, detail fractures from fatigue damage continue to be a concern.

Figure 4-6: Detail fracture defect in the rail head originating from a visible shell defect (Federal Railroad Administration, 2015).

An example of a rail defect arising from improper use is the engine burn fracture. Engine burn develops when the driving wheels of the locomotive slip on top of the rail head, generating significant amounts of heat (Federal Railroad Administration, 2015). The subsequent rapid cooling forms thermal cracks. Growth of engine burn fracture defects is slow until 10 to 15 percent of HA. Figure 4-7 illustrates a typical engine burn fracture defect with significant growth.

Figure 4-7: Engine burn fracture defect in the rail head (Federal Railroad Administration, 2015).

4.3 Ultrasonic Rail Inspection

Ultrasonic defect detection using phased arrays is currently used in the evaluation of rails and has been in use since the 1960s. Initial ultrasonic systems focused on detecting surface breaking and internal defects, but had low reliability in small surface breaking defects, such as those caused by RCF. An apparatus consisting of phased arrays coupled to the railroad track through a water-filled wheel was subsequently developed to better detect sub-surface and surface breaking defects (Pagano, 1979). Although phased arrays could detect the presence of defects, precise verification of the defect size and orientation was still not possible.

Current rail inspection procedure follows a “Stop and Confirm” process where the track inspection vehicles outfitted with the water-filled ultrasonic wheels called Rolling

Search Units (RSUs) flag a section of rail when a potential defect is detected (Mariani and Lanza di Scalea, 2018). Various factors such as poor signal-to-noise ratio limit the practical achievable speed by this kind of testing to between 20 and 45 mph (Ph Papaelias et al., 2008). This limitation results in the need for scheduling the inspection by specialized vehicles around normal rail revenue traffic, resulting in operational inefficiencies. After a suspect area is flagged, an operator hand verifies the flagged region of rail through an ultrasonic A-scan. Objective sizing of the defect is challenging with an A-scan due to operator judgement. Identification of the defect requires an imaging technique (Schmerr, 2016).

Looking forward, the research goal of passive defect detection is to augment RSUs by having sensors on the train while running at revenue speed. When an area of rail is flagged as suspect, ultrasonic imaging would be used to generate an image of the rail's internal volume for precise sizing of the defect.

Figure 4-8: Rolling Search Unit used in ultrasonic inspection of rails (Clark, 2004).

CHAPTER 5

HIGH-SPEED DEFECT DETECTION IN RAILS

5.1 Introduction

Rail inspection is commonly carried out by ultrasonic techniques that involve a pitch-catch or pulse-echo scheme to detect internal flaws. This method is usually implemented by Rolling Search Units (RSUs) whose maximum test speed is limited to 45 mph. These inspections must be carried out by specialized test vehicles requiring careful scheduling to minimize unavoidable disruptions to normal train traffic operations.

This chapter will present the concept and to-date results from a radically new ultrasonic testing method for rails. This technique exploits the natural wheel excitations of the rail and extracts a stable ultrasonic Transfer Function (Green's function) of the rail by utilizing pairs of air-coupled ultrasonic transducers. The sensing head is completely non-contact and it does not require an active or controlled ultrasonic excitation. The key to this concept is a special signal processing in Chapter 3.3 that is applied to the received signals

to eliminate or minimize the effect of the uncontrolled wheel excitation. Importantly, this method only works if the wheels excite a significant amount of ultrasonic energy at the appropriate frequencies. For ultrasonic guided wave rail inspection, the optimal frequency is between 20 kHz and 100 kHz. Current studies are aimed at understanding the operational limitations of the method. Results from three field tests conducted at the Transportation Technology Center (TTC) in Pueblo, CO, at testing speeds as high as 80 mph, will be shown to highlight the potential for this “high risk – high reward” approach. The “high reward” derives from (a) the possibility to inspect the rail at speeds at revenue speed or higher, which would enable a new concept of a “smart train” that performs inspections seamlessly during regular operations, and (b) the opportunity for great redundancy given the multiple passes of trains over the same track, naturally resulting in an improved probability of detection for any flaw that may be present.

While this high-speed mode of testing is not likely to replace conventional ultrasonic inspection, at least at the current stage, it would constitute an important tool in the hands of railroads and regulatory agencies to increase the safety of rail transportation and the efficiency of rail maintenance operations.

5.2 Prototype Design

Two generations of prototype designs based on the ideas of a passive non-contact inspection technique was designed, constructed, and field tested at TTC in Pueblo, CO, the largest facility for railroad transportation research testing in the US. The first-generation prototype was tested in 2016, followed by a second-generation prototype used in the 2018 and 2019 field tests. The second-generation prototype greatly expanded available reference data to validate the experimental data by adding GPS tracking and high-speed image acquisition. Furthermore, due to a change in the rail car used to host

the prototype, the attachment changed from the a rigid connection to the front axle of the rail truck to a connection to the equalizer beam of the rail truck, as shown in Figure 5-1.

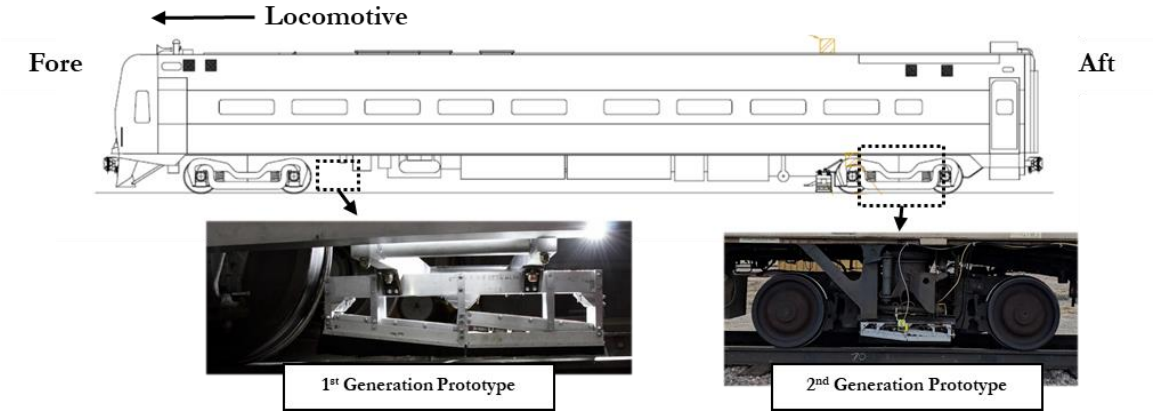

Figure 5-1: Passive Inspection Prototype Mounting Difference

For the first-generation prototype, the US Federal Railroad Administration (FRA) DOTX-216 test car was used to host the prototype, as shown in Figure 5-2. The second-generation prototype was mounted to the 5229 test car provided by TTC, illustrated in Figure 5-1. The sensing head was mounted on a beam that was rigidly connected to the front axle of the car. The sensing head consisted of two arrays of capacitive air-coupled receivers positioned at a minimum lift-off from the rail's top surface of 3 inches. This lift-off guaranteed true non-contact probing of the rail. The receivers were narrowband devices centered at three different frequency bands. All results shown in this chapter were obtained from receivers centered at 120 kHz. This was a reasonable frequency to examine for inspection purposes, since ultrasonic guided waves in rails are known to offer good sensitivity to defects in the range of 20 kHz - 500 kHz (Bartoli et al., 2005; Cawley, n.d.; Hesse and Cawley, 2006; Rose et al., 2004, 2002; Wilcox et al., 2003). The separation between two sensors in a pair was 18 inches (45 cm).

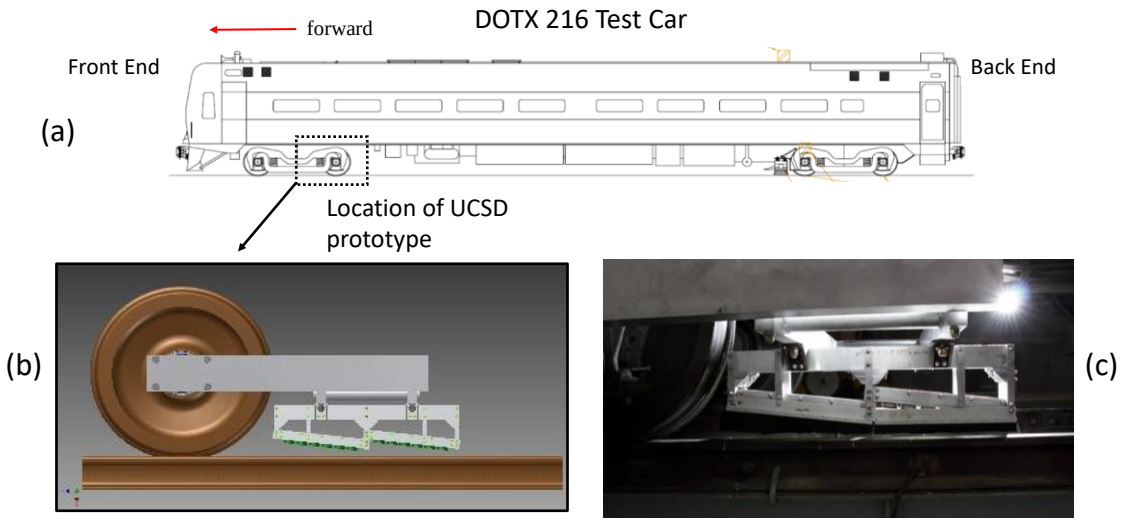

Figure 5-2: The passive inspection prototype for the first field tests at the Transportation Technology Center. (a) The FRA DOTX-216 test car. (b) and (c) The prototype's sensing head with non-contact air-coupled receivers.

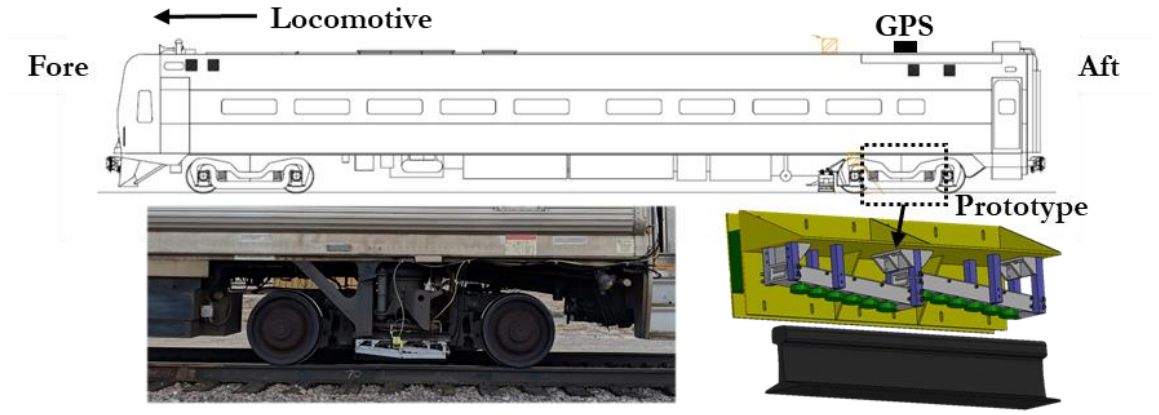

Figure 5-3: Schematic diagram of second-generation prototype mounted on the TTCI 5229 Test Car at the Transportation Technology Center. The prototype is attached to the equalizer beam of the rail car's truck, illustrated in the bottom pictures.

The receivers were opportunely inclined from the rail surface at 6 degrees from the vertical to best capture the leaky surface waves propagating in the railhead according to Snell's law. The leaky wave was previously used for air-coupled rail inspection systems with active excitation (Coccia et al., 2011b; Mariani et al., 2016). The receivers' orientation also effectively provided a directional sensing of the waves excited by wheels located to only one side of the arrays (front end), with virtually no sensitivity to waves propagating in

the opposite direction (as from reflections or excited from wheels located to the other side of the arrays – back end).

The array lay-out was such that up to four independent pairs of 120 kHz sensors could be utilized concurrently to increase the rate of convergence of the passively extracted transfer function G_{AB}, as illustrated in Figure 5-4. Data from sensors split into 3 individual groups. Each group consist of 4 sensors, two in the prototype's front end and two in the prototype's rear end. Thus, each group has 4 unique combinations of sensors that were used to generate a set of Damage Index values calculated through the Mahalanobis Squared Distance algorithm.

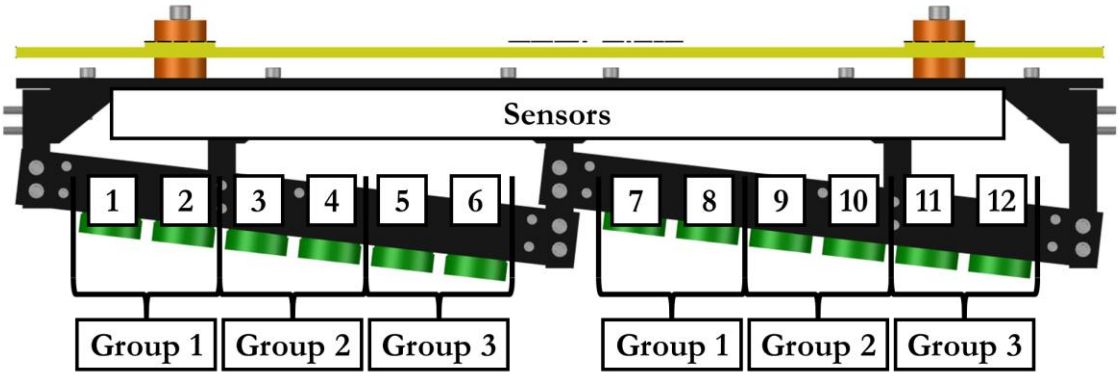

Figure 5-4: Passive Inspection Prototype Sensor Layout

5.3 System Overview

For the first-generation prototype, signal acquisition from the air-coupled receivers was accomplished by a National Instruments (NI) PXI unit running LabVIEW Real-time to guarantee deterministic processing. The data unit also recorded a tachometer TTL pulse that marked the spatial position of the test car with a resolution as small as 1" (2.54 cm). GPS and camera data were provided by ENSCO and synced to the encoder TTL pulse. A high-speed camera (SONY ICX-424 with a 6mm C-mount lens) with appropriate illumination (30k Lumens LED flood light) recorded images of the rail during each run. The

purpose of the camera was to verify the presence of visible discontinuities in the rail, i.e. joints and welds, when the prototype detected an anomaly. A diagram of the hardware connection is schematized in Figure 5-5.

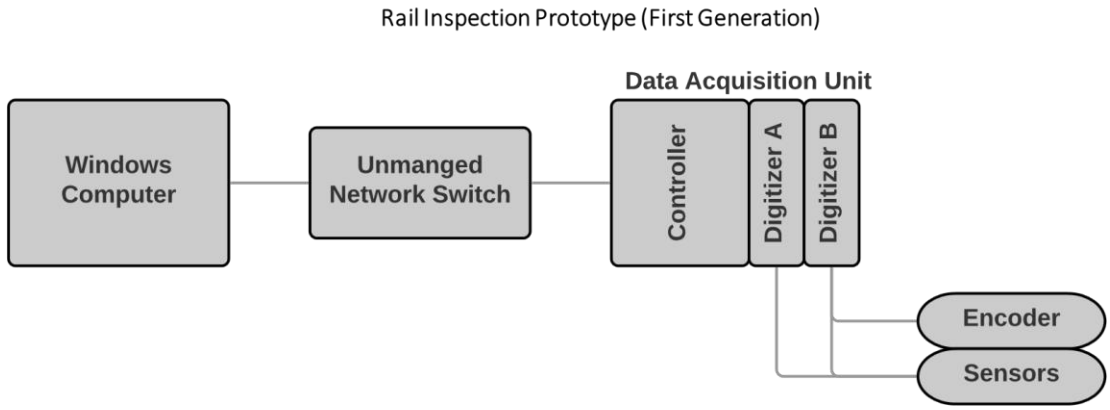

Figure 5-5: First-Generation Prototype Data Acquisition Diagram

Data for the first-generation prototype was gathered through a PXI-1042 chassis with a PXI-8119 embedded controller running LabVIEW Real-time. PXI-5105 digitizers were used to convert the analog signal after signal conditioning to a digital signal to be stored on the Solid-State Drive (SSD) located on the controller. A Windows laptop was remotely connected to the PXI for user control and monitoring, as shown in Figure 5-6.

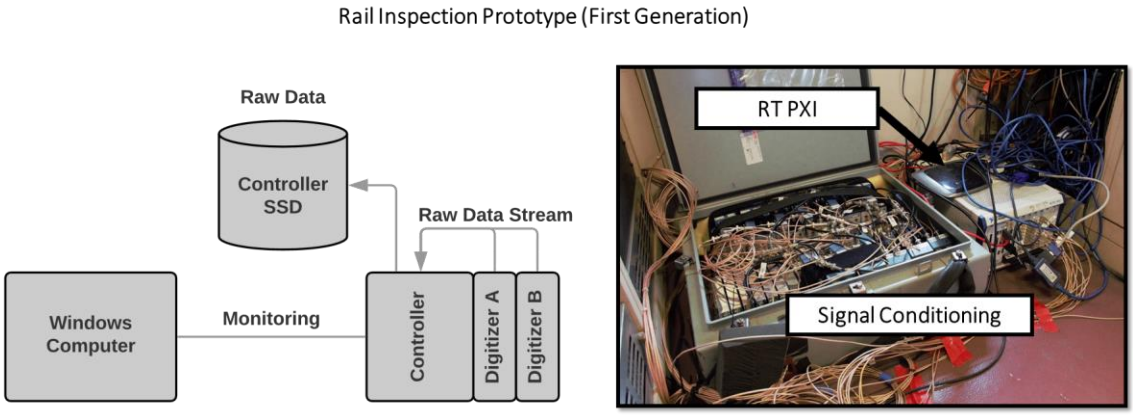

Figure 5-6: First-Generation Prototype Data Stream Diagram

The second-generation prototype expanded the resolution of reference data such as the camera and GPS location to the raw data. Furthermore, real-time transfer function reconstruction was demonstrated using an FPGA for deterministic processing. The prototype consists of the sensor hardware, positioning equipment, vision equipment, and the data acquisition and processing units. A general diagram of the second-generation prototype is provided in Figure 5-7.

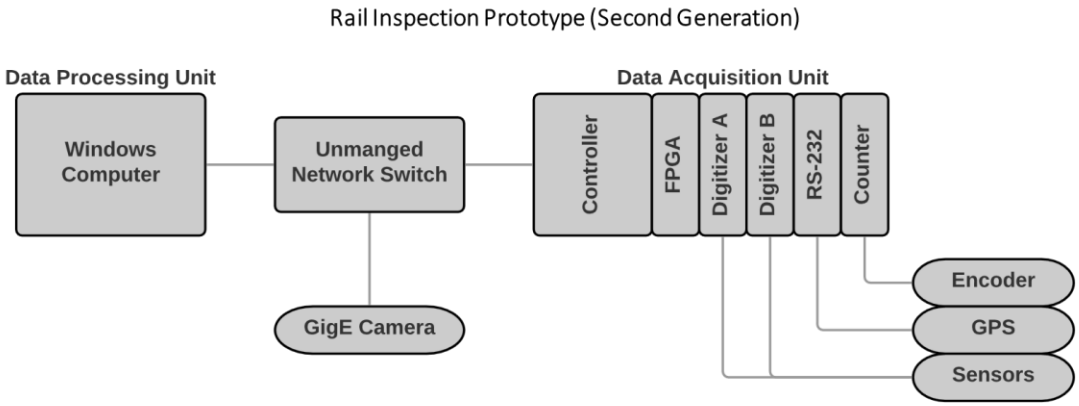

Figure 5-7: Second-Generation Prototype Data Acquisition Diagram

In addition to the 12 air-coupled, non-contact, acoustic transducers, 2 fore and 2 aft lasers are located on the prototype to provide alignment information between the sensor hardware and the rail. A later revision for the 2019 field test reduced the number of lasers to 1 fore and 1 aft. Using two pairs of laser sensors resulted in large amounts of false calls. Class 2 photoelectric laser sensors with PNP logic were used for determining the alignment of the prototype with the rail. A 15 V DC power supplied the required power to operate the sensor and logic. The capacitive and laser sensors signals were routed to Digitizers A and B on the data acquisition unit for further processing.

The positioning system consisted of the following: GPS receiver, GPS antenna, and encoder. The encoder was provided by TTCI during the field test and has a 2-inch resolution. The GPS unit provided the latitude, longitude, and speed. The GPS receiver

was a Novatel FLEX6-G1S-00G-0CN receiver with GPS, L1, SBAS, DGPS, GLIDE capabilities at 100 Hz position refresh rate with communication via RS-232. A GPS antenna, Novatel GNSS-501, received L1 GPS+GLONASS, BeiDou B1, Galileo E1 signals to determine the location of the prototype. A 12 V DC power supply provided power to the GPS unit. Data from the GPS unit is routed to the data acquisition unit in ASCII format and NMEA protocol. Lastly, the encoder TTL signal routed through a SCB-100 breakout box before connecting to the counter card, PXI-6624 isolated 48V counter/timer, on the data acquisition unit.

The vision system consisted of a Basler ace GigE, acA800-200gc color camera at 800 by 600-pixel resolution and 90 frames per second acquisition rate. Three Smart Vision OverDrive ODLW300-WHI-W LED Linear Lights to provided illumination for the camera. A variable focal length LMVZ4411 lens was mounted to the camera with the following specifications: 1/18”, 4.4 – 11mm, F1.6 Manual C-Mount. The Basler ace camera controls the Smart Vision strobe lights through TTL pulses to the linear light PNP input line that correspond to the camera’s exposure cycle. The linear lights are powered by an external DC power supply able to provide the 24 V DC at 19 Amps. A signal routing box takes the I/O cable from the GigE camera and routes it appropriately for the PNP trigger line for the linear lights. A 10 V DC power supply provides the required circuit voltage to trigger the lights. This ensures synchronization between the linear lights and the camera so that during exposure, the lights are on. Lastly, the Baser ace GigE camera is powered using a Power-Over-Ethernet (POE) Module so a common ethernet cable is used for data transmission and power. The connection diagram for the vision acquisition system is illustrated in Figure 5-8.

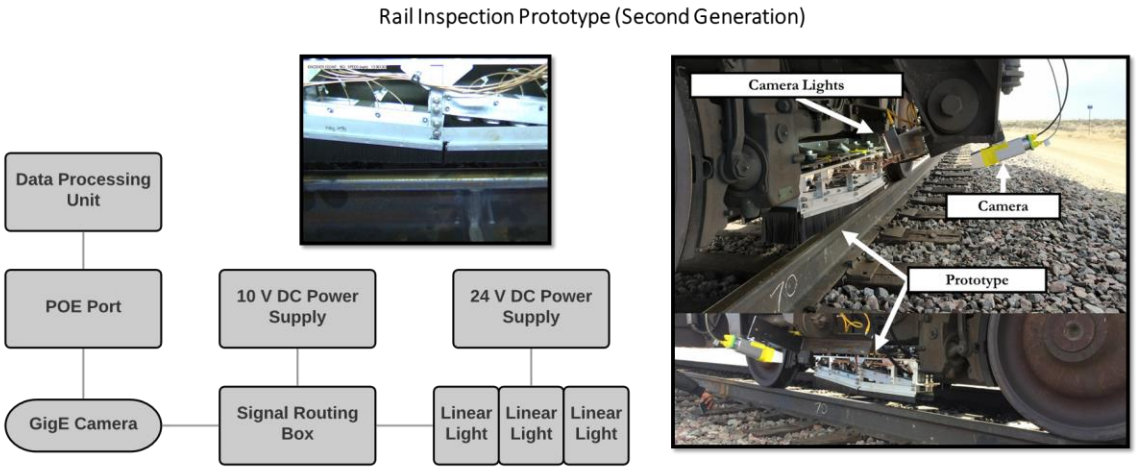

Figure 5-8: Vision Acquisition Connection Diagram for Second-Generation Prototype

The data acquisition and processing unit is composed of two systems. The first system is a National Instruments (NI) PXIe-8880 Real-Time (RT) controller, mounted on a NI PXIe-1082 chassis. The RT controller handles the signal routing for the NI FlexRIO PXIe-7975R Field Programmable Gate Array (FPGA). Data from the sensors is acquired on the NI PXI-5105 Digitizer A and B through SMB connection. GPS position is from the GPS receiver into NI PXI-8432/2 through RS-232., and encoder count is processed from the encoder TTL into NI PXI-6624 Counter/Timer through the SCB-100 breakout box. A frontal view of the data acquisition system is provided in Figure 5-9. The PXIe-8880 RT controller runs LabVIEW RT 18.0, a 32-bit Pharlap system utilizing 4 GB of Random-Access Memory (RAM) and contains a 700 GB Solid State Drive (SSD) for raw data storage. A real-time operating system was selected to ensure deterministic processing and ensure sustained run-time with reduced computational jitter and instability.

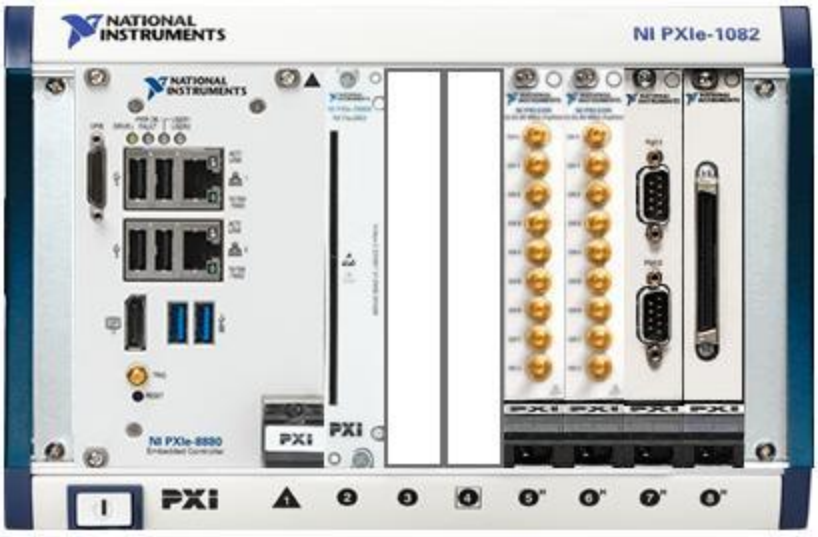

Figure 5-9: National Instruments Real-Time Second-Generation Data Acquisition Unit

The raw data from Digitizer A and B is routed to the NI FlexRIO PXIe-7975R FPGA running LabVIEW FPGA 2018 to be processed. A time domain transfer function is then extracted from the FPGA and routed back to the controller before being sent to the Windows computer via ethernet. At the same time, raw data from Digitizer A and B is tagged with the encoder count, GPS location, GPS speed, and laser Boolean before saving onto the RT controller's internal SSD. Digitizer A contains the front capacitive sensors, 1 through 6, and the front two laser sensors. Digitizer B contains the rear capacitive sensors, 7 through 12, and the rear two laser sensors. Reference Figure 5-4 for the sensor locations.

The LabVIEW Real-time algorithm is a state machine consisting of 3 main states: Initialize, Wait for Command, and Acquire Signal. The major components of each section in the RT controller are listed in the top diagram of Figure 5-11. An example of the front-end user control for the RT controller is displayed as Figure 5-10.

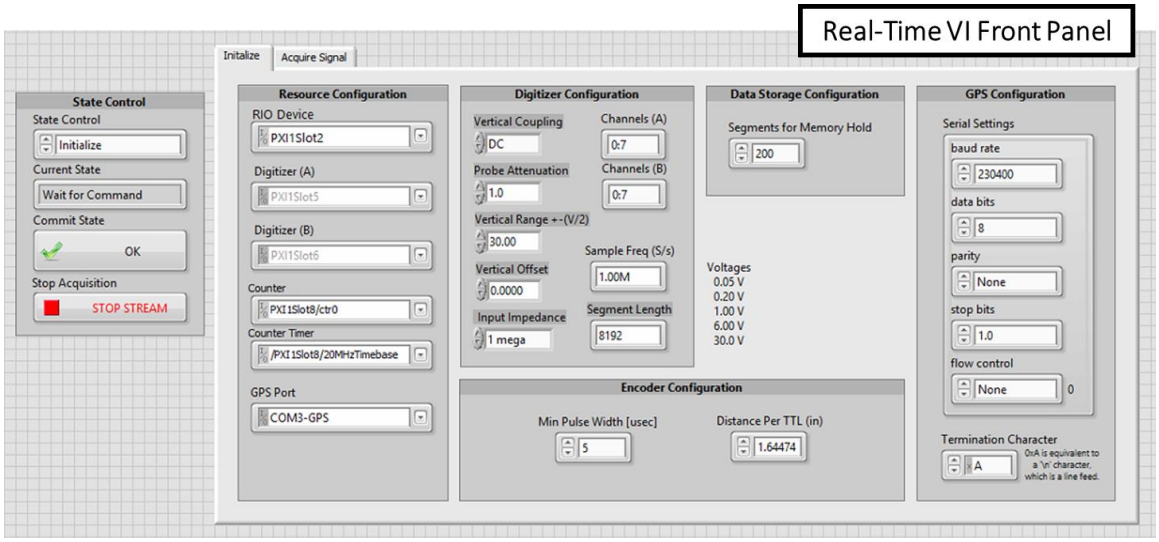

Figure 5-10: Front-End Display for the LabVIEW Real-Time controller system for the Second-Generation Prototype

The initialize state performs the following procedures: loads the FPGA bitfile and allocates the Dynamic Random Access Memory (DRAM) First-in-First-out (FIFO) for the PXIe-7975R FPGA, resets and configures the two PXI-5105 digitizers, resets and configures the PXI-6624 counter, resets and configures the RS-232 port on the PXI-8432/2 and verifies connection with the GPS unit, and configures network stream connection and network variables for communication with the host PC. After successful initialization, the controller moves into an idle state, Wait for Command. Once ready, the operator activates acquisition by selecting the Acquire Signal state. Once selected, the Real-time controller sends a synchronization signal to the two digitizers to synchronize the data acquisition clocks. If no faults are detected, a trigger to start acquisition is sent to the digitizers, encoder, and GPS to start acquisition. Raw data for each data stream is handed in separate loops and transported to a main Raw Data Routing Handler loop via FIFO buffers. From the Raw Data Routing Handler, the data is duplicated. One portion of the raw data goes to disk storage on the Real-Time controller while another is sent to the FPGA.

Before the data is ready to be sent to the FPGA for processing, the data must be downsampled from the acquisition rate of 1 MS/s to 500 kS/s. Next, the floating-point precision data is converted to fixed point. The raw data is then routed into a format where the data is threaded between various channels and duplicated for averaging. This is done for the FPGA to process as quickly as possible while accepting a requirement for higher throughput through the PXI chassis backplane. The ready-to-process data is sent to the FPGA through Direct Memory Access (DMA) FIFO. In a separate loop on the RT controller, the system waits for reconstructed impulse response data to appear in the DMA FIFO from the FPGA. The data is then tagged with the appropriate metadata and sent for feature extraction and outlier detection. The Damage Index data with the laser Boolean, GPS data, and encoder count metadata is then sent over to the host PC via Network Steam.

The LabVIEW FPGA algorithm consists of 7 main components in Single Cycle Times Loops (SCTL) and consist of the following processes: unaveraged auto-power spectrum calculation, unaveraged front sensor power spectral density calculation, unaveraged rear power spectral density calculation, unaveraged cross-power spectral density calculation, transfer function reconstruction, transfer function frequency selection, and impulse response reconstruction. Downsampled and fixed-point converted data is streamed from the RT controller via DMA FIFO. Data from the front and rear sensor is then split into its own Block Memory FIFO. The front sensor data is duplicated since it is used for the Auto-Power Spectral Density (APSD) and Cross-Power Spectral Density (CPSD) calculation. All data passes through a Hamming window, followed by a Fast Fourier Transform (FFT), and then a cross-correlation operation. For the APSD calculation, since the data does not need to be synchronized with another sensor, the process is contained within a single SCTL. For the CPSD calculation, since each sensor

needs its own FFT, a second SCTL is used to ensure the data is synchronized before cross-correlation is performed. Depending on the amount of noise in the system, either the inter-segment or intra-segment CPSD calculation can be performed in the cross-correlation portion. Utilizing the inter-segment calculation increases the resource usage significantly. A FIFO buffer is then used to store and synchronize the data processed by the APSD and CPSD calculation. After the individual APSD and CPSD segments have been averaged, the data is then sent to another SCTL for the deconvolution procedure. The resulting estimated transfer function is then sent to a frequency selection SCTL where the 20-40 kHz and 70-120 kHz frequency bands are extracted. Each frequency band is then sent through an Inverse Fast Fourier Transform (IFFT) SCTL to generate the estimate structural impulse response estimate (IRSE). Lastly, the IRSE is sent to the RT controller via DMA FIFO for further analysis. A summary of the major components for the processing performed on the FPGA is listed in the bottom diagram of Figure 5-11.

Figure 5-11: Real-Time (top) and FPGA (bottom) algorithm process diagram for second-generation prototype.

Real-Time Algorithm (Second Generation)

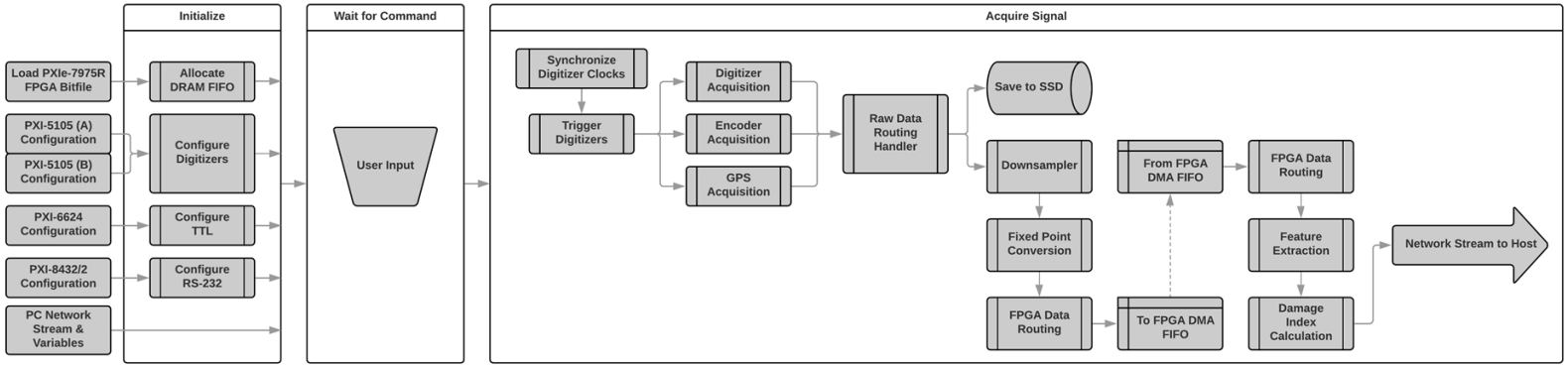

FPGA Algorithm (Second Generation)

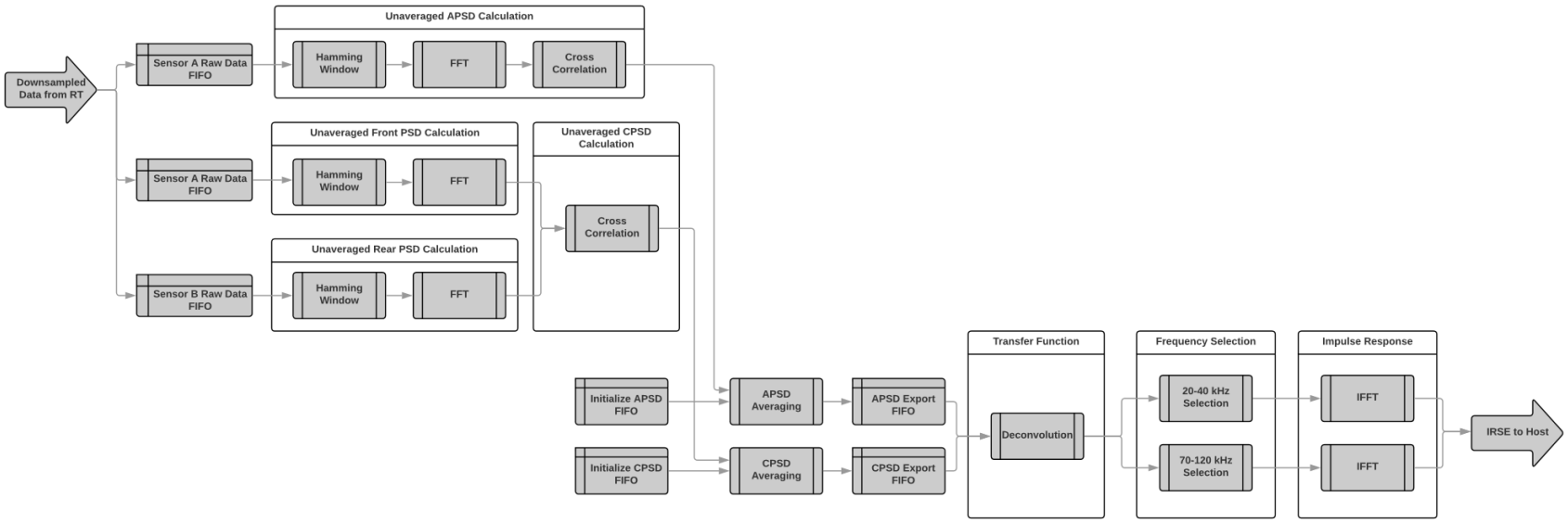

The data processing unit is a Windows 64-bit computer running LabVIEW 2018 whose primary purpose is to process the time-domain transfer function into a relevant Damage Index (DI) through a Mahalanobis Outlier Detection algorithm. An example of the front-end user control for the Windows PC is displayed as Figure 5-12.

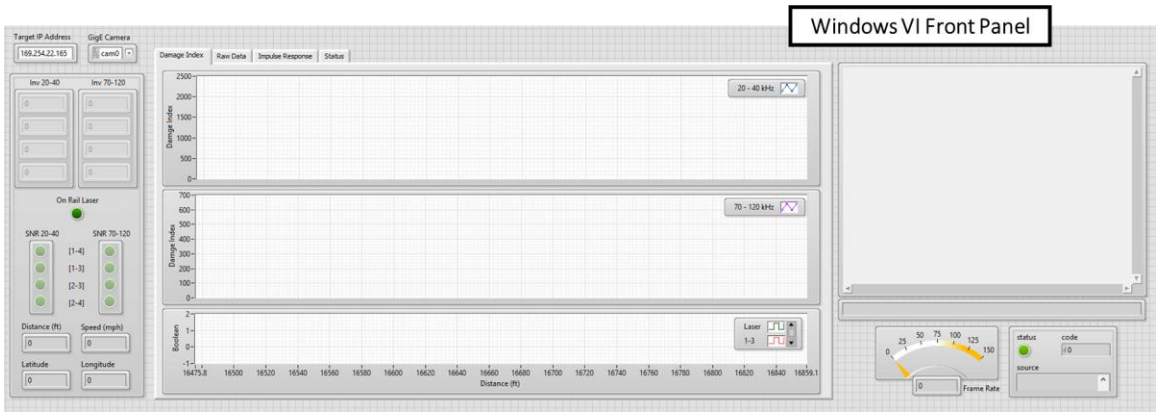

Figure 5-12: Front-End Display for the LabVIEW Windows PC system for the Second-Generation Prototype

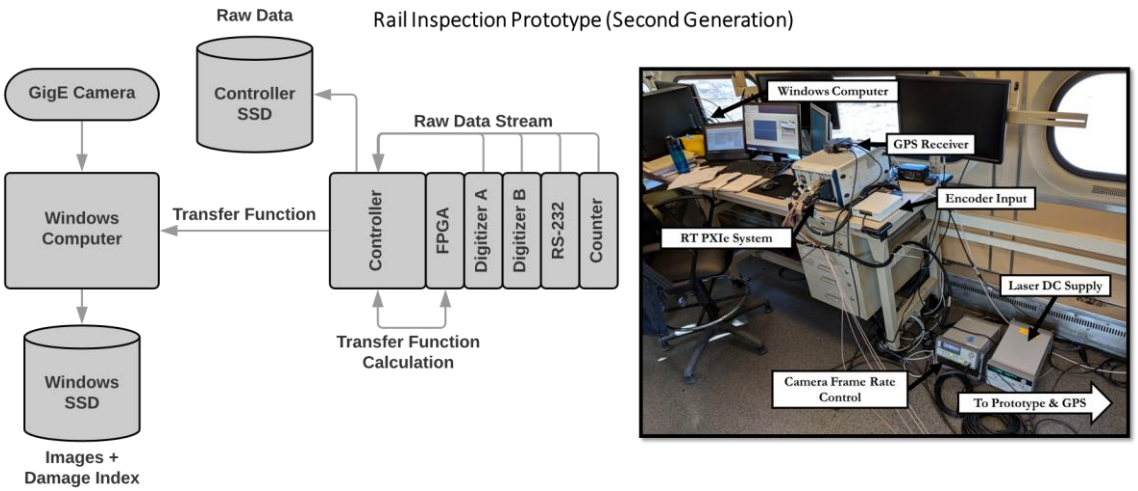

Figure 5-13: Second-Generation Prototype Data Stream Diagram

The DI is then saved onto the Windows computer SSD with the relevant encoder distance, GPS position, GPS speed, and laser Boolean. Concurrent to the DI calculation, images gathered at 800 by 600-pixel resolution are streamed through ethernet to the data

processing unit and tagged with the encoder count and GPS speed before saving on the SSD for the 2018 field test. Camera data for the 2019 field test is tagged with the GPS latitude and longitude instead. A summary of the Data Acquisition and Processing unit is illustrated in Figure 5-13.

5.4 Test Procedure

Test runs were performed at TTC's Railroad Test Track (RTT), which allowed maximum test speeds of up to 80 mph (128 km/h), TTC's Rail Defect Test Facility (RDTF), which allowed maximum test speeds of 25 mph (40 km/h), and TTC's High Tonnage Loop (HTL), which allowed maximum test speeds of 45 mph (72 km/h). A locomotive was used to tow the test car instrumented with the passive-only prototype. Locations of the RTT, RDTF, and HTL are shown in Figure 5-14.

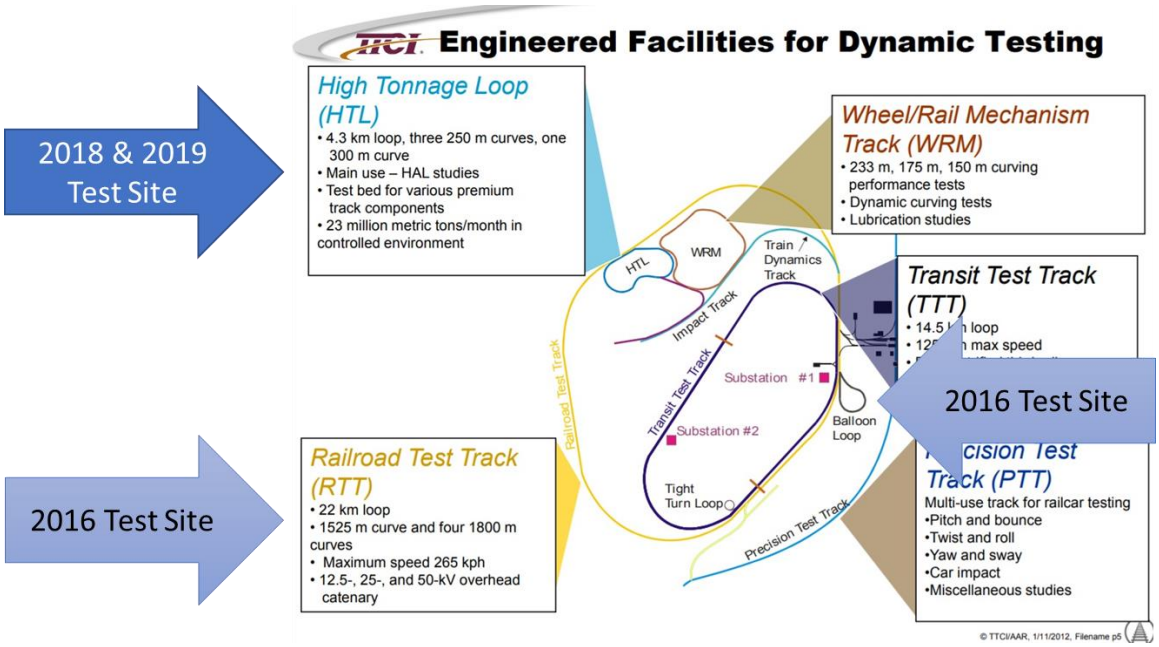

Figure 5-14: Transportation Technology Center, Inc (TTCI) test track facilities used in the 2016, 2018, and 2019 field test. Image courtesy of TTCI.

The runs at the RTT were conducted between markers R42 and R25. As shown in Figure 5-15 (a), this test zone featured a tangent track in the middle, with curved tracks at the beginning and at the end. As many as three joints and fourteen welds were identified in the RTT test zone through visual survey and the high-speed camera. A snapshot of a joint from the camera is shown in Figure 5-15 (a). Runs at the RTT test track were conducted at speeds of 30 mph (48 km/h) to 80 mph (128 km/h) in 10 mph (16 km/h) increments. In comparison, current ultrasonic inspection speeds in the United States are limited to 45 mph (70 km/h).

In addition to the high-speed tests at the RTT, some test runs were conducted at the RDTF at the maximum allowable speed of 25 mph (40 km/h). Specifically, these runs were conducted at the Technology Development Section of the RDTF facility, a mostly curved track with several known defects. The RTT and RDTF were used for the 2016 field test. Subsequent tests moved to the HTL in order to take advantage of natural transverse defects as a result of the testing performed with heavy trains and to test at higher speeds than allowed on the RDTF.

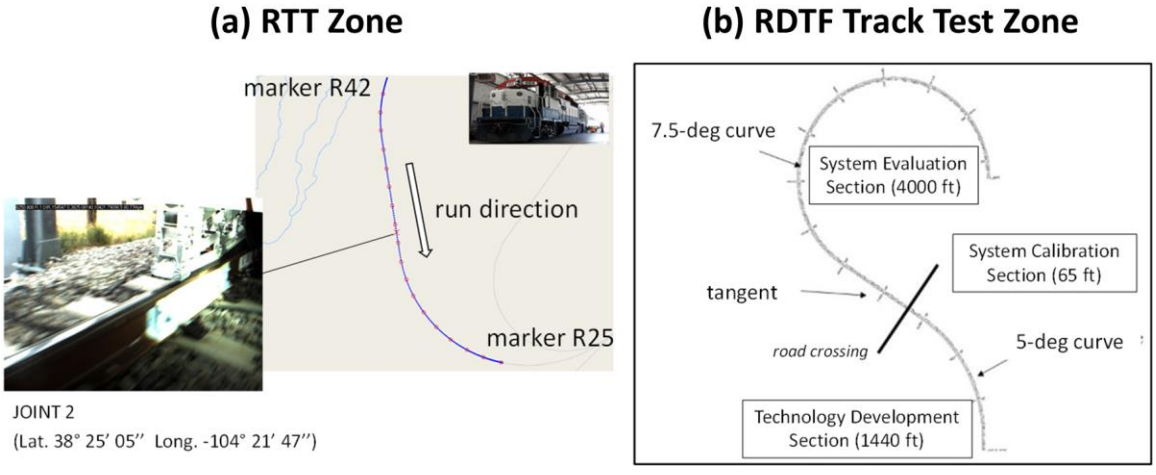

Figure 5-15: Diagram of the rail sections used in the 2016 field test at (a) Railroad Test Track (RTT) and (b) Rail Defect Test Facility (RDTF)

The runs at the High Tonnage Loop (HTL) test track utilized the entire test track. Multiple loops at speeds of 40, 33, and 25 mph were performed to test the prototype at varying levels of ambient excitation. The maximum allowable speed on the HTL was 40 mph. The HTL test track is unique due to its numerous joint and welds from the constant replacement of tracks as a result of damage from heavy freight cars. For instance, between the 2018 and 2019 field tests, there were three new transverse defects and a significant portion of the rail had new rail sections with different weld and joint locations. An aerial view of the test track is shown in Figure 5-16 along with the direction of the test run for the 2018 (counterclockwise) and 2019 (clockwise) field tests.

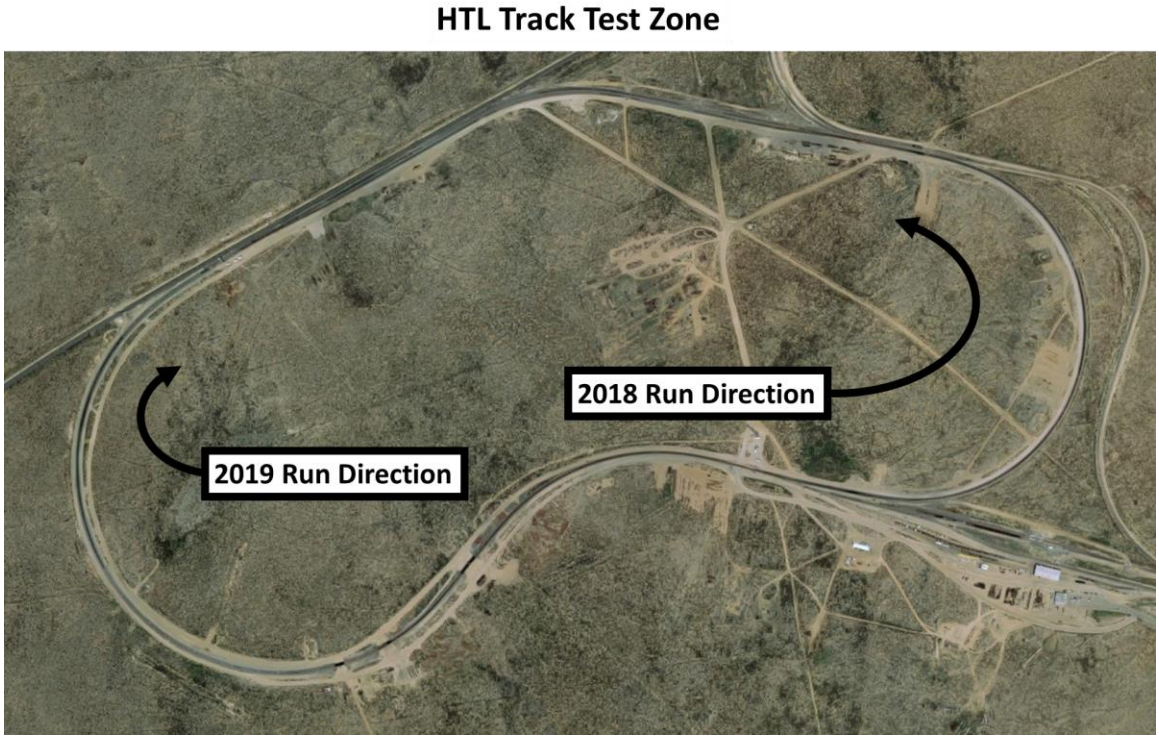

Figure 5-16: Satellite view of the HTL loop used in the 2018 and 2019 field test.

5.5 Proof-of-Concept Transfer Function Reconstruction

For each run, recordings from the pairs of air-coupled receivers located in the front (A) and rear (B) groups under continuous wheel excitation were transformed into the

frequency domain through an FFT algorithm before calculating the cross and auto power spectrums. The transfer function, $G_{AB}(f)$, was subsequently calculated before transformation through and IFFT to yield the time domain impulse response, $G_{AB}(t)$. Section 3.3 contains a more detailed theoretical treatment of the impulse response reconstruction for dual-output systems.

A summary of the entire impulse response reconstruction process is illustrated in Figure 5-17. The upper part, Figure 5-17 (a), demonstrates a representative recording from a front and back receiver on the RTT at 60 mph (96 km/h). The trace demonstrates a high signal strength variability. This is expected from the random wheel and rail contact conditions from surface unevenness, acceleration, braking, etc. The structural impulse response, $G_{AB}(t)$, of Figure 5-17 (b), is representative of a typical $160\ \mu s$ wave arrival for a 20 – 40 kHz wave mode (Rayleigh wave velocity of $2900\ m/s$ for steel and ~47 cm distance between two sensor pairs). The time-of-arrival corresponds to the expected travel time of a leaky surface wave in the rail between the two receiver locations.

In the outlier analysis step, a Damage Index was computed using the strength of the reconstructed impulse response, $G_{AB}(t)$. Experimental testing from the 2016 field test demonstrated that the inverse of the variance of the 20 – 40 kHz wave mode yielded the most stable results without sacrificing detectability. The multivariate Mahalanobis Squared Distance calculation utilized a feature vector consisting of the multiple pairs from each sensor group. The statistical computation of the damage index normalized the data by a baseline calculation from the preceding 10 ft (3 m) of rail. Compared to a simple deterministic metric, use of the Damage Index significantly improves the probability of detection and reduces the probability of false alarms.

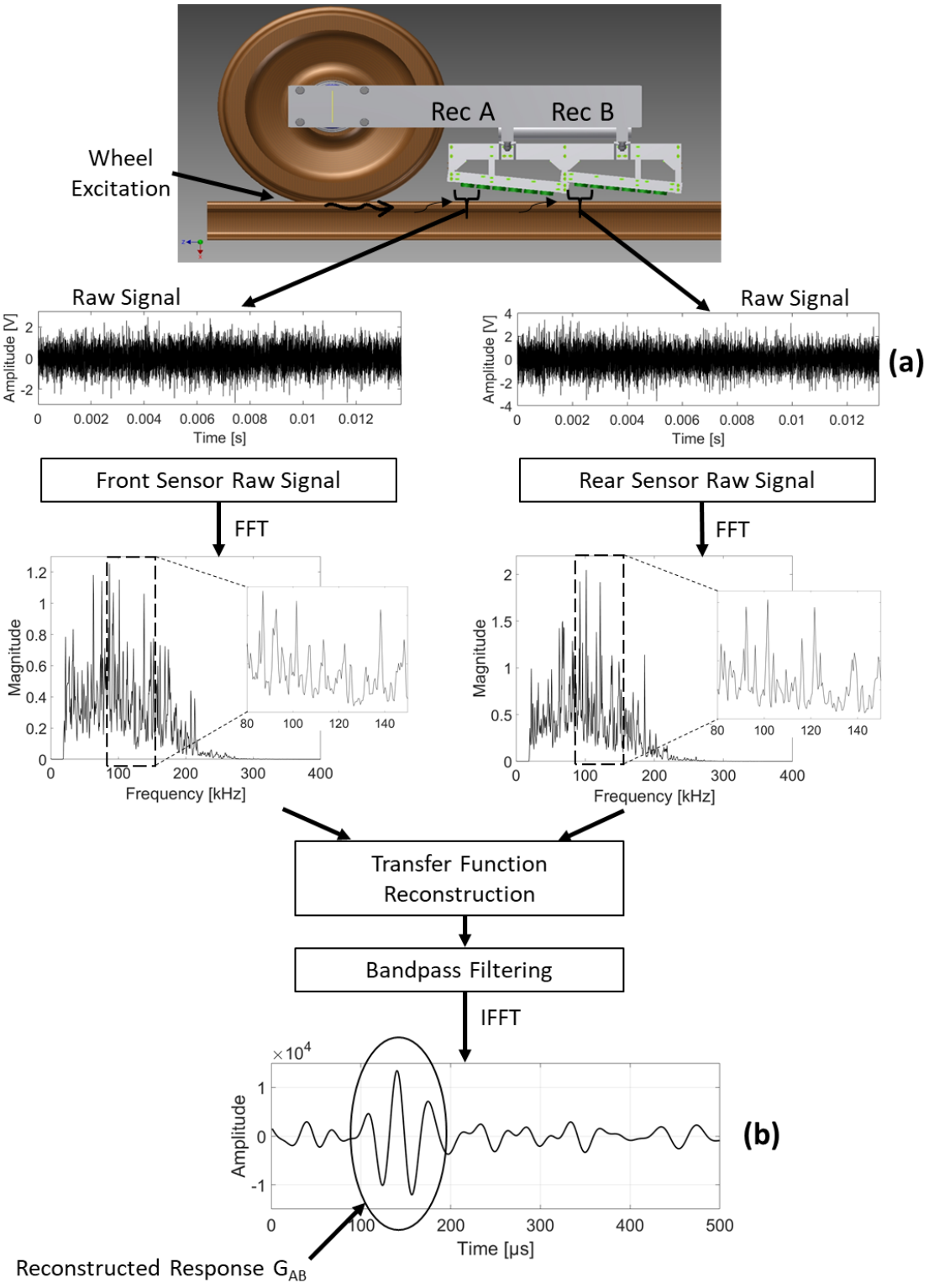

Figure 5-17: Summary of signal processing steps from the (a) the raw signal inputs from the front and rear sensors to (b) the reconstructed impulse response for feature extraction.

5.5.1 Bandpass Filtering

The 20 – 40 kHz band was determined to perform best for passive transfer reconstruction through analyzing reconstructed data passed through a wavelet transform. Furthermore, the lower frequency band has the added benefit of reduced sensitivity from surface damage such as rail shelling (Coccia et al., 2011a). The wavelet transform was performed in the reconstructed Impulse Response Estimate (IRSE) between the frequency range of 20 and 120 kHz. Representative results from the 60 mph run on the RTT are shown in Figure 5-18 when the wheel was flanging during a curved section of rail track, and Figure 5-19 when the wheel was no longer flanging during a straight section of rail track. Flanging is an audible effect when the wheel is scraping against the rail head during curves when the train is not at the balance speed of the track. The sharp cut-off at 20 Hz is due to the analog high-pass filter applied.

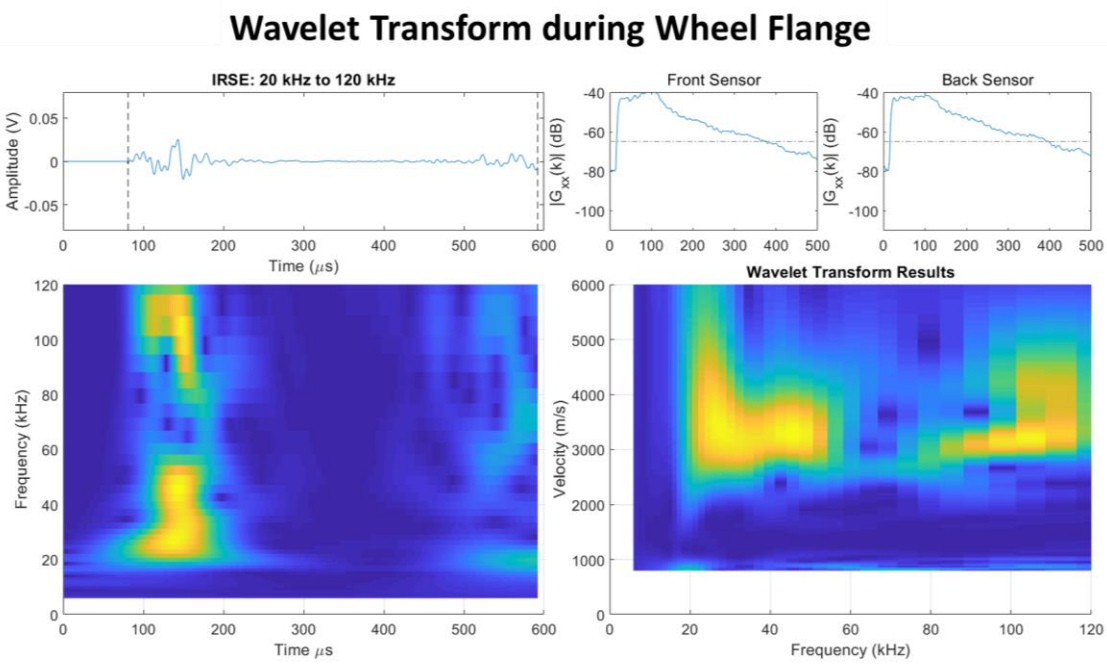

Figure 5-18: Wavelet transform results for 60 mph run during wheel flanging at a curved track section.

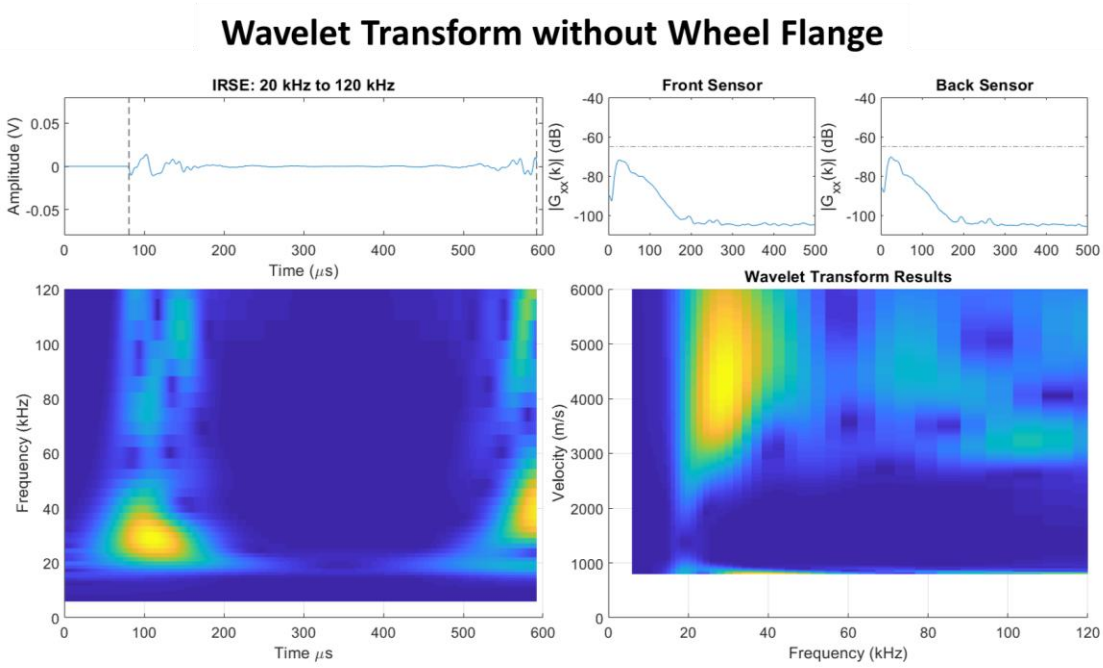

Figure 5-19: Wavelet transform results for 60 mph run without wheel flanging at a straight track section.

In both figures, the top left figure is the reconstructed impulse response estimate, top right graphs are the front and rear sensor power spectrums, bottom left is the wavelet transform time versus frequency, and bottom right is the wavelet transform frequency versus group velocity graph.

The results demonstrate that the 20 to 40 kHz signal band is stable across both straight and curved sections of the track; whereas, the 80 to 120 kHz signal band is prevalent only during the curved sections of track where the wheel is flanging. Furthermore, the time vs frequency graph illustrates that most of the signal arrives around $160\,\mu s$, as expected. A group velocity graph of the different guided wave modes in a 136RE rail, Figure 5-20, is provided for cross-reference with the results in Figure 5-18 and Figure 5-19. Although the non-dispersive Rayleigh wave is the primary wave type of interest for guided wave rail inspection, the experimental results demonstrate that multiple dispersive wave modes are present and detected. Simulation of internal guided wave

modes seem to suggest that the air-coupled system is detecting dispersive wave modes aside from the primary Rayleigh wave (Coccia et al., 2011a).

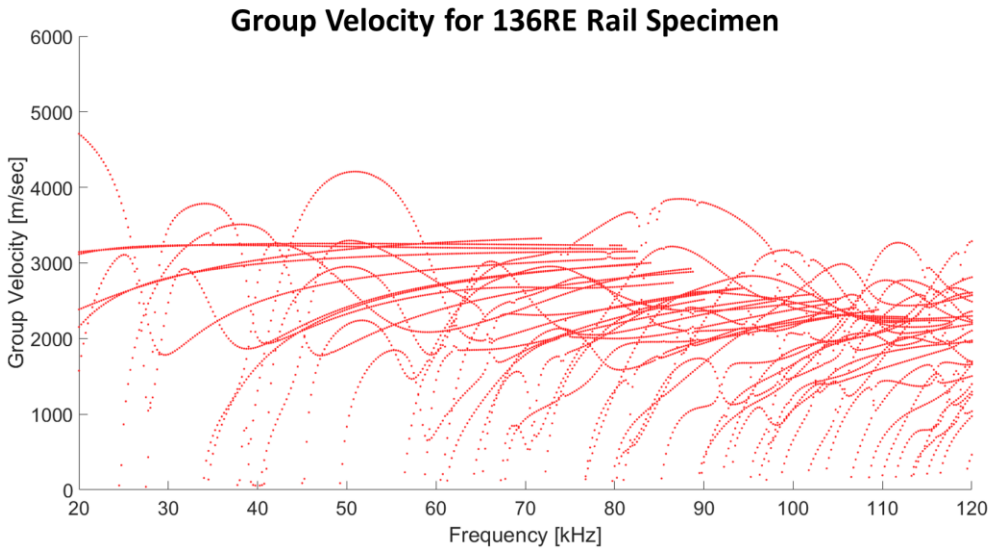

Figure 5-20: Group velocity graph of guided wave modes for 136RE rail.

5.5.2 Averaging to Increase Signal-to-Noise Ratio

The impulse response, $G_{AB}(t)$, emerges from the constructive interference of wave modes continuously excited by the random wheel excitation. The wave modes propagate in the rail along the line connecting the two receivers. Furthermore, the rails structure can be modeled as a one-dimensional waveguide where random wave fields travel along one direction. In this application, the direction is also the direction of alignment of the receiver pairs. This is a desirable feature since studies of cross-correlation of multidirectional diffuse acoustic field have demonstrated that the transfer function is mostly reconstructed by wave fields aligned with the receivers (Roux and Kuperman, 2004; Snieder, 2004; Woolfe and Sabra, 2015).

The constructive interference process under continuous excitation clearly benefits from signal averaging in time. Following a known result in cross-correlation of diffuse

fields, the rate of convergence or Signal-to-Noise Ratio (SNR) of this kind of can be written as:

$$SNR \propto \sqrt{T \cdot \Delta f \cdot e^{-\alpha D}} \tag{5.5.1}$$

where T is the length of the recording time window, Δf is the source bandwidth, α is the linear attenuation coefficient in the test material (dB/m), and D is the distance between the two receivers (Roux and Kuperman, 2004; Salvermoser et al., 2015; Snieder, 2004; Woolfe and Sabra, 2015).

Experimentally, the SNR can be determined by the peak amplitude of the reconstructed impulse response in the time domain, $G_{AB}(t)$, divided by the standard deviation of the total reconstructed signal taken away from the expected arrival time:

$$SNR = \frac{\max\left(G_{AB}(t)\right)}{\mathrm{std}\left(G_{AB}(t)\right)} \tag{5.5.2}$$

The directivity beam considerations do not apply to the rate of convergence for the rail inspection case since all sources are in the “end-fire” direction of the receiving array. Similarly, geometrical spreading effects can be neglected in a unidirectional waveguide. The primary focus in (5.5.1) is the fact that long recording time windows (besides large bandwidths) help with the emergence of the passively reconstructed transfer function.

An additional requirement, where both excitation and reception are moving along the test piece for in-motion scanning test, is that the stationarity of the reconstructed transfer function can only be ideally guaranteed for a fixed position of the test object. Therefore, a compromise must be found between long recording times required by the averaging process and the stationarity of the transfer function reconstruction. The test speed clearly influences this compromise since higher speeds will have to result in shorter

recording times to maintain enough spatial localization. Thus, a study was performed on the 2016 field test results to determine the time window length that resulted in the optimal compromise between the SNR of the prototype's reconstructed transfer function and spatial localization in the rail.

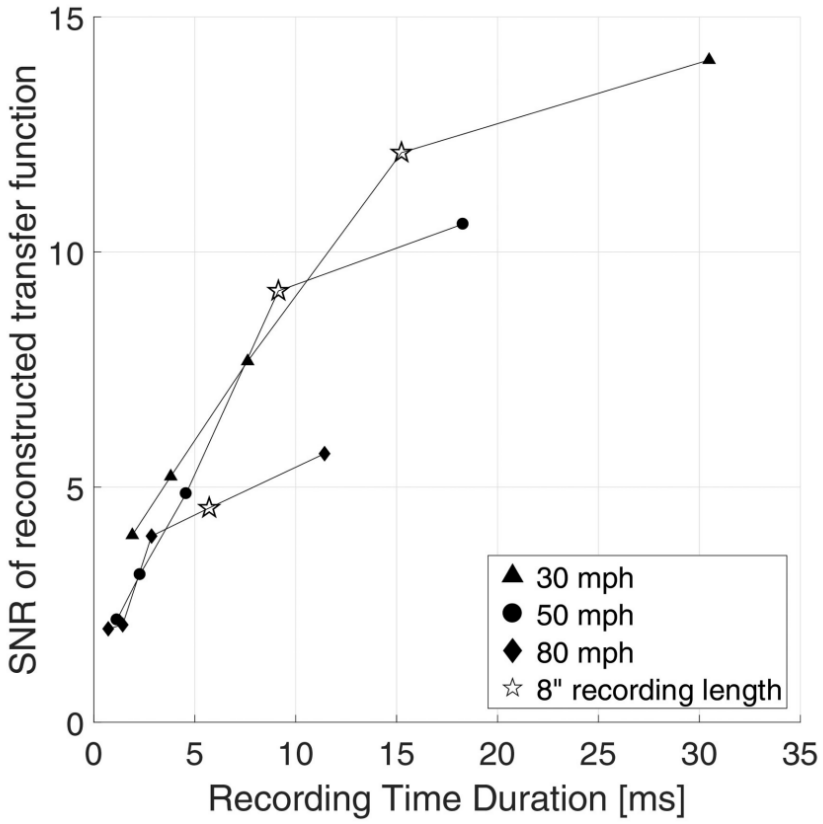

Figure 5-21: Signal-to-Noise Ratio (SNR) of passively reconstructed transfer function for increasing recording length from runs on the RTT track at 30, 50, and 80 mph. Star symbols correspond to an 8 in (20 cm) spatial gage length.

The results of the study are illustrated in Figure 5-21 for the reconstructed transfer function corresponding to the $140\ \mu s$ wave arrival for various recording time lengths and for three runs on the RTT track (2016 field test) at 30 mph, 50 mph, and 80 mph. The three curves end at different times since short time windows are required for higher speed, as discussed earlier. The first observation from the plots in Figure 5-21 is the confirmation

that the SNR generally increases with increasing recording time. However, the rate of increase is seen to drop for the longest recording times considered. This is due to the loss of spatial localization in the rail and consequent nonstationarity of the reconstructed transfer function. The figure also shows that the SNR generally decreases with increasing test speed as a result of the increased standard deviation of the incoherent portion of the wheel generated excitation. The time window durations that correspond to a spatial localization in the rail to within 8 inches (20 cm) are marked by stars for each of the three speeds. The points corresponding to a SNR of approximately 12 at 30 mph, 9 at 50 mph, and 4.5 at 80 mph. These values were chosen as the final recording time window to provide an acceptable compromise between achievable SNR and spatial localization. This choice effectively meant that the prototype "averages" the transfer function of the rail over an 8-inch gage length.

5.5.3 Transfer Function Reconstruction Algorithm

A case study to test the effects of the transfer function reconstruction algorithm using 100 kHz synthetic sinusoidal signal, $S_A(t)$, was used before verification on experimental data. The synthetic sinusoidal single was embedded in white Gaussian noise, $N_A(t)$, with power equal to 20 times the pure sinusoidal signal (Figure 5-22). The goal was to extract the power spectrum of the sinusoid signal at 100 kHz. For segmenting, the option of $n = 16$ segments and $n = 64$ segments were compared, corresponding to a total of 31 averages (16 segments) and 127 averages (64 segments) for the intra-segment procedure, and 120 averages (16 segments) and 2016 averages (64 segments) for the inter-segment procedure. A 50% overlap was used for the intra-segment procedure, and no overlap was used for the inter-segment procedure. The sampling frequency for these signals was 80 MHz. The time duration of each segment was 0.62 msec, resulting in a total time duration of 9.92 msec with 16 segments, and of 39.68 msec with 64 segments.

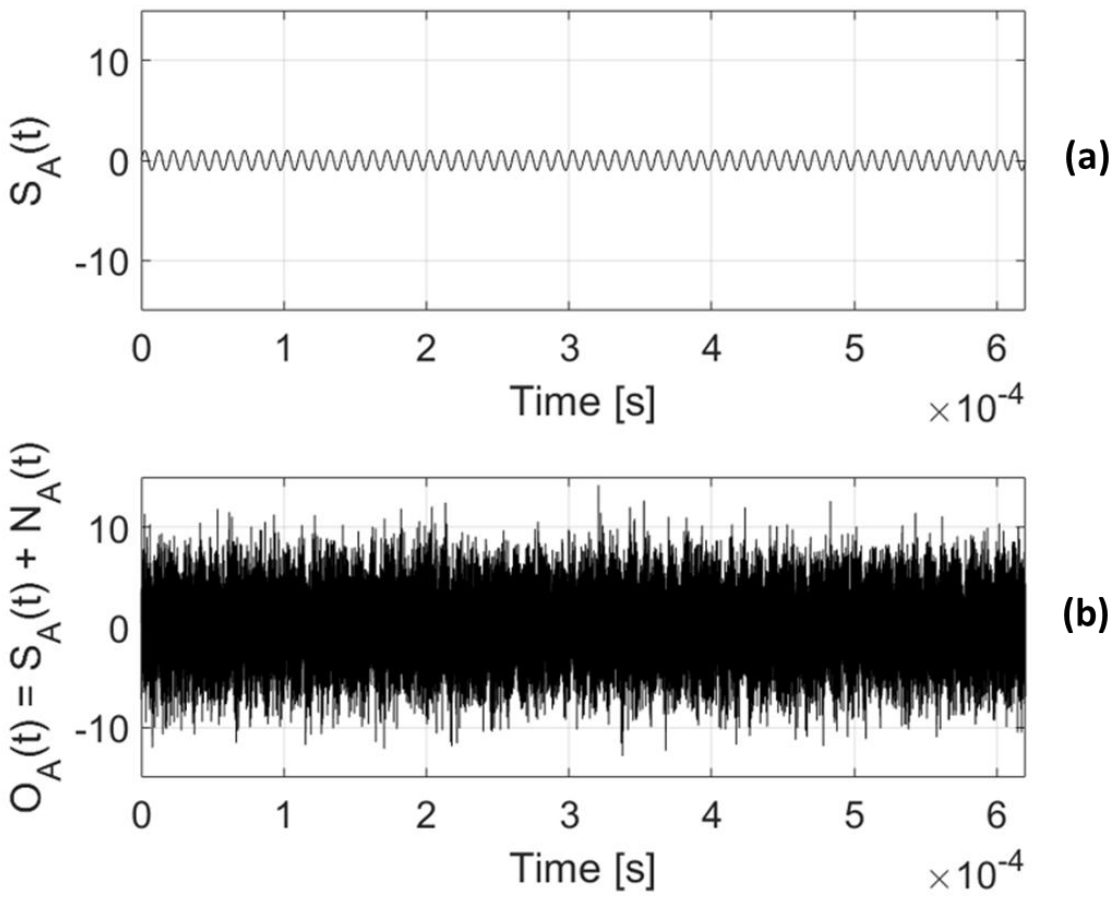

Figure 5-22: (a) Pure sinusoidal signal. (b) Sinusoidal signal with added white Gaussian noise at 20 times the sinusoidal signal energy.

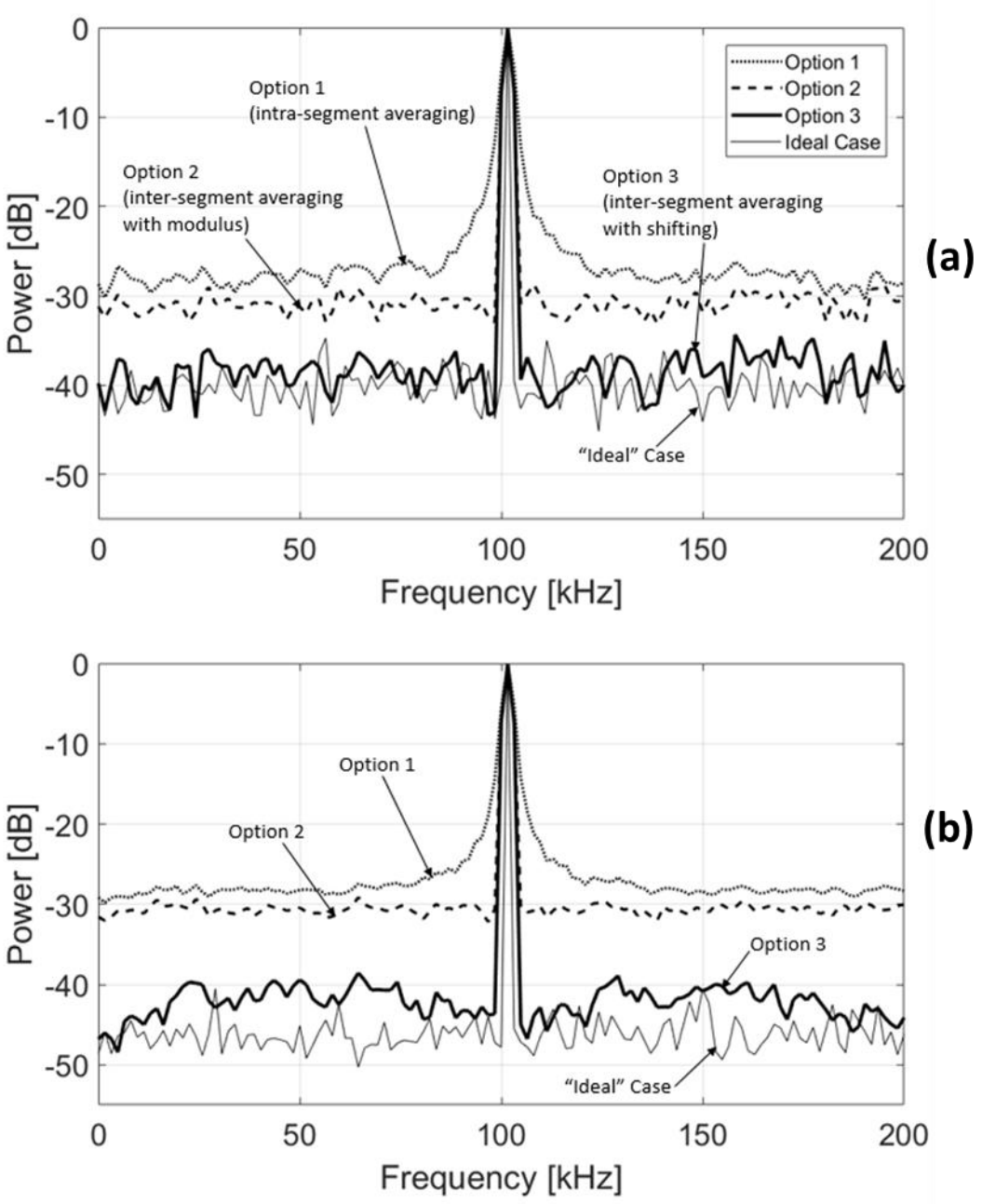

Figure 5-23: (a) Power spectra of sinusoidal signal with added noise extracted with intra-segment averaging (Option 1), inter-segment averaging with modulus (Option 2), inter-segment averaging with shifting (Option 3), and "ideal case" by using 16 segments. (b) Same as (top) by using 64 segments.

Figure 5-23 shows the power spectra extracted from the total signal $O_A(t) = S_A(t) + N_A(t)$ of Figure 5-22 with the traditional SISO intra-segment averaging (Option 1), dual output inter-segment averaging with modulus (Option 2), and dual output inter-

segment averaging with shifting (Option 3). In addition to the three options, an “ideal” case where the signal, $S_A(f)$, was artificially correlated in phase among the different segments (hence no need for segment shifting) is shown for comparison. The metric of comparison for these results is the SNR computed as the mean decibel value of the noise in the spectra provided (values around the 100 kHz peak).

The results using 16 segments are shown in the top plot of Figure 5-23 and clearly demonstrates Option 1 (intra-segment averaging) has the worst SNR, on the order of ~ 28.3 dB, as predicted by the theory. Option 1 also artificially broadens the signal peak at 100 kHz. This broadening is not caused by a specific window since all cases were Hamming windowed. Option 2 (inter-segment averaging with modulus) substantially sharpens the signal peak, but it brings only a slight improvement in SNR to ~ 30.7 dB, since it still contains a substantial amount of noise. The best result is obtained with Option 3 (inter-segment averaging with shifting) that maintains a sharp signal peak and achieves a SNR~ 39.2 dB. Furthermore, the performance of Option 3 is very close to that of the “ideal” case of perfect signal alignment, confirming that shifting by the maximum cross-correlation lag effectively aligns the correlated portion of the signal and hence allows the averaging process to eliminate the noise components.

The results using 64 segments are shown in the bottom plot of Figure 5-23. This figure confirms Option 3 as the best option of the three. The figure also shows that only a marginal improvement in SNR is obtained by the increased number of averages (for Option 3, for example, SNR is ~ 44.8 dB with 64 segments against ~39.2 dB with 16 segments). While the specific improvement with increasing the number of segments will obviously depend on the specific signals considered, the general encouraging conclusion is that a reasonable number of segments (e.g. 16) can be enough to mitigate noise.

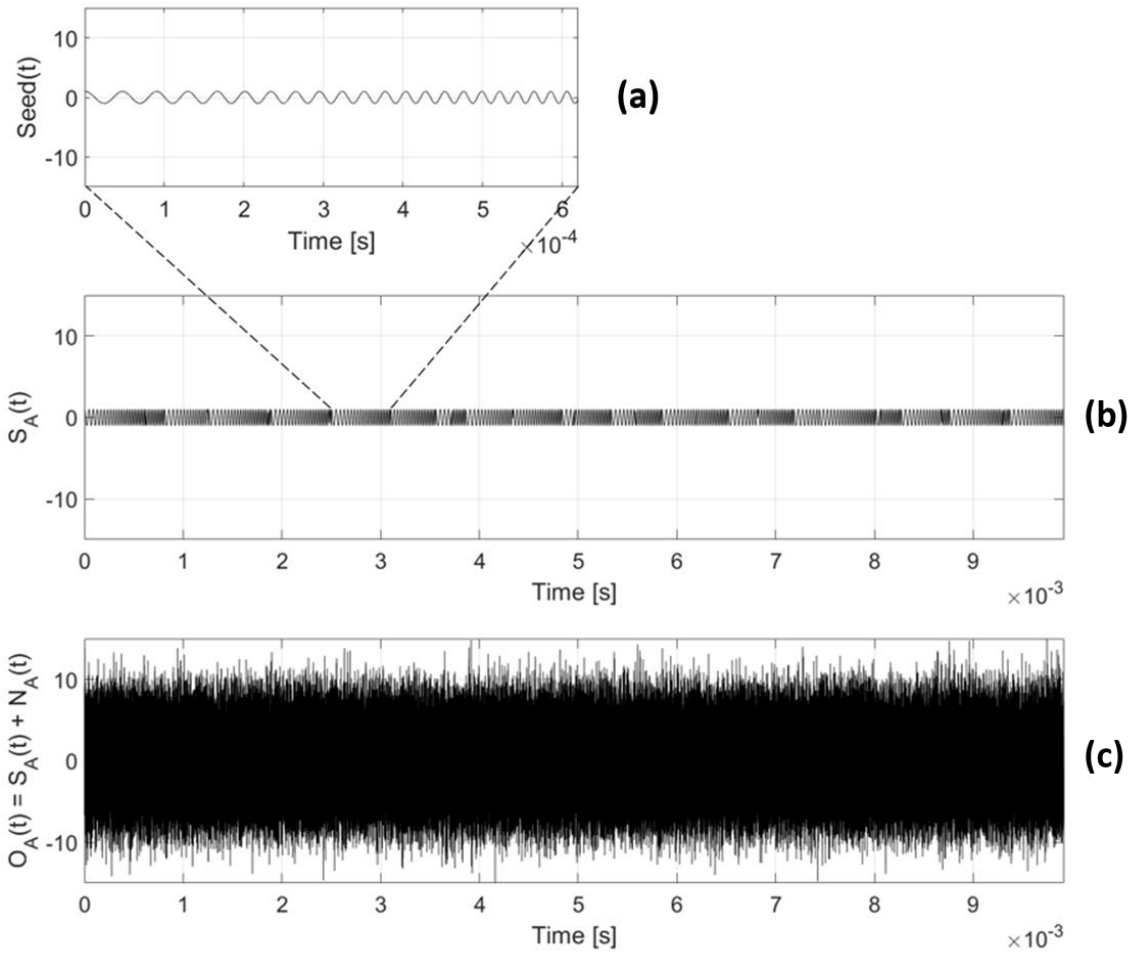

Figure 5-24: (a) “Seed” chirped signal. (b) Pure chirped signal. (c) Chirped signal with added white Gaussian noise (20x power).

The second case study was that of a synthetic signal with a broad frequency range of 20 kHz – 50 kHz, with added white Gaussian noise, 20 times the power of the synthetic signal (Figure 5-24). The frequency range of 20 kHz – 50 kHz was chosen to mimic the frequency bandwidth used for the rail defect detection prototype. This signal was created by a chirped “seed” waveform, Figure 5-24 (a), corresponding to an individual time segment, that was then replicated with a randomized phase either 16 times or 64 times to create the entire signal $S_A(t)$, as shown in Figure 5-24 (b).The total signal $O_A(t) = S_A(t) + N_A(t)$ for the 16 segment case is shown in Figure 5-24 (c). The sampling frequency for these signals was 80 MHz. The time duration of each segment was 0.62 msec, resulting

in a total time duration of 9.92 msec with 16 segments, and of 39.68 msec with 64 segments.

Figure 5-25 plots the signal spectra obtained with the three Options considered above, along with the “ideal” case of signal artificially correlated in phase among the different segments. The results for 16 segments are plotted in Figure 5-25 (a), that confirms Option 3 (inter-segment averaging with shifting) as having the best performance with SNR ~ 29.3 compared to ~19.9 for Option 2 (inter-segment averaging with modulus) and ~19.2 for Option 1 (intra-segment averaging). Also, the Option 3 spectrum is virtually equivalent to the “ideal” spectrum. In the 64 segment case, Figure 5-25 (b) confirms a slight improvement in SNR for Option 3 (~34.8 compared to ~29.3), in line with what was found in the previous sinusoidal signal case.

Additional studies were conducted on experimental signals consisting of ultrasonic waves propagating in steel rail tracks. In the first experimental study, a piezoelectric (PZT) stack actuator was used to excite an 80 kHz sinusoidal wave in an 8 ft long rail section in the laboratory. A capacitive air-coupled receiver was utilized to detect the waves from the rail section at a distance of ~ 2 ft from the PZT stack excitation. This was one of the sensors used by the UCSD prototype for passive high-speed rail inspection, shown in Figure 5-26. The sampling frequency of the acquisition was 80 MHz. Uncorrelated noise (white Gaussian, 20x power) was synthetically added to the measurements. The time duration of each segment was 0.625 msec, resulting in a total duration of 10 msec with 16 segments and of 40 msec with 64 segments.

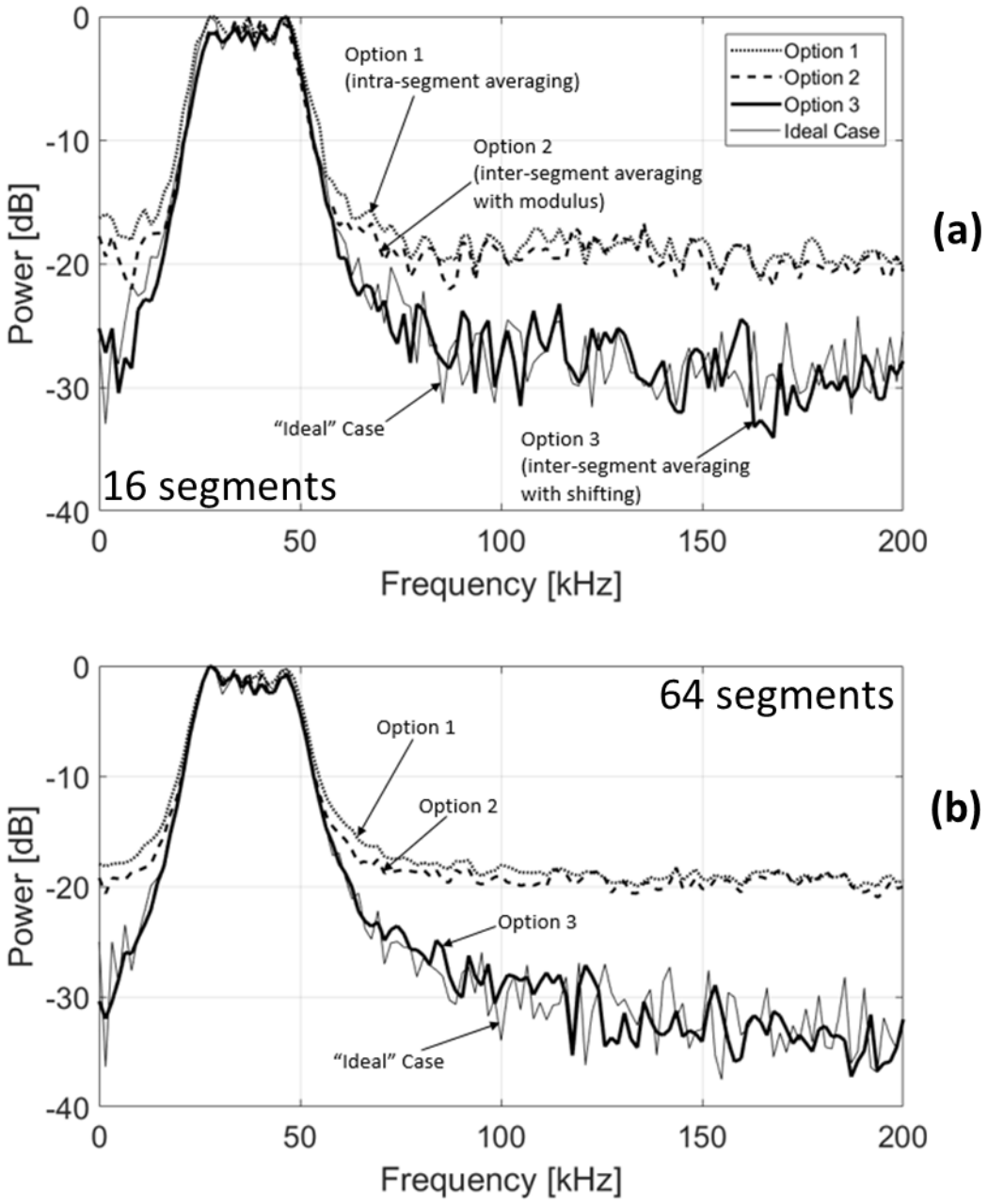

Figure 5-25: (a) Power spectra of chirped signal with added noise extracted with intra-segment averaging (Option 1), inter-segment averaging with modulus (Option 2), inter-segment averaging with shifting (Option 3), and "ideal case" by using 16 segments. (b) Same as (top) by using 64 segments.

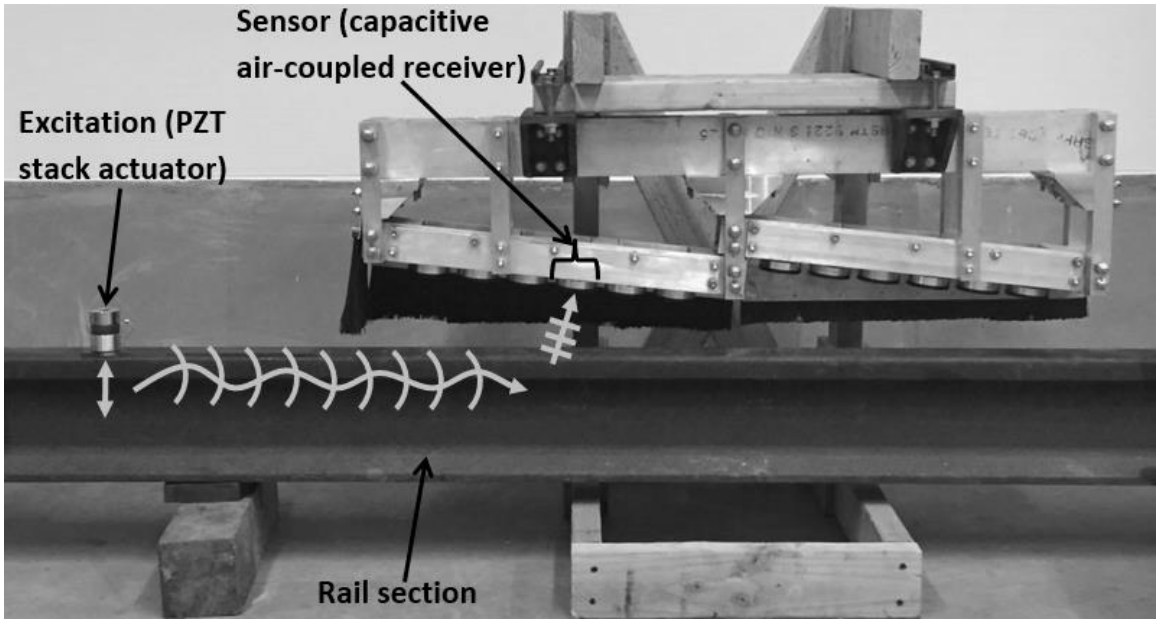

Figure 5-26: Setup for experimental validation using elastic waves in a rail track section.

Figure 5-27 shows the power spectra obtained from the signal using the three options. The experimental results confirm the conclusions of the synthetic results, i.e. that Option 3 (inter-segment averaging with shifting) is the best operation to isolate the signal power from the noise, with Option 1 (intra-segment averaging) and Option 2 (inter-segment averaging with modulus) retaining noise components. For the 16 segments in Figure 5-27 (a) Option 3 yields a SNR as high as 36 dB, against SNRs of 24 dB for Option 1 and 27 dB for Option 2.

Using 64 segments, Figure 5-27 (b), increases the SNR of Option 3 to ~ 41 dB, confirming the improvement already discussed for the synthetic signals. As discussed earlier, this improvement is not dramatic, suggesting that a small number of segments can be sufficient for a robust signal reconstruction.

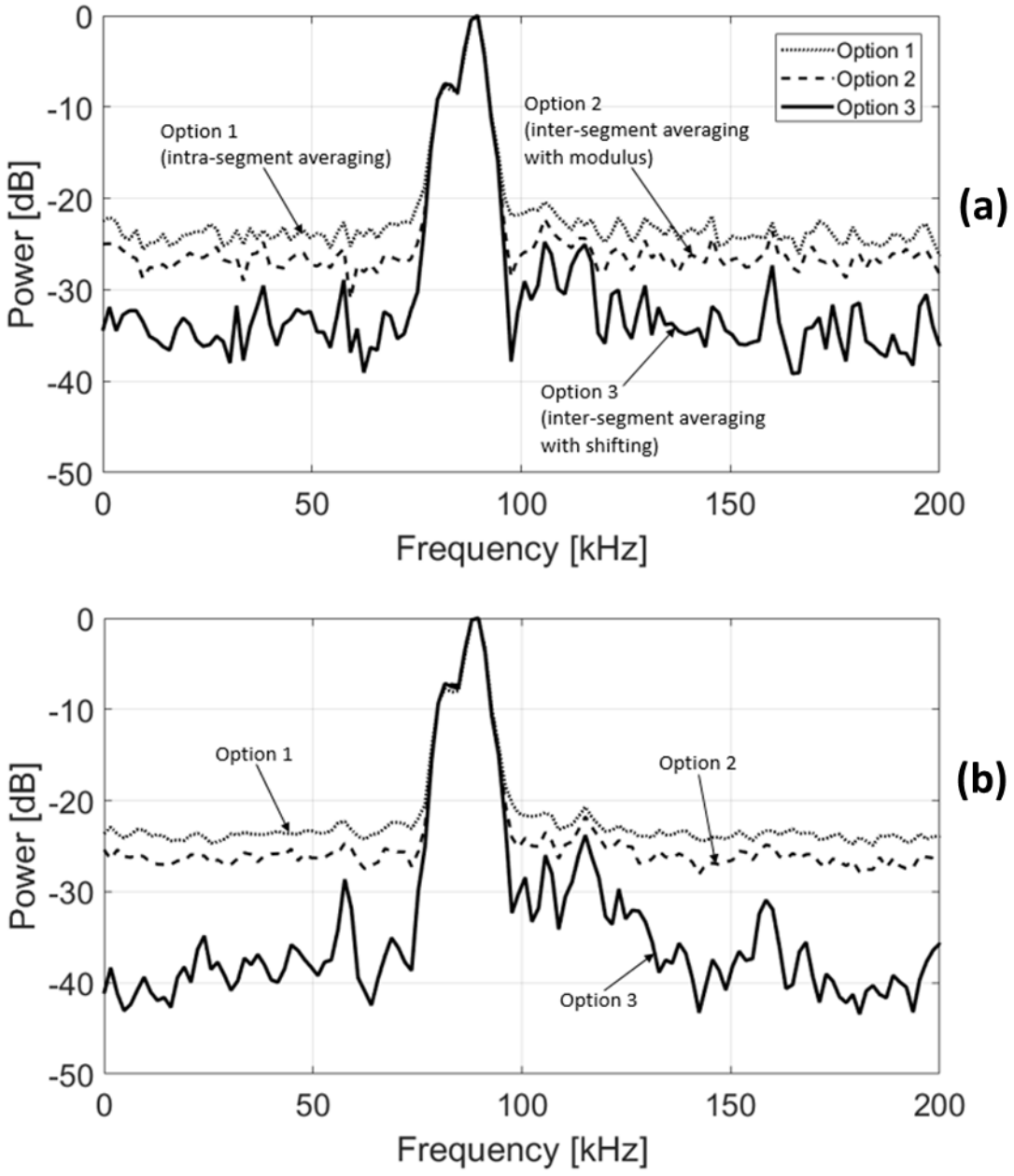

Figure 5-27: (a) Power spectra of experimental PZT actuated signal in the rail with intra-segment averaging (Option 1), inter-segment averaging with modulus (Option 2), inter-segment averaging with shifting (Option 3), and "ideal case" by using 16 segments. (b) Same as (top) by using 64 segments.

Lastly, a study was performed to understand the difference of the normalization options for the estimation of the complete transfer function, $H_{AB}(f)$, using the experimental data over 30 ft from the 60 mph run on the RTT. The comparison is done in terms of

sensitivity to a joint discontinuity, whose exact location in the track was well known. The distance A-B between two sensors in each pair was 18.75 in (~ 47 cm). The sampling frequency of the acquisition was 1 MHz. The transfer function of the rail between the sensor positions, $H_{AB}(f)$, was extracted in the frequency domain by using the normalized averaged cross-power spectrum. Also, 16 segments were used for these results (50% overlap for the intra-segment procedure, no overlap for the inter-segment procedure), corresponding to 31 intra-segment averages and 120 inter-segment averages. The total signal duration for the 16 segments was 7.62 msec, and each segment was 0.48 msec. The result was then transformed to the time domain via an inverse fast Fourier transform.

Figure 5-28 plots the "normalized signal loss" computed as the inverse of the passively reconstructed transfer function strength for the three normalization options. This metric effectively represents a "Discontinuity Index" for the rail. This index was calculated by plotting the inverse of the peak amplitude extracted from the time-domain reconstructed transfer function. Large values of this Index mean large loss of transmitted signal, as we would expect in the presence of a discontinuity or damage in the rail (e.g. a joint or a defect scattering the waves). The joint discontinuity is present at position ~ 14 feet in the x-axis of the graph. The best result is clearly obtained with normalization Option 3 (inter-segment averaging with shifting) yielding a sensitivity to the joint as high as 6.7 (max peak/mean noise level). Option 1 and Option 2, instead, both result in a much smaller sensitivity (~ 2), because of their ineffectiveness to eliminate the added noise generated by the harsh experimental conditions of this test. Hence, the conclusions from the previous case studies and from the theoretical derivations were confirmed.

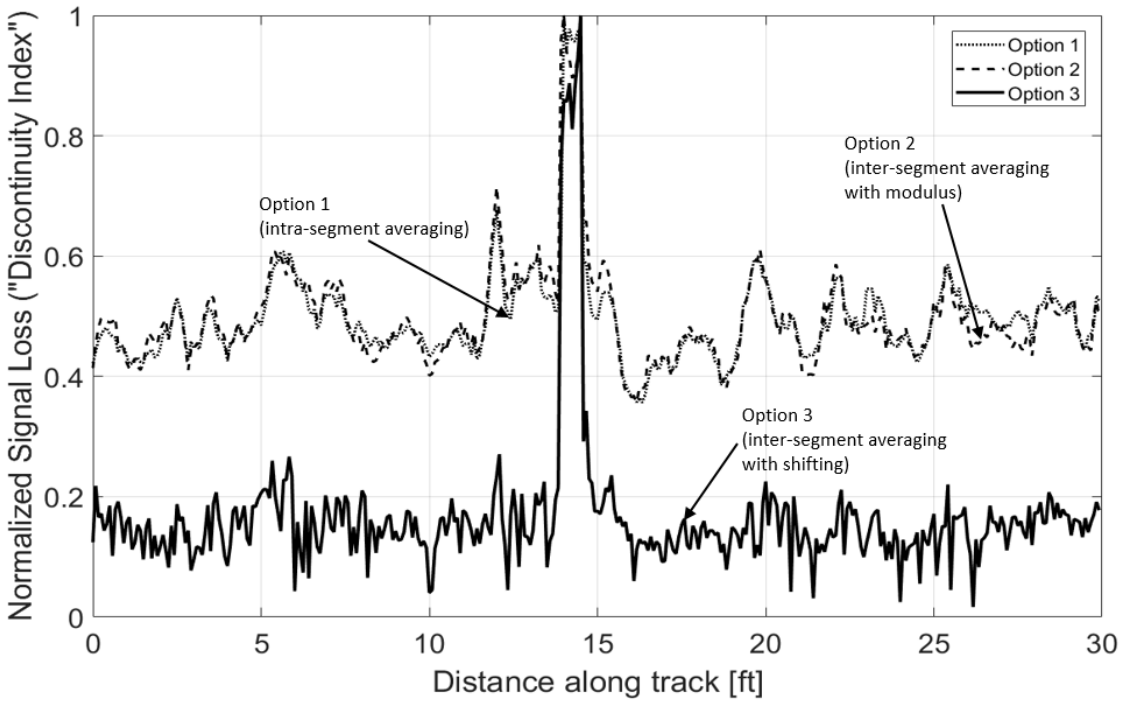

Figure 5-28: Normalized loss of passively reconstructed transfer function of the rail from 60 mph on a section of the RTT with a joint by using intra-segment averaging (Option 1), inter-segment averaging with modulus (Option 2), inter-segment averaging with shifting (Option 3), and “ideal case” by using 16 segments.

5.6 Results for Proof-of-Concept 2016 Field Test

Test runs were performed at both TTC’s RTT, which allowed maximum test speeds of up to 80 mph (128 km/h), and at TTC’s Rail RDTF, which allowed maximum test speeds of 25 mph (40 km/h) in 2016. A locomotive was used to two the DOTX-216 car instrumented with the passive-only prototype. The primary purpose of the 2016 field test was for a proof-of-concept before further trials were performed. The results from the RTT and RDTF are analyzed in the following sections.

5.6.1 Railroad Test Track (RTT)

The tested length on the RTT depended on the test speed and was approximately 18,000 ft. The runs at the RTT were conducted between markers R42 and R25, as shown

in Figure 5-29. This test zone featured a tangent track in the middle, with curved tracks at the beginning and end. As many as three joints and seven welds were identified in the RTT test zone through visual survey. A representative snapshot of a joint captured by the high-speed camera is illustrated in Figure 5-29. Runs are the RTT were conducted at speed of 10 to 80 mph in 10 mph increments.

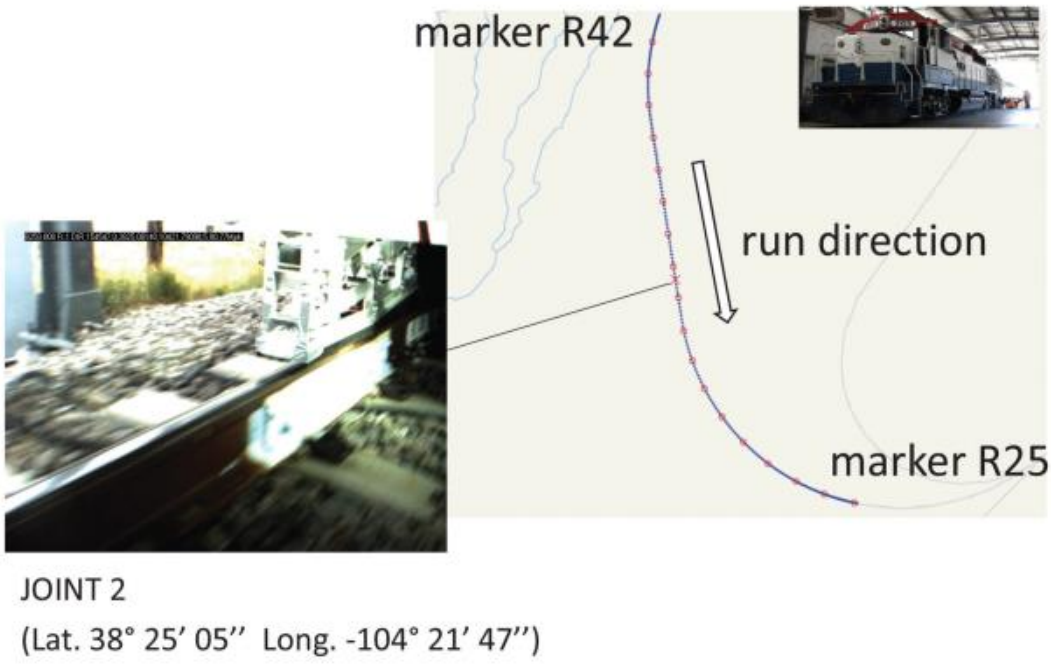

Figure 5-29: RTT rail track used for the 2016 field test at TTC.

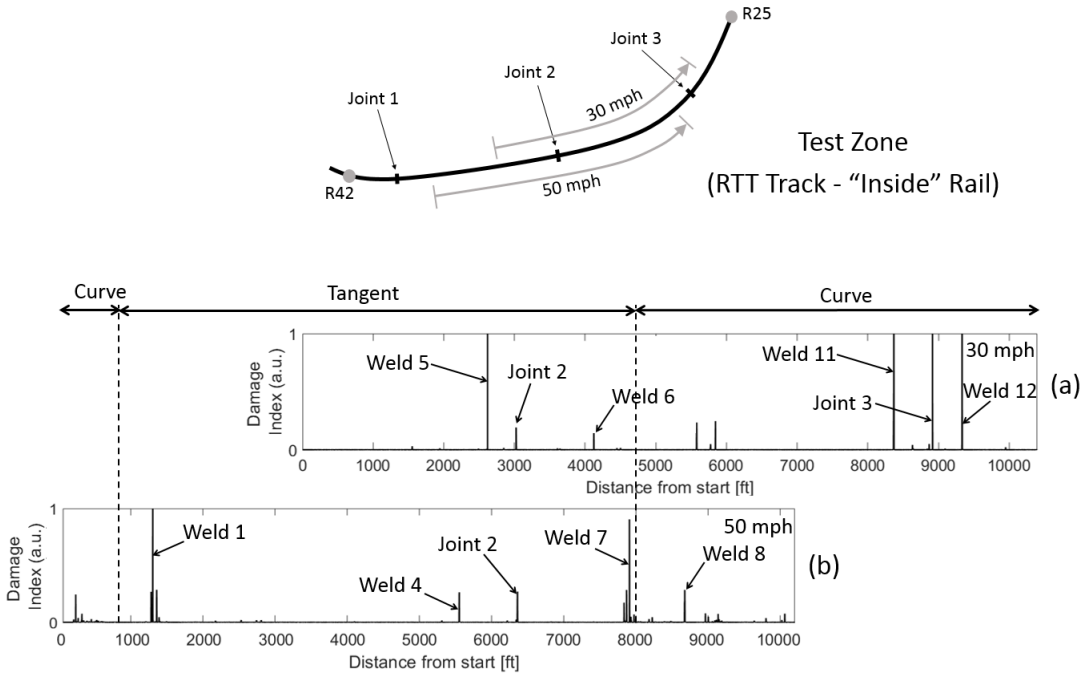

Figure 5-30: Representative results from the passive inspection of the RTT track at (a) 30 mph and (b) 50 mph

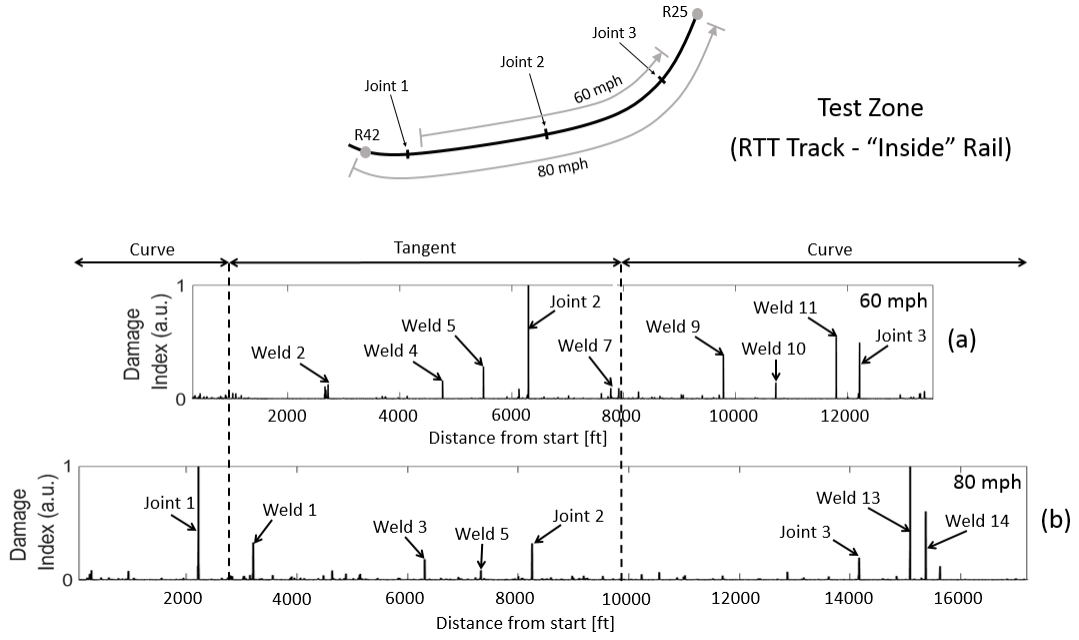

Figure 5-31: Representative results from the passive inspection of the RTT track at (a) 60 mph and (b) 80 mph.

Figure 5-30 and Figure 5-31 demonstrate representative results of the DI computed from the multivariate outlier analysis of the passively reconstructed transfer function for four runs at different test speeds. As mentioned previously, the distance covered by each run depended on the intended target speed, with longer distances required to reach the higher speeds at stead-state. The distances covered for each of the runs are schematized in the top drawings of Figure 5-30 and Figure 5-31. The peaks in the DI traces labeled as “Joint #” and “Weld #” were confirmed by either information provided by TTC staff or by images collected by the video camera at those specific locations.

The results for the 30 mph (48 km/h) run and the 50 mph (80 km/h) run are reported in Figure 5-30. At 30 mph, the plots demonstrate detection of two joints (Joint 2 and Joint 3) and four welds (Welds 5, 6, 11, and 12), coupled with a flat noise floor, highlighting the reduced risk of false positive detections in the pristine portions of the rail. Furthermore, the damage index does not degrade in quality when moving from the tangent portion of the track to the curved portion of the track (for example, from position ~4500 ft, or ~1371 m, in Figure 5-30). Similarly, the result for the 50 mph (80 km/h) run shows a clear trace. The damage index in Figure 5-30 confirms the detection of joint 2 of the 30 mph (48 km/h) run. Additional true detections (welds 1, 4, 7, and 8) are also annotated from the additional distance covered. The fact that welds 4, 7, and 8 were detected at 50 mph but not at 30 mph suggests that the lower speed may not contain adequate input excitation to distinguish discontinuities as compared to the wheel-to-rail interaction at higher speed. Furthermore, the results from Figure 5-30 also highlight the need for multiple passes across the same track for robustness.

A few small peaks that are also visible but not marked by a label (for instance, the peak at position ~6000 ft, or ~1828 m, in Figure 5-30) could be either an unknown

discontinuity in the track (such as a weld or internal discontinuity) or a false positive detection. Overall, Figure 5-30 demonstrates promise for the possibility to (1) extract a stable transfer function and impulse response of the rail in a passive-only manner by exploiting the natural wheel excitations, and (2) process the passively reconstructed transfer function to detect rail discontinuities in a statistically robust manner.

Figure 5-31 reports the results of a 60 mph (96 km/h) run and 80 mph (128 km/h) run. The 60 mph (96 km/h) run, shown at the top, continues to show a clear detection of confirmed discontinuities (joints 2 and 3). Furthermore, as in Figure 5-30, the clean portions of the rail have a nearly flat noise floor. The few peaks seen beyond the labeled discontinuities require further investigations to determine if they are discontinuities or false positives. The 80 mph (128 km/h) trace in Figure 5-31 confirms some of the 60 mph markings, but detects additional joints and a weld that were previously not detected on the 60 mph run. At the same time, some of the verified joints and welds found on the 60 mph run were not confirmed in the 80 mph (128 km/h) run. This highlights the importance of multiple redundant runs, as increasingly higher speeds generate different frequency contents in the rail. Additionally, increased mechanical vibrations (such as sensor misalignment) caused by the very high speed could contribute to some false negatives or false positives, and the higher noise floor in the 80 mph run. Regarding the mechanical vibration at high speeds, railroad contractors assisting with the field tests indicated that the accelerations expected at the car axle or below the primary suspension at high speeds can be as high as 30 g (rms) in the vertical direction (during sustained operation) and 100 g (rms) in all directions (during shocks). These operational conditions should be considered severe for a “typical” operation of an air-coupled ultrasonic receiver. Nevertheless, all three confirmed joints in the test track were detected at the 80 mph (128 km/h) speed. This is quite a remarkable result considering the potential difficulties

associated with attempting to operate an inspection system mounted to the axle of a train car running at 80 mph.

5.6.2 Rail Defect Test Facility (RTDF)

While the focus of the 2016 TTC field tests was to test the stability of the reconstructed structural impulse response at sustained speeds, the instrumented car was moved to the Technology Development Zone of the RTDF track for a preliminary test on discontinuity detection potential. The RDTF contains various known natural and artificial rail defects that are purposely placed in the track. The maximum allowable speed for the RDTF was 25 mph due to the tight curvature along with numerous natural and simulated defects in the technology development zone. At the highest speed, approximately 2,000 ft of track was used for testing. The RTDF technology development zone is also commonly referred to as the balloon loop, and is a mostly curved track, as shown in Figure 5-32. Defects labeled in Figure 5-33 are known defects verified through a map generated by handheld ultrasonic A-scan. Peaks without a label in the trace require further verification to determine if they are false positives or previously undetected discontinuities.

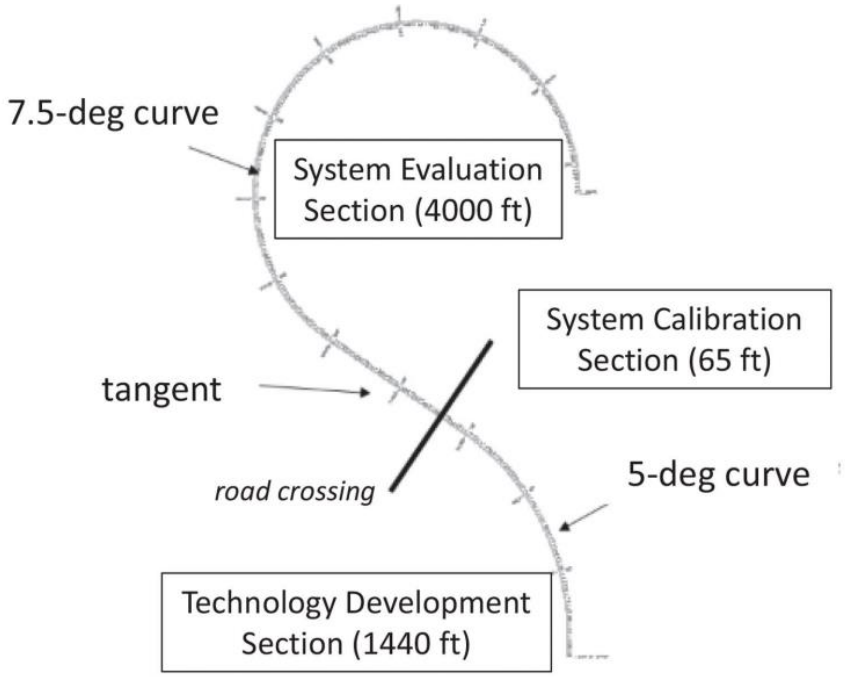

Figure 5-32: RTDF rail track used for the 2016 field test at TTC.

Zone 1 in Figure 5-33 (a), from left to right, shows the clear detections of a joint, a crushed head defect, and a weld. The several peaks seen between 4,880 and 4,890 ft are currently unexplained, possibly due to surface roughness/unevenness that produces false positive indications. Zone 2 in Figure 5-33 (b) demonstrates detection of the following: shelling defect, transverse defect simulated by a saw cut and extending for 20% of the rail HA, shelling, joint, detail fracture defect extending for 7% of the rail HA, and a second joint. The peak at position ~5,116 ft (1,559 m) prior to the first joint could be due to an unmapped rail condition, or it could be a false positive. Zone 3 in Figure 5-33 (c) shows the detection of a detailed fracture defect extending for 20% of the rail HA, a joint, a 20% HA transverse fissure defect, a 20% transverse defect, and another joint.

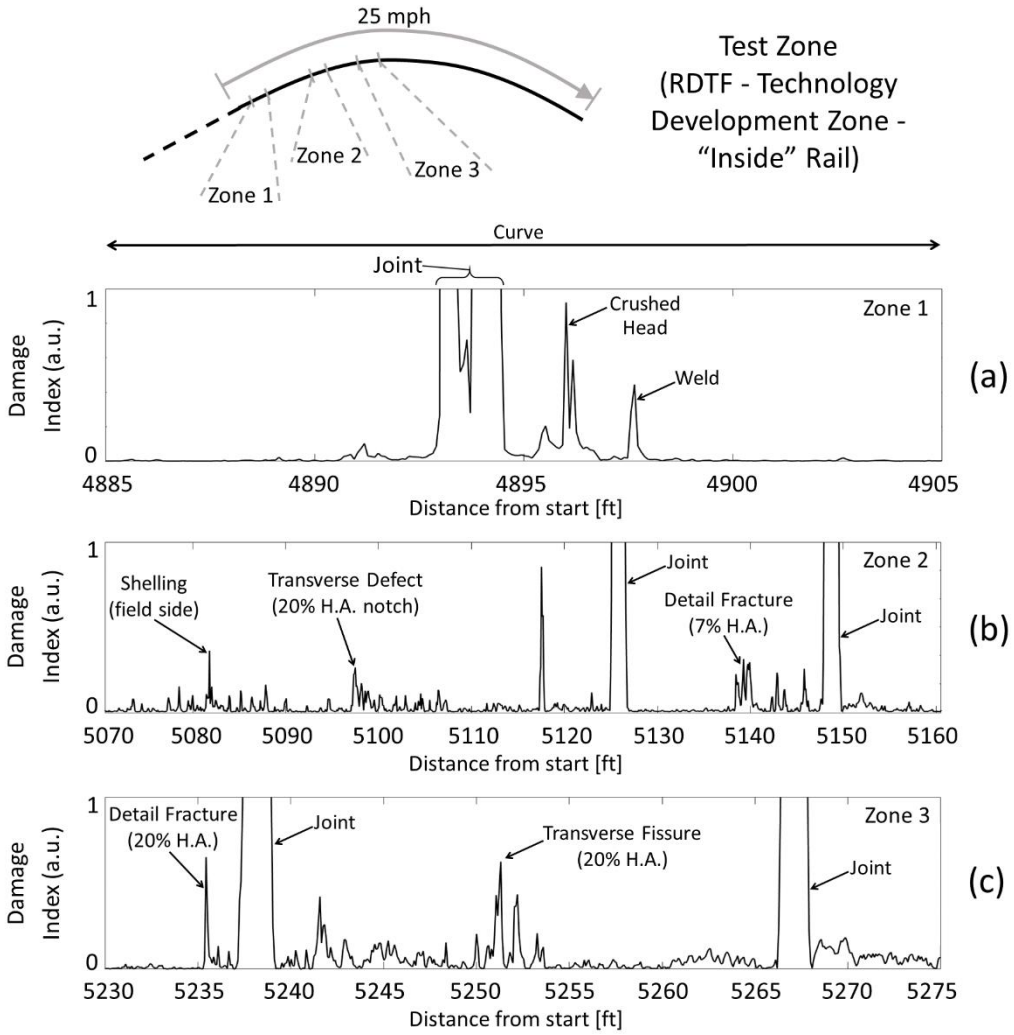

Figure 5-33: Representative results from the RDTF test track at 25 mph in three selected test zones (a) Zone 1, (b) Zone 2, and (c) Zone 3.

Overall, the results in Figure 5-33 demonstrate promising potential for detecting relevant rail defects by the passive reconstruction approach. The fact that 25 mph (40 km/h) was the maximum speed permitted on the RDTF track due to safety concerns did not allow complete study of the discontinuity detection performance revenue speeds. Since the approach relies on wheel-generated noise as the acoustic excitation of the rail, both signal strength and signal frequency bandwidth are expected to increase with faster wheel rotational speed.

5.7 Results for 2018 Field Test on High Tonnage Loop Track

The runs were conducted at the HTL test track at speeds of 40, 33, and 25 mph. The maximum allowable speed was 40 mph. The runs at 40 and 33 mph were conducted with two loops whereas the 25 mph only had 1 loop due to time constraints. The various speeds were used to test the effects of source excitation in relation to the stability of the reconstructed Green's Function. The HTL test track is unique due to the numerous joint and welds since portions of the track are constantly replaced from damage due to heavy freight cars. An aerial view of the test track is shown in Figure 5-34 along with the direction of the test run.

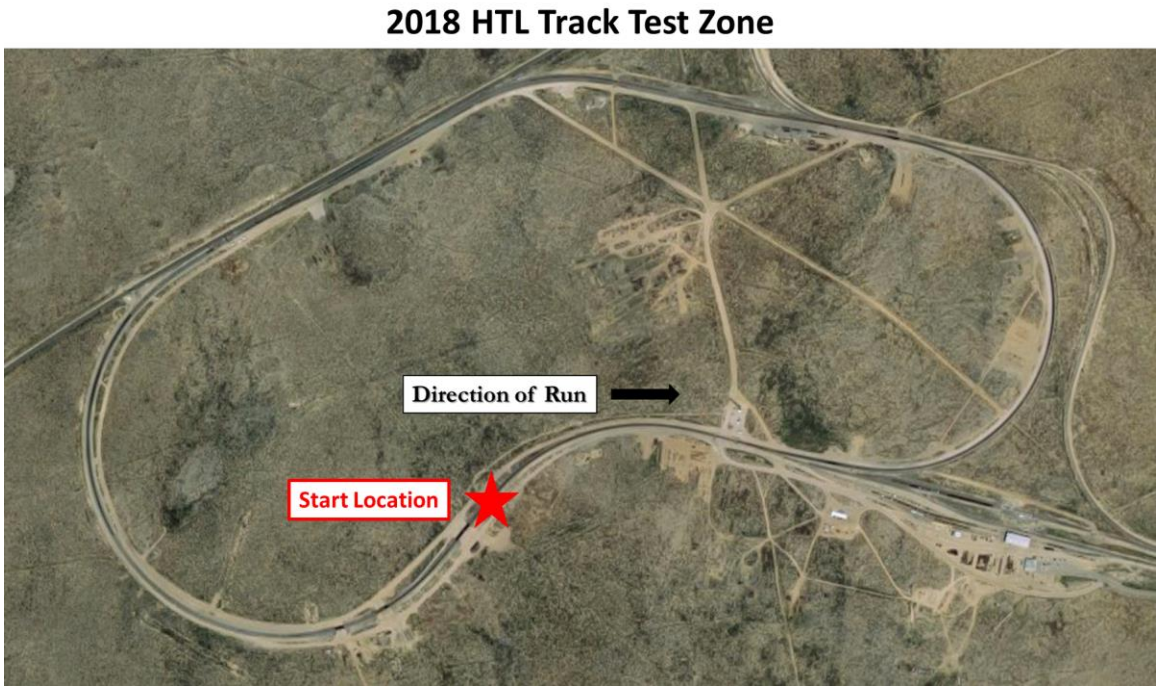

Figure 5-34: HTL rail track used for the 2018 field test at TTC.

The 2018 field test results are split into four distinct sections, the first, focuses on the effects of acoustic energy on the stability of the Damage Index. Second, a section is dedicated to the effects of choosing the correct threshold value that depends on each sensor group. Third, the results from sensor compounding are explored. Last, Receiver

Operating Characteristic (ROC) Curves are illustrated to quantitively assess the performance of the rail inspection prototype.

5.7.1 Signal Energy

Four zones are highlighted in Figure 5-35 corresponding to areas where the signal strength was higher than the sensor's electrical noise floor. The difference between the two regions is highlighted in Figure 5-36, where the low signal strength region has the stepped characteristic common of electrical noise. The zones where signal strength was adequate were primarily concentrated in sections of curved track where the wheels were suspected to be flanging. As the speed decreased, a larger portion of the run becomes suboptimal for defect detection. The 2016 results demonstrated that high speeds (more than 60 mph) generated the optimal source excitation energy for a stable Green's function. Due to the HTL track limitations, 40 mph was the maximum speed possible. Poor results were found in areas where the source excitation energy was too low to be detected by the receivers, e.g. in most of the tangent portion of the track.

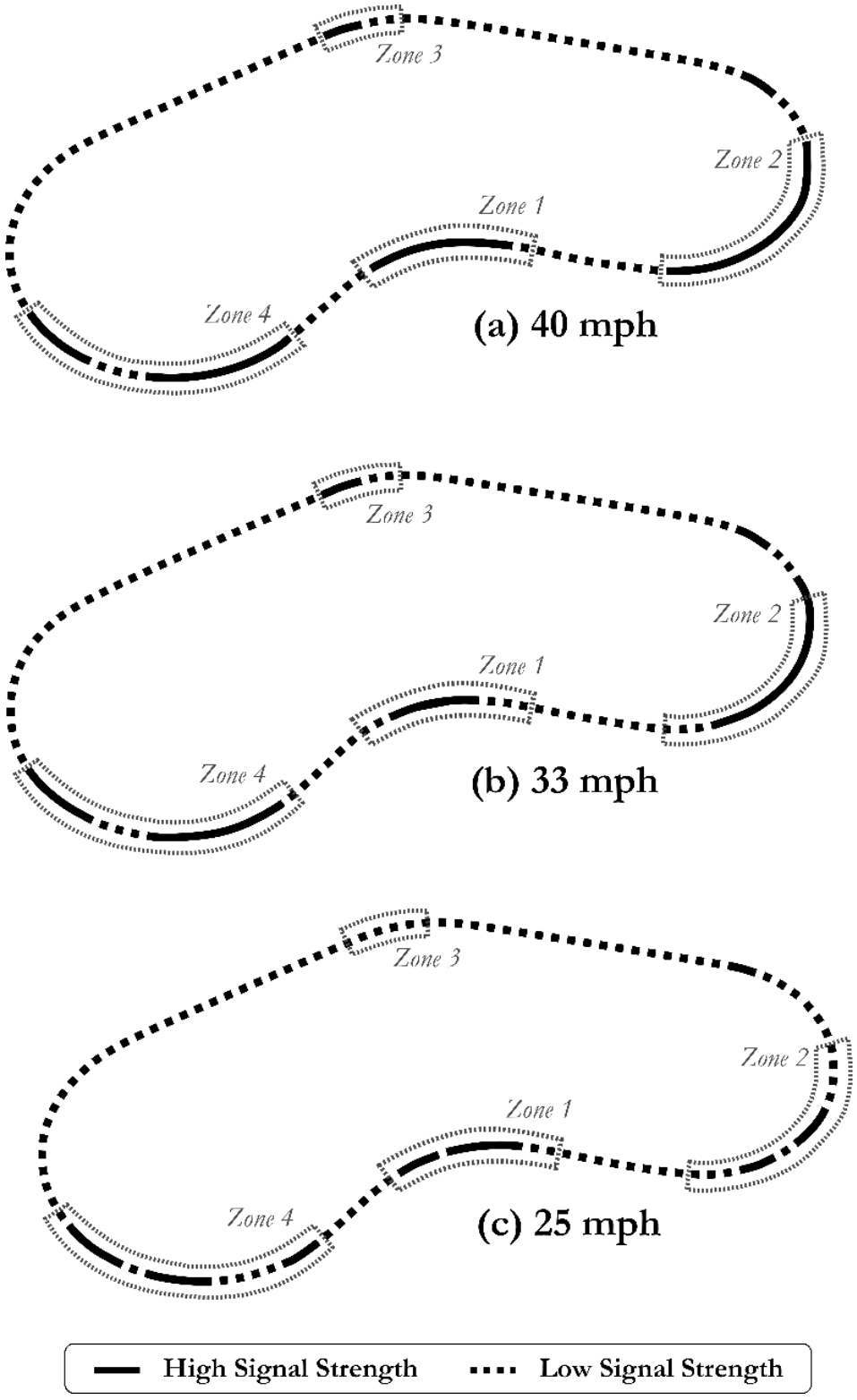

Figure 5-35: Acoustic signal energy strength for the 2018 HTL test for (a) 40 mph, (b) 33 mph, and (c) 25 mph.

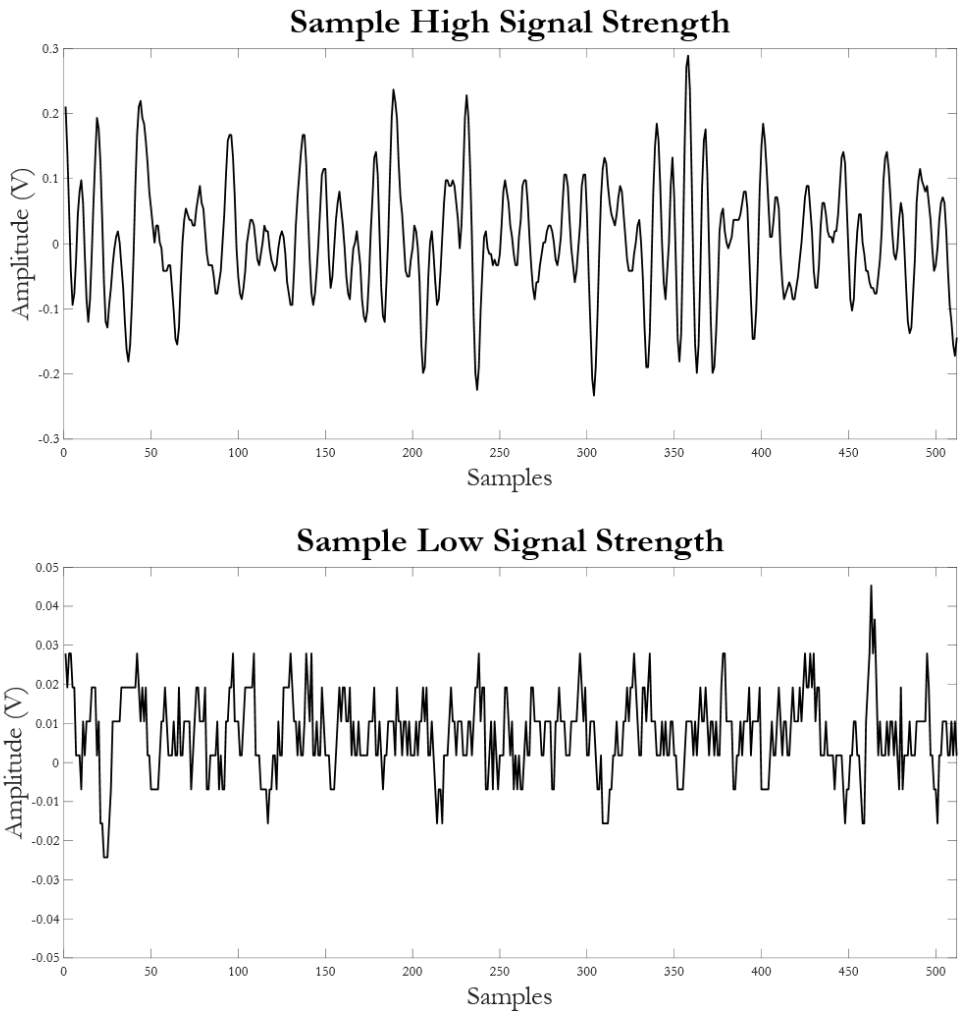

Figure 5-36: Representative high and low signal strength. Note the change in the amplitude scale and characteristic electrical noise pattern for the low signal strength.

The runs on the HTL, at the various zones of strong signal from Figure 5-35, are illustrated in Figure 5-37 for the 40 mph loop, Figure 5-38 for the 33 mph loop, and Figure 5-39 for the 25 mph loop. The upper right of the graph lists the sensor pair. Reference Figure 5-4 for the corresponding sensor group used in the analysis. In this section, all analysis was performed on the first group, corresponding to sensors 1, 2, 7 and 8. The black diamonds, labeled Damage Index, denote areas where the outlier detection algorithm crosses the 0.02% threshold in relation to the maximum Damage Index value at a certain speed's run. The threshold value is noted under the title in parenthesis. The blue

triangles denote joints and the orange triangles denote switches. Joints and switches are considered as large discontinuities in the rail. Yellow triangles denote a crossing where the rail surface may be covered, reducing the received signal strength. Welds are marked with blue asterisks. Although there are numerous welds shown, not all welds are expected to be detected. Welds that have good material continuity will not have discontinuities whereas welds with porosity, will. Poor welds will have a corresponding peak in the Damage Index. Lastly, the focus of the results is to determine the stability of the readings. In other words, the goal is to minimize the number of false positives. A subsequent section of the results will focus on analyzing ROC Curves for a quantitative treatment of the damage detection reliability in terms of probability of detection versus the probability of false positives.

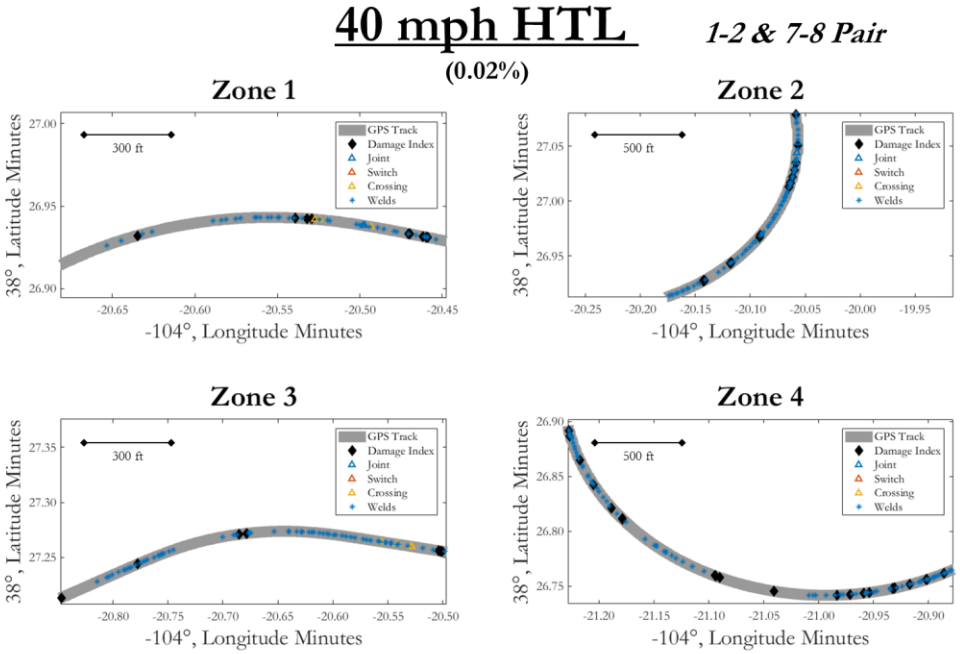

Figure 5-37: 2018 HTL results at 40 mph for Sensor Group 1 at 0.02% DI threshold.

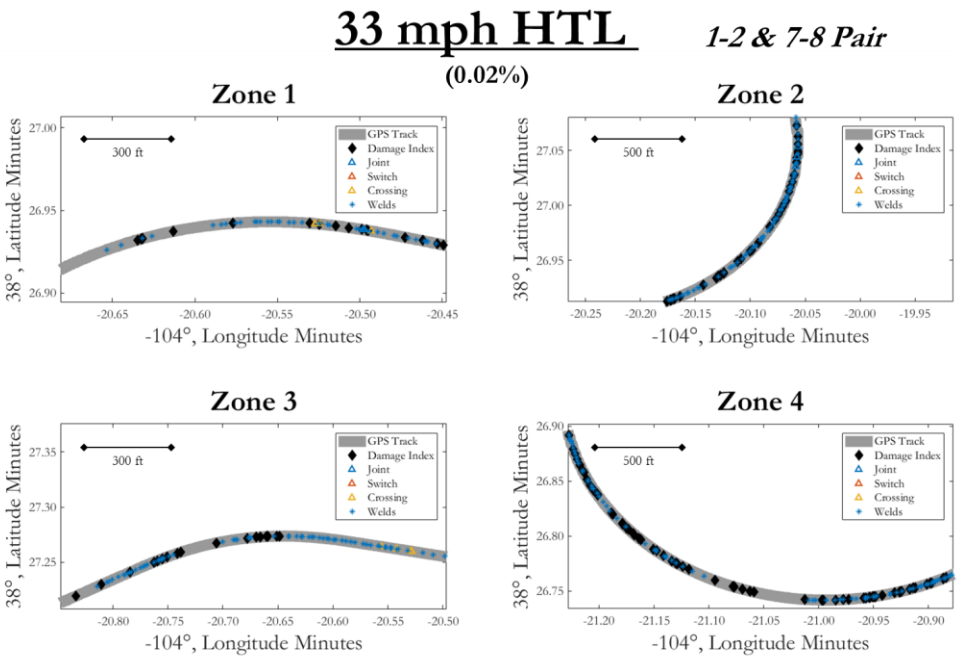

Figure 5-38: 2018 HTL results at 33 mph for Sensor Group 1 at 0.02% DI threshold.

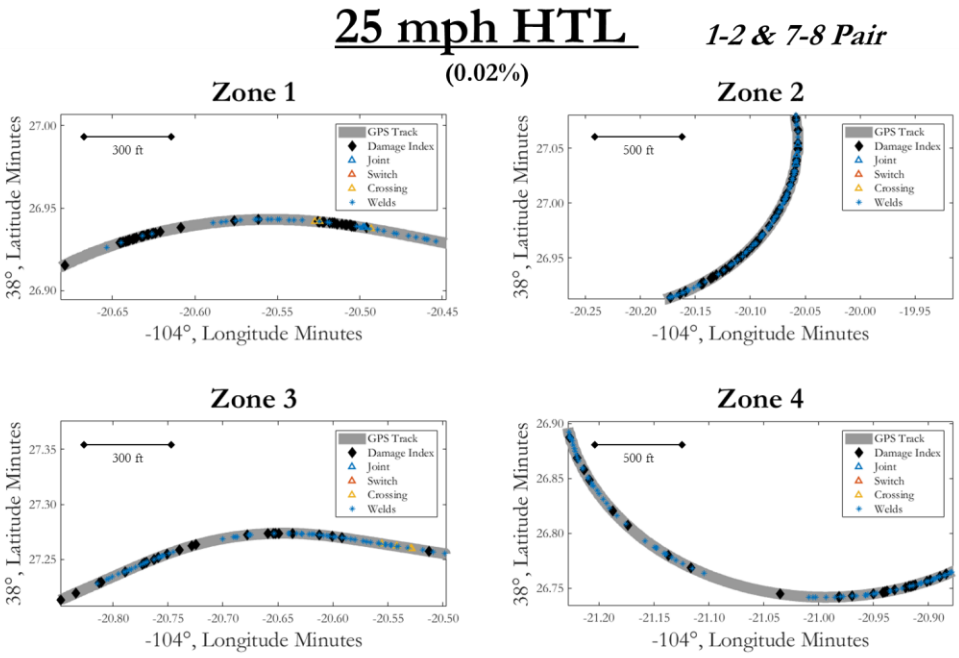

Figure 5-39: 2018 HTL results at 25 mph for Sensor Group 1 at 0.02% DI threshold.

In Zone 1, a reduction in speed and source excitation energy has a significant effect on the stability of the Damage Index. This phenomenon can be clearly seen at 25 mph where between -104° 20.65’ and -104° 20.60’ longitude a significant number of false positives are found. Similarly, between -104° 20.55’ and -104° 20.50’ longitude, additional false positives are shown. The 33 mph loop demonstrates an intermediary effect of source excitation reduction compared to the 25 mph run.

Zone 2 at 40 mph has a clean trace with no false positives. A joint marking was missed around 38° 27.05’. Additional work is in progress to determine the optimal threshold value to maximize the probability of detection while minimizing false positives. As seen in Zone 1, reduced speeds result in an increase in false positives due to the poor source excitation resulting in an unreliable Green’s Function reconstruction. Zones 3 and 4 also demonstrate the same issue at lower speeds.

In Zone 4, between -104° 21.10’ and -104° 21.05’ longitude, false positives can be seen at 40 mph and 33 mph. Referencing Figure 5-35, this area corresponds to poor signal strength caused by either sensor misalignment or the wheels no longer flanging. Thus, signal drops that are usually associated with discontinuities are erroneously listed as damage. Overall, the results highlight an important key parameter of minimal source excitation levels. After a minimal level has been reached, a stable Green’s Function can be reconstructed and be used to detect rail flaws.

5.7.2 Multiple Sensor Groups

Multiple sensors which correspond to 3 separate analysis groups were mounted to the prototype, as illustrated earlier in Figure 5-4. In total, 12 sensors were split into 3 groups of 4 sensors each. Each group contained 4 unique combinations of reconstructed signals. The Group 1 consisted of sensors 1-2 and 7-8, Group 2 consisted of sensors 3-4 and 9-10, and Group 3 consisted of sensors 5-6 and 11-12. Group 1 and 3 had identical

signal conditioning applied. Variation in the data is primarily attributed to the sensor's different response characteristics. Group 2 had a voltage divider reducing the received voltage at the Analog-to-Digital convertor at the PXIe unit by half. The voltage divider was used to test the effects of a reduced signal and to prevent potential oversaturation of the signal. The following analysis compares different sensor groups and the effects of various threshold levels on the results. The same four zones, as shown in Figure 5-35, are used. The threshold used is listed below the title in parentheses. The sensor group in the analysis is noted on the upper right corner of the figure. All runs in this section are at 40 mph.

In Figure 5-40 through Figure 5-44, the same 0.02% of each group's maximum damage index value was used as the threshold. The normalization to the maximum damage index value was used to account for the Damage Index noise floor and the sensitivity to discontinuities. Figure 5-43 and Figure 5-44 represent Group 2 and 3, respectively, where different threshold values were used to improve the resulting Damage Index detection algorithm.

Between Figure 5-40 and Figure 5-41, there is a substantial increase in the number of false positives. This is attributed to the reduced energy received, since Group 2 in Figure 5-41 had a voltage divider applied which reduced already low signals to half of the input value. Thus, the Damage Index trace has a high noise floor due to a baseline that primarily consists of electrical noise. Furthermore, the peak Damage Index will not be as significant since a characteristic loss of signal associated with a discontinuity will not be as high of an outlier. In this case, increasing the threshold will result in reduced false positives to push the threshold higher than the contaminated baseline as shown in Figure 5-43.

Group 3 results are illustrated in Figure 5-42. A comparison between Group 1, Figure 5-40, demonstrates a cleaner Damage Index trace which results in a reduced

probability of detection. Relaxing the Damage Index threshold crossing improves the detection rate, as expected (Figure 5-44). The results highlight the need for an adaptive baseline dependent on each sensor groups that accounts for the sensor's response characteristics. This baselining is similar to obtaining a reference standard in traditional ultrasonic techniques.

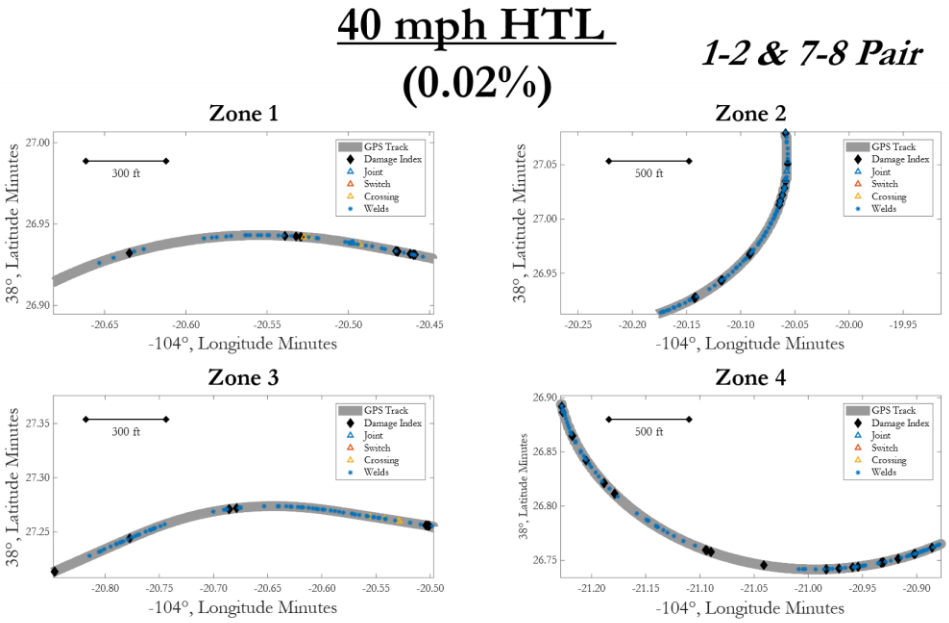

Figure 5-40: 2018 HTL results at 40 mph for Sensor Group 1 at 0.02% DI threshold.

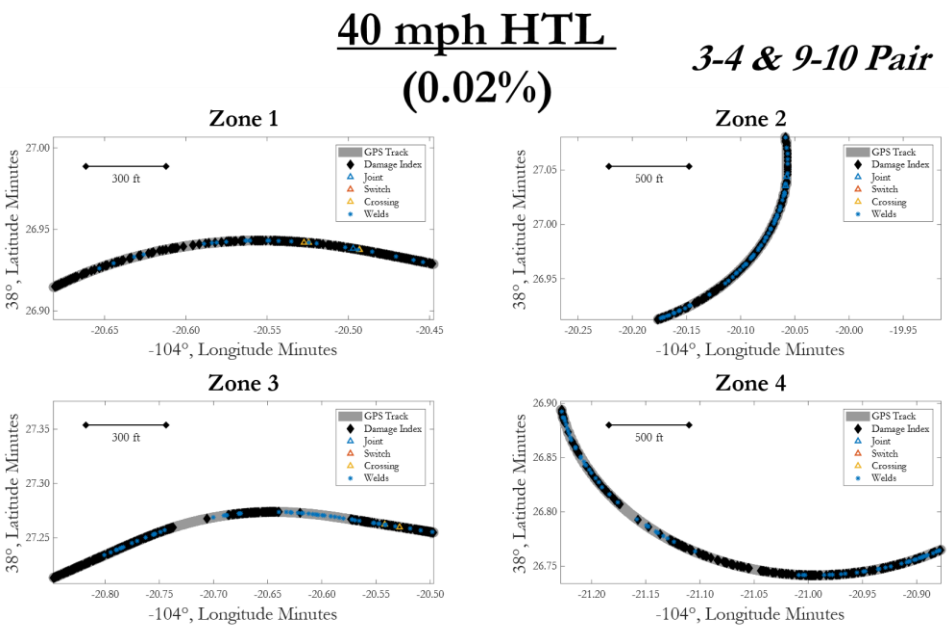

Figure 5-41: 2018 HTL results at 40 mph for Sensor Group 2 at 0.02% DI threshold.

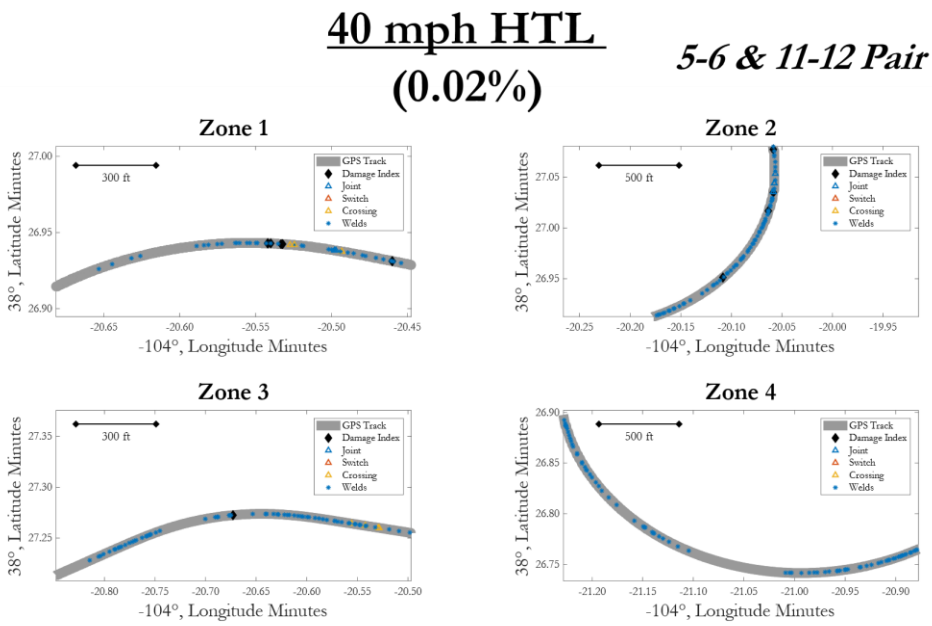

Figure 5-42: 2018 HTL results at 40 mph for Sensor Group 3 at 0.02% DI threshold.

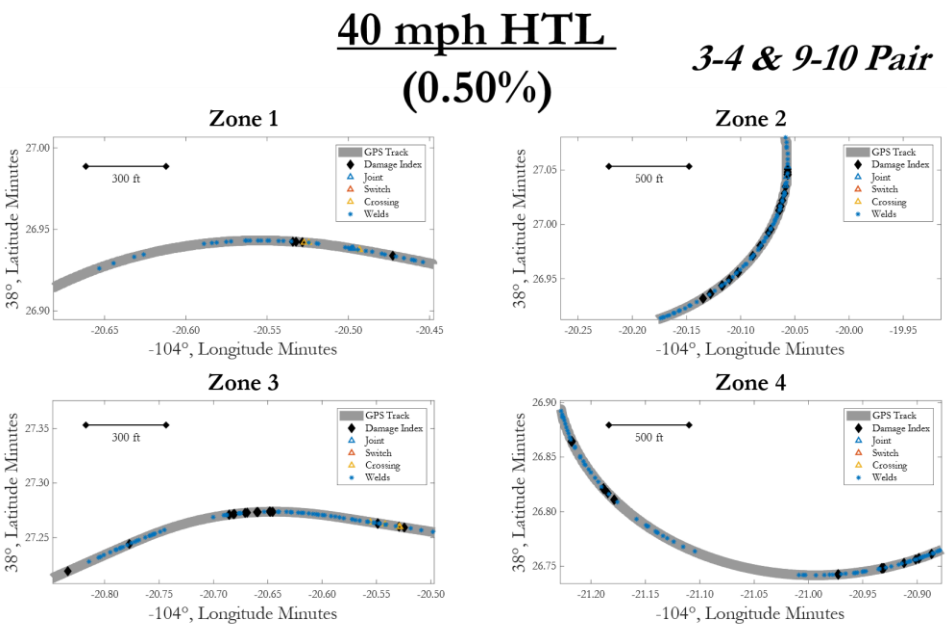

Figure 5-43: 2018 HTL results at 40 mph for Sensor Group 2 at 0.50% DI threshold.

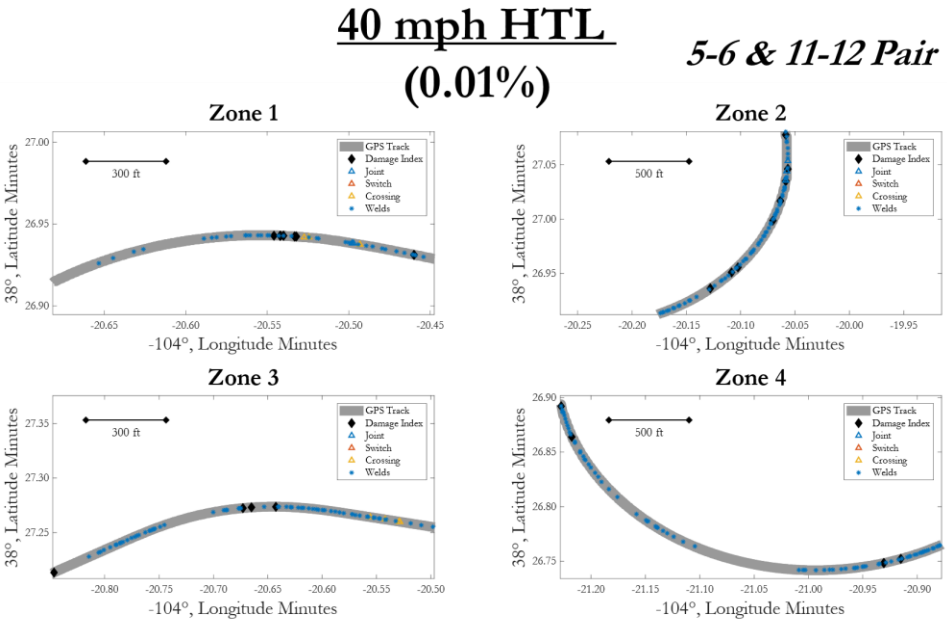

Figure 5-44: 2018 HTL results at 40 mph for Sensor Group 3 at 0.01% DI threshold.

5.7.3 Receiver Operating Characteristic Curves

A ROC curve is a graphical method of evaluating the performance of a damage detection system (in terms of positive detection and false alarms) as the threshold value of the damage index cutoff is varied. The ROC curve consists of a plot between the Probability of Detection (PD) vs Probability of False Alarms (PFA) for different values of the threshold level.

Calculation of the PD and PFA requires tracking the DI of the test run. The damage indices crossing a damage threshold were highlighted through black diamonds in the previous sections. These damage indices are relative values which can be attributed to the state of health of the segment of the track they are computed for. A high DI value indicates an outlier and may represent a possible location of some discontinuity/defect. A high value of DI in the vicinity of a known discontinuity would mean that the prototype gives a "true positive" result. Similarly, a high value of DI in the vicinity of a pristine segment of track means that the prototype gives a "false positive" result. An ideal scenario is when the number of "true positives" are high and the number of "false positives" are low. Since the number of "true positives" and "false alarms" would be different for different lengths of rail scanned, a probabilistic approach is taken which determines the probability of these "true positives" or "false positives". The Probability of Detection (PD) gives an estimate of the "true positives" and is calculated by the formula below:

$$PD = \frac{Number\ of\ \ discontinuities\ identified}{Total\ number\ of\ \ discontinuities} \tag{5.7.1}$$

Similarly, the Probability of False Alarms (PFA) gives an estimate of the "false positives" and is computed by the formula below:

$$PFA = \frac{Number\ of\ \ discontinuities\ identified\ in\ \ pristine\ rail\ \ segments}{Total\ number\ of\ \ pristine\ segments\ of\ \ the\ rail\ \ scanned} \tag{5.7.2}$$

A DI that exceeds a pre-determined threshold may be indicative of some discontinuity or defect. In order to determine the optimal threshold value across a run, a set of PDs and PFAs are calculated for varying threshold levels starting from zero up to the maximum DI value in the trace, as illustrated in Figure 5-45. The Number of Threshold Crossings (NTC) is defined as the number of times the DI value crosses the threshold level during each scan. Furthermore, one scan is defined as the number of points probed in the track that lie within the length of the prototype (1.5 ft). The exact knowledge of the test track condition or “ground truth” is required to compute the PD and PFA for each of the threshold value.

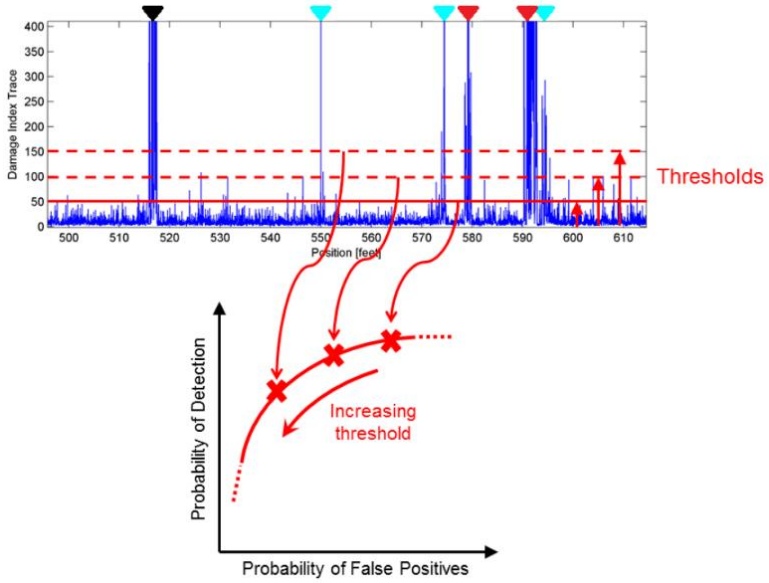

Figure 5-45: ROC curve computation through changing DI threshold values.

A sample DI trace for a representative portion of a scanned rail track is shown in Figure 5-45. At each threshold level, a PD and PFA value is computed. Depending on the resolution required in the ROC curve, the incremental increase in values of threshold are performed from zero to the maximum DI value in the trace. In Figure 5-45, the upper-right point on the curve represents the location where PFA = 1 and PD = 1. This location represents a case where all probed locations appear as discontinuities. As one moves

from the upper-right corner to the lower-left corner, the DI threshold increases until it reaches its maximum on the lower left corner of Figure 5-45 where PFA = 0 and PD = 0. The ideal case is where there is a high PD and low PFA which is represented by the upper-left corner of the plot where PFA = 0 and PD = 1. The random guess line is the $45°$ line joining the points (PFA = 0, PD = 0) and (PFA = 1, PD = 1). Hence, a curve lying above the random guess line would mean that the predictions are better than those obtained by randomly guessing discontinuity locations, and vice-versa.

ROC curves of known discontinuities are computed for the field tests conducted on the 2018 HTL field test. Known discontinuities are defined as joint and welds verified by the UC San Diego prototype camera system. Separate curves are plotted for different types of discontinuities because the detection performance depends on the type and size of the discontinuity. A discontinuity map containing the geographic locations of the joints and welds on the HTL track was compiled using the images of the track segments captured by a camera mounted with the prototype. Since the test was conducted at three different speeds of 25 mph, 33 mph, and 40 mph, a master-map of all the discontinuities was made by compiling flagged welds and joints across the different speeds. Hence, each discontinuity on the track (captured by the camera) is assigned a specific GPS coordinate and constitutes the “ground truth”. Similarly, the DI trace of the tests conducted at each speed will have a one-to-one mapping with the GPS coordinates on the ground. To compute the ROC curves, the rail track is first discretized into “pristine” and “defective” portions. The term “defect” and “feature” will be used synonymously with the term discontinuity in this text. Pristine sections of the track have no discontinuities, while the defective segments have either a joint or a weld. Since the locations of the discontinuities cannot be ascertained precisely, a portion of the track, the pristine margin, is eliminated before and after each feature to build the pristine sections of the rail, as shown in Figure

5-46. Similarly, for the defective population, a portion of the track, the defect margin, is included before and after each feature, as shown in Figure 5-47. The ROC curves are computed for each discontinuity by scanning the track from the start of the run till the end of the run and observing the number of times the DI value crosses the threshold within the scanning length (gauge length of the prototype at 1.5 ft). If the total count of crossings exceeds the NTC threshold in the defective segment of the track, a “positive detection” is counted. If the number of crossings exceeds the NTC threshold in the pristine segment of the track, a “false alarm” is counted.

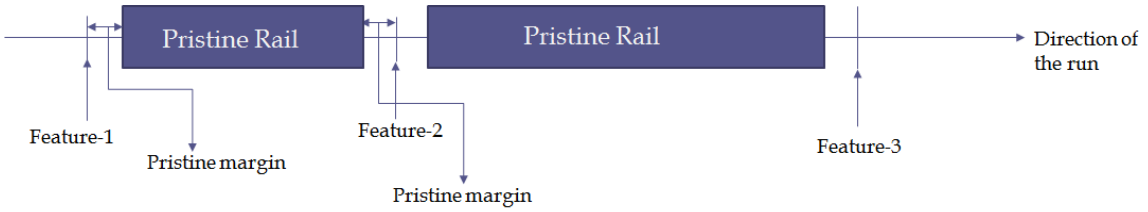

Figure 5-46: Computation of the pristine segments of rail track for ROC curve analysis.

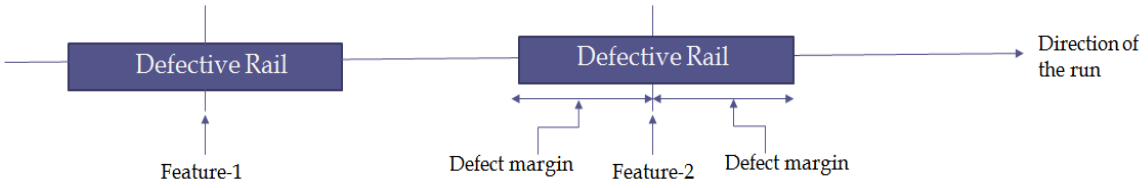

Figure 5-47: Computation of the defective segments of rail track for ROC curve analysis.

The defect margin used in the computation of the ROC curve represents the precision that the prototype has when flagging a section of rail as defective. Three defect margins were computed at ±3 ft, ±5 ft, and ±10 ft to understand the effects of the defect margin on the results. The analysis of the defect margin was performed on the 40 mph test with only one of the two loops used for analysis. An NTC threshold of 7 was used for the ROC curves of the joints and welds. The ROC curves for welds are shown in Figure 5-48, and those for joints are shown in Figure 5-49. As the “defect margin” increases, the

curves shift towards the upper-left, representing an improvement in the PD and reduction in PF. As expected, an increase in the “defect margin” means that the true defect now lies within a relaxed range from the identified location of the defect and still be considered a positive detection. The Area Under the Curve (AUC) is a metric for the overall damage detection performance for different threshold levels. A higher AUC represents better performance and visually represents a curve biased toward the upper-left corner.

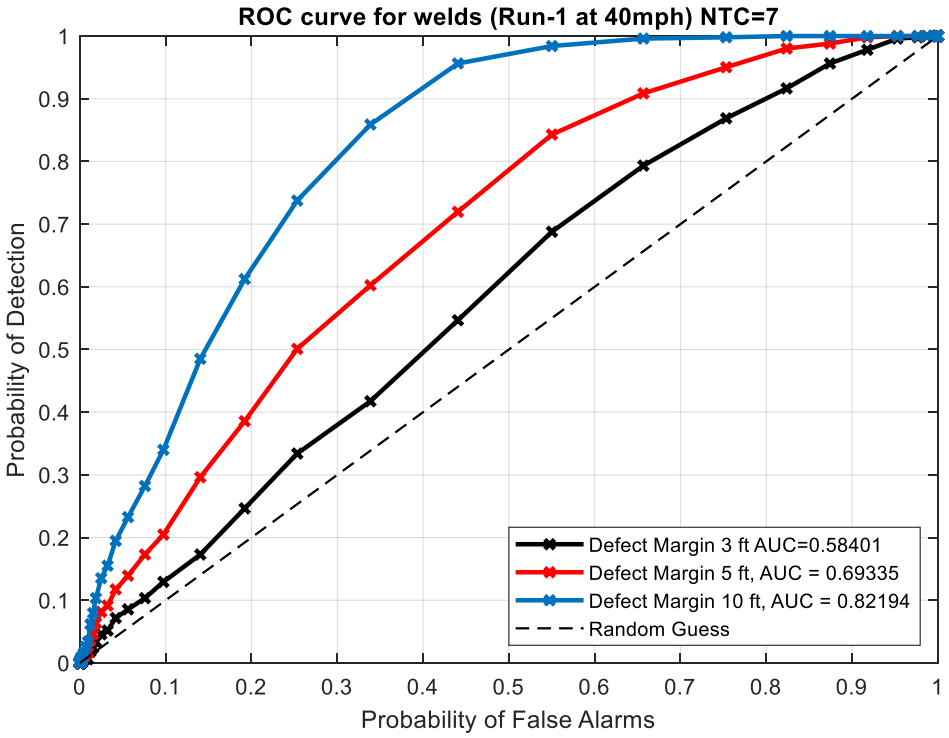

Figure 5-48: 2018 HTL ROC curves with defect margins at ±3 ft, ±5 ft, and ±10 ft for welds at 40 mph.

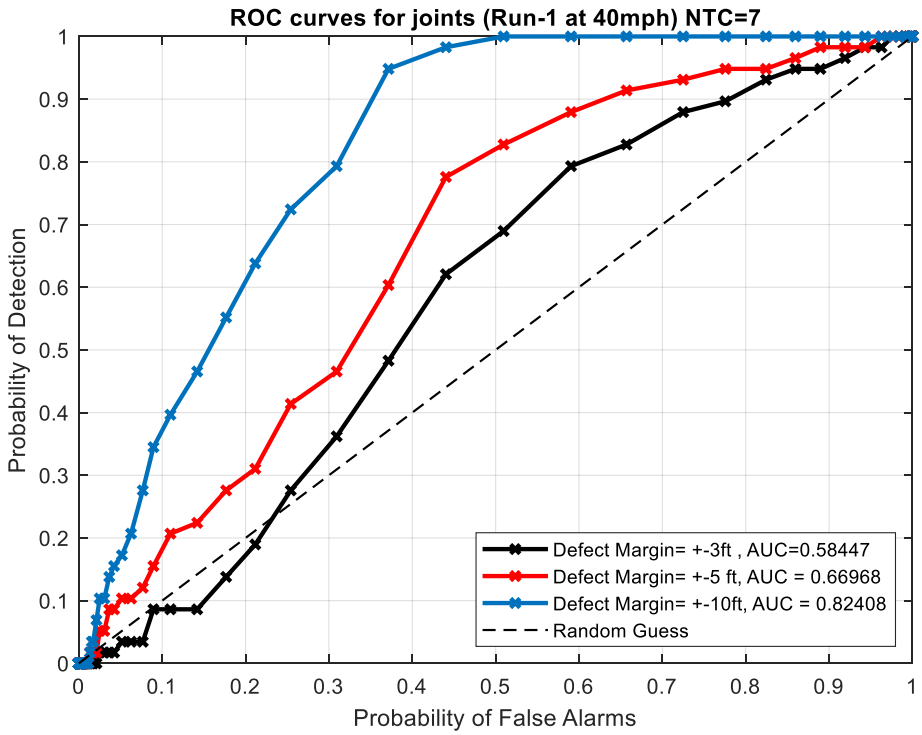

Figure 5-49: 2018 HTL ROC curves with defect margins at ±3 ft, ±5 ft, and ±10 ft for welds at 40 mph.

The next logic step is to test the improvement in the PFA vs PD, and subsequently, the AUC by compounding additional loops. A ROC curve with ±10 ft defect margin was computed for welds and joints (Figure 5-50 and Figure 5-51). Increasing the number of loops over the same track improves the results by introducing redundancy. The result improvement is quantified by a shift in the curve to the upper-left and increase in AUC values. For example, in Figure 5-50, an improvement for a PD of 70% has a reduction in the PFA from 23% to 20% and an increase in AUC from 0.82 to 0.84. A similar result is shown in Figure 5-51 for the joints.

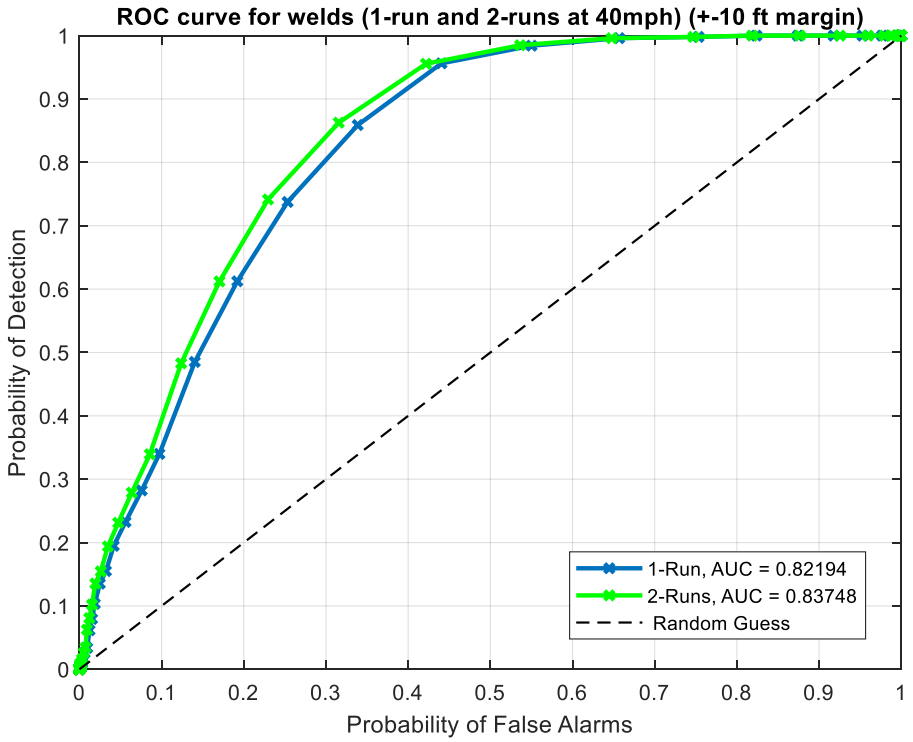

Figure 5-50: 2018 HTL ROC curves with 1 and 2 loops for welds at 40 mph.

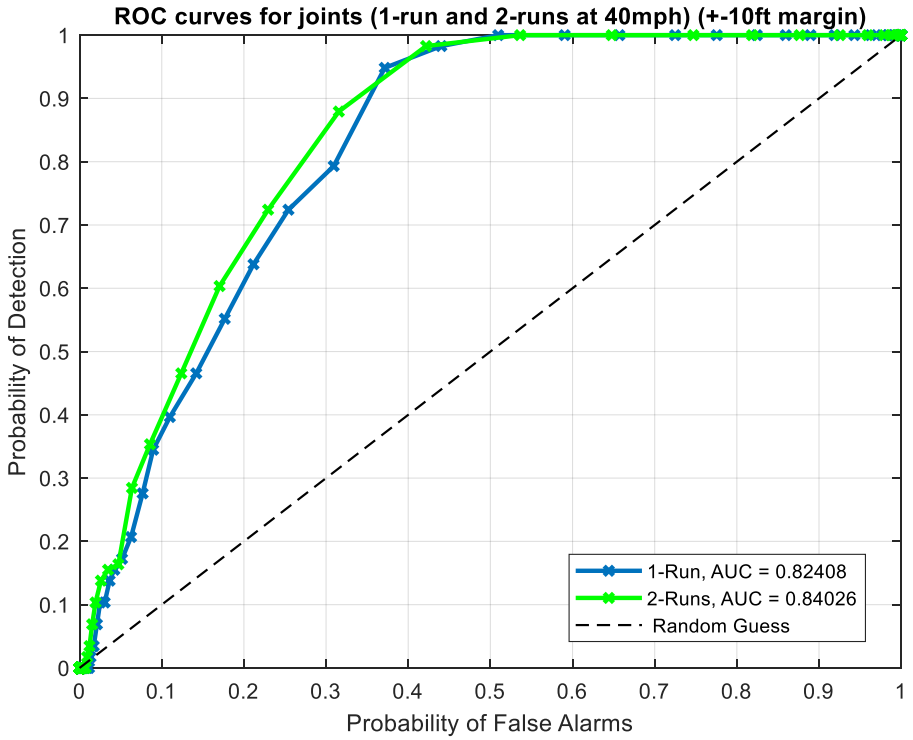

Figure 5-51: 2018 HTL ROC curves with 1 and 2 loops for joints at 40 mph.

The ROC curves previously shown were for the entire length of the track. This means that these curves include regions of high and low acoustic signal strengths, as illustrated in Figure 5-35. High acoustic signal strength corresponds to a value above the threshold variance of 0.05. The areas of high acoustic signal strength are represented in four distinct zones. The ROC curves in this section were computed over the four zones.

The ROC curves are shown in Figure 5-52 and Figure 5-53 for joints and welds, respectively. In Figure 5-53, the ROC curve is staggered since only 8 joints lie within the four zones, resulting in poor resolution across varying DI thresholds for the calculation of PD and PFA. Comparing Figure 5-48, the ROC curve for welds over the entire track, versus Figure 5-52, the ROC curve for welds over the four sections, highlights a noticeable improvement, as evident from the AUC value increase from 0.82 to 0.84 for the ±10 ft defect margin. Similarly, for the joints, a comparison between Figure 5-49 and Figure 5-53, highlights an improvement in the AUC value from 0.82 to 0.85 for the ±10 ft defect margin. Furthermore, for the ±10 ft defect margin case, a PF of 20% results in a PD of 62% while a PD of 70% is possible when looking only at the four zones of high acoustic signal energy. For the joints, in Figure 5-53, defect margins of ±10 ft and ±5 ft are nearly identical. This suggests that localization of the joints as a sparse, high acoustic signal areas is precise down to ±5 ft. The results in this section demonstrate considerable improvement in the PD for both joints and welds by limiting the analysis to areas of high acoustic signal energy.

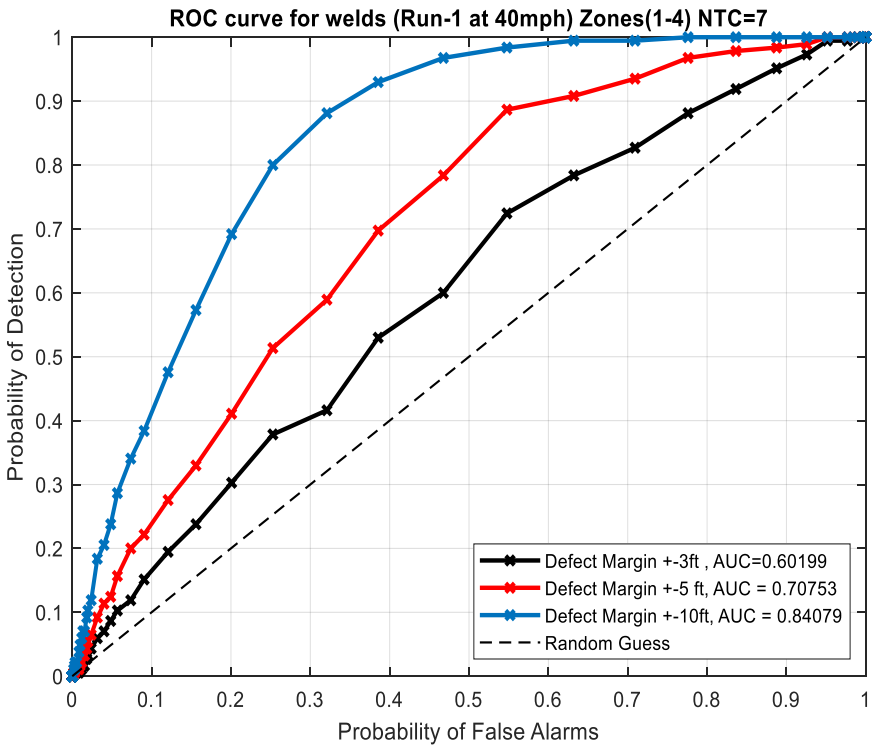

Figure 5-52: 2018 HTL ROC curves for welds in Zones 1 through 4 at 40 mph.

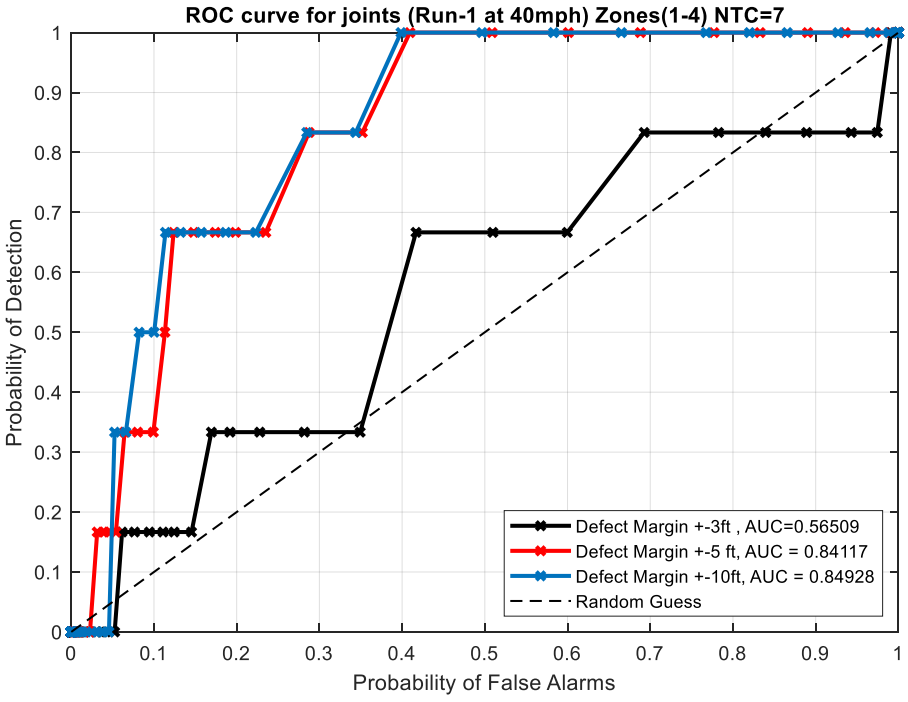

Figure 5-53: 2018 HTL ROC curves for joints in Zones 1 through 4 at 40 mph.

Instead of looking at four fixed geographic locations for the definition of high acoustic signal energy, additional controls can be applied through adaptive selection based off the 0.05 variance threshold. For instance, in Zone 4 (Figure 5-35), a section of low acoustic signal energy was included in the analysis based off fixed geographic locations. Instead, a more robust approach is used that calculates the average variance of the baseline used in the outlier detection calculation to determine if the output is in an area of high acoustic signal energy. This approach results in the NTC values in the scanning length changing considerably across the entire run as small sections of rail are adaptively removed. Hence, an adaptive NTC is introduced such that if more than 50% of the points within the scanning length cross the DI threshold, a flag is raised.

The ROC curves from the adaptive analysis are shown as Figure 5-54 and Figure 5-55. At first glance, comparison between the non-adaptive (Figure 5-52 and Figure 5-53) and adaptive (Figure 5-54 and Figure 5-55) ROC curves show a reduction in improvement. However, closer analysis demonstrates an improvement in PD for areas of low PFA. For example, for the ±10 ft defect margin case and a PFA of 20%, the adaptive analysis has a PD of 75% compared to a PD of 70% for the non-adaptive case. For the ROC curves for joints, the adaptive analysis also demonstrates improvement when comparing the AUC and discrete PD/PFA values primarily in the high PD regions. For example, comparing Figure 5-53 to Figure 5-55, for a PD of 90%, the PFA drops from 37% to 32%.

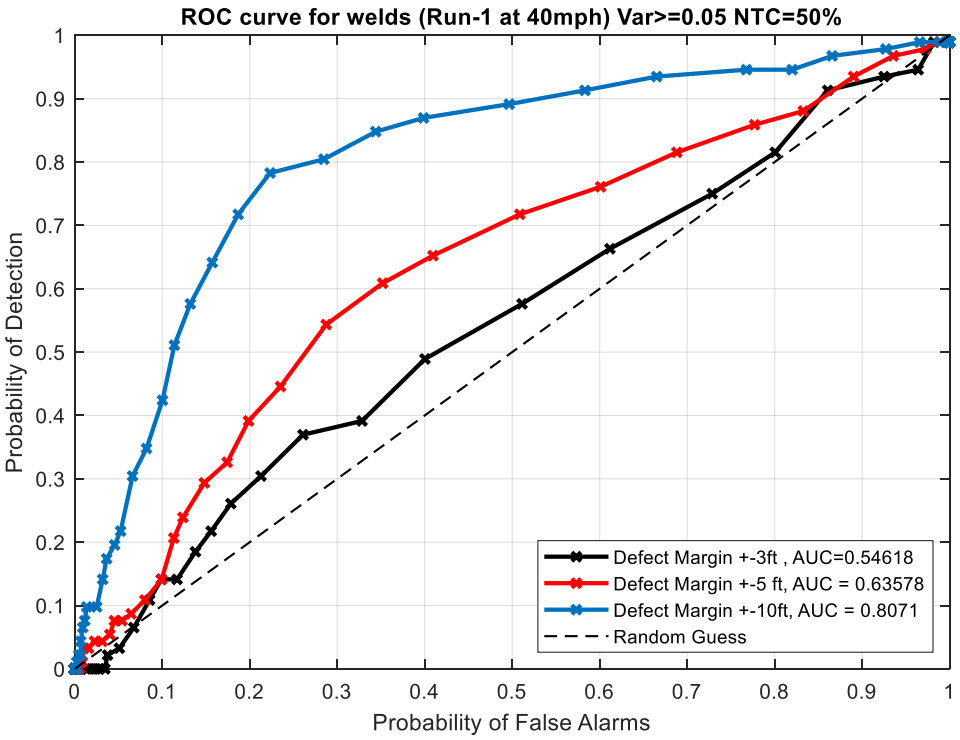

Figure 5-54: 2018 HTL ROC curves for welds with adaptive energy selection.

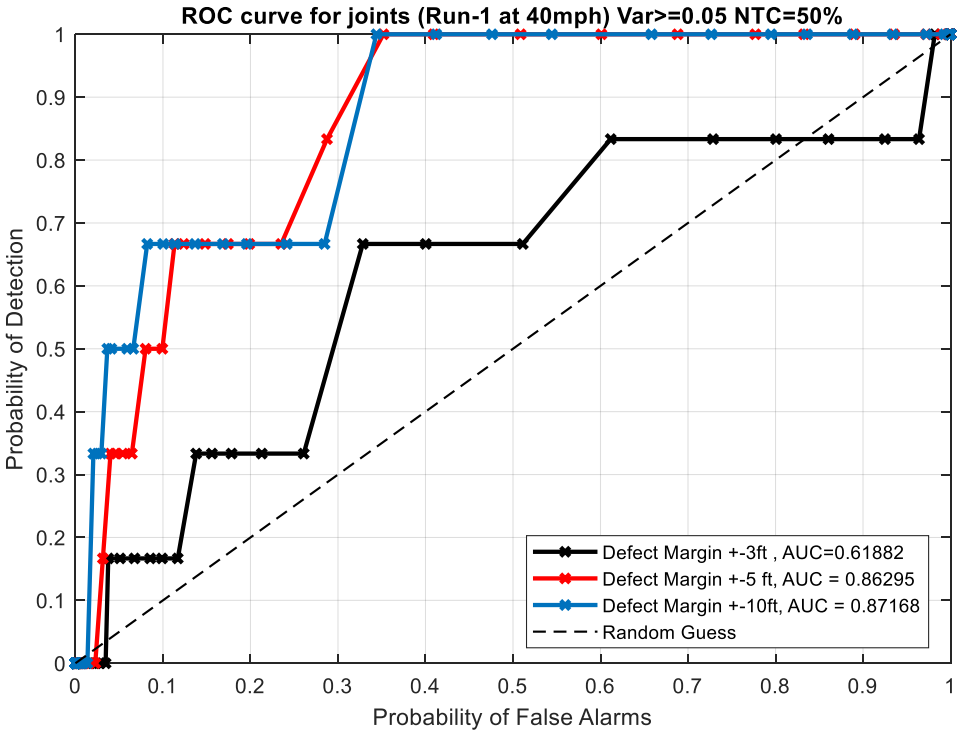

Figure 5-55: 2018 HTL ROC curves for joints with adaptive energy selection.

Lastly, a study on choosing the value of the acoustic signal threshold is explored by generating ROC curves for welds at 40 mph for variances of 0.001, 0.05, and 0.2. The results from previous sections of the report focused on an acoustic signal threshold value of 0.05 variance to determine an area of high versus low signal. Figure 5-56 demonstrates the results. Between 0.001 to 0.05, an increase in acoustic signal threshold results in an improvement from 0.78 to 0.80 AUC. Increasing further to 0.2 results in improved performance at the loss of sensitivity in the ROC curve, shown by the step-like result from the reduced number of features in the ROC computation. Thus, the 0.05 acoustic signal threshold was chosen for analysis.

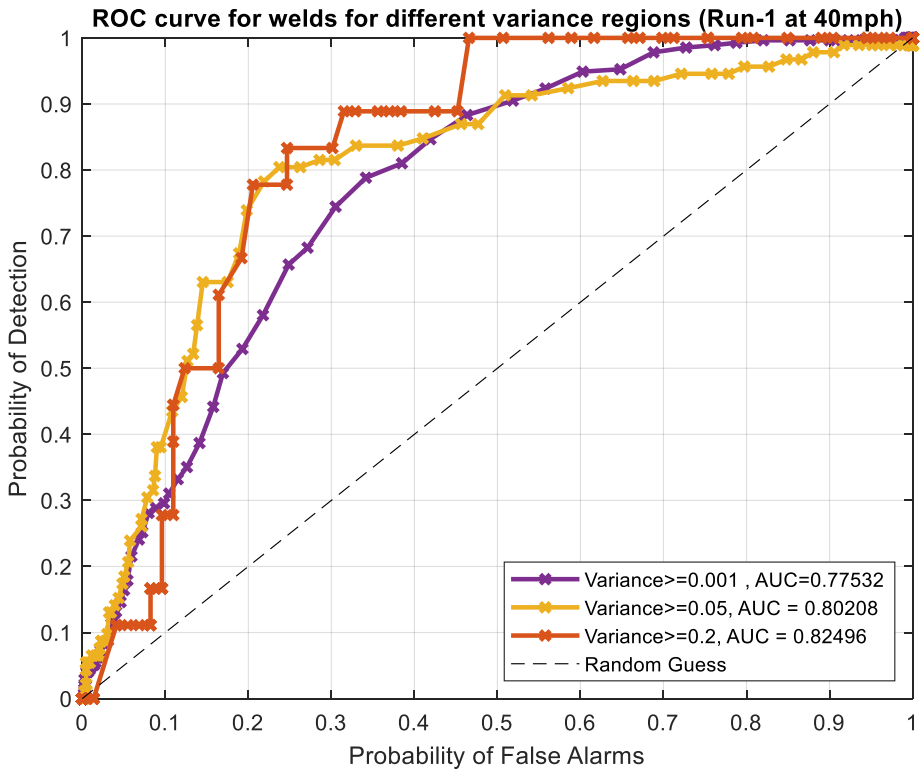

Figure 5-56: 2018 HTL ROC curves for varying acoustic signal threshold at 40 mph.

5.8 Results for 2019 Field Test on High Tonnage Loop Track

Runs, identical to those on the 2018 field test, were conducted at the HTL test track at speeds of 40, 33, and 25 mph. The maximum allowable speed was 40 mph. All runs consisted of 3 loops. An aerial view of the test track and direction of inspection is shown in Figure 5-57. The primarily purpose of this test was to verify that placing the prototype closer to the locomotive resulted in an increased signal energy. In the 2018 field test, significant portions of the rail were at the sensor noise floor and resulted in high amounts of false positives.

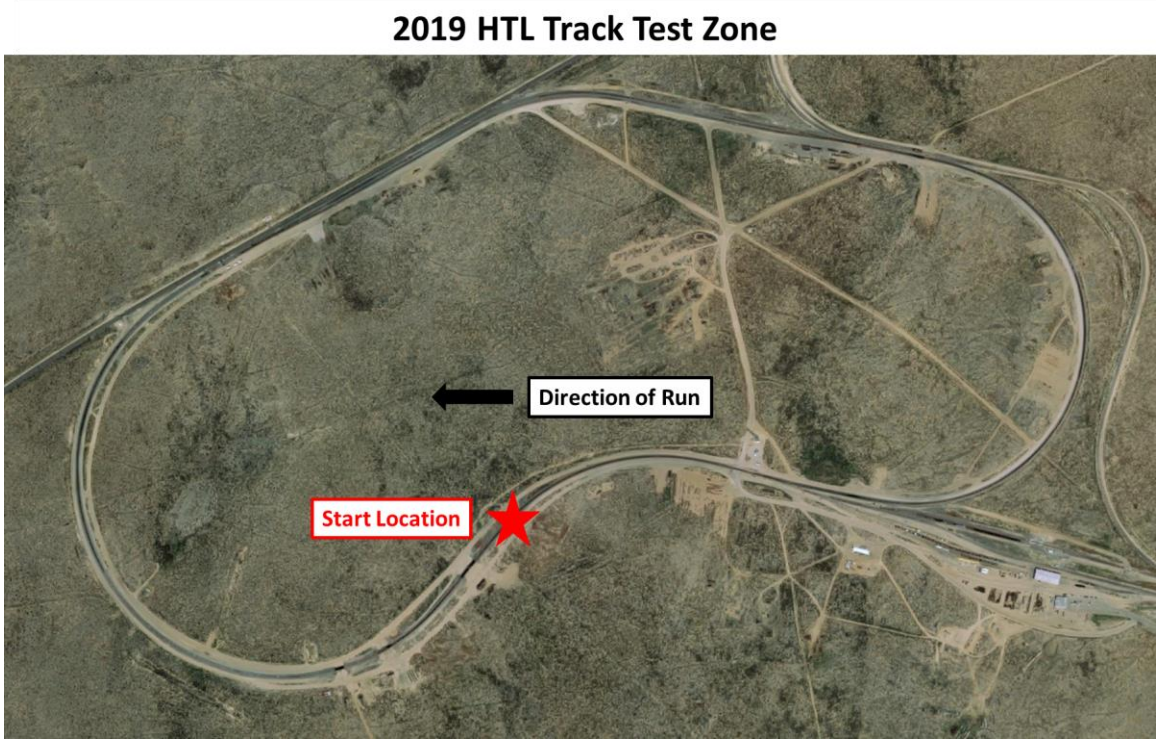

Figure 5-57: HTL rail track used for the 2019 field test at TTC.

5.8.1 Signal Energy Improvement

A comparison between the 2018 and 2019 was performed using a signal-to-noise ration metric to determine if placing the sensors closer to the locomotive resulted in an

increase in received signal. In order to normalize both runs. As the train is stationary, the average minimum signal variance, σ_{min}, was computed:

$$\sigma_{\min} = \frac{1}{n}\sum_{i=1}^{n}\sigma(Speed \ < \ 0.5 \ mph) \tag{5.7.3}$$

Next, the signal energy ratio, σ_{norm}, in decibels was computed through a ratio of the current signal snapshot variance to the average minimum signal variance at acceleration. This is to ensure that each sensor and test run has an independent baseline as signal gain may have changed:

$$\sigma_{norm} = 10\log_{10}\left(\frac{\sigma_i}{\sigma_{min}}\right) \tag{5.7.4}$$

Thus, if the signal energy ratio, σ_{norm}, falls below 3 dB, the reconstructed transfer function is poor and subject to be discarded in later analysis. The results for 40, 33, and 25 mph are shown in Figure 5-58, Figure 5-59, and Figure 5-60, respectively. A noticeable improvement in signal strength can be seen for all speeds resulting in more usable sections of track for analysis. The improvement is attributed to the closer proximity to the higher axle loading and count of the locomotive which improves the energy and frequency of excitation as the wheel moves across the track.

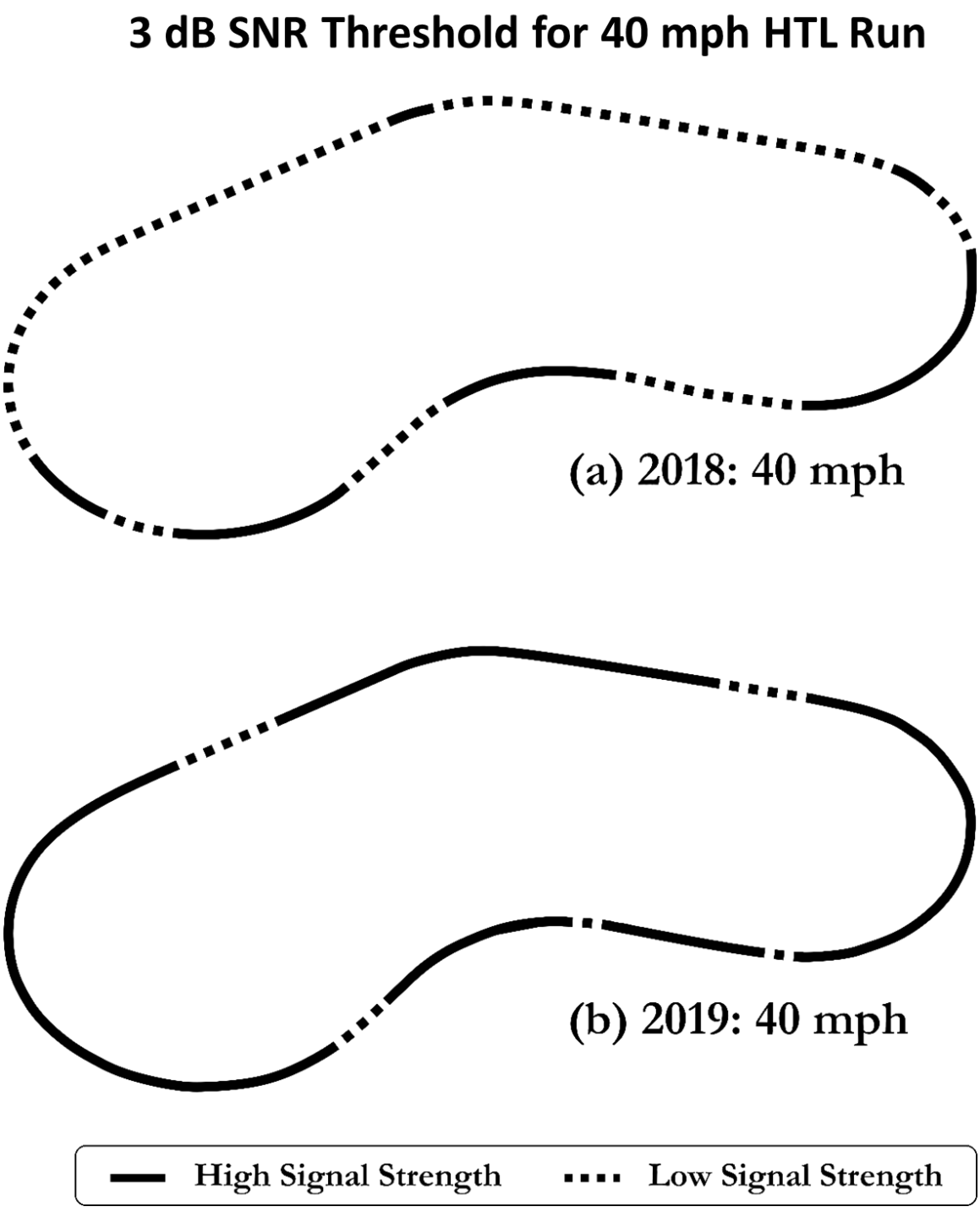

Figure 5-58: Comparison of 2018 and 2019 HTL signal energy result at 40 mph.

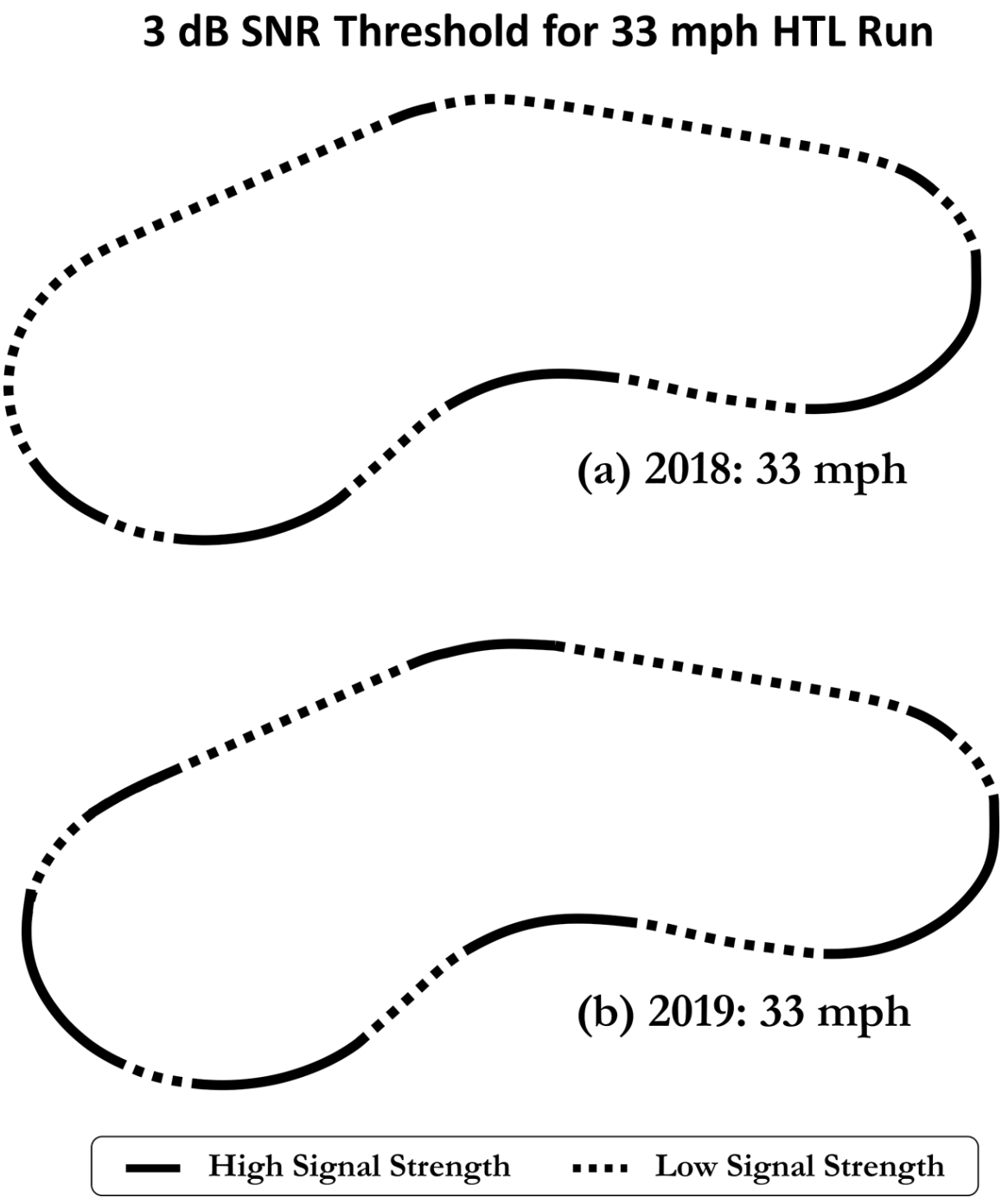

Figure 5-59: Comparison of 2018 and 2019 HTL signal energy result at 33 mph.

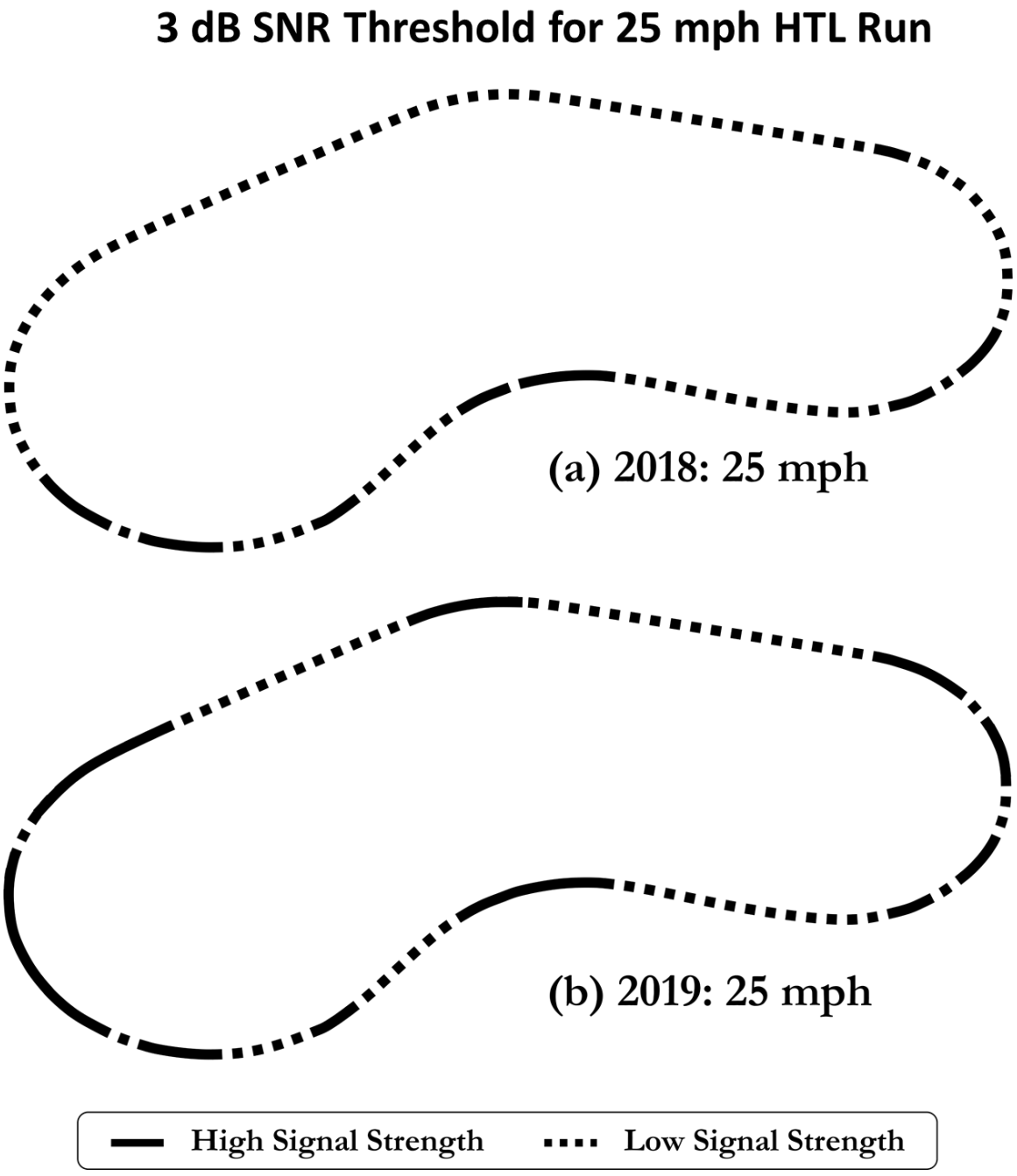

Figure 5-60: Comparison of 2018 and 2019 HTL signal energy result at 25 mph.

5.8.2 Optimization of Baseline Length

As previously discussed in the generation of the DI, the length of the baseline plays a key role in the detection of discontinuities in the rail. A longer baseline results in an averaged statistic of the rail. On the other hand, a shorter baseline results in a more localized statistic of the rail. Therefore, a longer baseline is expected to result in a reduced sensitivity to discontinuity detection. Conversely, a shorter baseline is expected to be more sensitive to discontinuities but may result in more false alarms. Baseline distribution lengths of 30, 60, 120, and 250 points were analyzed. A representative sample of normalized DI traces for 30 and 240 points at 40 mph are illustrated in Figure 5-61 and Figure 5-62 , respectively. Visually, the two figures demonstrate increasing the baseline length results in less sensitivity.

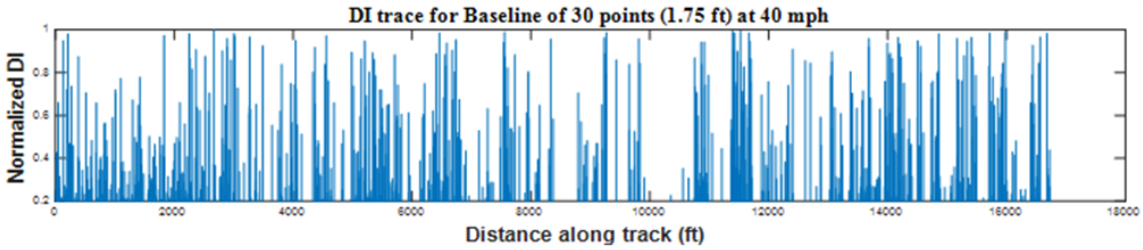

Figure 5-61: Damage Index trace at 40 mph for baseline length of 30 points (1.75 ft).

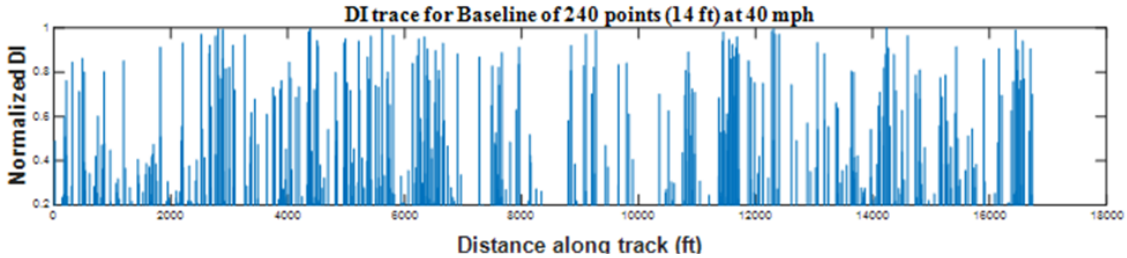

Figure 5-62: Damage Index trace at 40 mph for baseline length of 240 points (14 ft).

The effects of changing the length of the baseline distribution was analyzed with the help of Receiver Operating Characteristic (ROC) curves using the same method of generation as in Section 5.7.3 ROC curves for welds, joints, and defects were generated

to determine the optimal baseline length. In the case of welds, a total of 214 welds were captured by the camera mounted with the prototype on the inner rail for one loop of the HTL track. The weld locations were mapped through GPS coordinated acquired by the GPS antenna mounted on the top of the test vehicle.

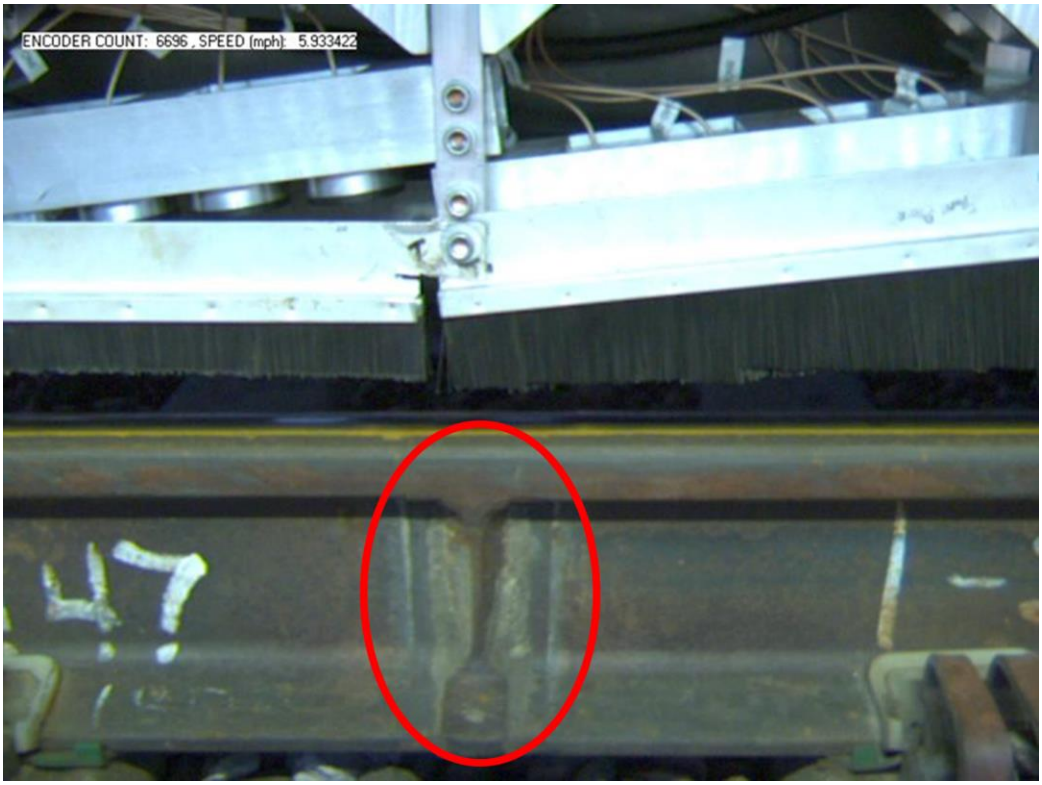

Figure 5-63: Example of weld captured by camera system.

The ROC curves for the three speeds at 25, 33, and 40 mph were generated for welds, joints, and defects. An optimal baseline distribution length of 60 points, corresponding to 2.2 ft for 25 mph and 3.5 ft for 40 mph, results in the highest AUC (area under the ROC curve) at 0.82 for 40 mph and 0.83 for 33 mph. For the 25 mph result in Figure 5-66, the 60-point baseline performed the worst. This was offset by the improved performance for joints and defects.

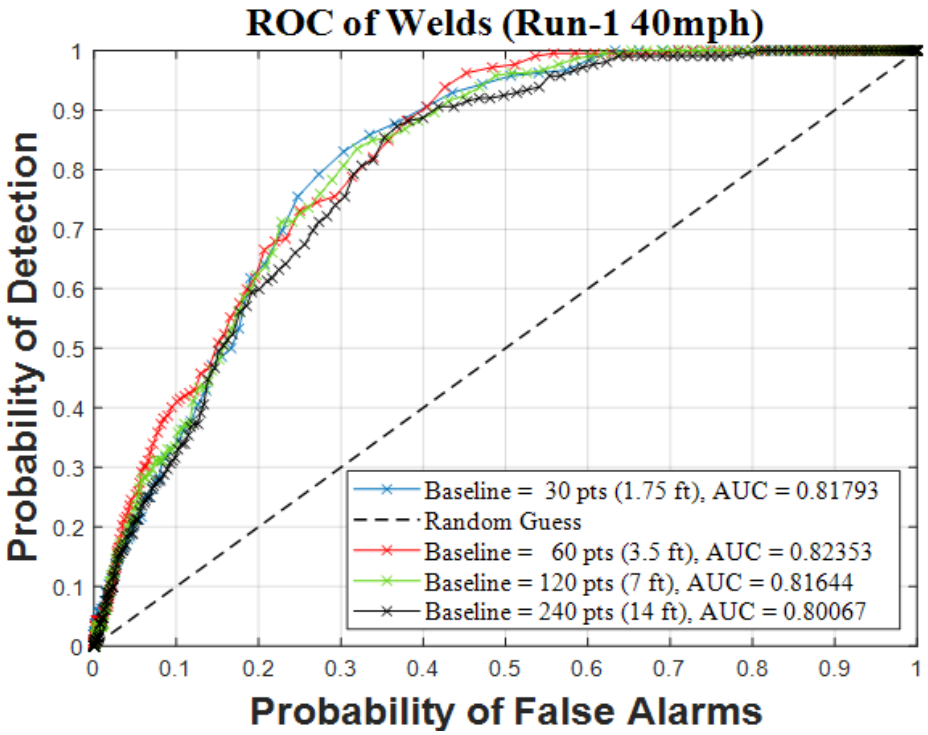

Figure 5-64: 2019 HTL ROC curves of welds at 40 mph at varying baseline lengths.

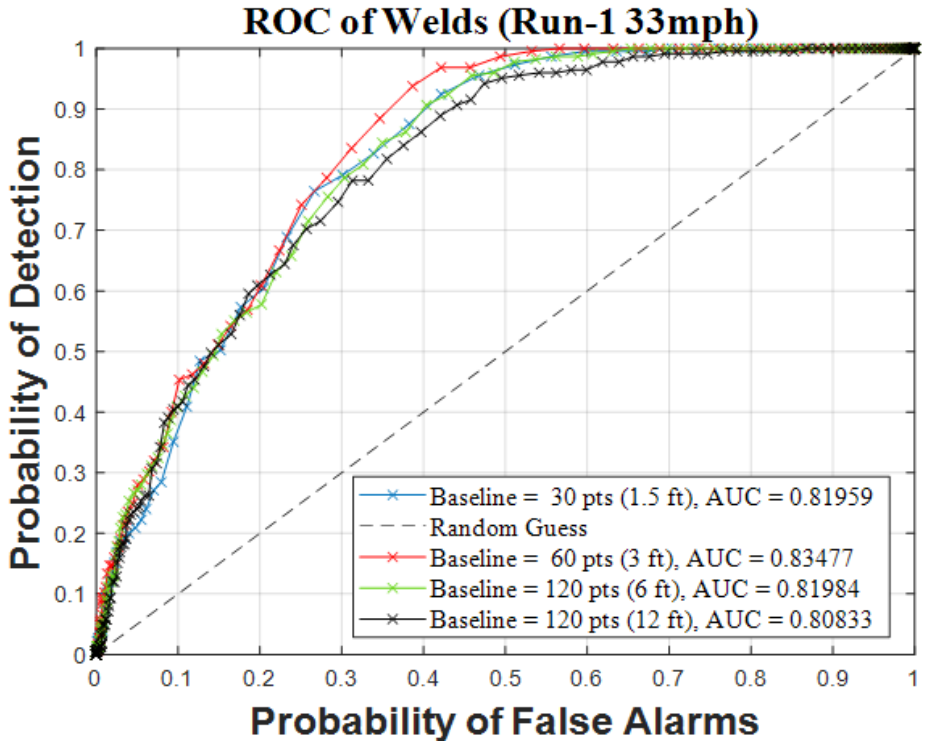

Figure 5-65: 2019 HTL ROC curves of welds at 33 mph at varying baseline lengths.

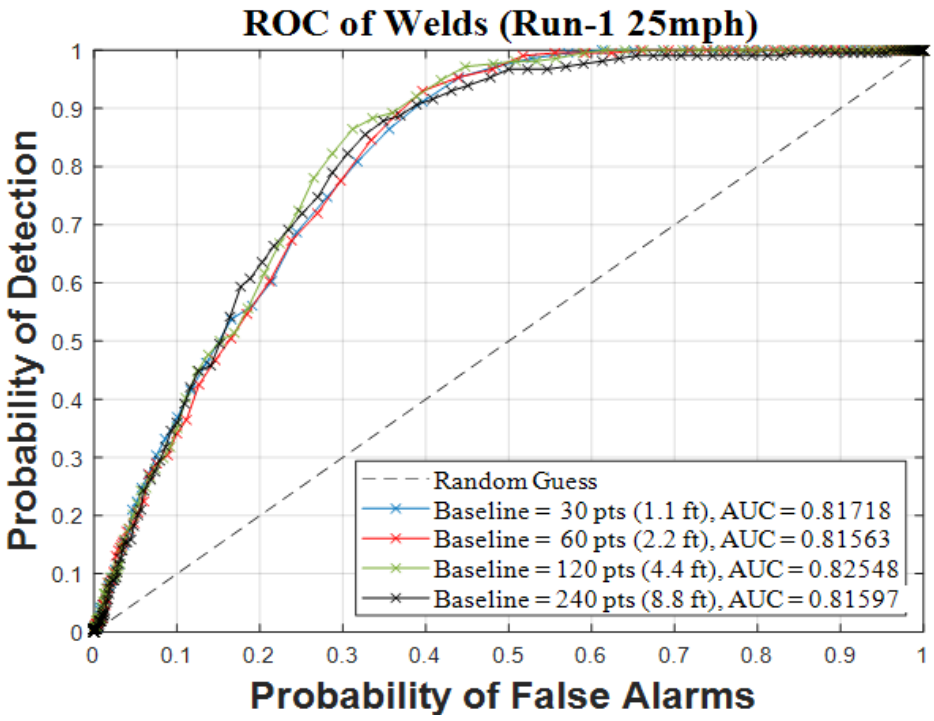

Figure 5-66: 2019 HTL ROC curves of welds at 25 mph at varying baseline lengths.

The ROC curves generated for joints used data from 18 GPS joint positions captured by the prototype camera. The ROC curves for the joints are shown in Figure 5-68 through Figure 5-70 for speeds of 25, 33, and 40 mph, respectively, with baseline lengths of 30. 60, 120, and 240 points. The staggered nature of the ROC curves is because there are fewer joints than welds. This results in fewer values to determine the POD. A baseline of 60 points corresponding to 3.5 ft for 40 mph, 3 ft for 33 mph, and 2.2 ft for 25 mph outperformed for the 40 mph and 25 mph but underperformed for the 33 mph run where the 30 point (1.5 ft) baseline performed the best.

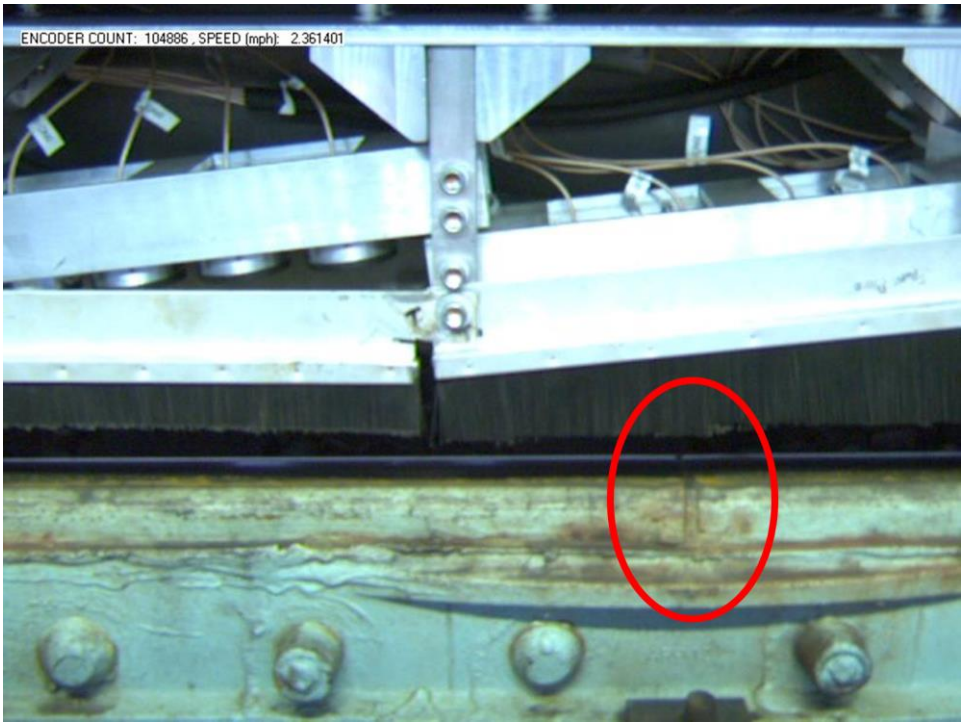

Figure 5-67: Example of a joint captured by camera system.

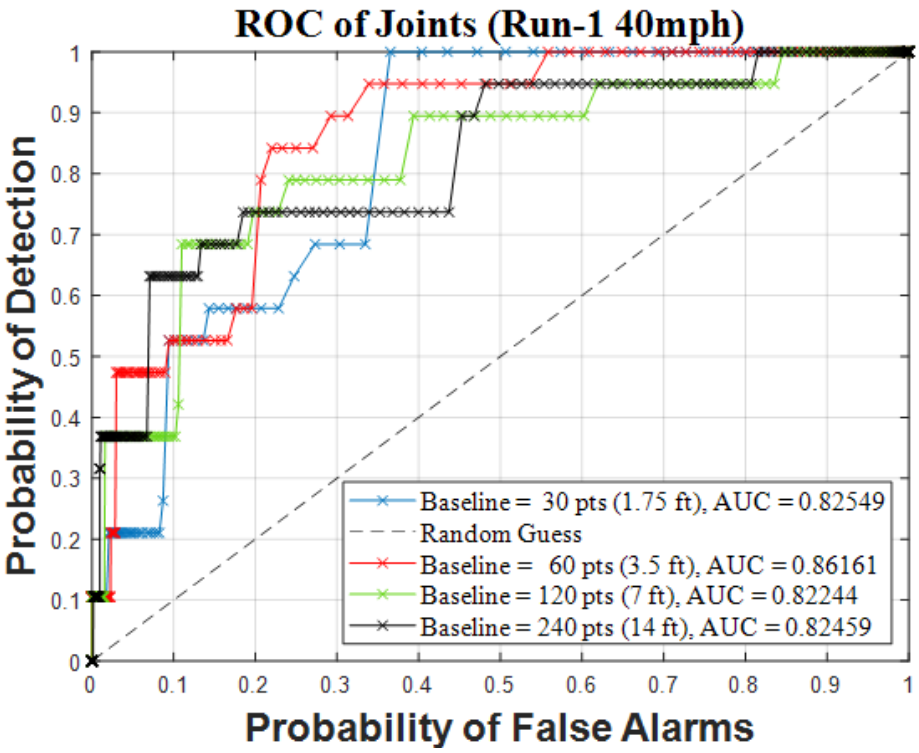

Figure 5-68: 2019 HTL ROC curves of joints at 40 mph at varying baseline lengths.

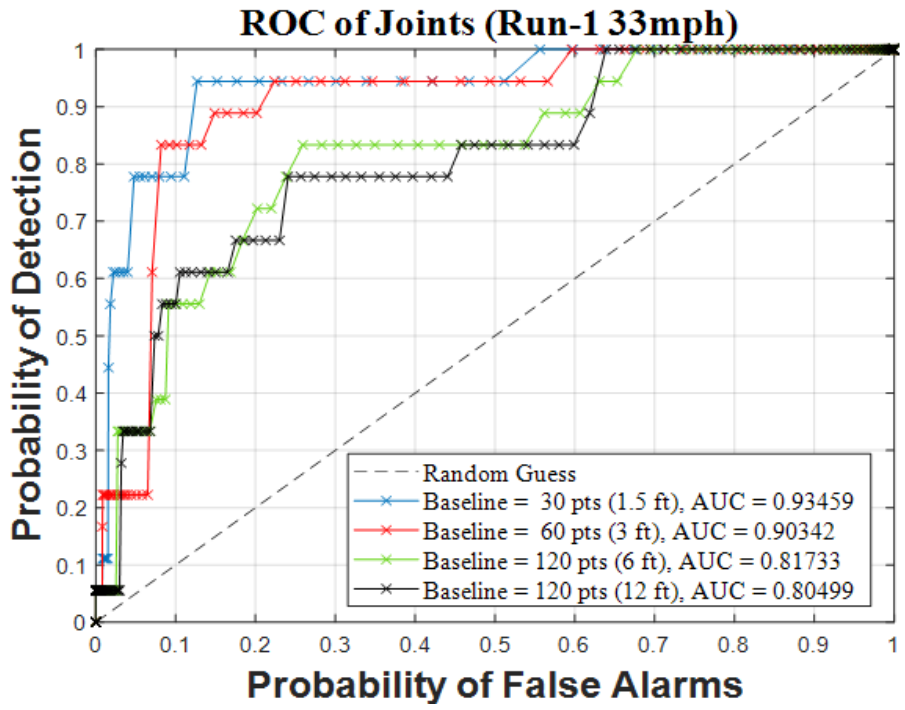

Figure 5-69: 2019 HTL ROC curves of joints at 33 mph at varying baseline lengths.

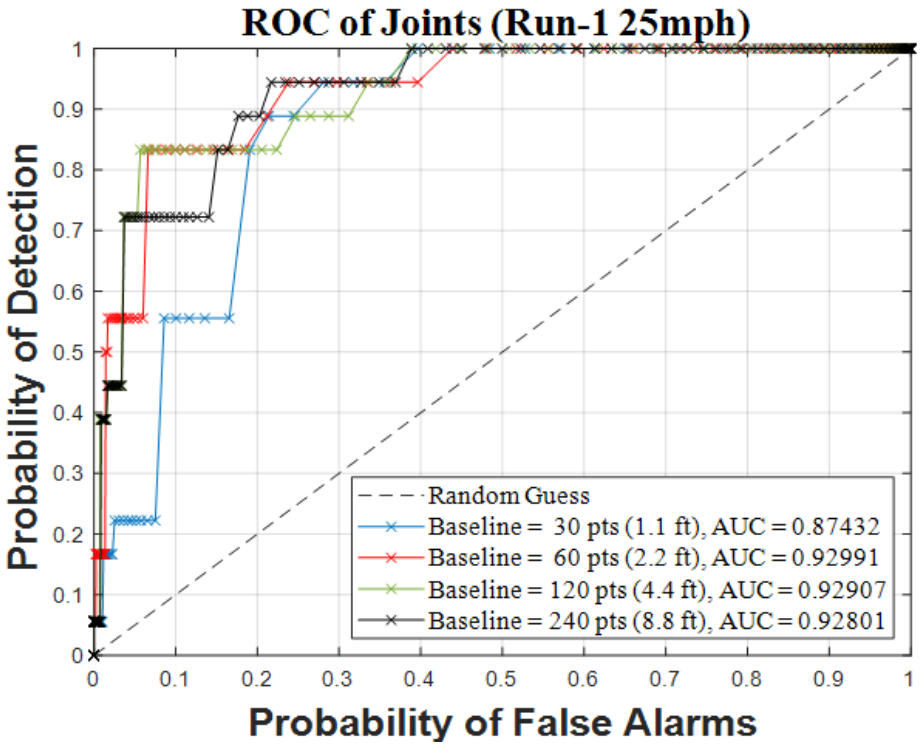

Figure 5-70: 2019 HTL ROC curves of joints at 25 mph at varying baseline lengths.

Lastly, a total of 3 transverse defects were marked by TTC personnel in the inner test rail of the HTL track. A standard RSU used for ultrasonic inspection of rails was used to detect the presence of a defect. An example of a marked defect captured by the imaging system is shown in Figure 5-71. Similar to the joints and welds, the location was mapped through GPS coordinates. As with the joints, since only 3 defects were available in the entire run, the ROC curve generated is discrete. The results are illustrated in Figure 5-72 for 40 mph, Figure 5-73 for 33 mph, and Figure 5-74 for 25 mph.

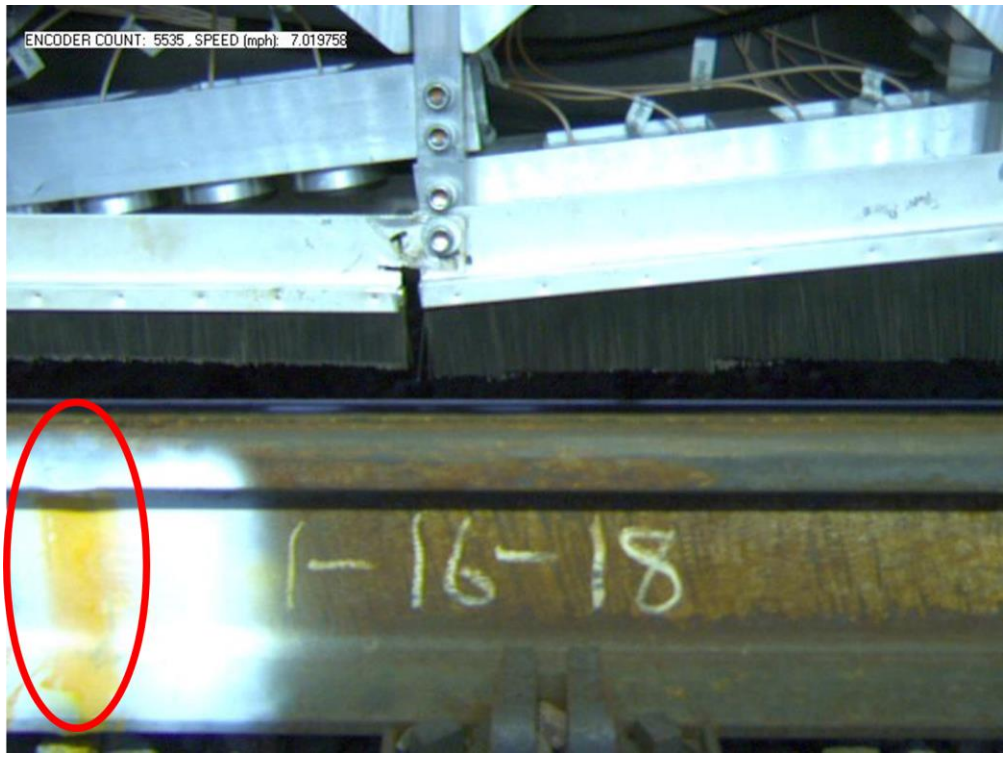

Figure 5-71: Example of marked transverse defects captured by camera system.

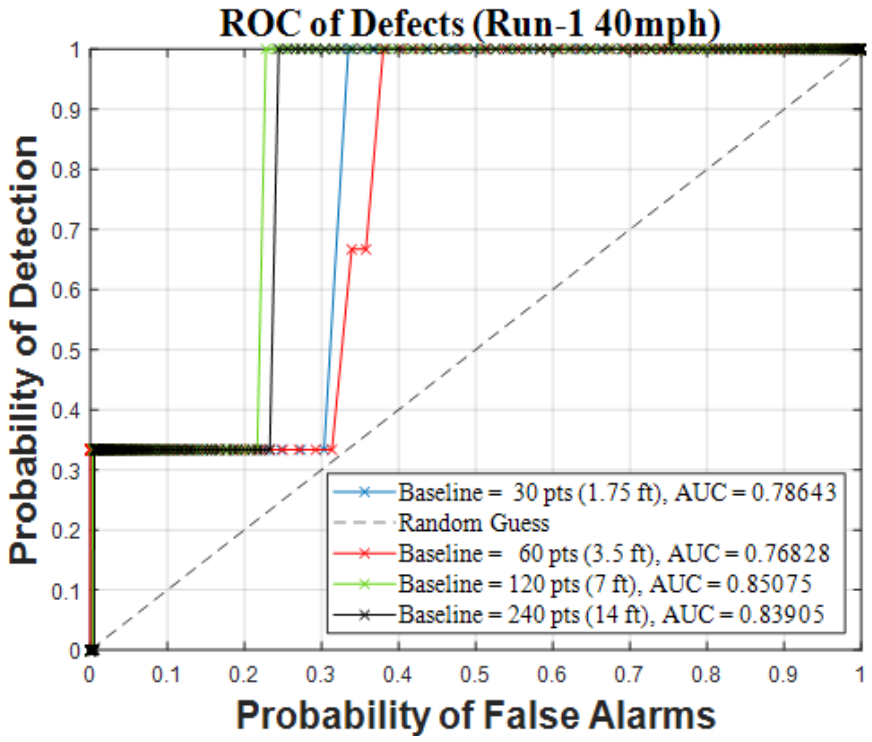

Figure 5-72: 2019 HTL ROC curves of defects at 40 mph at varying baseline lengths.

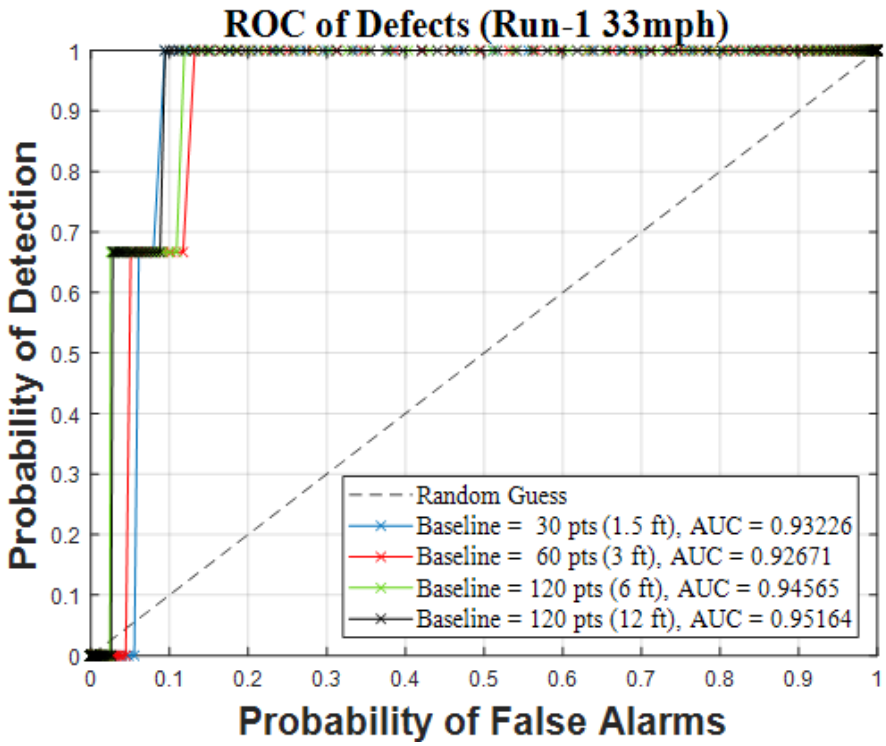

Figure 5-73: 2019 HTL ROC curves of defects at 33 mph at varying baseline lengths.

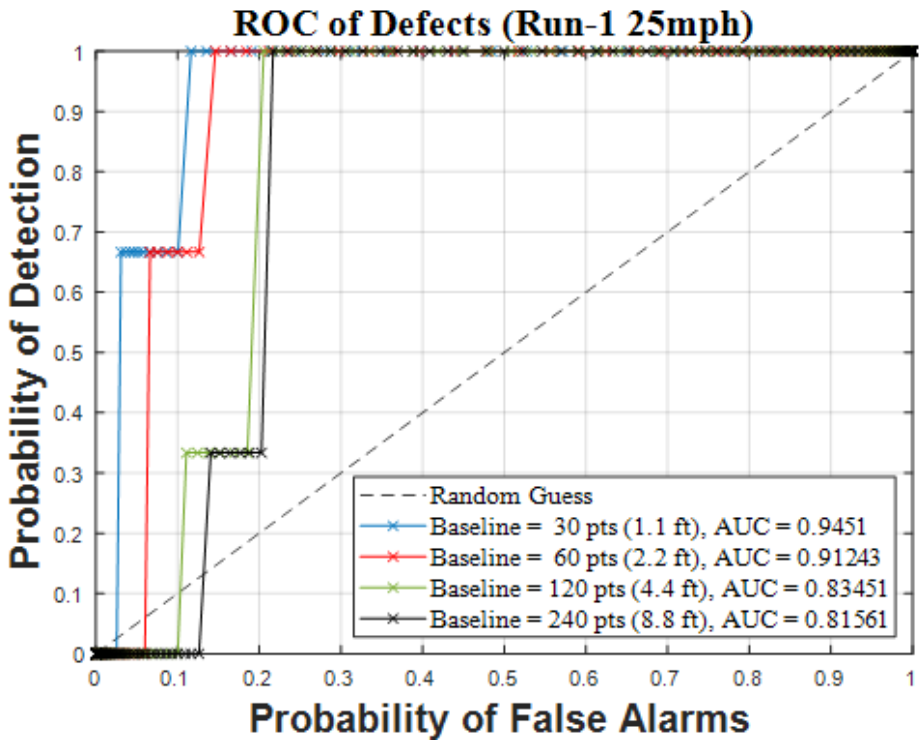

Figure 5-74: 2019 HTL ROC curves of defects at 25 mph at varying baseline lengths.

As expected, changing the baseline length has a significant impact on the detection performance. A baseline length of 60 points corresponding to 2.2 ft at 25 mph and 3.5 ft at 40 mph demonstrated the best overall performance across all discontinuity types (joints, weld, and defects) and all speeds (40, 33, and 25 mph). In case of the transverse defects, however, a baseline length of 240 points performs better than a baseline of 60 points for speeds of 33 mph and 40 mph. At speeds of 25 mph, the baseline length of 60 points outperforms the baseline length of 240 points for the defects. This anomaly was attributed to sample size of only 3 defects available as the ground truth. Therefore, the ROC curve results for defects might not represent the actual detection performance statistics of the system. Lastly, a small baseline length of 30 points, in general performs worse than a baseline of 60 points. For the same POD, a baseline length of 30 points has a higher PFA than a baseline of 60 points. The higher sensitivity of the shorter baseline leads to more false positives. Based on these results, a baseline length of 60

points (2.2 ft at 25 mph and 3.5 ft at 40 mph) can be considered as optimum to maximize the detection performance of the detection prototype as configured during the June 2019 field tests at the HTL.

5.9 Conclusions

Two generations of high-speed, passive-only, noncontact ultrasonic inspection of rails was designed, constructed, and tested. A first-generation prototype was mounted on the DOTX-216 test car for 2016 field tests at TTC in Pueblo, Colorado. A second-generation prototype was mounted on the TTCI 5229 test car in 2018 and 2019. The prototype utilizes pairs of capacitive air-coupled ultrasonic receivers for noncontact probing of the rail. Outlier analysis was applied to the reconstructed impulse response to increase the detection of rail discontinuities and limit the detection of false alarms.

The system relies on the assumption of “piecewise” stationarity of the wheel excitation. This means that the excitation should be stationary during the observation time window. For the results shown, the observation time window was quite small which makes this assumption quite reasonable. For example, the time window was as long as 15 ms for the 30 mph test speed and as short as 6 ms for the 80 mph [128 km/h] test run. The theory proposed also assumes linearity of the system. In accordance to assumptions taken in an earlier seminal paper on a similar topic (Roth, 1971), any nonlinearity in the transfer function system can be generally considered uncorrelated noise. In the application at hand, the acoustic path in air could bring nonlinearities, which would also be different for the two sensors constituting a pair. The fact that the test runs presented show a stable transfer function reconstruction seems to indicate that nonlinearities do not currently play a major role. Studying the effect of nonlinearities goes beyond the purposes of this study and could be the subject of further investigations. In addition, the proposed algorithm is

aimed at minimizing the effect of incoherent noise in the reconstructed impulse response. The effect of any coherent noise is reduced by appropriately time gating the signal around the expected arrival of the desired leaky wave mode in the rail.

The prototype was tested on the RTT track at TTC to speeds as high as 80 mph (128 km/h). The results demonstrate that there is potential to reconstruct a stable structural impulse response of the rail at high speeds, despite the variability of the wheel excitations. The results at various speeds do show some variability in the number of discontinuities detected, and this aspect will be the topic of further investigations and improvements to the system.

Limited tests were also conducted on the RDTF defect farm at TTC, where the speed is limited to 25 mph (40 km/h). Preliminary analysis of the RDTF test runs indicated the potential for the system to detect rail defects such as crushed heads, detail fractures, transverse defects, and transverse fissures. Clearly, for a true assessment of discontinuity detection performance, the trade-off between probability of detection and probability of false alarms will have to be quantitatively determined. One way to do this is to generate ROC curves on a well-mapped rail track. Unfortunately, the tests performed did not allow determination of the true repeatability of the system. Quantification through ROC curves was the focus of the second field test in 2018 on the HTL. Due to signal strength concerns, a third field test was performed in 2019 to demonstrate improved signal energy in closer proximity to the locomotive wheels and to finalize the optimal baseline length for the outlier detection. Although the elimination of an active excitation greatly improves the operational speed limitations, the random nature of passive excitation introduces another problem. The proof-of-concept results demonstrated in this chapter are promising, but significant work remains before this technology can be implemented in the field. Further exploration into integrating the redundancy through multiple passes over the same rail have the

potential to significantly improve the probability of defection and reduce the probability of false alarm and was outside the scope of this research.

The successful development of this concept would enable a new rail inspection paradigm of “smart trains” that perform inspections during regular operations. Besides simplifying inspection scheduling, this ability would result in increased reliability of discontinuity detection due to the redundancy afforded by multiple passes on the same track.

5.10 Acknowledgements

Chapter 5, in part, has been published in *Materials Evaluation*, Liang, A., Sternini, S., Lanza di Scalea, F. (2019) with the title “High-Speed Ultrasonic Rail Inspection by Passive Noncontact Technique”. The dissertation author was the primary author of this chapter.

Chapter 5, in part, has been published in *The Journal of the Acoustical Society of America*, Lanza di Scalea, F., Sternini, S., and Liang, A. (2018), with the title “Robust Passive Reconstruction of Dynamic Transfer Function in Dual-Output Systems”. The dissertation author was the primary author of this chapter.

Chapter 5, in part, has been published in *The Journal of Nondestructive Evaluation, Diagnostics, and Prognostics of Engineering*, Lanza di Scalea, F., Zhu, X., Capriotti, M., Liang, A., Mariani, S., Sternini, S. (2018), with the title “Passive Extraction of Dynamic Transfer Function from Arbitrary Ambient Excitations: Application to High-Speed Rail Inspection from Wheel-Generated Waves”. The dissertation author was the primary author of this chapter.

Chapter 5, in part, is coauthored with Datta, Diptojit. The dissertation author was the primary author of this chapter.

CHAPTER 6

DEFECT IMAGING IN RAILS

6.1 Introduction

The identification of internal defects in railroad tracks is critical for rail safety and risk management. The cost of rail failure can be catastrophic, and substantial effort is required to reduce the risk. Proper allocation of resources for rail defect management requires not only detection, but also precise localization and characterization. Current techniques are limited to detection and have difficulty identifying the size and locating the orientation of the railhead defects due to operator judgement.

Various steps were taken to improve the standard SAFT for ultrasonic imaging. Utilizing advanced weighting functions in conjunction with the traditional SAF algorithms, significant sidelobe reduction was achieved. Furthermore, by compounding various wave propagation modes in the material, image artifacts were reduced. The algorithms were then adapted to image transverse defects using a wedge. Lastly, due to the number of data points and pixels required, only near-real-time results are possible using the CPU for computation. By utilizing the parallel processing structure of the GPU architecture,

significant gains in image refresh rate were achieved for real-time processing. Lastly, an encoder was integrated to generate 3D images for visualization.

Experimental testing of the algorithms was performed on rail sections with simulated and natural flaws acquired from the FRA / TTC Rail Defect Library. Simulated flaws were done by drilling a Flat Bottom Hole (FBH) and Side Drilled Hole (SDH) through the rail head. Natural defects such as TDs and Weld Porosity were also used to test the ultrasonic imaging system. The results from the experimental testing demonstrated promise for ultrasonic imaging to augment current hand verification techniques.

6.2 Prototype Design

The ultrasonic imaging system consists of four major hardware components, shown in Figure 6-1: Host Computer with a GPU, DAQ Hardware, Ultrasonic Array with optional attached Ultrasonic Wedge, and a Linear Encoder. The Data Acquisition Hardware interfaces with both the ultrasonic array and linear encoder. A MATLAB GUI was created to easily interface with the hardware and software components.

Figure 6-1: Ultrasonic Imaging General Hardware Requirement

6.2.1 Host Computer

The host computer is responsible for the data processing and requires a GPU to process the data streamed from the DAQ. The GPU allows the system to process and display the ultrasonic data in real-time. MATLAB was used to process the data and run the GUI created to interface with the data acquisition hardware.

6.2.2 Data Acquisition Hardware

The data acquisition hardware should have the following specifications for optimal image quality: pulser specification (Table 6-1), receiver specification (Table 6-2), and system configuration specification (Table 6-3). The data acquisition hardware must be capable of Full Matrix Capture (FMC) with at least 32/32 element array capability.

Table 6-1: Hardware Pulse Specification

Pulse Voltage	145 V
Pulse Type	Negative Square
Pulse Width	10 – 1000 ns
Pulse Width Resolution	4 ns
Pulse Focusing Delay	0 – 40 µs
Maximum PRF	20 kHz

Table 6-2: Hardware Receiver Specification

Receiver Sensitivity	12 bits
Receiver Gain Range	16 – 110 dB
Receiver Bandwidth	500 kHz to 20 MHz

Table 6-3: System Configuration Specification

Full Matrix Capture Configuration	32/32, 64/64, 128/128, or 256/256
Max Number of Cycles	2048
A-Scan Resolution	12, or 16 bits
Encoder I/O Port Management	Yes

6.2.3 Ultrasonic Array Probe and Wedge

The ultrasonic array probe specification is listed in Table 6-4 and for the ultrasonic array wedge in Table 6-5. Use of higher frequency results in improved detectability at a cost of reduced signal amplitude from higher attenuation at higher frequencies. Increasing the element count results in slower image acquisition times but improves the image resolution. A wedge is used to image vertical defects at a normal incidence to extract sizing dimensions which would not be possible without a wedge.

Table 6-4: Ultrasonic Array Probe Specification

Frequency	2.25 or 5.0 MHz
Element Count	32, 64, or 128
Probe Type	Longitudinal
Matching Medium	Rexolite

Table 6-5: Ultrasonic Array Wedge Specification

Material	Rexolite
Angle	55° Shear or 60° Longitudinal

6.2.4 Linear Encoder

The linear encoder specification is listed in Table 6-6. Due to the requirement for couplant between the wedge and the specimen, the encoder must be watertight. For ferrous metals such as rails, a magnetic wheel type is recommended to ensure contact with the specimen. Large amount of couplant will introduce wheel slippage and result in off-dimensional 3D reconstruction. The encoder is tied to the signal processing algorithm to general a 3D visualization of the defect, as shown in a schematic in Figure 6-2.

Table 6-6: Linear Encoder Specification

Encoder Resolution	16.00 counts/mm
Environmental Sealing	Dust-tight, Water-tight
Loading Type	Spring Loaded
Wheel Type	Rubber or Magnetic

Figure 6-2: Schematic of 3D rail flaw imaging using a wheel encoder connected to the DAQ system.

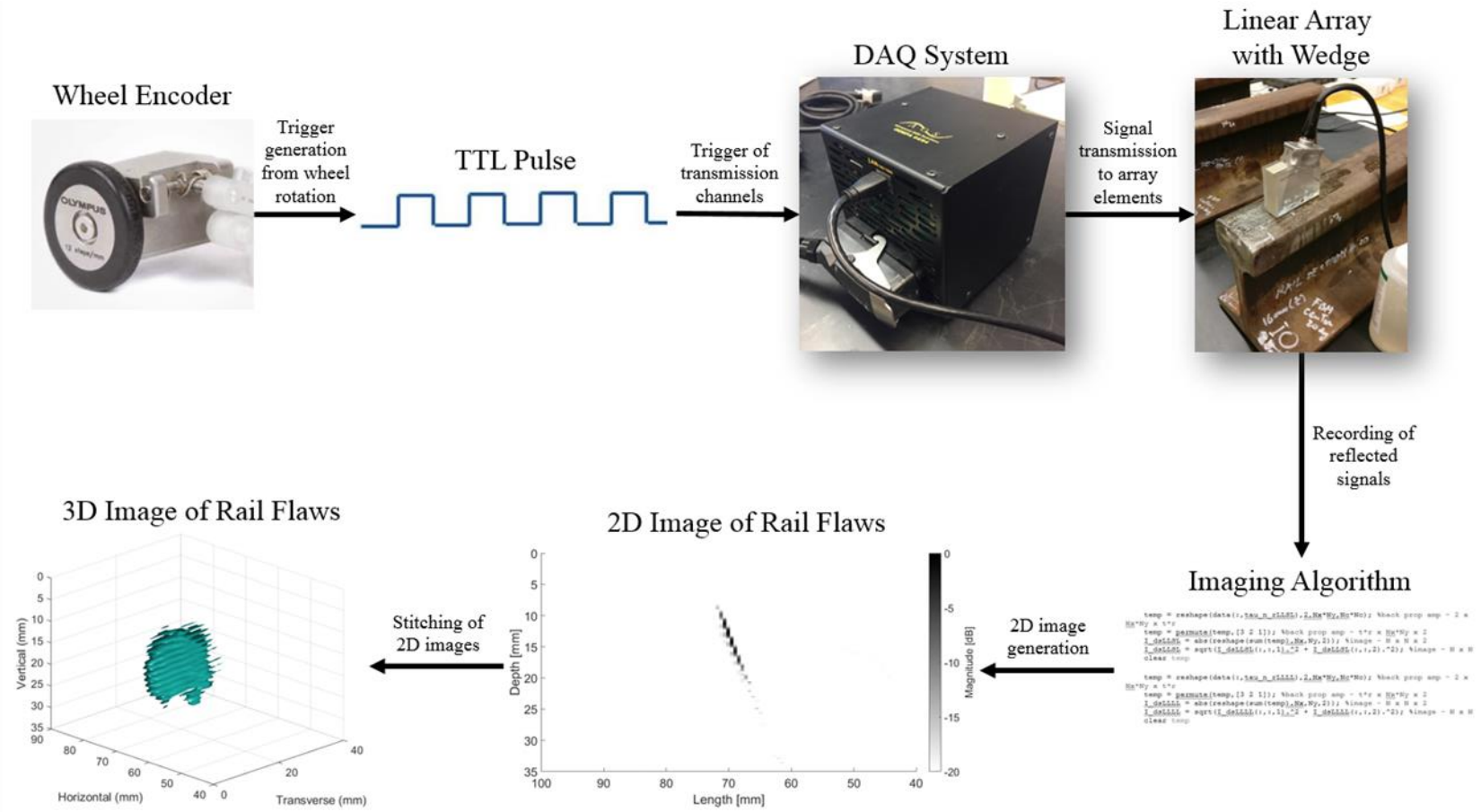
Wheel Encoder
Trigger generation from wheel rotation
TTL Pulse
Trigger of transmission channels
DAQ System
Signal transmission to array elements
Linear Array with Wedge
Recording of reflected signals
Imaging Algorithm
2D image generation
2D Image of Rail Flaws
Depth [mm]
Length [mm]
Magnitude [dB]
Stitching of 2D images
3D Image of Rail Flaws
Vertical (mm)
Horizontal (mm)
Transverse (mm)

6.2.5 Graphical User Interface

A GUI was developed in MATLAB to interface with the imaging algorithm and hardware. After starting the UCSD Imaging GUI, a window with the hardware connection and image calculation parameters appear, as shown in Figure 6-3. Three sections highlighted and labeled as (a), (b), and (c), represent the various operation state screens, hardware initialization parameters, and image calculation settings, respectively.

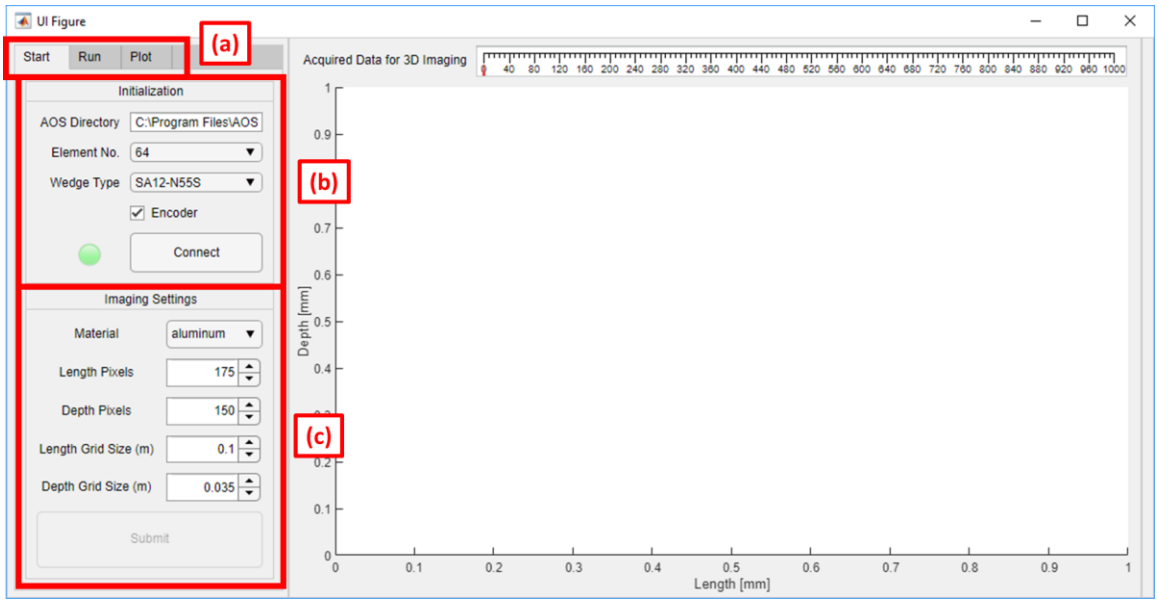

Figure 6-3: Imaging Algorithm MATLAB GUI – Start Screen

Section (b), “Initialization”, allows the user to set the hardware firmware directory, linear array element size, wedge type mounted to the linear array, and if an encoder is connected or not. The “AOS Directory” is where low-level communication files between the GUI software and multiplexed pulser-receiver board are stored. “Element No.” refers to the ultrasonic linear array size and can be 32 or 64 elements. “Wedge Type” refers to the type of wedge mounted to the ultrasonic linear array. In this current iteration, the following wedge types are available: SA12-N55S, SA12-N60L, and None. Pressing the

“Connect” button starts the connection process and loads the FMC options associated with the settings selected.

After successful connection, section (c) is used to determine additional parameters used in the imaging algorithm time-of-flight calculation. “Material” refers to the material type of the object under inspection. “Length Pixels” and “Depth Pixels” determine the pixel density whose physical size is determined by the “Length Grid Size (m)” and “Depth Grid Size (m)” options. The “Submit” button is enabled once section (b) is completed successfully.

The Run Screen is activated after hardware connection and imaging calculations are completed successfully. In this screen, there are four main options highlighted in Figure 6-4.

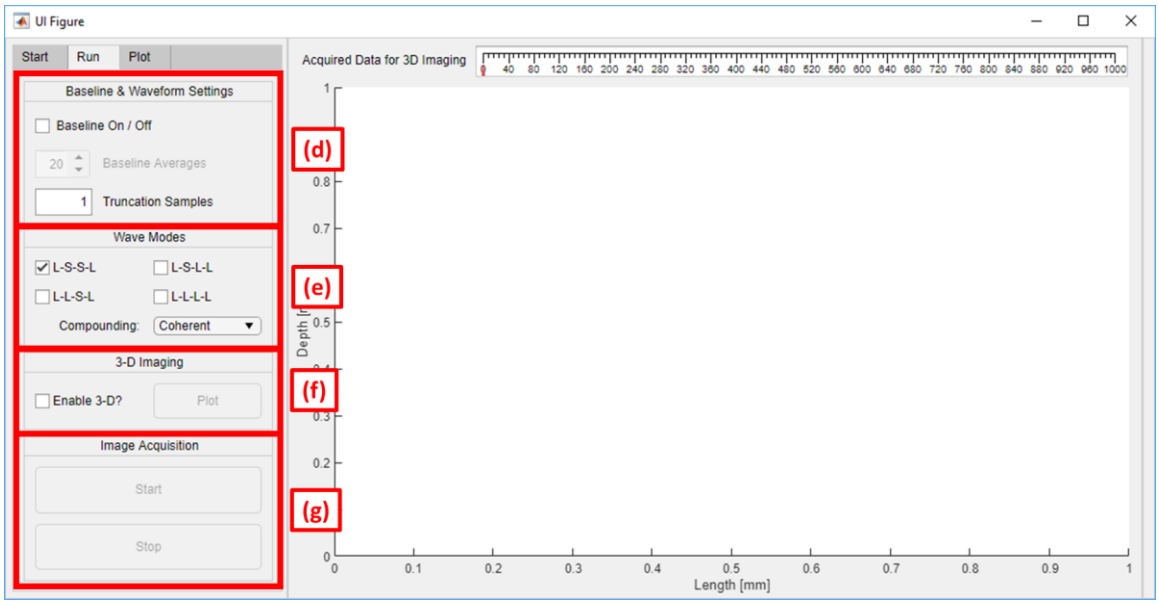

Figure 6-4: Imaging Algorithm MATLAB GUI – Run Screen

Sections (d) and (e) are the “Baseline & Waveform Settings” and “Wave Modes” options, respectively. The “Baseline & Waveform Settings” contains the option to turn on baselining which helps in reducing image artifacts. Once baselining is turned on, one can

change the number of acquisitions used to build the baseline data matrix for baseline subtraction. The “Truncation Samples” is to remove crosstalk interference when a wedge is not used. In Section (e), various wave modes can be selected for coherent or incoherent compounding. The wave modes used in compounding are dependent on the type of defect and type of wedge for imaging.

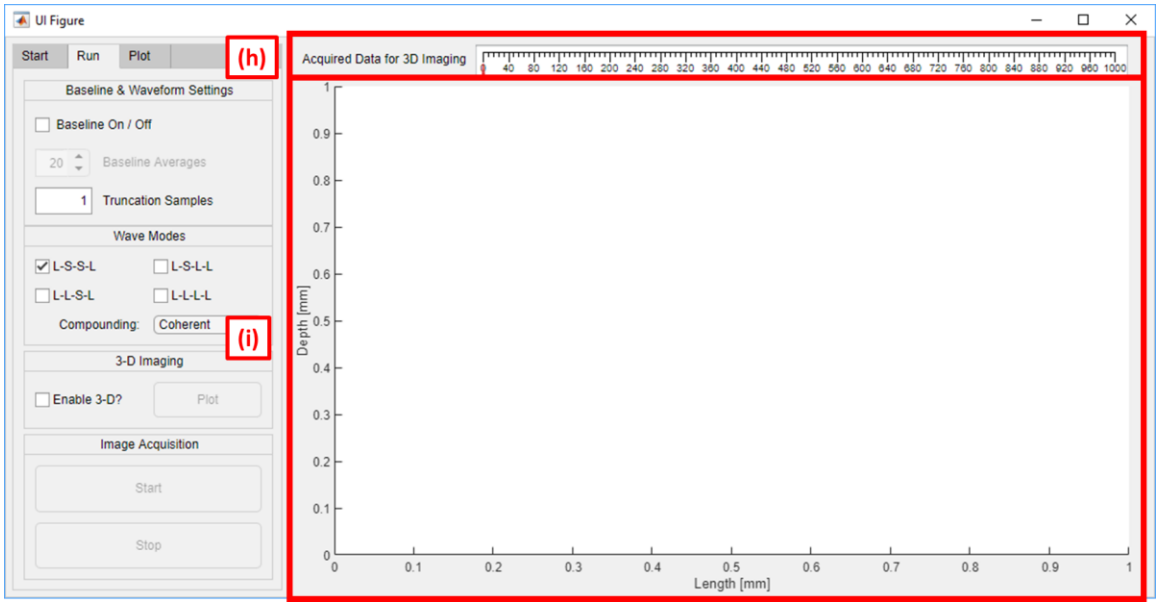

Figure 6-5: Imaging Algorithm MATLAB GUI – Plot Display

Sections (f) and (g) primarily deal with image acquisition and processing. Section (f) is used to control if 3D reconstruction is desired. If turned on, the algorithm will save the encoder value and scan data. 3D imaging is best used after an area of interest is found through 2D scanning. To enable 2D scanning only, the “Enable 3-D?” option should be unchecked. After successful hardware connection and imaging calculations, the “Start” button will be enabled. The algorithm will continue to display images in the plot display, Figure 6-5, until the “Stop” button is pressed. The plot display consists of (i), the main display for 2D images when scanning, and (h), a display for number of data points acquired for 3D imaging. Section (h) is only used when “Enable 3-D?” is checked.

After successful 3D imaging data acquisition, the “Plot” button in the Run Screen will be enabled. Pressing the “Plot” button will compile the image data into a 3D point cloud and enable 3D axis control, as shown in Figure 6-6. This option is only possible if the “Enable 3-D?” option in is checked in the Run Screen.

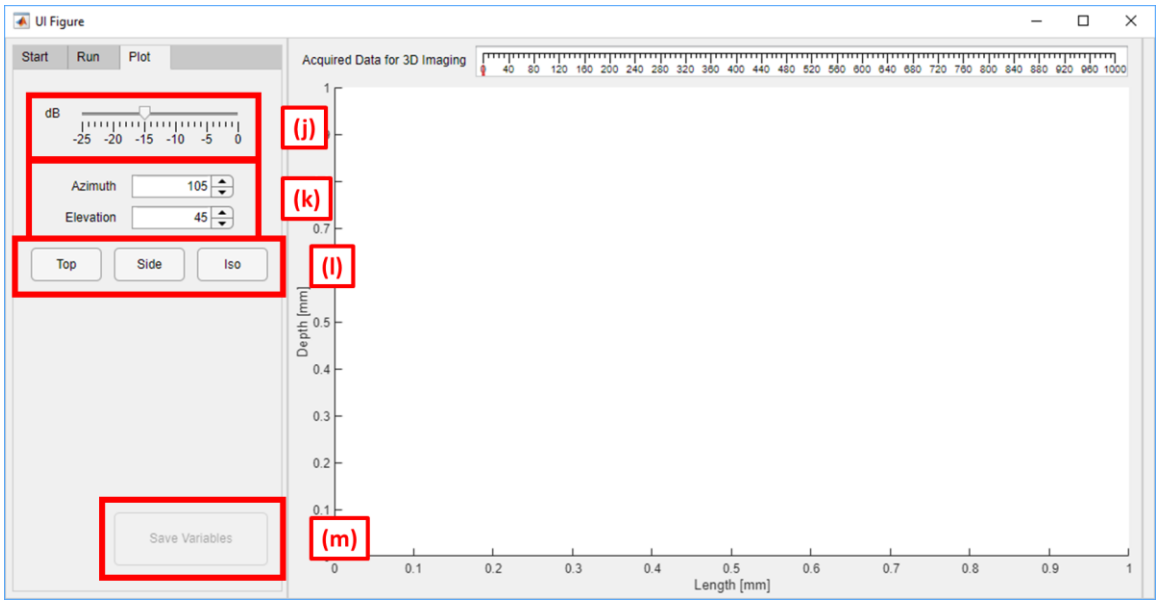

Figure 6-6: Imaging Algorithm MATLAB GUI – Plot Screen

Section (j) provides real-time control of the detection threshold. For most images, a threshold of 15 dB offers the best detection capability with the least artifacts. The controls in section (k) are for fine tune adjustment of the perspective to display the 3D results. To return to standard views, the buttons in section (l) are provided. Lastly, to save the raw 3D data, section (m)’s “Save Variables” button is used.

6.3 Technology Validation

Seven rail specimens from the FRA / TTC Defect Library were used for the experiment. Schematic examples are shown in Figure 6-7.

1. Section #20 141RE rail specimen with a drilled centered FBH inclined at 20° from the horizontal covering 20% of the head area
2. Section #12 141RE rail specimen with a drilled centered FBH inclined at 20° from the horizontal covering 10% of the head area
3. Section #14 141RE rail specimen with a drilled corner FBH inclined at 20° from the horizontal covering 10% of the head area
4. Section #36-168-I 136RE rail specimen with natural TD covering approximately 6% of head area
5. Section #UKN 136RE with a drilled centered SDH inclined at 0° from the horizontal covering 6% of head area
6. Section #B22 141RE rail specimen with natural TD.
7. Section #C34 141RE rail specimen with natural Weld Porosity.

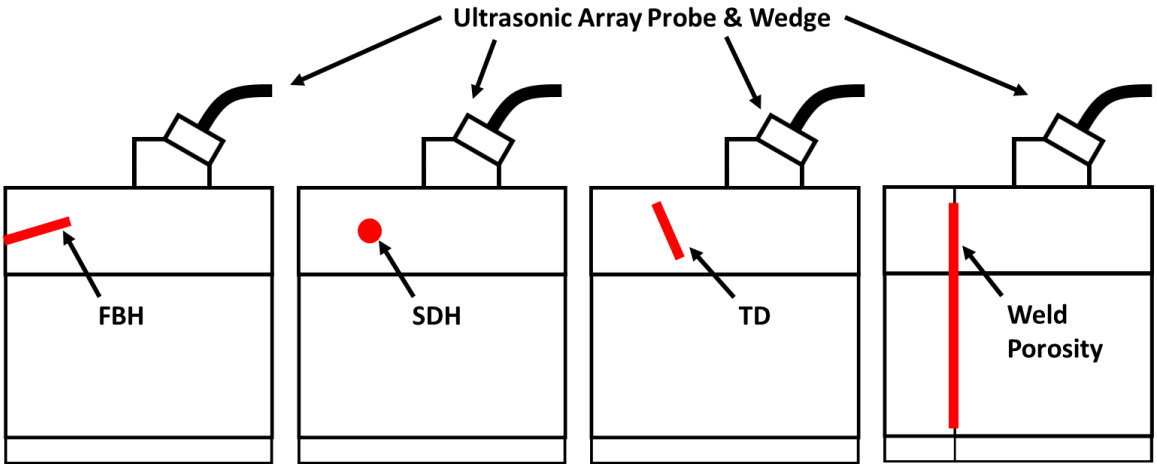

Figure 6-7: Rail Specimens with Simulated and Natural Defect for Ultrasonic Imaging

The HAs for the 136RE and the 141RE rail specimens are 4.75 in^2 (30.64 cm^2) and 5.27 in^2 (34.00 cm^2), respectively, as calculated from specifications of the American Railway Engineering and Maintenance-of-Way Association (AREMA). The areas of the FBHs covering 10% and 20% of the 141RE head area are 0.53 in^2 (3.40 cm^2) and 1.06 in^2 (6.80 cm^2), respectively. Similarly, the area of the TD covering 6% of the 136RE head area

is 0.29 in^2 (1.87 cm^2). Assuming a circular shape for the defects considered in the experimental tests, the diameters of the FBHs (10% and 20% of 141RE) and the TD are 0.82 in (2.09 cm), 1.16 in (2.95 cm), and 0.61 in (1.54 cm), respectively.

The probes used were a 32-element linear array probe (Olympus NDT P/N 2/25L32-192X10-A11-P-2.5-OM), with central frequency at 2.25 MHz and a 64-element linear array probe (Olympus NDT 5L64-38.4X10-A12-P-2.5-OM), with central frequency at 5 MHz. The ultrasonic array was attached to a 55-degree wedge (Olympus NDT SA11-N55S for the 32 element and Olympus NDT SA12-N55S for the 64 element).

The array was controlled by a FMC controller (Advanced OEM Solutions, Cincinnati, OH, USA) that generates pulsed excitations and allows access to raw waveforms in reception along with the encoder count. The arrays were coupled to the railhead using conventional ultrasonic gel couplant. The first specimen used for the tests was a 15-inch long 141RE rail segment with a flat bottom hole (FBH) centered in the rail head and covering 20% of the head area, which was drilled at a 20-degree orientation from the horizontal starting from 15 mm below the rail top surface. An FBH is commonly used to simulate a TD. The second specimen contains a smaller FBH, at 10% of head area. The third specimen has an FBH drilled into the head corner, at 10% of head area. The fourth specimen was a 136RE rail segment with a naturally occurring TD in the head field side extending for 6% of the head area (HA). The fifth specimen was a 136RE rail segment with a SDH centered in the rail head and covering 6% of the head area, which was drilled at a 0-degree orientation from the horizontal starting from 16 mm below the rail top surface and extending for 38 mm. The sixth specimen was a 141RE rail segment with a naturally occurring TD with unknown defect size. Lastly, the seventh specimen was a 141RE rail segment with a naturally occurring Weld Porosity with unknown defect size.

The experiments were conducted in either a 64 x 64 or in a 32 x 32 full-matrix capture scheme depending on the array used, with each of the elements firing sequentially, and all elements receiving at each firing, corresponding to 4096 or 1024 sets of raw waveforms, respectively. The waveforms were then transmitted via Ethernet to a CUDA enabled Alienware R13 Laptop with a NVIDIA GeForce GTX 1070 GPU.

Each of these waveforms was Hilbert transformed and then beamformed. The final image was obtained as the modulus of the Hilbert transformed images and plotted in dB scale. The purpose of these tests was to verify, experimentally, the effectiveness of ultrasonic imaging and 3D reconstruction for defect identification and quantification in railroad tracks.

6.4 Image Reconstruction in 2D

The first four rail sections with known defect sizing were used to test the 2D image reconstruction capabilities of the imaging system. In addition to improved defect location compared to traditional A-scan techniques, the ultrasonic imaging system reduces the time it takes to return quantitative results.

6.4.1 Results without Transducer Wedge

The experimental SAFT-DAS images obtained with no transducer wedge are from Section #20 141RE rail specimen with a head centered FBH covering 20% of the HA. The LL-mode reception of Figure 6-8 (a) has the highest SNR ratio with later artifacts arising from shear wave interference. The LS and SL modes of Figure 6-8 (b) and (d) are similar, with both modes producing numerous artifacts.

The artifacts are a result of the slower shear wave speed that produces a slower backpropagated time delay which, considering the longitudinal wave arrival packet, places

the defect in a region closer to the sensor array. Since shear waves possess lower energy than longitudinal waves in this array configuration, the SS-mode in Figure 6-8 (c) illustrates significant artifacts and poor results.

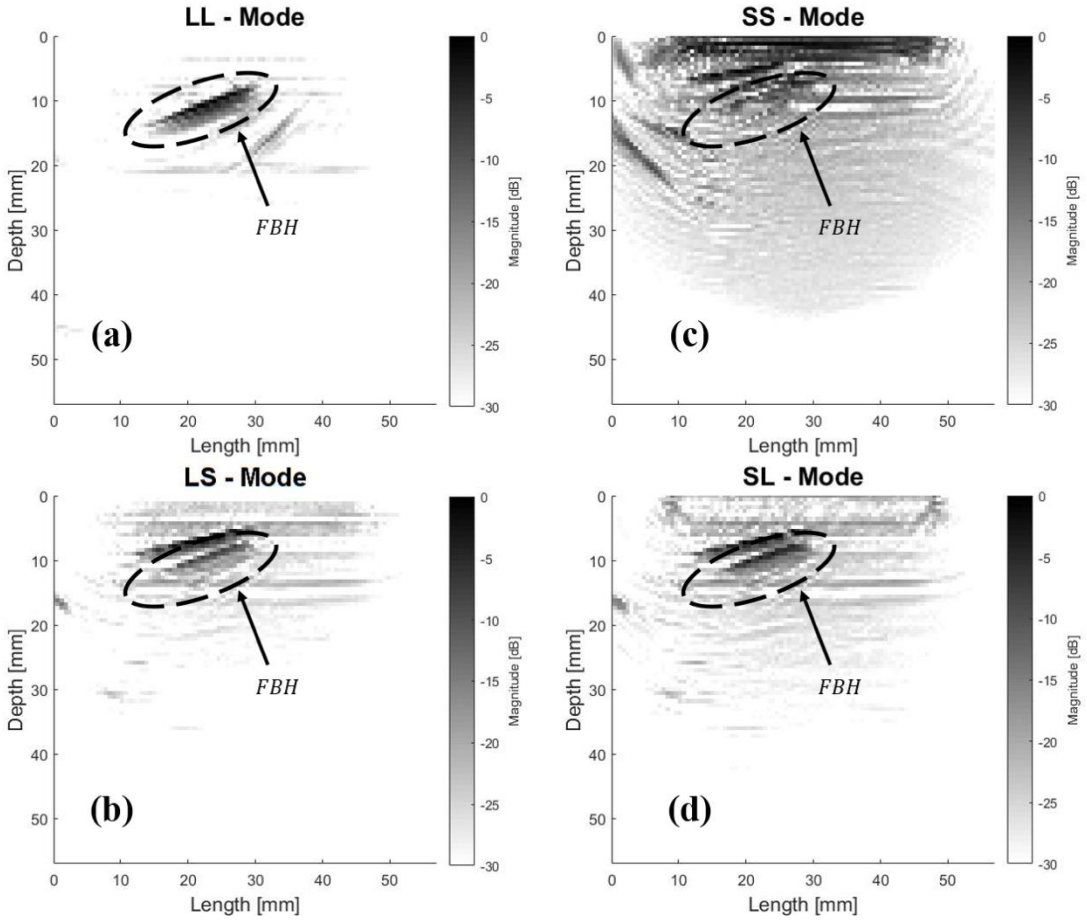

Figure 6-8: Images obtained from experimental testing of Section #20 141RE rail specimen with a drilled FBH for (a) LL Combination, (b) LS combination, (c) SS combination, and (d) SL combination.

6.4.2 Results with Transducer Wedge

Transverse defects are characterized by texture and growth rings that are traditionally detected using an angle of inspection that maximizes defect reflection oriented 20 degrees from the vertical. In this scenario, an ultrasonic transducer array oriented directly above the transverse defect is at a sub-optimal orientation, as shown in Figure 6-9 (a). As previously highlighted in the Section 3.2.3 , raytracing can be applied to angle the

ultrasonic waves and direct them in such a way that an optimal reflection from the defect can be obtained. From Figure 6-9 (b), the wedge increases the available surface area for the reflection of the ultrasonic wave from the transverse defect to the sensor, improving the identification characteristics.

The experimental results for the Section #36-168-I 136RE rail specimen with a natural TD are shown in Figure 6-10 (a) and (b) and have resolutions of 96 by 96 and 175 by 150 pixels, respectively. The images were captured using a 32-element linear array with and without a 55-degree wedge. An illustration of the sensor orientation was shown earlier in Figure 6-9. Figure 6-10 demonstrates the importance of the array orientation when defects are nearly perpendicular to the array surface. Figure 6-10 (a) was obtained by inspecting the rail specimen in the cross-sectional plane of the railroad track. Conversely, Figure 6-10 (b) was computed after scanning the specimen along the rail longitudinal axis. As shown in Figure 6-10 (a), only the top and bottom of the TD are reflected to the array when no wedge is used. By using a wedge, the actual shape and orientation of the TD are properly imaged, as shown in Figure 6-10 (b).

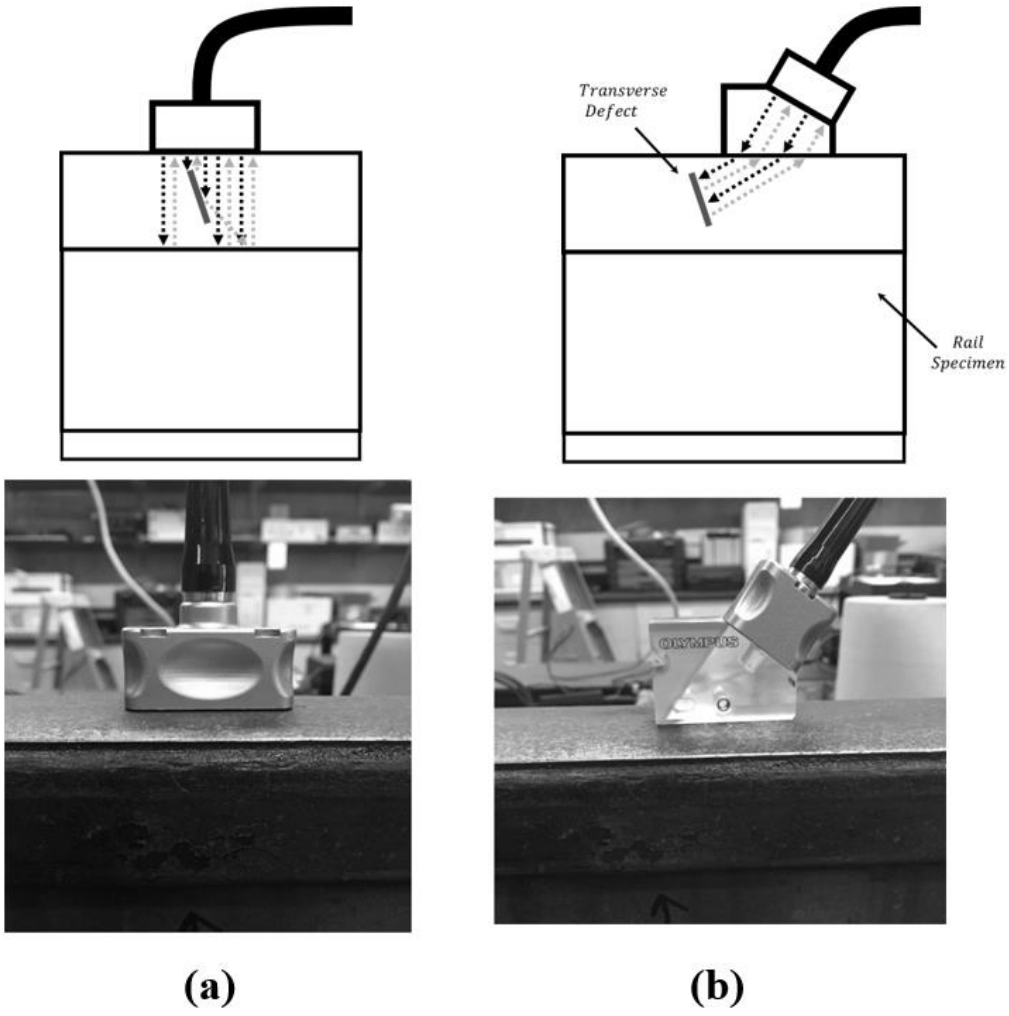

Figure 6-9: Ultrasonic array for TD imaging in rails (a) without a wedge and (b) with a wedge. Black arrow represents the transmitted wave. Grey arrow represents the reflected wave.

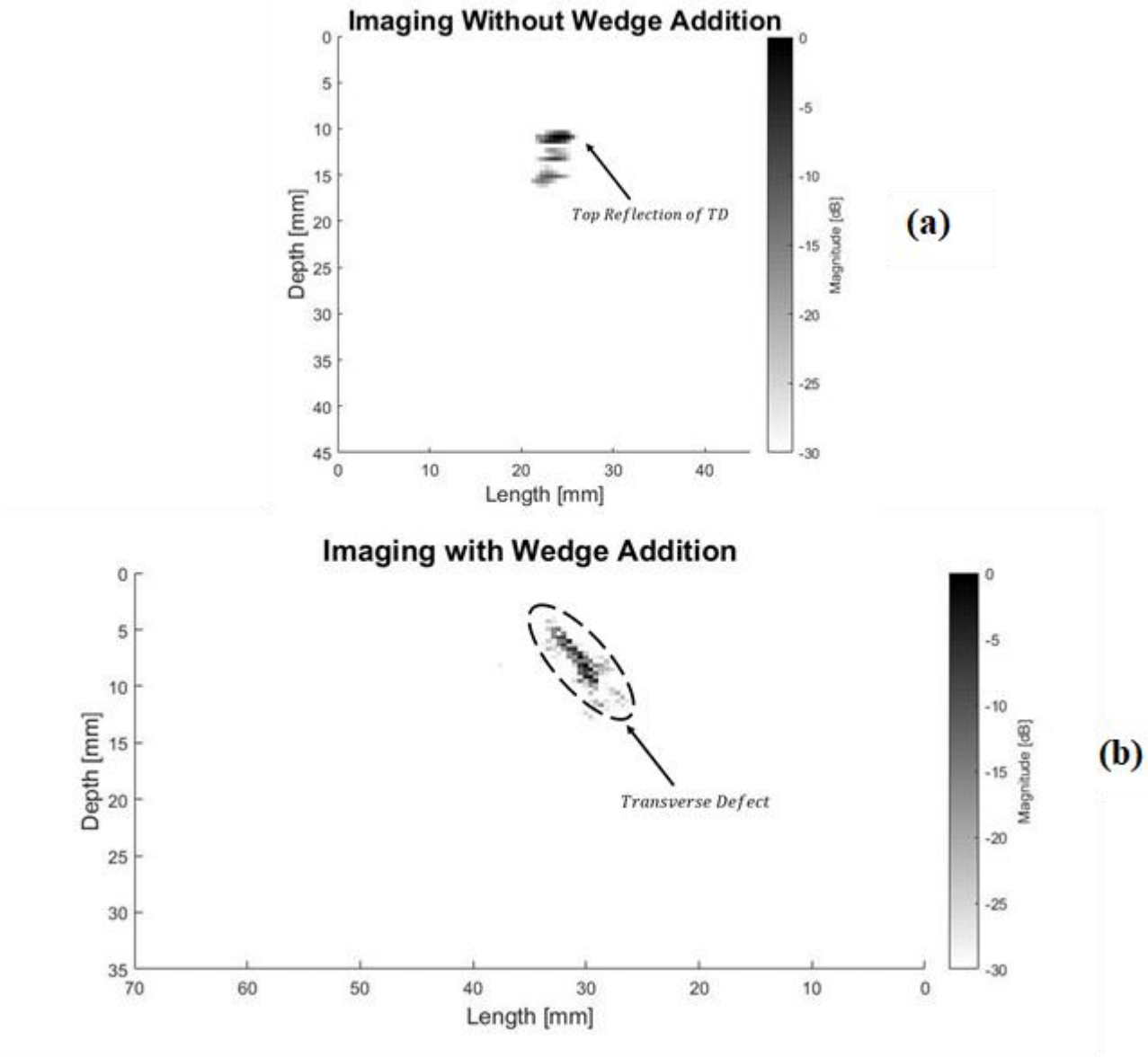

Figure 6-10: Image of Section #36-168-I 136RE rail specimen with a natural TD obtained using a 32-element linear array (a) without a wedge (cross-sectional image), and (b) with a 55-degree wedge (longitudinal section).

6.4.3 Results with Wave Mode Compounding

Utilizing wave mode compounding, detailed in Section 3.2.4 , Figure 6-11 demonstrates the dramatic improvement in array performance without increasing the number of physical elements. Only the LL and LS combinations were used in the case of no transducer wedge in Figure 6-11 (a). When the wedge was applied in Figure 6-11 (b),

the LSSL and the LSLL combinations were considered in the image compounding. In both cases, image compounding brings a dramatic improvement in terms of dynamic range and spatial resolution, as well as a considerable reduction of artifacts and noise. The two images of Figure 6-11 demonstrate that using the ultrasonic array with and without the wedge allows the reconstructing of the overall profile of the FBH (e.g. top profile without wedge and lateral profile with wedge).

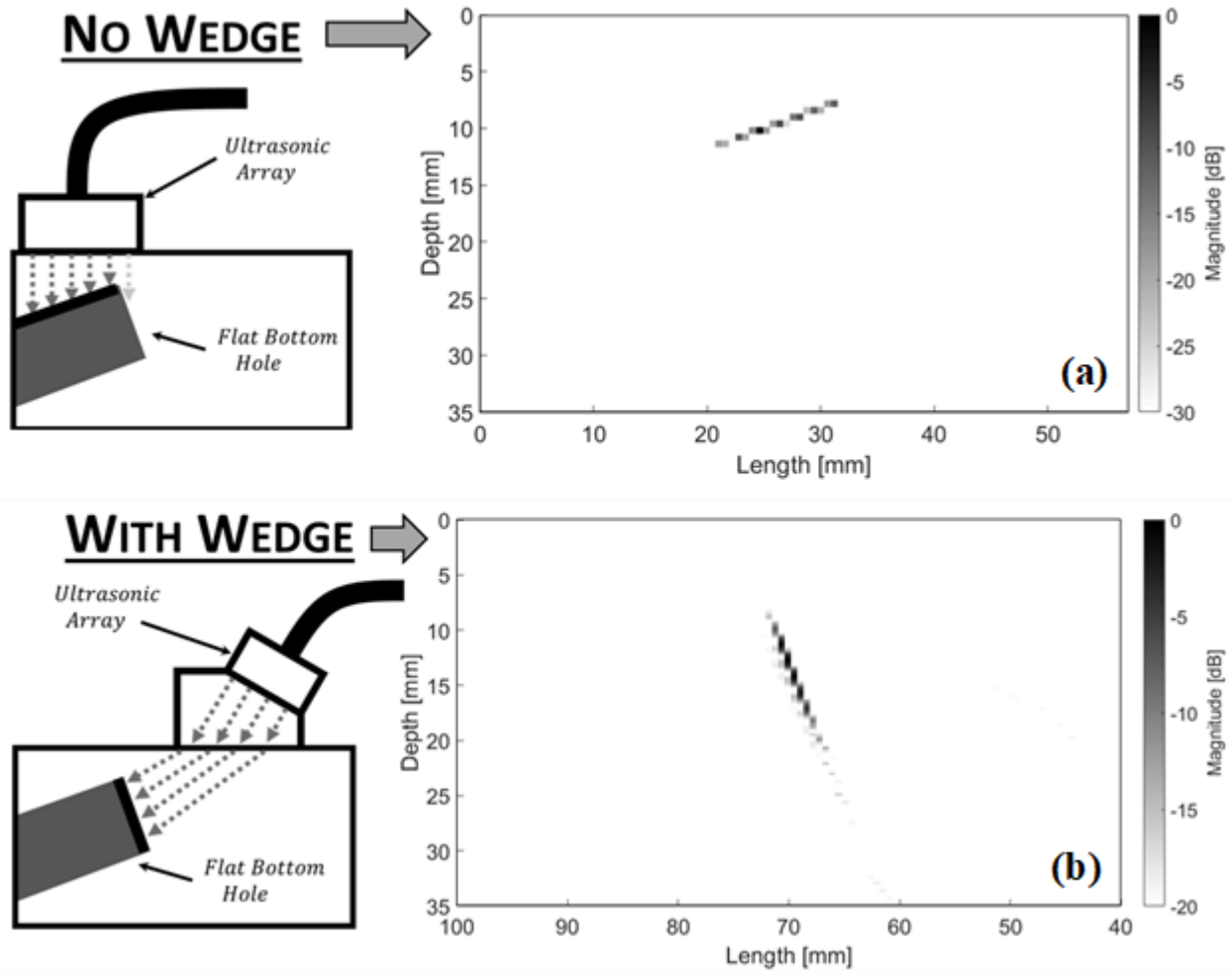

Figure 6-11: Images obtained from experimental testing of a Section #20 141RE rail specimen with a drilled FBH: comparison of wave mode compounding with (a) no wedge using LL + LS combinations, and (b) with wedge using LSSL + LSLL combinations.

6.4.4 Defect Sizing Comparison

A comparison between an ultrasonic A-scan (5 MHz single transducer) and the ultrasonic imaging system proposed was performed. Figure 6-12 is a representative comparison for an operator using an ultrasonic A-scan system on the left, and an ultrasonic imaging system on the right.

The illustration demonstrates the ease of determining the defect size and orientation using the ultrasonic imaging system versus an ultrasonic A-scan system. In addition to improved qualitative defect location, the SAF ultrasonic imaging system improves the time it takes to return quantitative results. The defect size was estimated using an ultrasonic A-scan by marking the location were the reflected waveform amplitude was half of the maximum value (known as the “-6dB amplitude drop method”). For the ultrasonic imaging system, defect sizing was performed by taking the tail ends of the reconstructed images and calculating the resulting distance. The tail ends represent the two visual extreme endpoints of the defect in the reconstructed image.

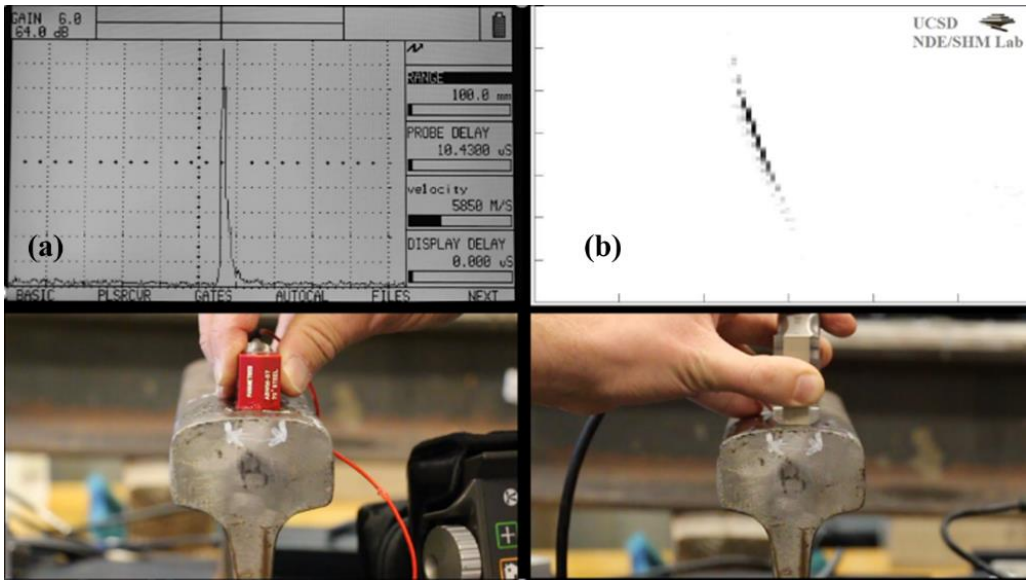

Figure 6-12: Comparison between (a) ultrasonic A-Scan and (b) proposed ultrasonic SAFT imaging system.

The ultrasonic images used for the defect sizing comparison are shown in Figure 6-13. The defect sizing procedure was performed on the four rail sections from the FRA / TTC Rail Defect Library with known defect sizes. All reconstructed images utilized an ultrasonic wedge.

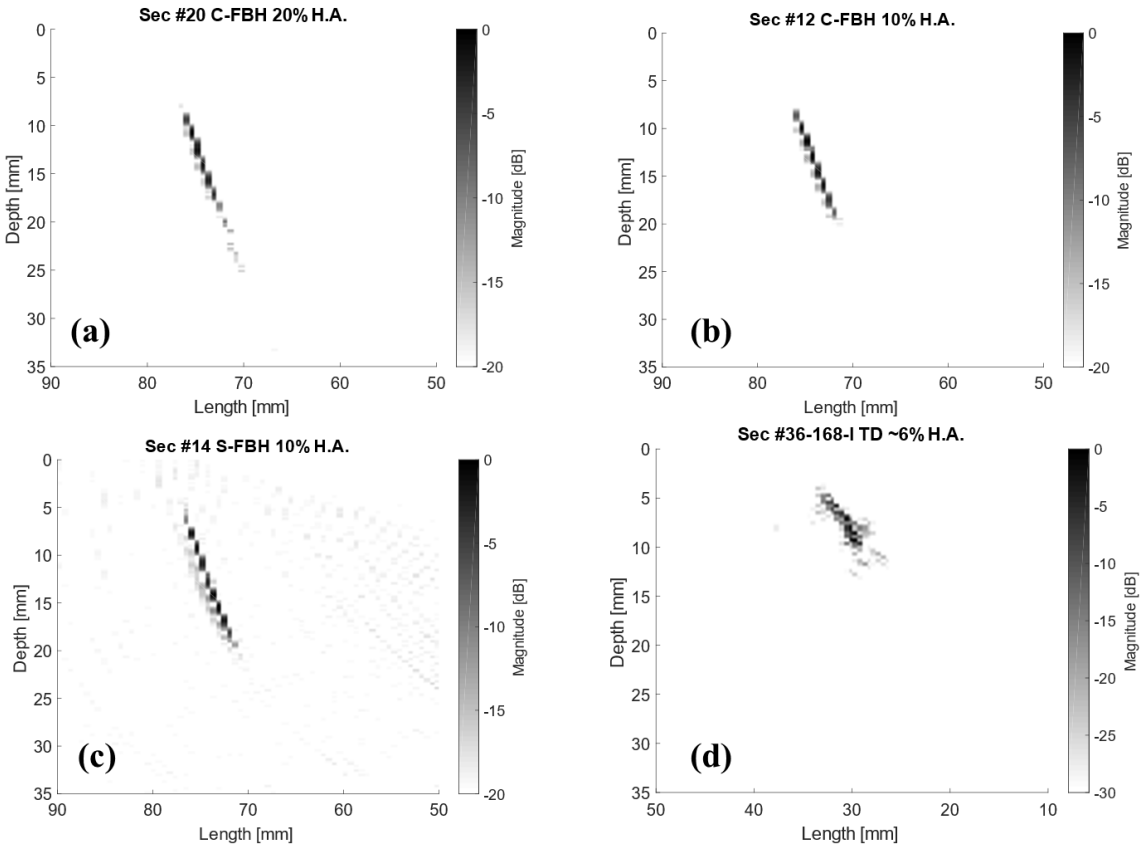

Figure 6-13: Ultrasonic images for (a) Section #20 with centered FBH at 20% HA, (b) Section #12 with centered FBH at 10% HA, (c) Section #14 with head corner FBH at 10% HA, and (d) Section #36-168-I with TD at approximately 6% of HA.

The calculated sizes for the A-scan and imaging system are listed in Table 6-7. For the Specification Sheet Estimate, the rail HA was estimated to be 22.45 cm² (3.28 in²). The defect is assumed round, and an approximate diameter was subsequently calculated from the rail HA listed. The values estimated from the Specification Sheet, A-Scan, and Imaging System for Rail sections #20, #12, and #14 are in good agreement, although the Specification Sheet consistently estimates a larger value than the A-Scan and Imaging

System result. For the rail section #36-168-I with a TD at approximately 6% of HA, the large variability from the A-Scan versus the Specification Sheet and Imaging System demonstrate the difficulties in estimating natural defect size using an A-Scan. The results tabulated in Table 6-7 highlight the potential for the ultrasonic imaging system for accurate and fast defect detection and characterization.

Table 6-7: Ultrasonic 2D Imaging Defect Size Comparison

Rail Section	Description	Spec Sheet Estimate	A-Scan Estimate	Imaging System Estimate
#20	Centered FBH at 20% HA	~ 20 mm	16 – 20 mm	17 mm
#12	Centered FBH at 10% HA	~ 17 mm	9 – 12 mm	12 mm
#14	Head Corner FBH at 10% HA	~ 17 mm	13 – 14 mm	14 mm
#36-168-I	TD at ~6% HA	~ 12 mm	18 – 25 mm	10 mm

6.5 Image Reconstruction in 3D

The final step for the characterization of rail flaws is the reconstruction of the 3D shape from the 2D “slice” images. For this purpose, the rail is scanned along a transverse direction perpendicular to the longitudinal axis, as shown in Figure 6-14 (a). At each scanning point, a 2D image is generated using the SAF algorithm. Once all the scanning locations have been inspected, the images are then stitched together to create a single volumetric image of the flaw.

Figure 6-14 (a) illustrates the scanning planes considered for the rail. As indicated by the black arrow, the 2D slice direction follows the transverse plane (scanning direction), whereas each 2D image represents the vertical plane at different scanning locations. Figure 6-14 (b) illustrates the result after all the 2D images have been combined using the

method of interpolation to stich the 2D images together. This image was obtained after inspecting Section #20 141RE, which presents an FBH extending for 20% of the HA. From this volumetric image, accurate sizing can be performed in order to estimate the extent of the defect, thus, allowing a more quantitative evaluation of the damage state of the rail specimen. From the 3-D results of Figure 6-14 (b), it can be inferred that the rail flaw has a pseudo-circular shape and its transverse dimension is about 22 mm. These estimations were previously not possible by only inspecting 2D images; therefore, the 3D representation of flaws is an important step to be performed in order to obtain a comprehensive image of the flaw. A field test was performed at Transportation Technology Center, Inc in 2019 where three rail specimens were used to demonstrate the 3D reconstruction capabilities with the point cloud method: 136RE with a side drilled hole, 141RE with a natural transverse defect, and a 141 RE with a natural weld porosity.

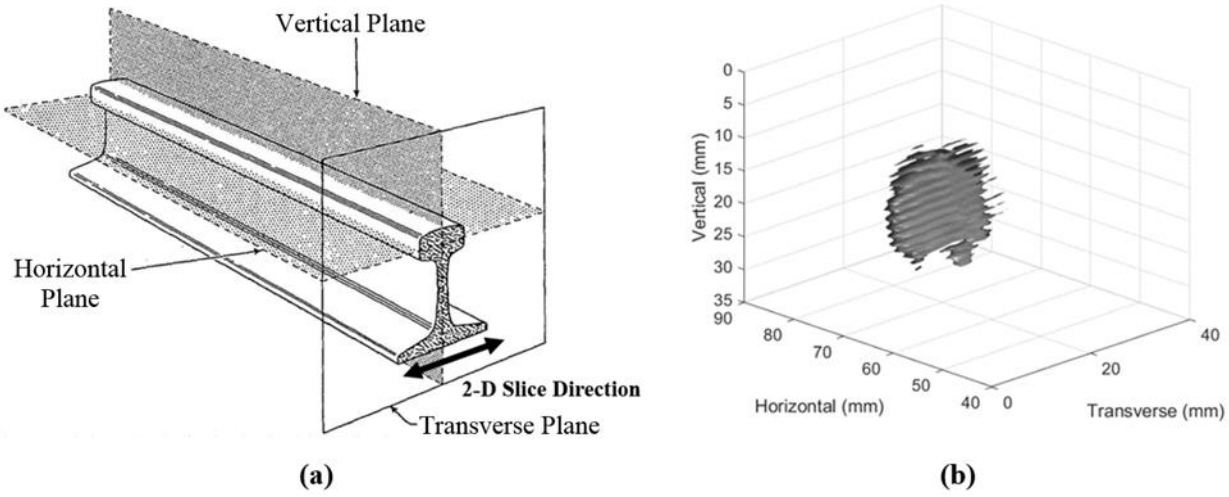

Figure 6-14: (a) Scanning planes in a rail specimen. (b) Reconstructed 3D image of a rail flaw obtained by combining multiple 2D images.

6.5.1 136RE with Side Drilled Hole

The 136RE rail segment consists of a SDH centered in the rail head and covering 6% of the head area, which was drilled at a 0-degree orientation from the horizontal

starting from 16 mm below the rail top surface and extending for 38 mm. This corresponds to a defect width of 5.5 mm and length of 38mm. In comparison, the ultrasonic 2D image results returned an estimated defect width of 4.6 mm and a depth of 16 mm while the ultrasonic 3D image estimated the defect length to be 35mm, as shown in Figure 6-15. A discontinuity in the 3D image is shown due to the sharp curvature on the side of the rail head resulting in encoder movement and temporary decoupling of the imaging system to the rail specimen.

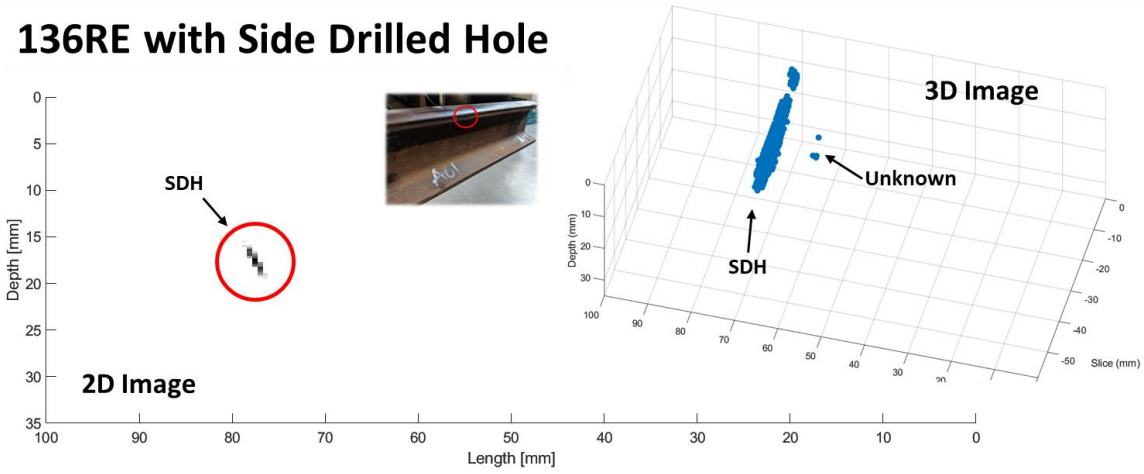

Figure 6-15: 136RE SDH 2D & 3D Image Reconstruction Results

6.5.2 141RE with Natural Transverse Defect

The 141RE rail segment consists of a naturally occurring TD with an unknown defect size. The main transverse defect has a defect length of 15.4 mm at a depth of 4.9 mm from the top of the rail head using the ultrasonic imaging system. A secondary, smaller, transverse defect was also found corresponding to a defect diameter of 5.9 mm at a depth of 5.7 mm from the surface. The results are illustrated in Figure 6-16.

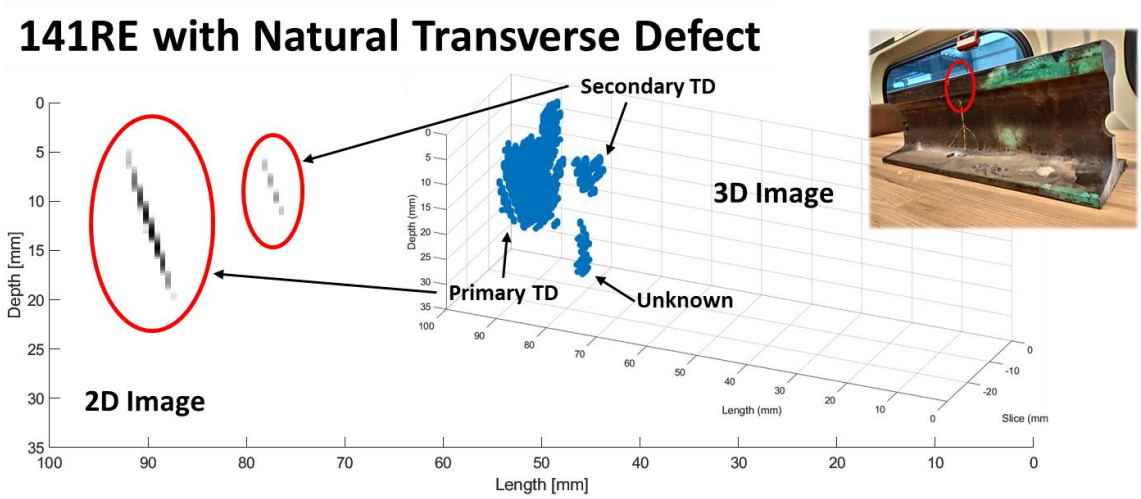

Figure 6-16: 141RE with Natural TD 2D & 3D Image Reconstruction Results

6.5.3 141RE with Natural Weld Porosity

The 141RE rail segment consist of a naturally occurring weld porosity extending for an unknown size. The results of the ultrasonic imaging system are shown in Figure 6-17. Poor signal-to-noise ratio was observed and likely attributed to the defect geometry resulting in large signal scatter. The resulting image artifacts in the nonfiltered 3D image are shown but can be removed through baseline subtraction using a pristine reference calibration block, which was unavailable at the time of the scan. The weld porosity is estimated to be 22 mm at its maximum length and have a depth of 13 mm from the surface.

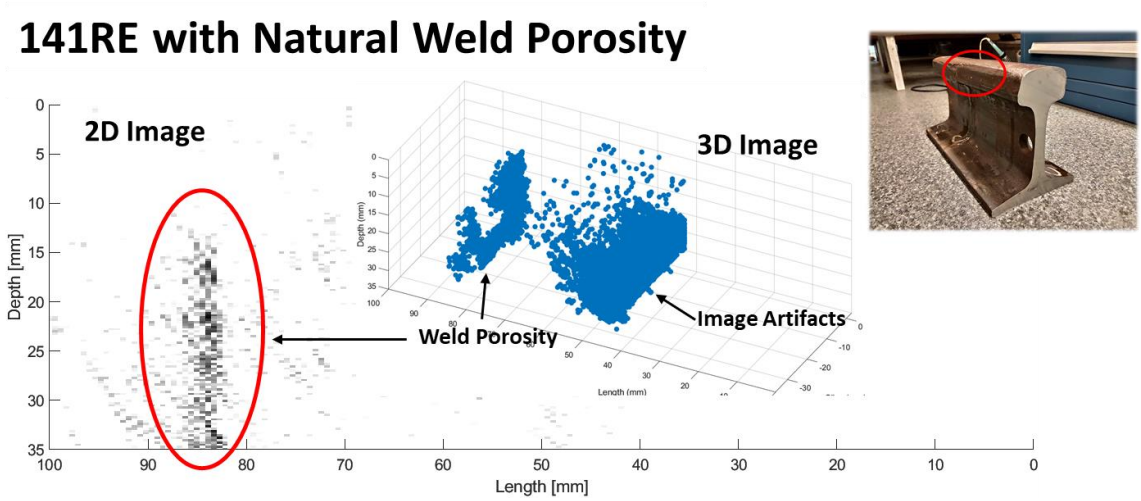

Figure 6-17: 141RE with Natural Weld Porosity 2D & 3D Image Reconstruction

6.6 Conclusion

Ultrasonic imaging has the potential for fast and quantitative detection and sizing of internal rail flaws, resulting in reduced maintenance costs through more informed decision making. The primary purpose of this kind of imaging system will be to augment or replace current hand verification techniques for rail flaws mandated following a positive detection by an inspection vehicle. The ultrasonic system provides 2D images used for fast scanning that can be compiled to generate 3D images for visualization, with the use of an encoder. A larger variety of defect sizes and orientations should also be tested to gain full confidence in the system. Finally, while the imaging prototype developed in this work is well suited for validation testing in a laboratory setting, a ruggedized more portable and lower-cost system should be developed for full deployment and commercialization.

6.7 Acknowledgements

Chapter 6, in part, has been published in *Materials Evaluation*, Sternini, S., Liang, A, Lanza di Scalea, F. (2019) with the title “Rail Flaw Imaging by Improved Ultrasonic

Synthetic Aperture Focus Techniques". The dissertation author was the primary author of this chapter.

CHAPTER 7

CONCLUSIONS

7.1 Summary of Results

The research in this dissertation investigated the use of ultrasonic passive transfer function reconstruction via non-contact air-coupled ultrasonic transducers for defect detection and the use of ultrasonic imaging via synthetic aperture focusing for defect characterization. Application results of both systems on rails were presented and demonstrated promising results for the in-field use. Passive ultrasonic inspection and ultrasonic imaging are complementary technologies: the first is for high-speed detection of suspect regions but does not label the type or size of defects; whereas, the second is for defect verification of suspect regions and visually displays the precise defect size and orientation. The ability to quickly inspection regions of interest and subsequently accurately quantify the extent of damage is integral for a reliable and cost-effective resource management program.

The results of both the first- and second-generation prototype for the passive defect detection were analyzed. A novel method of dual-output transfer function reconstruction was developed for the purpose of extracting a stable transfer function in an

environment subject to random, nonstationary excitation. Two generations of prototype were developed to test the ability to track and use the reconstructed impulse response for defect detection. Furthermore, a real-time system based on LabVIEW FPGA was developed to process massive amounts of data streamed from a suite of sensors. The proposed system is an upgrade over previous prototypes developed in the NDE & SHM research group at UC San Diego due to the elimination of the requirement for an active source (e.g. ultrasonic transducer). The use of natural wheel induced excitation eliminates signal-to-noise issues traditionally plaguing systems utilizing the active sensor approach as higher speeds are reached. Successful development of the concept of non-contact passive ultrasonic inspection would enable a new rail inspection paradigm of “smart trains” that perform inspections during regular operations. Besides simplifying inspection scheduling, this ability would result in increased reliability of discontinuity detection due to the redundancy afforded by multiple passes on the same track.

For the purpose of defect quantification, an ultrasonic imaging prototype was developed based on the synthetic aperture focusing technique. A weighting function based on the type of wave mode was implemented to reduce imaging sidelobes. To further improve the imaging ability for vertical and near-vertical flaws, a delay law that accounts for an ultrasonic wedge using ray-tracing is proposed. Once every wave mode image combination was computed, image compounding was used to further reduce noise levels without increasing the sensor’s physical aperture. The algorithm was ported over to the graphics processing unit for real-time processing of the ultrasonic image. Next, a maximum reflectivity logic was implemented to track the defect as the scanning progressed to enable the operator to quickly discern the scan result. Finally, an encoder was integrated with the system to generate a 3D image to stitch together the 2D images automatically when scanning across a specimen. The primary purpose of the ultrasonic

imaging will be to augment current hand verification techniques, although testing in motion is possible. Looking forward, this research paves the way for a system to automatically classify flagged regions of the rail and improve rail safety through the objective identification of rail flaws.

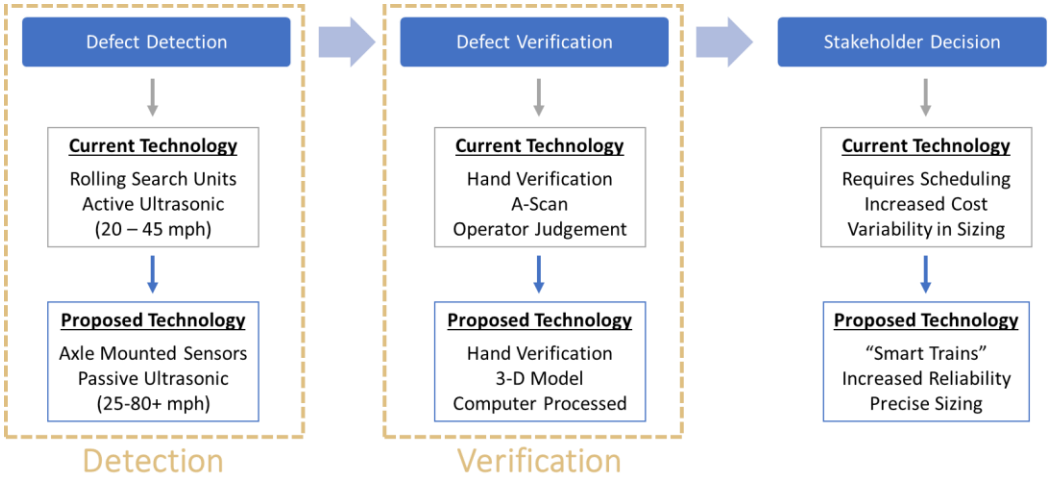

Figure 7-1: Asset Management System with Improved NDE Techniques

7.2 Recommendations for Future Work

Suggested improvements and areas for future work for the passive ultrasonic inspection and ultrasonic imaging technique are listed below:

- Use of Principal Component Analysis (PCA) to explore correlation of additional features in the outlier analysis to increase robustness of high-speed rail inspection.
- Explore generation of continuous consistent rail excitations to improve stability of passive transfer function reconstruction during train motion.
- Effects of environment on prototype for long term in-field use
- Plane wave imaging to improve signal response in high noise area
- Integration with automated crawler for full 3D reconstruction
- Implement image recognition algorithm to automatically size defects

REFERENCES

Alahakoon, S., Sun, Y.Q., Spiryagin, M., Cole, C., 2017. Rail Flaw Detection Technologies for Safer, Reliable Transportation: A Review. J. Dyn. Syst. Meas. Control 140, 020801. https://doi.org/10.1115/1.4037295

Baggeroer, A.B., Kuperman, W.A., Mikhalevsky, P.N., 1993. An overview of matched field methods in ocean acoustics. IEEE J. Ocean. Eng. 18, 401–424. https://doi.org/10.1109/48.262292

Baggeroer, Arthur B., Kuperman, W.A., Mikhalevsky, P.N., 1993. An overview of matched field methods in ocean acoustics. IEEE J. Ocean. Eng. 18, 401–424. https://doi.org/10.1109/48.262292

Baggeroer, A. B., Kuperman, W.A., Schmidt, H., 1988. Matched field processing: Source localization in correlated noise as an optimum parameter estimation problem. J. Acoust. Soc. Am. 83, 571–587. https://doi.org/10.1121/1.396151

Baggeroer, Arthur B., Kuperman, W.A., Schmidt, H., 1988. Matched field processing: Source localization in correlated noise as an optimum parameter esimation problem. J. Acoust. Soc. Am. 83, 571–587. https://doi.org/10.1121/1.396151

Bartoli, I., Lanza di Scalea, F., Fateh, M., Viola, E., 2005. Modeling guided wave propagation with application to the long-range defect detection in railroad tracks. NDT E Int. 38, 325–334. https://doi.org/10.1016/j.ndteint.2004.10.008

Basson, E., 2018. World Steel in Figures - 2018. World Steel Association.

Brath, A.J., Simonetti, F., 2017. Phased Array Imaging of Complex-Geometry Composite Components 64, 1573–1582.

Campillo, M., Paul, A., 2003. Long-Range Correlations in the Diffuse Seismic Coda. Science 299, 547–549. https://doi.org/10.1126/science.1078551

Cannon, D.F., Edel, K.-O., Grassie, S.L., Sawley, K., 2003. Rail defects: an overview. Fatigue Fract. Eng. Mater. Struct. 26, 865–886. https://doi.org/10.1046/j.1460-2695.2003.00693.x

Carter, G., Knapp, C., Nuttall, A., 1973a. Estimation of the magnitude-squared coherence function via overlapped fast Fourier transform processing. IEEE Trans. Audio Electroacoustics 21, 337–344. https://doi.org/10.1109/TAU.1973.1162496

Carter, G., Knapp, C., Nuttall, A., 1973b. Statistics of the estimate of the magnitute-coherence function. IEEE Trans. Audio Electroacoustics 21, 388–389. https://doi.org/10.1109/TAU.1973.1162487

Carter, G.C., 1987. Coherence and time delay estimation. Proc. IEEE 75, 236–255. https://doi.org/10.1109/PROC.1987.13723

Cawley, P., n.d. Practical Long Range Guided Wave Inspection - Applications To Pipes And Rail 16.

Clark, R., 2004. Rail flaw detection: overview and needs for future developments. NDT E Int. 37, 111–118. https://doi.org/10.1016/j.ndteint.2003.06.002

Coccia, S., Bartoli, I., Marzani, A., Lanza di Scalea, F., Salamone, S., Fateh, M., 2011a. Numerical and experimental study of guided waves for detection of defects in the rail head. NDT E Int. 44, 93–100. https://doi.org/10.1016/j.ndteint.2010.09.011

Coccia, S., Phillips, R., Nucera, C., Bartoli, I., Salamone, S., Scalea, F.L. di, Fateh, M., Carr, G., 2011b. UCSD/FRA non-contact ultrasonic guided-wave system for rail inspection: an update, in: Sensors and Smart Structures Technologies for Civil, Mechanical, and Aerospace Systems 2011. Presented at the Sensors and Smart Structures Technologies for Civil, Mechanical, and Aerospace Systems 2011, International Society for Optics and Photonics, p. 798113. https://doi.org/10.1117/12.880238

Dalitz, C., Pohle-Frohlich, R., Michalk, T., 2015. Point spread functions and deconvolution of ultrasonic images. IEEE Trans. Ultrason. Ferroelectr. Freq. Control 62, 531–544. https://doi.org/10.1109/TUFFC.2014.006717

Debever, C., Kuperman, W.A., 2007. Robust matched-field processing using a coherent broadband white noise constraint processor. J Acoust Soc Am 122, 1979–1986. https://doi.org/10.1121/1.2769830

Duroux, A., Sabra, K.G., Ayers, J., Ruzzene, M., 2010. Extracting guided waves from cross-correlations of elastic diffuse fields: Applications to remote structural health monitoring. J. Acoust. Soc. Am. 127, 204–215. https://doi.org/10.1121/1.3257602

Farrar, C.R., James III, G.H., 1997. System identification from ambient vibration measurements on a bridge. J. Sound Vib. 205, 1–18. https://doi.org/10.1006/jsvi.1997.0977

Federal Railroad Administration, 2015. Track Inspector Rail Defect Reference Manual (Publication No. 01574061).

Flaherty, J.J., Erikson, K.R., Lund, M.V., 1970. Synthetic aperture ultrasonic imaging systems. US3548642A.

Frazier, C.H., O'Brien, W.D., 1998. Synthetic aperture techniques with a virtual source element. IEEE Trans. Ultrason. Ferroelectr. Freq. Control 45, 196–207. https://doi.org/10.1109/58.646925

Hall, J.S., Michaels, J.E., 2010. Minimum variance ultrasonic imaging applied to an in situ sparse guided wave array. IEEE Trans. Ultrason. Ferroelectr. Freq. Control 57, 2311–2323. https://doi.org/10.1109/TUFFC.2010.1692

Hesse, D., Cawley, P., 2006. Surface wave modes in rails. J. Acoust. Soc. Am. 120, 733–740. https://doi.org/10.1121/1.2211587

Internation Union of Railways, 2017. Rail Lines (Total Route - km) [WWW Document]. Rail Lines Total Route - Km. URL https://data.worldbank.org/indicator/IS.RRS.TOTL.KM?most_recent_value_desc=true&view=chart (accessed 8.10.19).

Iturbe, I., Roux, P., Nicolas, B., Virieux, J., Mars, J.I., 2009. Shallow-water acoustic tomography performed from a double-beamforming algorithm: Simulation results. IEEE J. Ocean. Eng. 34, 140–149. https://doi.org/10.1109/JOE.2009.2015166

Jeong, D.Y., 2003. Correlations between rail defect growth data and engineering analyses, Part I: Laboratory tests [WWW Document]. URL https://rosap.ntl.bts.gov/view/dot/9896 (accessed 7.29.19).

Karaman, M., Atalar, A., Koymen, H., 1993. VLSI circuits for adaptive digital beamforming in ultrasound imaging. IEEE Trans. Med. Imaging 12, 711–720. https://doi.org/10.1109/42.251122

Kolsky, H., 1963. Stress Waves in Solids. Courier Corporation.

Lanza di Scalea, F., Sternini, S., Nguyen, T.V., 2017. Ultrasonic Imaging in Solids Using Wave Mode Beamforming. IEEE Trans. Ultrason. Ferroelectr. Freq. Control 64, 602–616. https://doi.org/10.1109/TUFFC.2016.2637299

Li, Y.D., Liu, C.B., Xu, N., Wu, X.F., Guo, W.M., Shi, J.B., 2013. A failure study of the railway rail serviced for heavy cargo trains. Case Stud. Eng. Fail. Anal. 1, 243–248. https://doi.org/10.1016/j.csefa.2013.09.003

Lindsay, R.B., 1966. The Story of Acoustics. J. Acoust. Soc. Am. 39, 629–644. https://doi.org/10.1121/1.1909936

Lobkis, O.I., Weaver, R.L., 2001. On the emergence of the Green's function in the correlations of a diffuse field. J. Acoust. Soc. Am. 110, 3011–3017. https://doi.org/10.1121/1.1417528

Mahmoud, A.M., Ngan, P., Crout, R., Mukdadi, O.M., 2010. High-Resolution 3D Ultrasound Jawbone Surface Imaging for Diagnosis of Periodontal Bony Defects: An In Vitro Study. Ann. Biomed. Eng. 38, 3409–3422. https://doi.org/10.1007/s10439-010-0089-0

Makris, N.C., 1995. A foundation for logarithmic measures of fluctuating intensity in pattern recognition. Opt. Lett. 20, 2012–2014.

Mariani, S., Lanza di Scalea, F, 2018. Predictions of defect detection performance of air-coupled ultrasonic rail inspection system. Struct. Health Monit. 17, 684–705. https://doi.org/10.1177/1475921717715429

Mariani, S., Nguyen, T.V., Zhu, X., Sternini, S., Lanza di Scalea, F., Fateh, M., Wilson, R., 2016. Non-Contact Ultrasonic Guided Wave Inspection of Rails: Next Generation Approach. ASME, Columbia, South Carolina, USA.

Mariani Stefano, Nguyen Thompson, Zhu Xuan, Lanza di Scalea Francesco, 2017. Field Test Performance of Noncontact Ultrasonic Rail Inspection System. J. Transp. Eng. Part Syst. 143, 04017007. https://doi.org/10.1061/JTEPBS.0000026

Martin-Arguedas, C.J., Romero-Laorden, D., Martinez-Graullera, O., Perez-Lopez, M., Gomez-Ullate, L., 2012. An Ultrasonic Imaging SystemBbased on a New SAFT Approach and a GPU Beamformer. IEEE Trans. Ultrason. Ferroelectr. Freq. Control 59, 1402–1412. https://doi.org/10.1109/TUFFC.2012.2341

Michaels, J.E., Michaels, T.E., 2005. Detection of structural damage from the local temporal coherence of diffuse ultrasonic signals. IEEE Trans. Ultrason. Ferroelectr. Freq. Control 52, 1769–1782. https://doi.org/10.1109/TUFFC.2005.1561631

Michalopoulou, Z.H., Porter, M.B., 1996. Matched-field processing for broad-band source localization. IEEE J. Ocean. Eng. 21, 384–391. https://doi.org/10.1109/48.544049

Montaldo, G., Tanter, M., Bercoff, J., Benech, N., Fink, M., 2009. Coherent Plane Wave Compounding for Very High Frame Rate Ultrasonography and Transient Elastography. IEEE Trans. Ultrason. Ferroelectr. Freq. Control 56, 489–506. https://doi.org/10.1109/TUFFC.2009.1067

Munk, W., Worcester, P., Wunsch, C., 1995. Ocean Acoustic Tomography.

Orringer, O., Tang, Y.H., Gordon, J.E., Jeong, D.Y., Morris, J.M., Perlman, A.B., 1988. Crack Propagation Life of Detail Fractures in Rails 199.

Orris, G.J., Nicholas, M., Perkins, J.S., 2000. The matched-phase coherent multi-frequency matched-field processor. J. Acoust. Soc. Am. 107, 2563–2575. https://doi.org/10.1121/1.428644

Pagano, D.A., 1979. Two wheel ultrasonic rail testing system and method. US4174636A.

Papadacci, C., Pernot, M., Couade, M., Fink, M., Tanter, M., 2014. High-contrast ultrafast imaging of the heart. IEEE Trans. Ultrason. Ferroelectr. Freq. Control 61, 288–301. https://doi.org/10.1109/TUFFC.2014.6722614

Peterson, J.C., Porter, M.B., 2013. Ray/beam tracing for modeling the effects of ocean and platform dynamics. IEEE J. Ocean. Eng. 38, 655–665. https://doi.org/10.1109/JOE.2013.2278914

Ph Papaelias, M., Roberts, C., Davis, C.L., 2008. A Review on Non-destructive Evaluation of Rails: State-of-the-art and Future Development. Proc. Inst. Mech. Eng. Part F J. Rail Rapid Transit 222, 367–384. https://doi.org/10.1243/09544097JRRT209

Pollard, H.F., 1977. Sound Waves in Solids. Pion.

Rose, J.L., 2004. Ultrasonic Waves in Solid Media. Cambridge University Press.

Rose, J.L., Avioli, M.J., Mudge, P., Sanderson, R., 2004. Guided wave inspection potential of defects in rail. NDT E Int. 37, 153–161. https://doi.org/10.1016/j.ndteint.2003.04.001

Rose, J.L., Avioli, M.J., Song, W.J., 2002. Application And Potential Of Guided Wave Rail Inspection. Insight Non-Destr. Test. Cond. Monit. 44, 353–358.

Roth, P.R., 1971. Effective measurements using digital signal analysis. IEEE Spectr. 8, 62–70. https://doi.org/10.1109/MSPEC.1971.5218046

Roux, P., Kuperman, W.A., 2004. Extracting coherent wave fronts from acoustic ambient noise in the ocean. J. Acoust. Soc. Am. 116, 1995–2003. https://doi.org/10.1121/1.1797754

Roux, P., Sabra, K.G., Gerstoft, P., Kuperman, W.A., Fehler, M.C., 2005. P-waves from cross-correlation of seismic noise. Geophys. Res. Lett. 32. https://doi.org/10.1029/2005GL023803

Sabra, K.G., Gerstoft, P., Roux, P., Kuperman, W.A., Fehler, M.C., 2005a. Extracting time-domain Green's function estimates from ambient seismic noise. Geophys. Res. Lett. 32. https://doi.org/10.1029/2004GL021862

Sabra, K.G., Roux, P., Kuperman, W.A., 2005b. Emergence rate of the time-domain Green's function from the ambient noise cross-correlation function. J. Acoust. Soc. Am. 118, 3524–3531. https://doi.org/10.1121/1.2109059

Sabra, K.G., Roux, P., Kuperman, W.A., 2005c. Arrival-time structure of the time-averaged ambient noise cross-correlation function in an oceanic waveguide. J. Acoust. Soc. Am. 117, 164–174. https://doi.org/10.1121/1.1835507

Sabra, K.G., Srivastava, A., Lanza di Scalea, F., Bartoli, I., Rizzo, P., Conti, S., 2007a. Structural health monitoring by extraction of coherent guided waves from diffuse fields. J. Acoust. Soc. Am. 123, EL8–EL13. https://doi.org/10.1121/1.2820800

Sabra, K.G., Winkel, E.S., Bourgoyne, D.A., Elbing, B.R., Ceccio, S.L., Perlin, M., Dowling, D.R., 2007b. Using cross correlations of turbulent flow-induced ambient vibrations to estimate the structural impulse response. Application to structural health monitoring. J. Acoust. Soc. Am. 121, 1987–1995. https://doi.org/10.1121/1.2710463

Salvermoser, J., Hadziioannou, C., Stähler, S.C., 2015. Structural monitoring of a highway bridge using passive noise recordings from street traffic. J. Acoust. Soc. Am. 138, 3864–3872. https://doi.org/10.1121/1.4937765

Schickert, M., Krause, M., Müller, W., 2003. Ultrasonic Imaging of Concrete Elements Using Reconstruction by Synthetic Aperture Focusing Technique. J. Mater. Civ. Eng. 15, 235–246. https://doi.org/10.1061/(ASCE)0899-1561(2003)15:3(235)

Schmerr, L.W., 2016. An Ultrasonic System, in: Schmerr Jr., L.W. (Ed.), Fundamentals of Ultrasonic Nondestructive Evaluation: A Modeling Approach, Springer Series in Measurement Science and Technology. Springer International Publishing, Cham, pp. 1–13. https://doi.org/10.1007/978-3-319-30463-2_1

Shapiro, N.M., Campillo, M., Stehly, L., Ritzwoller, M.H., 2005. High-Resolution Surface-Wave Tomography from Ambient Seismic Noise. Science 307, 1615–1618. https://doi.org/10.1126/science.1108339

Shull, P.J., 2002. Nondestructive Evaluation: Theory, Techniques, and Applications. CRC Press.

Snieder, R., 2004. Extracting the Green's function from the correlation of coda waves: A derivation based on stationary phase. Phys. Rev. E 69, 046610. https://doi.org/10.1103/PhysRevE.69.046610

Snieder, R., Şafak, E., 2006. Extracting the Building Response Using Seismic Interferometry: Theory and Application to the Millikan Library in Pasadena, California. Bull. Seismol. Soc. Am. 96, 586–598. https://doi.org/10.1785/0120050109

Tanter, M., Fink, M., 2014. Ultrafast imaging in biomedical ultrasound. IEEE Trans. Ultrason. Ferroelectr. Freq. Control 61, 102–119. https://doi.org/10.1109/TUFFC.2014.2882

Tippmann J. D., Zhu X., Lanza di Scalea F., 2015. Application of damage detection methods using passive reconstruction of impulse response functions. Philos. Trans. R. Soc. Math. Phys. Eng. Sci. 373, 20140070. https://doi.org/10.1098/rsta.2014.0070

Tippmann, J.D., Lanza di Scalea, F., 2015. Passive-only damage detection by reciprocity of Green's functions reconstructed from diffuse acoustic fields with application to wind turbine blades. J. Intell. Mater. Syst. Struct. 26, 1251–1258. https://doi.org/10.1177/1045389X14538539

van Wijk, K., 2006. On estimating the impulse response between receivers in a controlled ultrasonic experiment. GEOPHYSICS 71, SI79–SI84. https://doi.org/10.1190/1.2215360

Welch, P., 1967. The use of fast Fourier transform for the estimation of power spectra: A method based on time averaging over short, modified periodograms. IEEE Trans. Audio Electroacoustics 15, 70–73. https://doi.org/10.1109/TAU.1967.1161901

Wilcox, P., Evans, M., Pavlakovic, B., Alleyne, D., Vine, K., Cawley, P., Lowe, M., 2003. Guided wave testing of rail [WWW Document]. https://doi.org/info:doi/10.1784/insi.45.6.413.52892

Woolfe, K.F., Sabra, K.G., 2015. Variability of the coherent arrivals extracted from low-frequency deep-ocean ambient noise correlations. J. Acoust. Soc. Am. 138, 521–532. https://doi.org/10.1121/1.4923447

Worden, K., Manson, G., Fieller, N.R.J., 2000. Damage detection using outlier analysis. J. Sound Vib. 229, 647–667. https://doi.org/10.1006/jsvi.1999.2514

Worden, K., Sohn, H., Farrar, C.R., 2002. Novelty detection in a changing environment: regression and interpolation approaches. J. Sound Vib. 258, 741–761. https://doi.org/10.1006/jsvi.2002.5148

Zerbst, U., Beretta, S., 2011. Failure and damage tolerance aspects of railway components. Eng. Fail. Anal., The Fourth International Conference on Engineering Failure Analysis Part 1 18, 534–542. https://doi.org/10.1016/j.engfailanal.2010.06.001

Zhang, J., Drinkwater, B.W., Wilcox, P.D., 2008. Defect characterization using an ultrasonic array to measure the scattering coefficient matrix. IEEE Trans. Ultrason. Ferroelectr. Freq. Control 55, 2254–2265. https://doi.org/10.1109/TUFFC.924